

Advances in Sustainability Science and Technology

Dharmendra Tripathi
Ravi Kumar Sharma
Hakan F. Oztop
Rajamohan Natarajan *Editors*

Nanomaterials and Nanoliquids: Applications in Energy and Environment

AES
International

 Springer

Advances in Sustainability Science and Technology

Series Editors

Robert J. Howlett, Bournemouth University and KES International,
Shoreham-by-Sea, UK

John Littlewood, School of Art and Design, Cardiff Metropolitan University,
Cardiff, UK

Lakhmi C. Jain, KES International, Shoreham-by-Sea, UK

The book series aims at bringing together valuable and novel scientific contributions that address the critical issues of renewable energy, sustainable building, sustainable manufacturing, and other sustainability science and technology topics that have an impact in this diverse and fast-changing research community in academia and industry.

The areas to be covered are

- Climate change and mitigation, atmospheric carbon reduction, global warming
- Sustainability science, sustainability technologies
- Sustainable building technologies
- Intelligent buildings
- Sustainable energy generation
- Combined heat and power and district heating systems
- Control and optimization of renewable energy systems
- Smart grids and micro grids, local energy markets
- Smart cities, smart buildings, smart districts, smart countryside
- Energy and environmental assessment in buildings and cities
- Sustainable design, innovation and services
- Sustainable manufacturing processes and technology
- Sustainable manufacturing systems and enterprises
- Decision support for sustainability
- Micro/nanomachining, microelectromechanical machines (MEMS)
- Sustainable transport, smart vehicles and smart roads
- Information technology and artificial intelligence applied to sustainability
- Big data and data analytics applied to sustainability
- Sustainable food production, sustainable horticulture and agriculture
- Sustainability of air, water and other natural resources
- Sustainability policy, shaping the future, the triple bottom line, the circular economy

High quality content is an essential feature for all book proposals accepted for the series. It is expected that editors of all accepted volumes will ensure that contributions are subjected to an appropriate level of reviewing process and adhere to KES quality principles.

The series will include monographs, edited volumes, and selected proceedings.

Dharmendra Tripathi · Ravi Kumar Sharma ·
Hakan F. Oztop · Rajamohan Natarajan
Editors

Nanomaterials and Nanoliquids: Applications in Energy and Environment

 Springer

Editors

Dharmendra Tripathi
Department of Mathematics
National Institute of Technology
Srinagar Garhwal, Uttarakhand, India

Ravi Kumar Sharma
Department of Mechanical Engineering
Manipal University Jaipur
Sanganer, Rajasthan, India

Hakan F. Oztop
Department of Mechanical Engineering
Firat University
Elazig, Türkiye

Rajamohan Natarajan
Faculty of Engineering
Sohar University
Sohar, Oman

ISSN 2662-6829

ISSN 2662-6837 (electronic)

Advances in Sustainability Science and Technology

ISBN 978-981-99-6923-4

ISBN 978-981-99-6924-1 (eBook)

<https://doi.org/10.1007/978-981-99-6924-1>

© The Editor(s) (if applicable) and The Author(s), under exclusive license to Springer Nature Singapore Pte Ltd. 2023

This work is subject to copyright. All rights are solely and exclusively licensed by the Publisher, whether the whole or part of the material is concerned, specifically the rights of translation, reprinting, reuse of illustrations, recitation, broadcasting, reproduction on microfilms or in any other physical way, and transmission or information storage and retrieval, electronic adaptation, computer software, or by similar or dissimilar methodology now known or hereafter developed.

The use of general descriptive names, registered names, trademarks, service marks, etc. in this publication does not imply, even in the absence of a specific statement, that such names are exempt from the relevant protective laws and regulations and therefore free for general use.

The publisher, the authors, and the editors are safe to assume that the advice and information in this book are believed to be true and accurate at the date of publication. Neither the publisher nor the authors or the editors give a warranty, expressed or implied, with respect to the material contained herein or for any errors or omissions that may have been made. The publisher remains neutral with regard to jurisdictional claims in published maps and institutional affiliations.

This Springer imprint is published by the registered company Springer Nature Singapore Pte Ltd.

The registered company address is: 152 Beach Road, #21-01/04 Gateway East, Singapore 189721, Singapore

Paper in this product is recyclable.

Preface

Nanomaterials and nanoliquids are having unique thermal and physical properties which play a vital role in enhancing the performance of various energy- and environment-related applications. Energy requirement/storage and environmental issues/problems are also the demanding challenges in front of the world. Due to increasing human population, the energy needs are also increasing which is causing adverse effects on environment too. To mitigate this, there has to be a sustainable system to balance the energy need and its availability. It should also ensure that the environment remains safe during the increased use of energy resources. To do so, there is a need to develop more new and renewable energy sources and also to design effective energy storage systems based on nanomaterials, nanoliquids, and nanotechnology. Environmental sustainability also depends on global climate change and pollutions, such as air, soil, nanomaterials, nanoparticles, and water.

A collaborative effort from people, researchers, industries, and the government is required to make the environment sustainable. The United Nations have given 17 sustainable development goals for this purpose which focus on various aspects of human lives and also emphasize on environmental protection. Although there is a need to develop more and new renewable system, there is also a need to improve the performance of such existing systems. The use of nanomaterials is a proven way to enhance the performance of such systems. Nanomaterials now can be implemented in almost any applications ranging from simple solar systems to medical processes. They have proven their suitability in various forms in various applications. They have the capability to improve the performance of any such system significantly.

This book comprises 14 chapters and compiles the recent work on the use of nanoparticles in energy- and environment-related work. This presents experimental, numerical, analytical, and theoretical work on the use of nanomaterials in energy and environment. This compilation will help to highlight cutting-edge research and will be a ready reference for the researchers working in this arena of academia and industries. This book emphasizes on the adoptability of nanomaterials in energy- and environment-related areas. The readers will find this book useful for research contribution as well as it can also be referred to as a reference book for courses of graduate and undergraduate students. This book will provide insights related to

various forms of nanotechnological applications in green buildings, environmental and electrochemical, solar distillation systems, Green energy, storage tank of the SWH system, solar concentrator system's receiver, and CFD simulations of various aspects of nanofluids/hybrid nanofluids, which are particularly useful, valuable for the betterment of society, culture, and ultimately human beings of the universe.

Early chapters of the book focus on the environmental impact in Indian context and abroad along with the techniques to preserve it. They discuss on the various classification techniques for nanomaterials, their uses, and limitations in various applications which provides a useful insight into this domain.

Mediocre chapters of the book discuss about the energy material development and their uses for sustainable development goals. They primarily discuss the use of different materials including nanomaterials for energy efficiency. Various applications such as food drying, solar desalination, solar cooking, and battery thermal management using energy storage materials have also been highlighted in these chapters. Later chapters of this book emphasize on the use of nanofluids/nanoparticles/composite nanoparticles for various applications in energy systems and nanotechnologies. Some of these studies highlight the computational modeling and simulation-based findings which are very important to predict/estimate the dynamical behavior of a system to be designed. Lastly, the chapters report the physical and chemical behavior of hybrid nanofluid fluid flow driven by emerging pumping mechanisms through the complex geometries which are applicable in various nanotechnology-based systems. The chapters included in this book cover various environmental aspects, renewable energy- and energy storage-based systems, and nanofluids/hybrid nanofluid-based analysis for the development of nanotechnologies which will be a very much useful and ready information for future applications of engineers, industrialists, and researchers.

Srinagar Garhwal, India
Sanganer, India
Elazig, Türkiye
Sohar, Oman

Dharmendra Tripathi
Ravi Kumar Sharma
Hakan F. Oztop
Rajamohan Natarajan

Contents

1	Overview of the Major Types of Nanomaterials Used for Environmental and Energy Applications: Challenges and Prospects	1
	Amina Othmani	
2	Graphene and Its Derivatives for Desalination Membrane and Environmental Applications	15
	Sachin Sharma Ashok Kumar, J. Liew, K. H. Loh, Z. L. Goh, Khishn K. Kandiah, K. Ramesh, and S. Ramesh	
3	An Impact of Nanotechnology for Water Treatment Process	31
	A. D. Dhass, N. Beemkumar, K. Venkadeshwaran, and M. K. Aravindan	
4	Adoption of the Green Energy Technology for the Mitigation of Greenhouse Gas Emission: Embracing the Goals of the Paris Agreement	47
	Sarika, Abhishek Anand, Ramovatar Meena, Usha Mina, Amritanshu Shukla, and Atul Sharma	
5	Prospects of Alcohols with Nanoparticles as an Alternative & Renewable Automotive Engine Fuels	73
	Nitya Talwar, Gurtej Singh, Sumit Taneja, and Gurjeet Singh	
6	Battery Thermal Management (BTM) Using Hybrid Nanofluid and Porous Medium in the Cooling Channel	103
	Fatih Selimefendigil, Aykut Can, and Hakan F. Öztop	
7	Phenolic Effluent Treatment Using Advanced Nanomaterials	115
	Baskaran Sivaprakash, Natarajan Rajamohan, Angeline Reshmi, and Vedula Sairama Srinivasa Phanindra	

8	Nanoparticles and Nanocomposites for Heavy Metals Removal	139
	Gopalakrishnan Sarojini, P. Kannan, Natarajan Rajamohan, and Manivasagan Rajasimman	
9	Advances in Solar Desalination System by the Application of Nanotechnology	163
	Rahul Agrawal, Kshitij Yugbodh, and Abhishek Shrivastava	
10	Mixed Convective Flow on Nanoparticle Shape Effects Over a Stretching Sheet	175
	R. Hemalatha, Peri K. Kameswaran, and P. Sibanda	
11	Entropy Generation Analysis During Heat Transfer by Darcy-Forchheimer Flow of Water-Based Al_2O_3 Nanofluid over a Curved Stretchable Surface	193
	Kh. S. Mekheimer, M. A. Seddeek, R. E. Abo-Elkhair, Ahmed M. Salem, and Ayman A. Gadelhak	
12	Numerical Modelling of Electromagnetohydrodynamic (EMHD) Radiative Transport of Hybrid $Ti_6Al_4V-AA7075/$ H_2O Nanofluids from a Riga Plate Sensor Surface	225
	M. Gnaneswara Reddy, D. Tripathi, O. Anwar Bég, and Abhishek Kumar Tiwari	
13	Heat Transfer in EMHD Hyperbolic Tangent Ternary Hybrid Nanofluid Flow Over a Darcy-Forchheimer Porous Wedge Surface: A Numerical Simulation	249
	V. Bharathi, J. Prakash, Dharmendra Tripathi, O. Anwar Bég, Ashish Sharma, and Ravi Kr. Sharma	
14	Sensitivity Analysis and Numerical Investigation of Hybrid Nanofluid in Contracting and Expanding Channel with MHD and Thermal Radiation Effects	281
	Ahmad Zeeshan, M. Zeeshan Khan, Imran Khan, and Zeshan Pervaiz	

Editors and Contributors

About the Editors

Dharmendra Tripathi has been working as Associate Professor at the Department of Mathematics, National Institute of Technology. He completed his Ph.D. in Applied Mathematics (Mathematical Modeling of Physiological flows) in 2009 from Indian Institute of Technology BHU and M.Sc. in Mathematics from Banaras Hindu University. He has supervised 06 Ph.D. students, and 03 are working under his supervision. He has published more than 180 research papers in reputed international journals, 02 edited books in Springer, 01 edited book in CRC, 12 book chapters, and presented more than 50 papers in international and national conferences. He has delivered more than 100 lectures as Invited Speaker, Keynote Speaker, and Resource Person in various conferences, workshops, FDP, STTP, STC, refresher courses, etc. His research h-index is 49, i-10 index is 152, and his papers have more than 6800 citations. He has been listed in top 2 % researchers/scientist across the world as per updated science-wide author databases of standardized citation indicators in year 2020, 2021, and 2022. He has received President Award in 2017 by the Manipal University Jaipur for outstanding contribution, Prof. P. R. Sharma Memorial Award from International Academy for Physical Sciences (IAPS) in 2021, and also become Associate Fellow of IAPS in 2022. He was awarded some prestigious fellowships INAE fellowship in 2015 and 2016, 2017, and 2018, postdoctoral fellowships (NBHM, Dr. D. S. Kothari and Indo-EU) in 2010, etc. His research work is focused on the mathematical modeling and simulation of CFD, biomechanics; heat transfer; nanofluids; energy systems; numerical methods; etc.

Ravi Kumar Sharma has been working at Manipal University Jaipur as Professor and Director of Entrepreneurship cell at Manipal University Jaipur. He has total of 16 years of teaching and research experience in various reputed Indian and foreign universities. He earned his Ph.D. in Thermal Engineering from the University of

Malaya, Malaysia, in 2016. He has published more than 60 research papers in international journals of repute and presented his research work in many international conferences in India and abroad. He has also written 6 book chapters and two edited books published by Springer and Reviewer of many international journals. He has also delivered numerous invited/keynote speeches in FDP/STTP/workshop and conferences. His current area of research is renewable energy and thermal energy storage, in particular solar energy. His primary research is focused on the development of phase change materials or rapid heat transfer by enhancing their thermal conductivity. Dr. Sharma has supervised 3 Ph.Ds. successfully and currently supervising 04 Ph.Ds. He is also working on the development of carbon-based materials. His research is being cited globally, and one of his papers has been in the top downloaded articles and most cited in the journal for more than a year.

Hakan F. Oztop has been working as Full Professor in the Department of Mechanical Engineering, Technology Faculty, Firat University, Elazig, Turkey. He got his master's and Ph.D. degrees in Computational Fluid Dynamics (CFD) in the same university. He had been in Universite De Montreal, Canada, during his Ph.D. studies. And, he worked as Postdoc Student in the Department of Mechanical Engineering, Auburn University, Alabama, USA. He has supervised 4 Ph.D. students and 13 master's students under his supervision. His research h-index is 87, i-10 index is 399, and his papers have more than 26000 citations. He is in Highly Citation Researchers (HCR) list since 2018. His research areas are nanofluids, CFD, energy storage, drying applications, solar energy and natural, and mixed convection heat transfer and combustion.

Rajamohan Natarajan is working as Professor of Chemical Engineering at Sohar University, Oman. He earned his Ph.D. from Annamalai University, India, and since then he has been actively working in various teaching and research institutions across the globe. He has a wide research experience in nanotechnology and environmental science. He has more than 150 research papers with h-index of 26 and i-10 index of 64. Dr. Natarajan has won various awards including vice chancellor award for outstanding research at Sohar University. He is Professional Member of various international acknowledged bodies and very active in research.

Contributors

R. E. Abo-Elkhair Department of Mathematic, Faculty of Science (Boys), Al-Azhar University, Cairo, Egypt;
Department of Basic Sciences, October High Institute of Engineering and Technology-OHI, 6th of October, Giza, Egypt

Rahul Agrawal Department of Mechanical Engineering, Sagar Institute of Science, Technology and Research, Bhopal, Madhya Pradesh, India

Abhishek Anand Non-Conventional Energy Laboratory, Rajiv Gandhi Institute of Petroleum Technology, Jais, Amethi, India

M. K. Aravindan Department of Mechanical Engineering, Faculty of Engineering and Technology, JAIN (Deemed-to-be University), Karnataka, India

N. Beemkumar Department of Mechanical Engineering, Faculty of Engineering and Technology, JAIN (Deemed-to-be University), Karnataka, India

V. Bharathi Department of Mathematics, Rajalakshmi Engineering College (Autonomous), Chennai, Tamil Nadu, India

O. Anwar Bég Multi-Physical Engineering Sciences Group, Department of Mechanical and Aeronautical Engineering, Salford University, Manchester, UK

Aykut Can Department of Mechanical Engineering, Celal Bayar University, Manisa, Turkey

A. D. Dhass Mechanical Engineering Department, Indus Institute of Technology and Engineering, Indus University, Ahmedabad, India

Ayman A. Gadelhak Department of Mathematic, Faculty of Science, Helwan University, Cairo, Egypt

Z. L. Goh Department of Physics, Faculty of Science, Centre for Ionics University of Malaya, Kuala Lumpur, Malaysia

R. Hemalatha Department of Mathematics, Siddartha Institute of Science and Technology, Puttur, India

Peri K. Kameswaran Department of Mathematics, School of Advanced Sciences, Vellore Institute of Technology, Vellore, India

Khishn K. Kandiah Higher Institution Centre of Excellence (HICoE), UM Power Energy Dedicated Advanced Centre (UMPEDAC), Kuala Lumpur, Malaysia

P. Kannan Department of Chemistry, V.S.B College of Engineering Technical Campus, Coimbatore, India

Imran Khan Department of Maths and Stats, International Islamic University, Islamabad, Pakistan

M. Zeeshan Khan Department of Maths and Stats, International Islamic University, Islamabad, Pakistan

Sachin Sharma Ashok Kumar Department of Physics, Faculty of Science, Centre for Ionics University of Malaya, Kuala Lumpur, Malaysia

J. Liew Department of Physics, Faculty of Science, Centre for Ionics University of Malaya, Kuala Lumpur, Malaysia

K. H. Loh Department of Physics, Faculty of Science, Centre for Ionics University of Malaya, Kuala Lumpur, Malaysia

Ramovatar Meena Department of Environmental Sciences, Jawaharlal Nehru University, New Delhi, India

Kh. S. Mekheimer Department of Mathematic, Faculty of Science (Boys), Al-Azhar University, Cairo, Egypt

Usha Mina Department of Environmental Sciences, Jawaharlal Nehru University, New Delhi, India

Amina Othmani Faculty of Sciences of Monastir, University of Monastir, Monastir, Tunisia

Hakan F. Öztıp Department of Mechanical and Nuclear Engineering, College of Engineering, University of Sharjah, Sharjah, United Arab Emirates;
Department of Mechanical Engineering, Technology Faculty, Fırat University, Elazığ, Turkey

Zeshan Pervaiz Department of Maths and Stats, International Islamic University, Islamabad, Pakistan

Vedula Sairama Srinivasa Phanindra Department of Chemical Engineering, Annamalai University, Annamalainagar, India

J. Prakash Department of Mathematics, Avvaiyar Government College for Women, Karaikal, U.T of Puducherry, India

Natarajan Rajamohan Chemical Engineering Section, Faculty of Engineering, Sohar University, Sohar, Oman

Manivasagan Rajasimman Department of Chemical Engineering, Annamalai University, Annamalai Nagar, India

K. Ramesh Department of Physics, Faculty of Science, Centre for Ionics University of Malaya, Kuala Lumpur, Malaysia

S. Ramesh Department of Physics, Faculty of Science, Centre for Ionics University of Malaya, Kuala Lumpur, Malaysia

M. Ganeswara Reddy Department of Mathematics, Acharya Nagarjuna University Campus, Ongole, A.P, India

Angeline Reshmi Department of Chemical Engineering, Annamalai University, Annamalainagar, India

Ahmed M. Salem Department of Mathematic, Faculty of Science, Helwan University, Cairo, Egypt

Sarika Department of Environmental Sciences, Jawaharlal Nehru University, New Delhi, India;
Ashoka Trust for Research in Ecology and the Environment, Bangalore, India

Gopalakrishnan Sarojini Department of Food Technology, Dhanalakshmi Srinivasan College of Engineering, Coimbatore, India

M. A. Seddeek Department of Mathematic, Faculty of Science, Helwan University, Cairo, Egypt

Fatih Selimefendigil Department of Mechanical Engineering, College of Engineering, King Faisal University, Al Ahsa, Saudi Arabia;
Department of Mechanical Engineering, Celal Bayar University, Manisa, Turkey

Ashish Sharma Department of Mechanical Engineering, Manipal University, Jaipur, India

Atul Sharma Non-Conventional Energy Laboratory, Rajiv Gandhi Institute of Petroleum Technology, Jais, Amethi, India

Ravi Kr. Sharma Department of Mechanical Engineering, Manipal University, Jaipur, India

Abhishek Shrivastava Department of Mechanical Engineering, VIT Bhopal University, Sehore, M.P, India

Amritanshu Shukla Non-Conventional Energy Laboratory, Rajiv Gandhi Institute of Petroleum Technology, Jais, Amethi, India;
Department of Physics, University of Lucknow, Lucknow, India

P. Sibanda School of Mathematics, Statistics and Computer Science, University of KwaZulu-Natal, Pietermaritzburg, South Africa

Gurjeet Singh Mechanical Engineering, Punjab Engineering College, Chandigarh, India

Gurtej Singh Mechanical Engineering, Punjab Engineering College, Chandigarh, India

Baskaran Sivaprakash Tamilnadu Government Polytechnic College, Madurai, India

Nitya Talwar Mechanical Engineering, Manipal University Jaipur, Jaipur, Rajasthan, India

Sumit Taneja Mechanical Engineering, Manipal University Jaipur, Jaipur, Rajasthan, India

Abhishek Kumar Tiwari Department of Applied Mechanics, Motilal Nehru National Institute of Technology Allahabad, Prayagraj, Uttar Pradesh, India

D. Tripathi Department of Mathematics, National Institute of Technology, Uttarakhand, Srinagar, Uttarakhand, India

Dharmendra Tripathi Department of Mathematics, National Institute of Technology, Srinagar, Uttarakhand, India

K. Venkadeshwaran Department of Mechanical Engineering, Faculty of Engineering and Technology, JAIN (Deemed-to-be University), Karnataka, India

Kshitij Yugbodh Department of Mechanical Engineering, Sagar Institute of Science, Technology and Research, Bhopal, Madhya Pradesh, India

Ahmad Zeeshan Department of Maths and Stats, International Islamic University, Islamabad, Pakistan

Chapter 1

Overview of the Major Types of Nanomaterials Used for Environmental and Energy Applications: Challenges and Prospects



Amina Othmani 

Abstract Due to several global energy and environmental issues like global warming, rising energy consumption, and severe ecological degradation, researchers have dedicated a lot of efforts to overcome these issues, such as seeking out clean energy sources (such as solar, wind, and nuclear energy), developing effective energy storage devices (such as batteries and supercapacitors), researching new technology for pollution purification, using environmentally friendly products rather than over-using natural resources and causing serious pollution, etc., it is urgent to continue studying the development of new high-performance nanomaterials. Batteries, supercapacitors, fuel cells, solar cells, photocatalysis/electrocatalysis, and other energy-related nanomaterials are used to store and convert energy. Nanomaterials have been successfully used for many applications. Thanks to their excellent optical, electrical, and magnetic properties, these last have gained a huge interest for many applications especially, environmental and energy applications. This chapter highlights the major types of nanomaterials and nanoliquids, their properties, and their fundamental applications. Also, some merits and demerits of the use of these last in energy and environment applications were given. This is followed by a critical discussion of the current challenges and some prospects.

Keywords Nanomaterials · Environmental and energy applications

A. Othmani (✉)

Faculty of Sciences of Monastir, University of Monastir, Avenue of the Environment, 5019 Monastir, Tunisia

e-mail: othmaniamina@gmail.com

1 Introduction

The issues related to water and environmental contamination expanded day after day, which needs serious control of the generated pollution from industrial and human activities. A deep understanding of the main causes of this contamination and the proposed solutions can be seriously taken into consideration [20, 21]. Recently, researchers have dedicated great efforts for the use of nanotechnology, which offered creative solutions to many environmental issues [23]. Improved techniques for environmental monitoring, water treatment, pollution abatement, cleanup, and the affordability of alternative energy sources are some of these sources [5, 23]. The properties of nanomaterials allowed them to successfully address environmental challenges sustainably. Thanks to their high sensitivity, portability, easiness, low cost, and suitability for online and in-situ measurements compared to other methods, nanomaterials present excellent candidates for water monitoring [16]. Nanotechnology offers creative solutions to a variety of environmental problems [6]. Numerous governments, researchers, and engineers are investigating the potential of nanotechnology to bring reasonable, high-technology, and energy-efficient items to millions of individuals around the world [24]. Nanotechnology has made strides in the plan of items such as light bulbs, paints, computer screens, and fuels. Energy nanotechnology is making a difference educate the advancement of elective vitality sources, such as sun-powered and wind control [16]. Sun-oriented cells, for occurrence, turn daylight into electric streams. Nanotechnology seems to alter the way sun-based cells are utilized, making them more proficient and affordable. Solar cells, too called photovoltaic cells, are more often than not collected as an arrangement of expansive, level boards. Based on the literature, nanomaterials have been massively used for the removal of hazardous pollutants like heavy metals, dyes, phenols, etc., therefore, they can be adopted as potential candidates for water remediation applications [18]. Nanomaterials like nanocellulose are known by their, high conductivity, very high tensile strength, and the main important feature is the abundance of the raw material, which presents the most abundant polymer on the earth [18, 21]. Also, some pollution detection technologies are more widely accessible due to their low cost and excellent ecosystem monitoring, and environmental control abilities [14]. Recently, the ability of humans to support sustainable human health and the environment are improved by quick and precise sensors that can identify contaminants at the molecular level [11]. Actually, sensors, these types of energy converter can identify specific physical, chemical, mechanical, or other qualities or events in their environment and output the information as a signal, typically an electrical or optical signal. As a result, numerous sensors have been created in numerous disciplines and found numerous applications. Nanosensors are currently one of the most widely used sensors. Essentially, nanosensors are tiny chemical, physical, or biological sensors that can assess changes in the nanoscale with extremely high precision. In this context, this chapter highlights some applications of nanoparticles and nanomaterials used for environmental and energy applications, their properties, classifications, and applications. Furthermore, some

merits and demerits of nanoparticles are described. Followed by some challenges and prospects are given.

2 Nanomaterials: Definition, Properties, Classification, and Applications

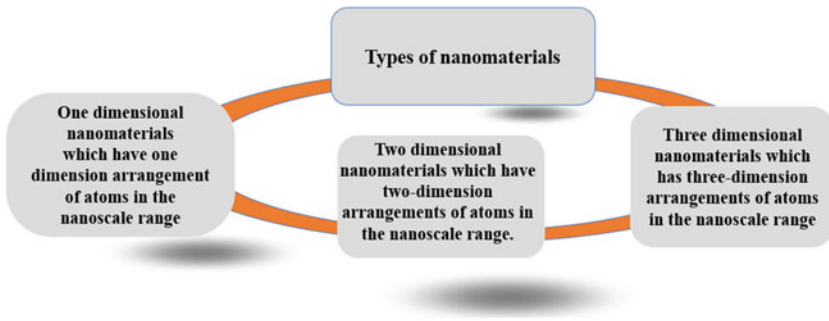
Nanomaterials are substances that have at least one exterior dimension or internal structure that is 100 nm (nm) or smaller. Based on the literature, the classification of nanomaterials can be based on their dimensions, shapes, sizes, compositions, porosity, phases, and uniformity [4]. Depending on where they came from, nanomaterials can too be broken down into normally happening, coincidental, bioinspired, and built categories [2]. During natural physicochemical processes, naturally occurring nanomaterials are formed. Accidental nanomaterials, also known as anthropogenic or waste particles, are the result of industrial processes that have been created by humans [4]. To produce materials with characteristics, engineered nanomaterials are manufactured in the laboratory or industry. Bioinspired nanomaterials are engineered materials whose properties are like those of living things or natural nanomaterials [15]. Researchers are paying more attention to bioinspired and engineered nanomaterials, but their mass is only a small fraction of that of natural nanomaterials [8]. Due to the need for large-scale production and risk assessment processes, few engineered and bioinspired nanomaterials have been approved for use in the industry despite their unique properties [7]. Nanomaterials are the mainstay of nanotechnology, a rapidly expanding field of study during the past few decades [4]. As a result, their creation and manufacture using green methods have drawn a lot of interest from the research community [6]. Four types of nanomaterials can be distinguished: those based on inorganic substances, those made of carbon, those made of organic substances, and those made of composite substances [19]. The physicochemical characteristics of the nanomaterials that share the same composition as bulk materials may vary. Materials that have been scaled down to the nanoscale can suddenly display significantly different characteristics from those that are seen on a macro scale [13]. For instance, opaque compounds can become transparent (like copper), inert substances can act as catalysts (like platinum), stable substances can catch fire (like aluminum), solids can convert into liquids at ambient temperature (like gold), and insulators can turn into conductors (silicon). Nanomaterials are more than just a subsequent stage in the downsizing of materials or particles [5].

They frequently need quite distinct production techniques. There are several “top-down” and “bottom-up” processes for producing nanomaterials of different sizes [15]. Due to their adaptable chemical, physical, and mechanical properties, nanomaterials (NMs) are becoming more important in technological applications [23].

2.1 Applications of Nanomaterials

The use of nanomaterials like carbon-based, composites, bulk-type material, metal-based materials have facilities the modern loge in many fields like medicine, environmental problems, energy storage, industry, cosmetics, sports, automotive industry, electronics, construction, and engineering materials [10].

Nanomaterials can be used for **production of more efficient solar cells and fuel cells** as an alternative clean energy source device such as environmentally friendly batteries [5]. Figure 1 presents the classification and applications of some of the nanomaterials.



Classification and applications of some of the nanomaterials

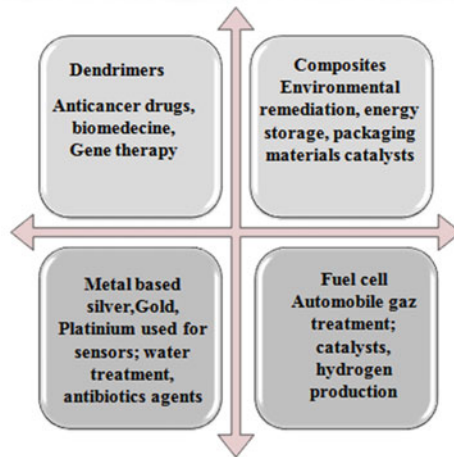


Fig. 1 Types, classifications, and applications of some of the nanomaterials

2.2 Nanotechnology and the Environment

Up to date, the use of electrochemical sensors including potentiometric (measure voltage), amperometric (measure current), and conductometric (measure conductivity) ones has offered a performing ability for environmental applications due to their ones must offer short response time, sufficient sensitivity, and good selectivity. Many researchers have confirmed the effectiveness of the use of electrochemical systems for water monitoring, in this context, Alam et al. [1] who have introduced the use of electrochemical sensing methods for water quality detection as a conversion of the chemical interactions to electrical signals. They showed that the sensing system can be easily modified and programmed to integrate other sensors, a capability that can be exploited to monitor a range of water quality parameters [1].

Liao et al. [17] have tested the performance of the use of electrochemical sensors and a smartphone for water quality monitoring and spatial mapping with disposable whole-copper. They introduced a system composed of a whole-copper electrochemical sensor, a hand-held detector, a smartphone installed with custom application program, and a cloud map website for the detection of the presence of Pb^{2+} ions and chemical oxygen demand (COD) at an exact location [17]. Table 1 presents some applications of nanomaterials for water depollution.

2.3 Nanomaterials for Electrochemical Applications

Electrochemistry has provided a powerful and promising analytical tool for research purposes in various sectors such as medical, pharmaceutical, environmental, water, wastewater, and food contributing to the health, safety, and property of human life [13].

Voltammetry, amperometry, and potentiometry are the most prominent methods extensively used for diverse analyses. Electrochemical (bio) sensors transform the electrochemical information into measurable electrical signals.

Linear Sweep Voltammetry (LSV), Cyclic Voltammetry (CV), Differential Pulse Voltammetry (DPV), and Anodic Stripping Voltammetry (ASV) are the most used techniques in electrochemical sensors.

The application of the electrochemical sensors has attracted growing interest owing to their great sensitivity, low cost, short analysis time, and instrumental robustness [23].

The electrochemical sensors are capable of an accurate analysis of various organic and inorganic compounds in a wide linear concentration range with a detection limit of as low as nano, femtomolar, or even lower concentrations that make them powerful devices for various practical applications [5]. The low power consumption along with the possibility of miniaturization and integration of the electrochemical sensors in portable tools leads to “sample-to response” devices, which can allow rapid, reproducible, and reliable real-time field analysis. Moreover, they do not need

Table 1 Some applications of nanomaterials based on cellulose for the water decontamination [3, 9, 12]

Nanomaterials	Environmental application and main achievement	
Cellulose nanocrystals (CNC) prepared from rice straw by acid hydrolysis	These nanomaterials were successfully used for the adsorption of Pb^{2+} , Ni^{2+} , and Cd^{2+} and the adsorption capacity uptakes reached, respectively, 9.7, 9.42, and 8.55 $mg.g^{-1}$	
CNC prepared via H_2SO_4 hydrolysis	The adsorption capacity of Ag^+ , Cu^{2+} , and Fe^{3+} reached, respectively, 56, 20, and 6.5 $mg.g^{-1}$	
Modified CNC by phosphate groups	The adsorption of Ag^+ , Cu^{2+} , and Fe^{3+} reached, respectively, 136, 117, and 115 $mg.g^{-1}$	
Porous calcium alginate/graphene oxide composite aerogel	The capacity uptakes of these materials for the adsorption of Pb^{2+} , Cu^{2+} , and Cd^{2+} reached, respectively, 368.2, 98.1, and 183.6 $mg.g^{-1}$	
Succinic anhydride modified mercerized nanocellulose	Adsorption of Zn^{2+} , Ni^{2+} , Cu^{2+} , Co^{2+} , and Cd^{2+}	The maximum adsorption capacities of adsorbent (Langmuir/Sips) ranged from 0.14/0.16 to 0.37/0.40 $mmol/g$
Bisphosphonate nanocellulose	Adsorption of vanadium (V)	The maximum adsorption capacity of 1.98 $mmol/g$ was attained with the CNCs that had 0.32 $mmol/g$ of bisphosphonate content
Phosphorylated nanocellulose papers	Adsorption of copper from water	The result shows that nanomaterials were able to adsorb copper from aqueous solutions up to 200 mg per one m^2 filtration area equivalent to almost 20 mg copper per one g phosphorylated CNF
Nanocomposite based on nanocellulose and silver nano-embedded pebbles	These materials have been successfully used for the removal of 99.48% of Pb^{2+} and 98.30% of Cr^{3+}	
Hydrogel composites containing nanocellulose	The results revealed that the highest adsorption of Pb^{2+} (818.4 $mg.g^{-1}$) and Cu^{2+} (325.5 $mg.g^{-1}$) is obtained within 30 min, at pH 4.0, using 20 mg of the hydrogel composite	

a specialist operator due to simplicity of working with the electrochemical devices and their operation [5]. The high sensitivity, low detection limit, wide dynamic range, reasonable selectivity, reliable and fast response, and durability are the requisite parameters of efficient analytical sensors.

However, the slow kinetics of the electron exchange process between some analytes and the bare electrode surface with restricted surface area sometimes leads to a poor and insensitive response, especially at low concentrations.

Moreover, the bare electrodes suffer from the fouling process and lack of selectivity when analyzing real complex samples that effectively restrict their performance.

Table 2 Applications of some nanomaterial-based electrochemical sensors [5, 13, 15]

Nanomaterial type	Application
Nanomaterials	Security and quality control of food and beverages
Nanomaterials	Simultaneous measurement of uric acid, ascorbic acid, and dopamine
Nanomaterials	Electroanalysis of isoniazid and rifampicin
Nanomaterials	Nonenzymatic direct detection of pesticides
Nanomaterials	Detection of neurotransmitters
Nanomaterials	Detection of hypertension markers
Nanomaterials	Cancer diagnosis
Nanomaterials	Sensors for narcotics
Carbon-based nanomaterials	Electrochemical sensors
Carbon nanostructures	Electrochemical sensors

The electrode modification process could overcome these problems and improve the sensitivity, selectivity, and longtime stability of the electrochemical sensing. Among the various electrode modifiers, nanomaterials have been in the focus of attention because of their ability to effectively improve the stability, selectivity, sensitivity, and detecting capabilities of the electrochemical sensor pollutants [11]. They have facilitated the high-performance analysis of trace level of various analytes in diverse real samples with high reliability and rapid testing capabilities [5].

In recent years, extensive studies have been conducted to develop efficient electrochemical sensors based on diverse nanomaterials to overcome these problems and improve the sensitivity, selectivity, and longtime stability of the electrochemical sensing. Among the various electrode modifiers, nanomaterials have been the focus of attention because of their ability to improve effectively the stability, selectivity, sensitivity, and detecting capabilities of the electrochemical sensors [5].

They have facilitated the high-performance analysis of trace levels of various analytes in diverse real samples with high reliability and rapid testing capabilities [15]. Table 2 shows some applications of nanomaterials based on electrochemical sensors.

2.4 Nanomaterials for Environmental Applications

Nanoparticles that are produced deliberately using specific processes are called engineered or manufactured nanoparticles, for example, fullerenes and carbon nanotubes (CNT_s). Regarding environmental issues, the system of one-dimensional (1D), thin films, or surfaces of two-dimensional (2D), this can be used in applications of electronics, chemistry, and engineering as thin films at the range of sizes (1–100 nm) or monolayer in the field of solar cells or catalysis. These thin films are inserted in

Table 3 Applications of some sensors based on nanomaterials for monitoring water pollutants [11]

Pollutants	Detection techniques
Ammonium	Differential pulsed voltammetry
Nitrate	Differential pulsed voltammetry
Nitrite	Differential pulse voltammetry
Mercury (II)	Differential pulse voltammetry
Chromium (VI)	Anodic stripping voltammetry
Lead (II)	Square-wave anodic stripping voltammetry
Arsenic (III)	Square-wave anodic stripping voltammetry
Cyanide	Square wave voltammetry
Sulfites	Square wave voltammetry
Polychlorinated biphenyl	Cyclic voltammetry
Hydroquinone catechol	Differential pulse voltammetry
Hydroquinone	Differential pulse voltammetry
Bisphenol A	Cyclic voltammetry
Carbofuran	Differential pulse voltammetry
Diisopropyl fluorophosphate	Amperometry
Isoproturon carbendazim	Square-wave anodic stripping voltammetry

different technological applications, including development of a new generation of environmental sensing systems, chemical and biological sensors, fiber-optic systems, and magneto-optic and optical device [14].

The sun sends an infinite light free from environmental pollution and noise is a renewable source of energy. The energy drawn from the sun can easily compensate for nonrenewable sources of energy such as fossil fuels and petroleum deposits on the earth. The solar cells have passed through a large number of improvement steps from one generation to another because of their importance for the generation of alternative energy [5, 15] (Table 3).

3 Merits and Demerits of the Use of Nanomaterials in Energy and Environment Applications

Nanotechnology has offered great solutions for clean, affordable, and renewable energy sources, however, decreasing energy consumption and lessen the toxicity burdens on the environment are still among the main concerns [11]. One of the main advantages offered by the use of nanotechnology for energy applications is the ability to improve the efficiency of fuel production from raw petroleum materials through better catalysis. It is also enabling reduced fuel consumption in vehicles and power plants through higher-efficiency combustion and decreased friction. Also,

nanotechnology has been successfully applied to oil and gas extraction through, such as its use for the lift valves in offshore operations or the use of nanoparticles to detect microscopic down-well oil pipeline fractures.

Up to date, researchers have succeeded to investigate carbon nanotube “scrubbers” and membranes to separate carbon dioxide from power plant exhaust. Furthermore, they have developed wires containing carbon nanotubes with low resistance compared to the high-tension wires currently used in the electric grid, thus reducing transmission power loss.

More than this, nanotechnology was incorporated into solar panels to convert sunlight to electricity. Nanostructured solar cells could be cheaper to manufacture and easier to install, since they can use print-like manufacturing processes and can be made in flexible rolls rather than discrete panels.

Therefore, nanotechnology is already being used to develop many new kinds of batteries that are quicker charging, more efficient, lighter weight, have a higher power density, and hold electrical charge longer [22].

An epoxy containing carbon nanotubes is being used to make windmill blades that are longer, stronger, and lighter-weight than other blades to increase the amount of electricity that windmills can generate.

In the area of energy harvesting, researchers are developing thin-film solar electric panels that can be fitted onto computer cases and flexible piezoelectric nanowires woven into clothing to generate usable energy on the go from light, friction, and/or body heat to power mobile electronic devices. Similarly, various nanoscience-based options are being pursued to convert waste heat in computers, automobiles, homes, power plants, etc., to usable electrical power.

There are numerous ways that nanotechnology can help identify and remove environmental toxins in addition to ways that it can improve energy.

With quick, inexpensive detection and treatment of water contaminants, nanotechnology may be able to help address the need for accessible, clean drinking water.

A thin film membrane with nanopores has been created by engineers for energy-efficient desalination. Compared to current conventional filters, this molybdenum disulfide membrane filtered two to five times more water.

By chemical reactions that render the contaminants harmless, nanoparticles are being created to remove industrial water pollution from groundwater.

Compared to approaches that call for pumping the water out of the earth for treatment, this procedure would be less expensive. For use in cleanup applications, researchers have created a nanofabric “paper towel” made of microscopic wires of potassium manganese oxide that can absorb 20 times its weight in oil.

Researchers have also utilized magnets to mechanically remove oil from water by putting magnetic, water-repellent nanoparticles in oil spills.

Many airplane cabin and other types of air filters are nanotechnology-based filters that allow “mechanical filtration,” in which the fiber material creates nanoscale pores that trap particles larger than the size of the pores. The filters also may contain charcoal layers that remove odors.

Nanotechnology-enabled sensors and solutions are now able to detect and identify chemical or biological agents in the air and soil with much higher sensitivity than ever before.

The promise of nanotechnology is the creation of multifunctional materials that will aid in the construction and upkeep of lighter, safer, more intelligent, and more effective ships, planes, and automobiles. Moreover, nanotechnology provides several ways to enhance the transportation system:

In addition to the structural components made of polymer nanocomposites discussed above, nano-engineered materials used in automotive products also include high-power rechargeable battery systems, thermoelectric materials for temperature control, lower rolling resistance tires, highly efficient/cheap sensors and electronics, thin-film smart solar panels, fuels additives, and improved catalytic converters for cleaner exhaust and longer range.

Nano-engineering holds great promise for enhancing the performance, resiliency, and longevity of highway and transportation infrastructure components while lowering their life cycle costs. These materials include aluminum, steel, asphalt, concrete, and other cementitious materials, as well as their recycled forms.


Innovative features, including self-healing structures or the capacity to produce or transport energy, may be incorporated into conventional infrastructure materials via new systems.

Nanoscale sensors and devices may provide cost-effective continuous monitoring of the structural integrity and performance of bridges, tunnels, rails, parking structures, and pavements over time [14]. Nanoscale sensors, communications devices, and other innovations enabled by nanoelectronics can also support an enhanced transportation infrastructure that can communicate with vehicle-based systems to help drivers maintain lane position, avoid collisions, adjust travel routes to avoid congestion, and improve drivers' interfaces to onboard electronics [15].

Despite the huge number of merits offered by nanotechnology and nanomaterials for environmental and energy applications, it still presents some demerits as shown in Fig. 2.

4 Nanomaterials' Limitations and Future Prospects

Even though nanoparticles have distinctive chemical and physical characteristics and a wide variety of uses, several difficult problems must be resolved before industrialization, impact, and full realization of these materials are possible. The industrialization of innovative nanomaterials with cheaper prices, higher functionality, and more manufacturing ability depends on the development of fabrication technique [15]. A significant obstacle is the lack of a manufacturing method that can produce them continuously and reproducibly on a wide scale. For the widespread promotion of emerging nanotechnology, investigating synthetic ways to large-scale production at low cost is crucial. Since the properties of nanomaterials change with time and the surrounding environment, therefore, the development of nanometrology



Benefits		Potential risks
Replacement of toxic components and less energy use	Materials and energy efficiency	Unpredicted effects
Water sterilization	Toxity	Ecotoxicological properties
Groundwater remediation	Mobility	Ecotoxicological properties
Removal of pollutants in different media	Sorption capacity	Mobilization and transport of pollutants
Degradation of pollutants	Catalyst activity	Ecotoxicological properties
Tailoring of end-use properties	Functionalization	Mobility, ecotoxicological properties
Medical purpose	Human cells	Ecotoxicological properties

Fig. 2 Main advantages and disadvantages of nanomaterials

and further advancement in the existing measurement techniques and designing of new ones is required; nanoscale structures cannot be manufactured unless appropriate characterization methodologies are used. One of the main challenges facing the industrialization of nanomaterials for catalysis is the lack of in-situ information about catalysts. This factor has limited the understanding of catalytic mechanisms and the development of catalysts with high selectivity and activity. Selectivity is a critically important issue for the commercialization of nanocatalysts; achieving 100% selectivity to minimize the formation of byproducts is a crucial challenge in catalysis that is not fully addressed. Cost and time-effective technologies for recovery of nanocatalysts and nanoadsorbents used in industrial processes are other critical issues that need more research and investigations. Increasing the sensor sensitivity, operational lifetime, and cost are also among the challenging issues faced by the industrialization of nanosensors. Reproducibility, reliability, and stability of devices based on nanomaterials are the main factors that need to be considered. Researchers must keep in mind that when dealing with complex or hybrid structures, stability may be reduced, therefore, it is important to study the device, not just the nanomaterial. Furthermore, a general challenge faced by the manufacturing technologies of nanomaterials is the use of capping ligands. The capping ligands can potentially interfere with the final application of the nanomaterials in microdevices. The development of novel manufacturing technologies must be addressed in further research for the

continuous synthesis of nanomaterials with tailored compositions and tunable sizes in the absence of capping ligands [15].

5 Conclusions

The presence of many types of hazardous pollutants in natural waters and wastewater resources was a serious concern of the environment due to their high toxicity, which resulted in many dangerous effects, which are also associated with very small concentrations. Nanomaterials have offered a highly performing ability for monitoring water, air, and soil. The use of nanomaterials for many applications such as electrochemical sensors based on advanced nanomaterials helped for an intelligent quality of environmental monitoring. Shortly, improvements in nanoscience and nanotechnology will make it possible to create electrochemical sensors that are more precise, environmentally friendly, and have lower maintenance needs.

The creation of new technologies for integrating electrode materials, including nanomaterial inclusion, selective coatings, and inkjet printing, has paved the way for novel electrode designs and architectures and made it easier to include nanocomposite materials in microchips.

Several researches concluded that the variations in nanomaterial-based electrochemical sensors were balanced out by their measurement reproducibility, long lifetime, and self-calibration.

Also, there aren't many little versions of highly sensitive portable electrochemical equipment for environmental monitoring.

References

1. Alam AU, Clyne D, Jin H, Hu NX, Deen MJ (2020) Fully integrated, simple, and low-cost electrochemical sensor array for in situ water quality monitoring. *ACS Sens* 5:412–422. <https://doi.org/10.1021/acssensors.9b02095>
2. Adeleye AS, Conway JR, Garner K, Huang Y, Su Y, Keller AA (2016) Engineered nanomaterials for water treatment and remediation: costs, benefits, and applicability. *Chem Eng J* 286:640–662. <https://doi.org/10.1016/j.cej.2015.10.105>
3. Ali Azadi N, Mansouri B, Spada L, Sinkakarimi MH, Hamesadeghi Y, Mansouri A (2018) Contamination of lead (Pb) in the coastal sediments of north and south of Iran: a review study. *Chem Ecol* 34:884–900
4. Adeola A, Fapohunda O, Jimoh AT, Tunde T (2019) Scientific applications and prospects of nanomaterials: a multidisciplinary review. <https://doi.org/10.5897/AJB2019.16812>
5. Aghababai A, Jabbari H (2022) Results in engineering nanomaterials for environmental applications. *Results Eng* 15:100467. <https://doi.org/10.1016/j.rineng.2022.100467>
6. Ali HR (2017) Applications of bio-waste materials as green synthesis of nanoparticles and water purification. *Adv Mater* 6:85. <https://doi.org/10.11648/j.am.20170605.16>

7. Barhoum A, Jeevanandam J, Hussien EA, Mekkawy SA, Mostafa M, Omran MM, Abdalla MS, Bechelany M (2022) Review on natural, incidental, bioinspired, and engineered nanomaterials: history, definitions, classifications, synthesis, properties, market, toxicities, risks, and regulations
8. Barhoum A, Jeevanandam J, Rastogi A, Samyn P, Boluk Y, Dufresne A, Danquah MK, Bechelany M (2020) Plant celluloses, hemicelluloses, lignins, and volatile oils for the synthesis of nanoparticles and nanostructured materials. *Nanoscale* 12:22845–22890. <https://doi.org/10.1039/d0nr04795c>
9. Bankole MT, Abdulkareem AS, Mohammed IA, Ochigbo SS, Tijani JO, Abubakre OK, Roos WD (2019) Selected heavy metals removal from electroplating wastewater by purified and polyhydroxybutyrate functionalized carbon nanotubes adsorbents. *Sci Rep* 9(1)
10. Bissessur R (2020) Chapter 18-nanomaterials applications, polymer science and nanotechnology. Elsevier Inc. <https://doi.org/10.1016/B978-0-12-816806-6.00018-2>
11. De Quadros Melo D, De Oliveira Sousa Neto V, De Freitas Barros FC, Raulino GSC, Vidal CB, Do Nascimento RF (2016) Chemical modifications of lignocellulosic materials and their application for removal of cations and anions from aqueous solutions. *J Appl Polym Sci* 133:1–22. <https://doi.org/10.1002/app.43286>
12. Fathima SZ, Pandith AH (2016) Synthesis and characterization of zirconium-resorcinol phosphate; a new hybrid cation exchanger and dye adsorbent for water treatment. *Mater Sci Forum* 842:196–208
13. Gatoo MA, Naseem S, Arfat MY, Dar AM, Qasim K, Zubair S (2014) Physicochemical properties of nanomaterials: implication in associated toxic manifestations 2014. <https://doi.org/10.1155/2014/498420>
14. Hayat A, Marty JL (2014) Disposable screen printed electrochemical sensors: tools for environmental monitoring. *Sens (Switz)* 14:10432–10453. <https://doi.org/10.3390/s140610432>
15. Kammakakam I (2021) As featured in: materials advances. <https://doi.org/10.1039/d0ma00807a>
16. Kanoun O, Lazarević-Pašti T, Pašti I, Nasraoui S, Talbi M, Brahem A, Adiraju A, Sheremet E, Rodriguez RD, Ben Ali M, Al-Hamry A (2021) A review of nanocomposite-modified electrochemical sensors for water quality monitoring. *Sensors* 21. <https://doi.org/10.3390/s21124131>
17. Liao J, Chang F, Han X, Ge C, Lin S (2020) Wireless water quality monitoring and spatial mapping with disposable whole-copper electrochemical sensors and a smartphone. *Sens Actuators B Chem* 306:127557. <https://doi.org/10.1016/j.snb.2019.127557>
18. Mahfoudhi N, Boufi S (2017) Nanocellulose, cellulose-reinforced nanofibre composites, pp 277–304
19. OECD International Futures Programme (2007) Small sizes that matter: opportunities and risks of nanotechnologies, p 46. Allianz
20. Othmani A, Kesraoui A, Akrouit H, Elaissaoui I, Seffen M (2020) Coupling anodic oxidation, biosorption and alternating current as alternative for wastewater purification. *Chemosphere* 249:126480. <https://doi.org/10.1016/j.chemosphere.2020.126480>
21. Othmani A, Magdoui S, Kumar PS, Kapoor A (2021) Agricultural waste materials for adsorptive removal of phenols, chromium (VI) and cadmium (II) from wastewater: a review. *Environ Res.* <https://doi.org/10.1016/j.envres.2021.111916>
22. Park J, Kim KT, Lee WH (2020) Recent advances in information and communications technology (ICT) and sensor technology for monitoring water quality. *Water (Switz)* 12. <https://doi.org/10.3390/w12020510>
23. Saleh TA (2020) Nanomaterials: classification, properties, and environmental toxicities. *Environ Technol Innov* 20:101067. <https://doi.org/10.1016/j.eti.2020.101067>
24. Ziyatdinova G, Guss E, Yakupova E (2021) Electrochemical sensors based on the electropolymerized natural phenolic antioxidants and their analytical application. *Sensors* 21. <https://doi.org/10.3390/s21248385>

Chapter 2

Graphene and Its Derivatives for Desalination Membrane and Environmental Applications



Sachin Sharma Ashok Kumar, J. Liew, K. H. Loh, Z. L. Goh,
Khishn K. Kandiah, K. Ramesh, and S. Ramesh

Abstract As the global freshwater crisis worsens, this has resulted in the demand for new desalination approaches in order to provide clean water to the human population around the world. Furthermore, it has been known that high cost and energy intensive are some of the major disadvantages that are associated with the desalination methods. Moreover, reverse osmosis (RO) has been considered as one of the most popular desalination techniques, whereby this technique can be further enhanced by having a more effective membrane. Lately, due to its atomically thin two-dimensional (2D) material, permeability, selectively, tunable functionalities and along with other excellent features, graphene and its nanomaterials such as graphene oxide (GO) have shown its highest potential to serve as a key material for advanced membranes. In overall, after an introduction of membrane, graphene and its nanomaterials, this chapter presents a short overview of the current progress of the graphene-based separation membranes and its environmental applications. In our opinion, graphene and its nanomaterials are an ideal candidate for future membrane separation technology, as they offer a unique solution to the growing issue of water scarcity.

Keywords Graphene-based membranes · Graphene oxide (GO) · Reverse osmosis (RO) · Photocatalysis · Desalination · Environmental applications

S. S. A. Kumar · J. Liew · K. H. Loh · Z. L. Goh · K. Ramesh (✉) · S. Ramesh (✉)
Department of Physics, Faculty of Science, Centre for Ionics University of Malaya, Universiti
Malaya, 50603 Kuala Lumpur, Malaysia
e-mail: rameshkasi@um.edu.my

S. Ramesh
e-mail: rameshtsubra@gmail.com

K. K. Kandiah
Higher Institution Centre of Excellence (HICoE), UM Power Energy Dedicated Advanced Centre
(UMPEDAC), Level 4, Wisma R&D, Universiti Malaya, Jalan Pantai Baharu, 59990 Kuala
Lumpur, Malaysia

1 Introduction

According to research conducted by World Atlas, about 2.5% of water on Earth is freshwater, whereby from the 2.5% of the non-saline water, only 0.775% of it is available and safe for drinking. Due to climate change, places all around the world have experienced drought for the past few years for example the worst being California, USA where people are suffering from constant water shortages and Australia where the drought is so bad that the plants dry up and become fuel for fire, causing forest fires during 2019–20 [1]. Moreover, less developed countries over in the African continent have been struggling with getting clean water supply for the past few decades. Most of the desalination plants in the world use RO at 61% market share while multistage flash distillation (MSF) and multi-effect desalination (MED) are 26% and 8%, respectively. RO desalination plants apply excess pressure to reverse the osmosis process, where water passes through a semi-permeable membrane from lower to higher solute concentration [2]. The issue with RO desalination plants is their energy consumption and low efficiency. Industrial desalination plants use 3.5–4.2 kWh of energy per m³ of water, and the recovery efficiency of freshwater from seawater is about 30–45% [2]. Thus, development of desalination technology should have the utmost priority to ensure humans and other living organisms have access to freshwater for generations to come.

Because of its unique features, graphene has been touted as the wonder material ever since its discovery in 2004 [3–5]. Globally, graphene has been explored for energy storage devices due to its high conductivity, surface area, high theoretical electric double-layer capacitance. Furthermore, carbonaceous materials play a vital in supercapacitors as they serve as electrodes to store energy [6]. Moreover, derived from activated carbon, more than 80% commercial supercapacitors are currently being utilized globally [7]. Alternatively, GO has been known to be the most widely explored nanomaterial for desalination purposes as it has outstanding properties for desalination. In addition, some of the extraordinary properties of GO include high absorption, high chemical stability, porous structure, high hydrophilicity, and exceptional anti-fouling properties, respectively [6, 7]. Moreover, GO has been researched in various desalination applications such as membrane filtration, pervaporation, Air Gap Membrane Distillation (AGMD), Direct Contact Membrane Distillation (DCMD), etc. and has shown potential as the best-performing desalination membrane. Finally, for batteries and supercapacitors applications, the unique 2D structure and the properties of graphene related materials make them ideal as electrode materials as it can result in fast electron transport, superior ion storage ability, fast ion diffusion and remarkably increasing the electrochemical energy storage performances, respectively.

2 A Brief Overview on Graphene Fabrication Methods

There are various methods associated with graphene fabrication. However, it is desirable that the fabrication of graphene and graphene-based nanomaterials to be controlled in a specific manner to cater properties for specific applications. In the past years, the graphene synthesis has been conducted by two main techniques, the bottom-up and top-down approach respectively, as illustrated in Fig. 1 [9]. For instance, the bottom-up approach comprises the fabrication of graphene from alternative carbon sources, whereas the top-down approach involved the separation of staked graphite layers to yield single graphene sheets respectively [10]. Additionally, sonochemical, chemical reduction, electrochemical, and laser ablation are some other techniques that have been developed to synthesize graphene [11]. Furthermore, it was reported that the bottom-up approach involved methods such as pyrolysis, epitaxial growth and chemical vapor deposition (CVD) [8–12]. Moreover, despite having various methods available for graphene synthesis, there are still challenges that are needed to be addressed particularly to produce high-quality graphene with minimum or no contaminants, on a large scale and at low cost, respectively. For instance, liquid phase exfoliation (LPE) method has been employed to synthesize graphene at large scale, however, it exhibits low electrical characteristics. Alternatively, the mechanical exfoliation method has been widely utilized to fabricate graphene that is used for fundamental studies and research. Finally, for industrial production, the CVD has been considered to be a cheap and effective ecological method [13–15].

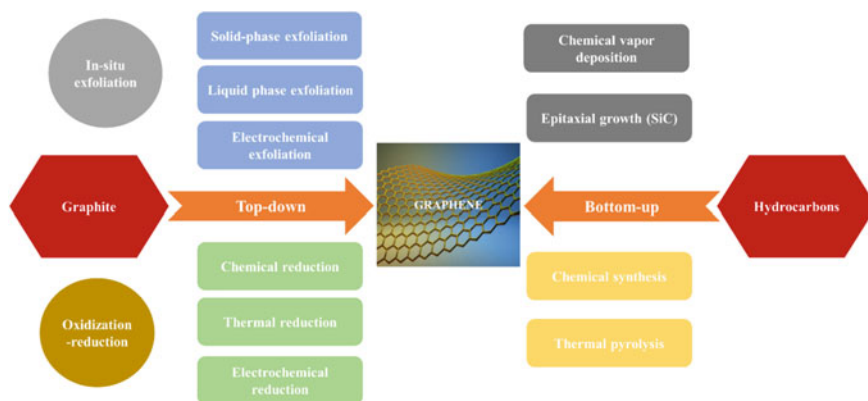


Fig. 1 Schematic diagram illustrates the bottom-up and top-down methods for graphene fabrication [9]

3 Graphene Properties

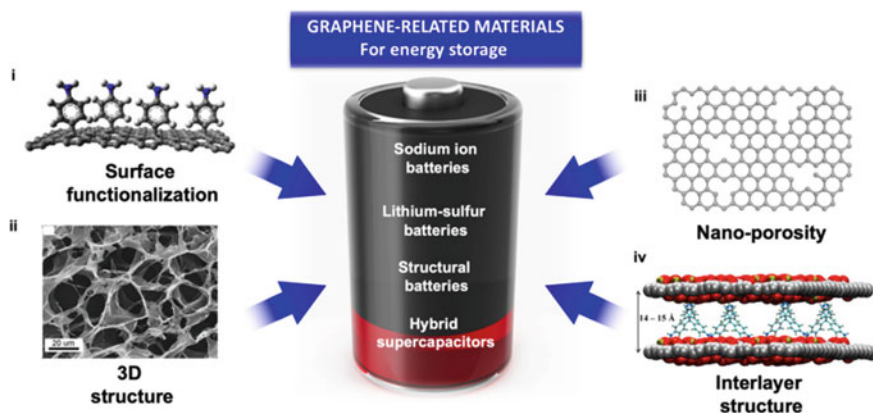
It has been reported that graphene has a theoretically large surface area of approximately $2630 \text{ m}^2/\text{g}$ and has excellent mechanical properties. For instance, a Young's modulus and an intrinsic strength of 1 TPa and 130 GPa, respectively, have been exhibited by the graphene material [8–11]. Moreover, a high thermal conductivity of approximately 5300 W/m.K was also exhibited by the graphene. Furthermore, it was reported that graphene had also exhibited very high electron density properties of $2 \times 10^{11} \text{ cm}^{-2}$ and intrinsic carrier mobility values of $2 \times 10^5 \text{ cm}^2/\text{V.s}$, respectively [11]. In addition, over a wide range of wavelength, high optical attributes have also been revealed by the graphene, whereby a single layer of graphene had demonstrated approximately 97.7% maximum light transmittance of the total incident light [11]. Moreover, it was reported that the light absorption in optical image contrast was observed to increase with the increment in graphene layers [9]. At room temperature, an electrical conductivity of 10^4 S/cm was exhibited by the defect-free monolayer graphene [9]. Overall, the extraordinary thermal, electrical, and other fascinating properties that are associated with graphene make this material a potential candidate to be broadly used globally in numerous applications including the electronic and biomedical sectors.

4 Applications

Lately, the employment of graphene and its derivatives for sustainable developments and advancements for water resources have been known to be a promising application and this technology has attracted significant attention in the research community. As mentioned above, due to their unique surface wettability function and their nano-porous structure, graphene and its derivatives are able to act as an ultrafiltration medium for chloride ions with frictionless solid–water interface, thus, resulting in more rapid water transport [16]. Table 1 distinguishes the different features of graphene-based membranes in desalination application [16]. Hence, in the upcoming subsections, the recent advancements of graphene and its nanomaterials for desalination and environmental applications will be described. Moreover, depicted in Fig. 2 are some great potentials of graphene and its nanomaterials for numerous energy storage-related applications [17].

Table 1 Comparison of different features of graphene and GO in water desalination application [16]

Features	Porous graphene membrane	GO membrane
Synthesis cost	Expensive	Cheaper according to the methodology and raw material use (graphite)
Mechanical stability	Good (resistance for water pressure)	Unsatisfactory due to unstable chemical structure
Water transport	Fast	Slow
Molecule separation performance	Excellent	Less performance
Scalability	Poor and highly dependent on the fabrication methods and handling	Good
Water flux	High with better selectively for salt ions	Restricted by tortuosity (twisted) although thinner GO sheets provide high water flux

**Fig. 2** Schematic model illustrates the typical structures of graphene and graphene-based materials and its significance in energy storage-related applications [17]

4.1 Energy and Environment Applications

4.1.1 Energy Storage Devices

Graphene and its nanomaterials have demonstrated considerable potential for its use in energy storage devices like lithium-ion batteries (LIB) and supercapacitors. Due to its high surface area, which may be further expanded chemically, makes it possible to fabricate better electrodes for energy storage devices, thus resulting in the enhancement of the device performance. Electronic conductivities of typical pure

Table 2 Summary of electrode materials containing graphene for energy storage devices

Materials	Electrode	Performance	References
Graphene-embedded lithium iron phosphate	Cathode	Initial capacity 153 mAh/g, 135 mAh/g after 100 cycles	[21]
Tin oxide nanocrystal/nitrogen-doped rGO	Anode	Initial capacity 1352 mAh/g, 1346 mAh/g after 500 cycles	[22]
Graphene-encapsulated silicon microparticles	Anode	Initial capacity 3300 mAh/g, 1400 mAh/g after 300 cycles	[23]
Iron oxide/graphene sheets aerogel	Anode	Initial capacity 930 mAh/g, 733 mAh/g after 1000 cycles	[24]
Nitrogen-doped rGO/cobalt oxide nanosheets	Anode	Initial capacity 1305 mAh/g, 1501 mAh/g after 50 cycles	[25]
Graphene paper pillared carbon black nanoparticles	Anode and cathode	Initial capacitance 138 F/g, 83.2 F/g after 2000 cycles	[26]

lithium-based cathode materials used in LIB (between 10^{-4} and 10^{-9} S/cm) are relatively low [15–17]. Electron-conducting additives are widely incorporated to such materials to enhance their electrochemical properties, thus resulting in higher device performance. However, due to graphene properties such as poor cycle stability and low coulombic efficiency, pure graphene cannot be used as a straight replacement for the present carbon-based commercial electrode materials in LIB [20]. Alternatively, graphene can be highly useful when utilized as a matrix in composite electrode materials. Lately, investigations have shown that using graphene derivatives as a cathode material can greatly improve the cathode electrochemical performance. This is due to its superior electrical conductivity and high specific surface area, which are advantageous for LIB charge transfer. Moreover, graphene has also shown its potential in the anode materials for LIB. Currently, silicon-based, transition metal-based, and tin-based electrode materials make up the majority of non-carbon-based LIB anode materials. The ever-increasing demands for the performance of LIB have been satisfied by integrating these materials with a graphene network. The graphene component in these composites performs a number of functions, including preventing undesirable volumetric changes, boosting rate capability and cyclability, and improving mechanical strength. Furthermore, graphene has been frequently employed as electrodes for supercapacitors. The researchers have reported different dimensions of graphene-based electrodes for supercapacitors with various graphene structures (i.e., film, foam, fiber, particles). Table 2 summarizes some of the current investigations and the performance of the energy storage devices [18–23].

4.1.2 Energy Conversion Devices

The incorporation of graphene in energy conversion devices has also been a fundamental topic of interest among researchers, as illustrated in Fig. 3 [27]. In addition, this material is used in the fabrication of photoanode and counter electrode

in solar cells, particularly dye-sensitized solar cells (DSSC) and quantum-dot solar cells (QDSC). Graphene is typically incorporated in the metal oxide layer of the DSSC photoanode. Here, it was reported that the graphene was able to improve the electron transfer, which increased both short-circuit photocurrent density and efficiency of the devices. For instance, by incorporating 0.5 wt.% graphene into titanium dioxide (TiO_2) nanoparticles, Sun et al. reported that 66% and 59% of the short-circuit photocurrent density ($5.04\text{--}8.38\text{ mA/cm}^2$) and efficiency (2.70%–4.28%) of DSSC were, respectively, achieved [28]. Moreover, graphene could grow by chemical vapor deposition (CVD) on platinum nanoparticles [29]. It was revealed that the electrocatalytic activity of the DSSC clearly improved by using such composite material as the counter electrode material. A smaller charge-transfer resistance was observed between the counter electrode and electrolyte. As a result, electron recombination will be inhibited, preventing the occurrence of dark current induced by back electron. Additionally, graphene has been applied in QDSC as a sensitizer. The progress of QDSC toward the goal of a sustainable future has been hampered by the widespread use of poisonous metal sulfide materials in the common quantum dots that have been developed over the years. Researchers were drawn by the development of graphene quantum dots (GQDs) as a potential substitute for sensitizers. Moreover, the good crystallinity and high conductivity are mainly attributed by the presence of the aromatic sp^2 domains in GQDs [30]. Due to their strong edge effect, great visible light absorption, and strong quantum confinement effect features, this made them a perfect candidate among ecologically benign materials for the use in QDSC. For instance, Dey et al. synthesized red nitrogen-doped graphene quantum dots and achieved 5.3% of cell efficiency, which its cell efficiency was comparable to some of the traditional solar cells [31].

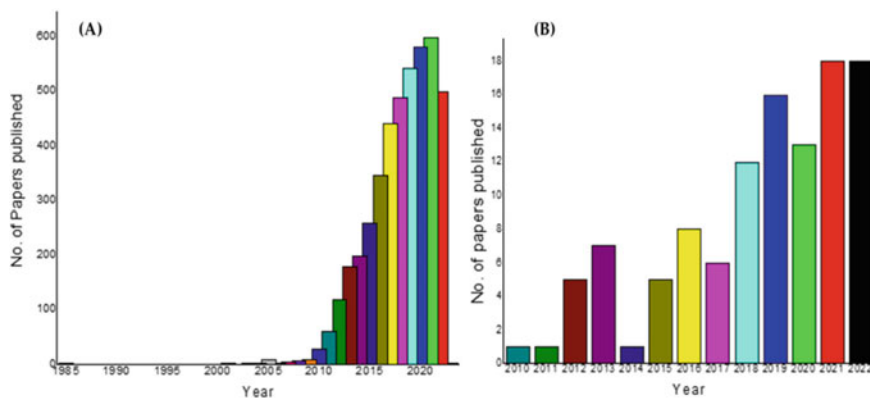


Fig. 3 A comparison between **a** graphene and energy storage and **b** graphene-based nanocomposites and energy storage, respectively, in terms number of published literatures over the past decade according to PubMed [27]

4.1.3 Environmental Applications

Interestingly, graphene and its nanomaterials have also been extensively researched for environmental applications, namely, water decontamination and gas separation. Because of their large surface areas and powerful adsorption capacities, GO and rGO were efficient adsorbents for contaminants in both air and water, respectively. Currently, wastewater contained more heavy metals, dyes, organic contaminants, and pharmaceutical waste as a result of growing industrialization. Therefore, a method must be developed that is both economical and environmentally beneficial to eliminate all of these harmful and persistent pollutants. Therefore, due to possessing 2D nanochannels and pores, graphene-based composite membranes have been viewed as highly potential membranes for wastewater treatment to remove heavy metals [32]. For instance, Noureen et al. developed a bismuth vanadate and rGO composite hydrogel for the purification of polluted water [33]. Here, the hydrogel was observed to successfully broken down harmful organic dyes that was found in the water source. Alternatively, graphene-based membranes have also been utilized to develop flexible materials for gas separation. Unlike the majority of other nanoporous materials, graphene demonstrated the ability to hold a nanopore. The top-down and bottom-up techniques are typically used to create holes in graphene sheets [34]. As mentioned previously, the nanoporous graphene membranes have been frequently used in the process of gas separation, which includes flue gas purification, carbon dioxide capture, natural gas sweetening, and gas storage, respectively. For instance, the nanoporous graphene as the separation membrane was used for hydrogen gas in coal gas [35]. The size and form of the porous graphene might be used to adjust the hydrogen permeability and selectivity. The selectivity for hydrogen gas may decline for graphene with larger holes. The geometry of the pore may have an impact on the hydrogen gas selectivity in porous graphene with the same pore area. Hence, in short, due to their unique features, namely, high surface area, high electrical conductivity, and superior mechanical qualities, graphene-based materials have demonstrated enormous potential for numerous energy and environmental applications. However, more investigation is required to enhance their functionality and scale up their manufacture for real-world uses. To ensure graphene and its derivatives are used safely and sustainably in a variety of applications, it is also necessary to thoroughly examine the effects that they have on the environment and human health.

4.2 Desalination Membranes

Desalination of seawater is considered an alternative solution for water treatment to overcome the water crisis in the future. Currently, the RO membrane technology is able to minimize the overall cost and produce high-quality water with less energy consumption than the thermal-based desalination processes. However, RO based on conventionally used polymeric membranes is currently providing insufficient performance due to its severe membrane fouling and undesirably slow water transport

[36]. This is because a separation membrane acts as a semi-permeable barrier between two phases, which allows or limits specific molecules to pass through it [37].

As mentioned previously, graphene has been considered as an ideal material for seawater desalination membranes application due to its excellent properties [38]. Hence, Gao et al. stated that graphene revolutionized the desalination industry due to its unique high selectivity and permeability where the fabricated graphene-based membranes with 1D nanopores or 2D nanochannels have been considered as high potential desalination membranes [39]. In general, the inclusion of the nanopore structures with different geometries, sizes, and functional groups between the graphene layers via physical/chemical approaches have boosted their selectivity for solute molecules/ions in aqueous solutions which could then be applied to the seawater desalination industry. Besides, A.S. Kazemi et al. reported that there were requirements to design for graphene-based membranes for desalination applications such as suspension to allow water to pass through, decoration with nanopores smaller than the diameter of rejecting ions, and mechanical stability to withstand realistic pressures [40]. Furthermore, recent studies showed that graphene membranes are highly potential materials for the water desalination industry due to the water flow rate across the graphene membrane for the same salt rejection up to 3 times higher than common RO membranes [41].

Almomani et al. demonstrated that the nonporous graphene membranes provide the same level of sodium chloride rejection and better water flow rate compared to RO membranes, and this is proved by molecular dynamic simulations [42]. Besides, the design of the nonporous graphene membranes with continuous channels enabled a greater volume of water to pass at a pressure way below compared to the conventional-based membranes [43]. Hence, the atomic thickness of graphene boosts its water permeability to a higher level and it is economically feasible as it significantly reduced the initial capital investment and the operating costs of the desalination plants. Another type of graphene-based membrane is multilayer GO which is known as stacked GO nanosheets. The formation of interlayer hydrogen bonds of GO structure makes the nanosheets highly stackable and forms a stable freestanding membrane. Thus, these phenomena allow their arrangement to be tuned into highly ordered films that enabled water permeation and rejection on undesired solutes [42]. Also, the unoxidized regions that are formed on the GO resulted in the water to pass between GO layers through the narrow hydrophobic channels [43]. In addition, the nanoporous graphene prevented the passage of the salt to pass through due to the large sizes of ions and electrostatic interactions. However, stacked GO membranes contribute higher water permeation mainly because of the formation of 2D nanochannels and the low friction compared to nanoporous graphene membranes [38].

The capacitive deionization is an electrochemically controlled method, which is based on electric double-layer capacitors (EDLCs), and it has also been considered as an eco-friendly desalination method. When an external voltage is applied, the EDLCs can be formed when the charged ions are adsorbed onto the surface or pores of porous electrodes, while the ions are released from the electrodes when the charge is removed or reversed. Graphene is one of the most optimistic capacitive deionization

electrode materials with good salt removal ability due to its fascinating properties as ascribed above [43]. In short, whenever a new technology comes in, both positive and negative views or talks pop up to criticize the outcomes based on it since they are important to improve the current efficiency and provide a modification across the existing systems and technologies. However, graphene-based nanomaterials with their outstanding properties are able to play a significant role in the desalination industry [36].

4.3 Photocatalysis

The graphene materials are gaining traction in photocatalysis due to possessing outstanding electronic properties arising from its unique Dirac cone band structure near the Fermi level, thus resulting this material to have a zero-gap semiconductor attribute [40, 41]. Moreover, the graphene is a versatile platform for numerous nanostructured semiconductors, namely, 0D QDs, 1D nanorods, 2D nanosheets and porous structures coupling, thus enabling an integrated multi-functional modification of graphene-based composite photocatalysts [45].

Furthermore, its unique properties make it an excellent use in photocatalysis to enhance photocatalytic activities. Graphene has a strong affinity to accepting electrons and is essential as conductive supports and alternative electron sinks to accept, store, and transfer photo-induced electrons, extending the lifetime of photo-generated charge carriers and enhanced charge extraction and separation [45]. Furthermore, its electronic properties can be altered by functionalization modification. For example, the electrical properties of GO are strongly dependent on its oxidation level, hence the bandgap of GO can be adjusted by varying its degree of oxidation [41]. Moreover, functional groups (e.g., carboxyl, carbonyl, hydroxyl, and epoxide) attachment to GO and defect management of GO's surface can alter its specific surface area, and adsorption capacity and behavior, thus influencing its photocatalytic properties [46].

In a photocatalytic system, GO can brace several roles: a photocatalyst, a cocatalyst, and/or a photosensitizer. The unique electronic and charge transport properties allow graphene-based cocatalysts to capture electrons in an effective manner from the semiconductor and to reduce the photogenerated charge recombination [47]. Graphene-based photosensitizers can have bandgaps suitable for a wide spectrum of visible light absorption to generate charge carriers to catalyze different species, initiating the photocatalytic process, and increasing the absorption spectra and efficiency of a photocatalytic system [47]. The principal roles of graphene in photocatalysis will be described below.

4.3.1 Graphene-Based Photocatalyst

Yeh et al. evaluated the band positions of GO from the study of GO with varying oxygenated levels in hydrogen and oxygen production from water [48]. Furthermore, the photocatalytic hydrogen generation in water is possible if the bandgap of the photocatalyst ranges between 2.4 and 4.3 eV [49]. The study reported that a well-oxidized GO possesses the suitable conduction band maxima and valence band minima for hydrogen and oxygen evolution, and that only its GO with the highest oxidation level could generate oxygen under light irradiation. Even though GO with lower degree of oxidation could also possess sufficient bandgap, however, they did not generate oxygen under light irradiation. To support this statement, Nasir et al. mentioned that when GO experiences reduction under light irradiation, the position of the valence band minima was tuned [44]. Hence, only the GO with the highest degree of oxidation could generate oxygen because it had a valence band minima “buffer” and remained positive enough after reduction by visible light irradiation for water oxidation. Nonetheless, the photo-induced deterioration can be impeded by functionalization modification of GO, and it is a metal-free, eco-friendly, and economical photocatalyst candidate [44].

4.3.2 Graphene-Based Cocatalyst

Interestingly, graphene also acted as a cocatalyst to enhance the catalytic performance of photocatalysts. For instance, Zhang et al. have demonstrated that NiCu/graphene cocatalysts have enhanced the conductivity and dye adsorption amount, resulting in an outstanding electro- and photo-catalytic HER performance [50]. Graphene has good dispersity in aqueous solutions and strong interactions between metal cations and oxygen-containing groups, and moreover be reduced in-situ to highly conductive rGO during the calcination of the catalyst preparation, thus resulting in to be a promising supporting material [51]. Hence, it is a very flexible platform for various nanostructure attachment and functionalization, enabling a wide variety of modification and alteration of nanocomposites.

4.3.3 Graphene-Based Photosensitizer

Graphene is deemed a potential macromolecular photosensitizer in a composite catalyst because of its wide visible light spectrum absorption owing to its suitable bandgap, promoting photocatalytic activity [48, 49]. For instance, GO is a great photosensitizer in a visible-light-driven photocatalysis, whereby it was revealed that the irradiation of a photocatalytic system with TiO₂/GO as the photocatalyst and GO as a sensitizer degrades methylene blue, suggesting the initiation of reactive oxygen species by transfer of electrons to TiO₂ and by direct interaction between valence band holes with water [52]. Du et al. theorized using large-scale DFT calculations

that a graphene/titania interface in the ground electronic state formed a charge-transfer complex that allowed electrons in the upper valence band to be directly excited from graphene to the conduction band under visible light irradiation, yielding well-separated electron–hole pairs with high photocatalytic performance in hybrid graphene and titania nanocomposites [53]. In other words, this theory revealed that the graphene/titania photoanode demonstrated significant visible light response.

In overall, the nature of graphene continues to be explored and exploited for the benefit on mankind. Its surface chemistry and physical properties allow graphene to be an outstanding supporting material for cocatalysts, whilst remaining as a lower cost alternative to noble metal cocatalysts [44]. In short, graphene has been considered to provide a versatile platform, whereby it was tunable and can be doped to have specific ranges of bandgap using various nanostructures, thus resulting it to function as a photocatalyst or a photosensitizer, whilst enhancing the performance and efficiency of a photocatalytic system.

4.4 Other Potential Applications

Globally, enormous amount of research has been devoted towards the use of GO for numerous potential biomedical applications, namely, cancer treatment through stimuli-responsive heating, antimicrobial activities, tissue engineering, biosensing and monitoring and drug delivery, respectively [54]. Even though majority of the research have revealed no noticeable impact of GO on the rats and mice, either in the long-term or on acute toxicities, however, the safety concerns are still controversial. In addition, in a short-term, the antimicrobial performance of the GO may be the most accessible application since antimicrobial effect of graphene materials has been clarified [55]. For instance, the effect of GO coating previously has been demonstrated via the use of dental care and GO-based bandage [53–55]. Besides, in the previous years, it was also reported that graphene and its nanomaterials have been utilized as an additive for lubricating oils [56]. For instance, via electrophoretic deposition (EPD) method, the GO films with tunable thickness were coated onto a silicon (Si) wafer [57]. Here, it was observed that the wear volume and the friction coefficient of the Si wafer were, respectively, reduced to 1/6 and 1/24 of the original value [57]. In addition, fabricated via spray-drying at 400 °C followed by thermal reduction at 700 °C, the resulted rGO was observed to be dispersed in polyalphaolefin-based oil [58]. For instance, in terms of friction and wear reduction, it was revealed that the incorporation of 0.01–0.1 wt.% rGO in polyalphaolefin-based oil had surpassed a fully formulated commercial 5W30 lubricant oil [58]. Furthermore, via hydrogen bonding, an attempt was made to chemically link rGO with polyethylene glycol (PEG) molecules [59]. For instance, compared to a bare PEG lubricated steel–steel contact, a friction coefficient of 0.06 and reduced wear of up to 50% was exhibited when 0.2 mgm/L of rGO was loaded into the lube medium [59]. Last but not the least, Gupta et al. investigated two different rGO samples terminated by hydroxyl and epoxy-hydroxyl groups, respectively [60]. Here, it was reported that the rGO sample

terminated by the epoxy-hydroxyl group exhibited a much lower friction coefficient compared to the other sample [60]. Hence, the aforementioned results conclude that the intercalation of the PEG molecules had occurred between the basal planes of the graphene via epoxy-hydroxyl interactions between the PEG and rGO, respectively.

5 Conclusion

This chapter describes the pragmatic application of graphene in desalination and water purification technology. The use of graphene in this technology can greatly reduce the cost of operation and improve the efficiency. Graphene remains one of the most versatile platforms for functionalization and modification, along with flexible fabrication methods, which allows researchers to produce graphene for a plethora of applications, including the field of energy storage and energy conversion, photocatalysis, and other environmental applications. The outstanding mechanical, physical, and chemical properties have made them a great candidate for desalination and water purification technology. This chapter has also discussed how graphene has been applied, implemented, and excelled in the fields of energy conversion and storage. Certainly, the raw materials to synthesize graphene are ubiquitous and readily available, making graphene commercialization feasible while exhibiting its highest potential for an evolutionary sustainable future.

Acknowledgements We want to thank the Ministry of Higher Education for the Fundamental Research Grant Scheme grants FRGS/1/2022/STG05/UM/01/2 and FRGS/1/2022/STG05/UM/02/15. The authors are extremely thankful to Universiti Malaya for providing necessary laboratory facilities for this research.

Author Contributions Sachin Sharma Ashok Kumar wrote the original draft, reviewed, and edited the draft, Liew. J, Loh K. H., Z. L. Goh, and Khishn K. Kandiah contributed and wrote the original draft, K. Ramesh supervised, reviewed, and edited the draft, and S. Ramesh supervised, reviewed, and edited the draft.

Conflict of Interest Authors have no competing interests.

References

1. Coleman J (2022) Australia's epic wildfires expanded ozone hole and cranked up global heat. *Nature*
2. Darre NC, Toor GS (2018) Desalination of water: a review. *Curr Pollut Rep* 4:104–111
3. Soldano C, Mahmood A, Dujardin E (2010) Production, properties and potential of graphene. *Carbon* 48(8):2127–2150
4. Stoller MD, Park S, Zhu Y, An J, Ruoff RS (2008) Graphene-based ultracapacitors. *Nano Lett* 8(10):3498–3502

5. Kumar SSA, Ma IW, Ramesh K, Ramesh S (2023) Development of graphene incorporated acrylic-epoxy composite hybrid anti-corrosion coatings for corrosion protection. *Mater Chem Phys* 127731
6. Kumar SSA et al (2023) A review on the recent progress of the plant-based porous carbon materials as electrodes for high-performance supercapacitors. *J Mater Sci* 1–40
7. Mishra AK, Ramaprabhu S (2011) Functionalized graphene sheets for arsenic removal and desalination of sea water. *Desalination* 282:39–45
8. Homaeigohar S, Elbahri M (2017) Graphene membranes for water desalination. *NPG Asia Mater* 9(8):e427–e427. <https://doi.org/10.1038/am.2017.135>
9. Kumar SSA, Bashir S, Ramesh K, Ramesh S (2022) A review on graphene and its derivatives as the forerunner of the two-dimensional material family for the future. *J Mater Sci* 57(26):12236–12278
10. Coroş M, Pogăcean F, Măgeruşan L, Socaci C, Pruneanu S (2019) A brief overview on synthesis and applications of graphene and graphene-based nanomaterials. *Front Mater Sci* 13:23–32
11. Kumar SSA, Bashir S, Ramesh K, Ramesh S (2022) Why is graphene an extraordinary material? A review based on a decade of research. *Front Mater Sci* 16(2):220603
12. Kumar SSA, Bashir S, Ramesh K, Ramesh S (2022) A comprehensive review: super hydrophobic graphene nanocomposite coatings for underwater and wet applications to enhance corrosion resistance. *FlatChem* 31:100326
13. Sharma SSA, Bashir S, Kasi R, Subramaniam RT (2022) The significance of graphene based composite hydrogels as smart materials: a review on the fabrication, properties, and its applications. *FlatChem* 100352
14. Kumar SSA, Bashir S, Ramesh K, Ramesh S (2021) New perspectives on graphene/graphene oxide based polymer nanocomposites for corrosion applications: the relevance of the graphene/polymer barrier coatings. *Prog Org Coat* 154:106215
15. Saeed M, Alshammari Y, Majeed SA, Al-Nasrallah E (2020) Chemical vapour deposition of graphene—synthesis, characterisation, and applications: a review. *Molecules* 25(17):3856
16. Eltigani HHI, Boonyongmaneerat Y (2022) Progress of water desalination applications based on wettability and surface characteristics of graphene and graphene oxide: a review. *J Met Mater Miner* 32(3):15–26
17. Sun Y et al (2023) Surface chemistry and structure manipulation of graphene-related materials to address the challenges of electrochemical energy storage. *Chem Commun* 59(18):2571–2583
18. Pan A et al (2011) High-rate cathodes based on $\text{Li}_3\text{V}_2(\text{PO}_4)_3$ nanobelts prepared via surfactant-assisted fabrication. *J Power Sources* 196(7):3646–3649
19. Levasseur S, Ménétrier M, Delmas C (2002) On the dual effect of Mg doping in LiCoO_2 and $\text{Li}_{1+\delta}\text{CoO}_2$: structural, electronic properties, and ^7Li MAS NMR studies. *Chem Mater* 14(8):3584–3590
20. Mazar Atabaki M, Kovacevic R (2013) Graphene composites as anode materials in lithium-ion batteries. *Electron Mater Lett* 9:133–153
21. Kim W, Ryu W, Han D, Lim S, Eom J, Kwon H (2014) Fabrication of graphene embedded LiFePO_4 using a catalyst assisted self assembly method as a cathode material for high power lithium-ion batteries. *ACS Appl Mater Interfaces* 6(7):4731–4736
22. Zhou X, Wan L-J, Guo Y-G (2013) Binding SnO_2 nanocrystals in nitrogen-doped graphene sheets as anode materials for lithium-ion batteries. *Adv Mater* 25(15):2152–2157
23. Li Y, Yan K, Lee H-W, Lu Z, Liu N, Cui Y (2016) Growth of conformal graphene cages on micrometre-sized silicon particles as stable battery anodes. *Nat Energy* 1(2):1–9
24. Wang R et al (2014) Solvothermal-induced self-assembly of $\text{Fe}_2\text{O}_3/\text{GS}$ aerogels for high Li-storage and excellent stability. *Small* 10(11):2260–2269
25. Sennu P, Kim HS, An JY, Aravindan V, Lee Y-S (2015) Synthesis of 2D/2D structured mesoporous Co_3O_4 nanosheet/N-doped reduced graphene oxide composites as a highly stable negative electrode for lithium battery applications. *Chem Asian J* 10(8):1776–1783
26. Wang G et al (2012) Flexible pillared graphene-paper electrodes for high-performance electrochemical supercapacitors. *Small* 8(3):452–459

27. Gopal J, Muthu M, Sivanesan I (2023) A comprehensive compilation of graphene/fullerene polymer nanocomposites for electrochemical energy storage. *Polymers* 15(3):701
28. Sun S, Gao L, Liu Y (2010) Enhanced dye-sensitized solar cell using graphene-TiO₂ photoanode prepared by heterogeneous coagulation. *Appl Phys Lett* 96(8):083113
29. Dao V-D, Nang LV, Kim E-T, Lee J-K, Choi H-S (2013) Pt nanoparticles immobilized on CVD-grown graphene as a transparent counter electrode material for dye-sensitized solar cells. *Chemosuschem* 6(8):1316–1319
30. Mahalingam S et al (2021) Functionalized graphene quantum dots for dye-sensitized solar cell: key challenges, recent developments and future prospects. *Renew Sustain Energy Rev* 144:110999
31. Dey T, Ghorai A, Das S, Ray SK (2022) Solvent-engineered performance improvement of graphene quantum dot sensitized solar cells with nitrogen functionalized GQD photosensitizers. *Sol Energy* 236:17–25
32. Bhol P, Yadav S, Altaee A, Saxena M, Misra PK, Samal AK (2021) Graphene-based membranes for water and wastewater treatment: a review. *ACS Appl Nano Mater* 4(4):3274–3293
33. Noureen L et al (2021) BiVO₄ and reduced graphene oxide composite hydrogels for solar-driven steam generation and decontamination of polluted water. *Sol Energy Mater Sol Cells* 222:110952
34. Zhou D, Cui Y, Xiao P-W, Jiang M-Y, Han B-H (2014) A general and scalable synthesis approach to porous graphene. *Nat Commun* 5(1):4716
35. Li D et al (2015) Separation of hydrogen gas from coal gas by graphene nanopores. *J Phys Chem C* 119(45):25559–25565
36. Goh P, Ismail A (2015) Graphene-based nanomaterial: the state-of-the-art material for cutting edge desalination technology. *Desalination* 356:115–128
37. Song N, Gao X, Ma Z, Wang X, Wei Y, Gao C (2018) A review of graphene-based separation membrane: materials, characteristics, preparation and applications. *Desalination* 437:59–72. <https://doi.org/10.1016/j.desal.2018.02.024>
38. Mortazavi V, Moosavi A, Nouri-Borujerdi A (2022) Water desalination by charged multilayer graphene membrane: a molecular dynamics simulation. *J Mol Liq* 355:118953
39. Gao Y, Wang Y, Zhou D, Lv W, Kang F (2022) Permselective graphene-based membranes and their applications in seawater desalination. *New Carbon Mater* 37(4):625–640
40. Kazemi AS, Hosseini SM, Abdi Y (2019) Large total area membrane of suspended single layer graphene for water desalination. *Desalination* 451:160–171
41. Chogani A, Moosavi A, Sarvestani AB, Shariat M (2020) The effect of chemical functional groups and salt concentration on performance of single-layer graphene membrane in water desalination process: a molecular dynamics simulation study. *J Mol Liq* 301:112478
42. Almomani F, Vasseghian Y, Vilas-Boas JA, Dragoi E-N et al (2021) Graphene-based nanomaterial for desalination of water: a systematic review and meta-analysis. *Food Chem Toxicol* 148:111964
43. Ahmed M, Giwa A, Hasan S (2019) Challenges and opportunities of graphene-based materials in current desalination and water purification technologies. *Nanoscale Mater Water Purif* 735–758
44. Nasir A, Khalid S, Yasin T, Mazare A (2022) A review on the progress and future of TiO₂/graphene photocatalysts. *Energies* 15(17):6248
45. Li X, Yu J, Wageh S, Al-Ghamdi AA, Xie J (2016) Graphene in photocatalysis: a review. *Small* 12(48):6640–6696
46. Nasir A, Raza A, Tahir M, Yasin T (2020) Free-radical graft polymerization of acrylonitrile on gamma irradiated graphene oxide: synthesis and characterization. *Mater Chem Phys* 246:122807
47. Raghavan A, Sarkar S, Nagappagari LR, Bojja S, MuthukondaVenkatakrishnan S, Ghosh S (2020) Decoration of graphene quantum dots on TiO₂ nanostructures: photosensitizer and cocatalyst role for enhanced hydrogen generation. *Ind Eng Chem Res* 59(29):13060–13068
48. Yeh T-F, Chan F-F, Hsieh C-T, Teng H (2011) Graphite oxide with different oxygenated levels for hydrogen and oxygen production from water under illumination: the band positions of graphite oxide. *J Phys Chem C* 115(45):22587–22597

49. Yeh T-F, Syu J-M, Cheng C, Chang T-H, Teng H (2010) Graphite oxide as a photocatalyst for hydrogen production from water. *Adv Funct Mater* 20(14):2255–2262
50. Zhang W, Mei X, Yuan L, Wang G, Li Y, Peng S (2022) Tuning metal-support interaction of NiCu/graphene cocatalysts for enhanced dye-sensitized photocatalytic H₂ evolution. *Appl Surf Sci* 593:153459
51. Zhang W, Zou Y, Mei X, Li Y, Peng S, Xu J (2020) Facile synthesis of CO₂(OH)₃Cl/cobalt carbide/reduced graphene oxide composites for enhanced dye-sensitized photocatalytic H₂ evolution. *Sustain Energy Fuels* 4(12):6181–6187
52. Nasir A et al (2022) Photocatalytic synthesis of oxidized graphite enabled by grey TiO₂ and direct formation of a visible-light-active titania/graphene oxide nanocomposite. *ChemPhotoChem* 6(6):e202100274
53. Du A, Ng YH, Bell NJ, Zhu Z, Amal R, Smith SC (2011) Hybrid graphene/titania nanocomposite: interface charge transfer, hole doping, and sensitization for visible light response. *J Phys Chem Lett* 2(8):894–899
54. Ma Y, Zheng Y, Zhu Y (2020) Towards industrialization of graphene oxide. *Sci China Mater* 63:1861–1869
55. Zou X, Zhang L, Wang Z, Luo Y (2016) Mechanisms of the antimicrobial activities of graphene materials. *J Am Chem Soc* 138(7):2064–2077
56. Berman D, Erdemir A, Sumant AV (2014) Graphene: a new emerging lubricant. *Mater Today* 17(1):31–42
57. Liang H, Bu Y, Zhang J, Cao Z, Liang A (2013) Graphene oxide film as solid lubricant. *ACS Appl Mater Interfaces* 5(13):6369–6375
58. Dou X et al (2016) Self-dispersed crumpled graphene balls in oil for friction and wear reduction. *Proc Natl Acad Sci* 113(6):1528–1533
59. Gupta B, Kumar N, Panda K, Dash S, Tyagi A (2016) Energy efficient reduced graphene oxide additives: mechanism of effective lubrication and antiwear properties. *Sci Rep* 6(1):1–10
60. Gupta B, Kumar N, Panda K, Kanan V, Joshi S, Visoly-Fisher I (2017) Role of oxygen functional groups in reduced graphene oxide for lubrication. *Sci Rep* 7(1):1–14

Chapter 3

An Impact of Nanotechnology for Water Treatment Process



A. D. Dhass, N. Beemkumar, K. Venkadeshwaran, and M. K. Aravindan

Abstract Water resource conservation and management require innovative ideas and improved materials in the today's era. Nanotechnology has the potential to assure the long-term availability of safe drinking water and the protection of water resources by employing cutting-edge materials and technologies for water purification, conservation and reuse. This chapter is primarily concerned with the nanotechnology-based water treatment techniques being developed and used for water augmentation, safe wastewater reuse, water disinfection and decontamination, through nanoadsorption for contaminant removal. This chapter also discusses noble metal nanoparticles, nanocomposites of organic supports and developing approaches to improve water filtration, such as biologically activated carbon.

Keywords Nanoparticles · Absorbents · CNTs · Activated carbon method · Biologically activated carbon method

A. D. Dhass (✉)

Mechanical Engineering Department, Indus Institute of Technology and Engineering, Indus University, Ahmedabad 382115, India

e-mail: addhass.me@indusuni.ac.in

N. Beemkumar · K. Venkadeshwaran · M. K. Aravindan

Department of Mechanical Engineering, Faculty of Engineering and Technology, JAIN (Deemed-to-be University), Karnataka 562112, India

e-mail: n.beemkumar@jainuniversity.ac.in

K. Venkadeshwaran

e-mail: k.venkadeswaran@jainuniversity.ac.in

M. K. Aravindan

e-mail: mk.aravindan@jainuniversity.ac.in

1 Introduction

Water pollution is defined as any contaminant existing in a body of water that has a negative influence on living organisms. Organic, inorganic and biological pollutants can all be found in wastewater. Some pollutants are poisonous and carcinogenic, inflicting human and environmental harm. Pharmaceuticals and personal care (PPCs) products are among the emerging pollutants. PPCs are usually resistant to spontaneous biodeterioration.

There are two types of water contaminants: point sources (wastewater from industries) and non-point sources (rain water). Around 800 million people in the universe has insufficient access to clean water. There are physical, chemical and biological ways for removing toxins from water, and each has advantages and disadvantages. Nanoparticles have unique properties, and numerous nanoparticles are utilised to remove pollution from water bodies.

1. Numerous atoms and molecules on the surface.
2. Surface forces are critical, while bulk forces are not.
3. Metal nanoparticles offer unique light scattering characteristics.

Nanoparticles are utilised in removal methods, and the product should be inexpensive, recyclable, cost-effective and non-toxic. Nanoadsorption, nanocatalyst, nanomembrane and nanofiltration are the methods by which nanoparticles will be adsorbed to various water pollutants [1]. Carbon nanotubes (CNTs) are a well-researched substance that may remove heavy metals, dyes and a variety of organic pollutants from wastewater via adsorption. When compared to ordinary granular and powder activated carbon, it has a high adsorption capability. CNTs' adsorption ability for heavy metal ions is mostly determined by pH, and it is effective over a wide pH range.

The graphene embedded with CNTs to serve as nanofilters is more effective for dye rejection in water effluent, salt ion removal and antifouling. Electrochemical carbon nanotubes can readily be utilised to remove amino group-based colours from wastewater [2, 3]. The majority of drinking water originates from rivers, lakes, wells and natural springs. These sources are subjected to a range of chemicals, which pollute our water resources. The various types of conventional wastewater treatment techniques and their drawbacks are enlisted in Table 1. The following are water pollutants that occur as a result of products that we commonly employ to improve our quality of life [4, 5]:

1. Burning of conventional energy sources.
2. Soap flakes.
3. Fertilisers.
4. Phthalates.

One of the most crucial components for all living things to maintain life is requirement of clean water. Water resources have been contaminated internationally, nevertheless, as a result of the accelerated industrialization and enormous population

Table 1 Water treatment methods and their drawbacks [6]

Wastewater treatment methods	Drawbacks
Distillation	The vast majority of pollutants are still present Pollutants with high boiling points are inefficient (>100 °C)
Coagulation and flocculation	Method with lower precision – To reduce the pH, alkaline substances must be added
Chemical transformation	– Reagents in excess are required
Ultraviolet irradiation	– Heavy metal removal is inefficient – Expensive process
Biological treatment	– Microorganisms are difficult to control – Extravagant – Tedious
Carbon filter	– Mould prone Filters are frequently changed Clogging
Ultrafiltration	– Particulate plugging is possible – Dissolved inorganics are inefficient

growth. Heavy metal ions and dyes are two significant types of aquatic contaminants. When these are present, the water is no longer fit for human consumption and is sometimes exceedingly difficult to properly purify. Aquatic toxins frequently present major health concerns to life and have a negative impact on the environment. It is essential to eliminate these toxins from contaminated water in order to prevent the negative effects on ecosystem health and human health.

Many incredible materials, including fullerenes, nanofibers, nanowires, and zeolites, have been made possible through the development of nanotechnology. Dendrimers are a type of polymeric nanoadsorbent that is used to remove organics and heavy metals. While heavy metals can be eliminated by combining with silver atoms, organic substances can be absorbed by interior hydrophobic shells. Zeolites have a particularly porous structure that allows for the incorporation of nanoscale silver ions. When used for hygienic purposes, the silver attracts bacteria and stops their growth.

Membrane filtration is crucial in removing many forms of contaminants and enabling highly purified water. Water produced through nanofiltration satisfies extremely strict standards for water reusing. The need for additional water disinfection is limited because this technique is very effective at removing bacteria, viruses, and organic and inorganic materials. Utilising membrane separation methods, water and wastewater treatment applications are expanding significantly (like nanofiltration, nanocomposites, self-assembling, nanofiber and aquaporin-based membranes).

Despite various drawbacks, it was noted that adsorption will soon be regarded as a reliable water treatment technology. Numerous studies have investigated the efficacy of batch mode adsorption for purifying water from a wide range of pollutants. Initially, activated carbon was employed to remove contaminants from water; however, other more affordable adsorbents have since taken their place. With its use

Table 2 Different nanoparticles used for water pollutant removals [7]

S. no	Types of nanoparticles	Types of pollutant removals
1	CNT	Organic contaminant
2	Nanoscale metal oxide	Heavy metals, radionucleids
3	Nanocatalyst	Azodyes, pesticides
4	Biomimetic membranes	Removing salts

in virtually every field of science and technology over the past 20 years, nanotechnology has considerably advanced. Adsorption is one of the most important methods for treating wastewater since it is simple to implement, inexpensive, and a wide range of adsorbents are readily available. In addition to soluble and insoluble organic, inorganic and biological pollutants, adsorption is also effective at removing insoluble contaminants. Adsorption also makes it possible to reduce sources and reuse water for industrial, potable and other purposes. Despite these benefits, adsorption does not operate effectively at commercial scales, among other limitations. This is probably due to the scarcity of large-capacity adsorbents and the limited number of commercially used columns for adsorption-based processes. In addition, a single adsorbent could not be effective against all possible pollutants. Depending on the characteristics of the contaminants, different adsorbents are utilised. Other water treatment systems were compared to the adsorption approach.

In reality, several nanomaterials have been created and employed to remove aquatic contaminants. A variety of issues of water treatment by adsorption utilising nanoparticles have been attempted to be discussed in light of the significance of water quality and growing nanotechnology applications. Nanoparticles are utilised to remove contaminants from water, as shown in Table 2. In this regard, encouraging nanomaterials offers chances to create regional and useful remedies for addressing global water pollution.

In this chapter, the importance of various wastewater treatment techniques and nanoparticles used for this process are discussed. Similarly, emerging techniques like activated carbon and biologically activated carbon methods were discussed to removal contaminants in wastewater.

2 Nanotechnology

Traditional water treatment methods, including coagulation, flocculation and sedimentation, are inadequate for removing cyanotoxin. Furthermore, if cells lyse, cyanotoxins can be generated in significant amounts during such activities. Therefore, it is necessary to create novel approaches to risk management in order to mitigate the consequences of harmful algal blooms [8, 9]. Nanomaterials exhibit structural components, crystallites, molecules and clusters in zero, one, two and three dimensions [10]. Nanotechnology integrates diverse disciplines such as physics, chemistry

and biotechnology (nanostructured materials). Numerous advantages of nanomaterials have been noted, including tissue-specific targeting, decreased dose and toxicity, improved medication efficacy and fewer unintended side effects [11, 12]. Nanoparticles of many sizes and shapes, including dendrimers, nanocapsules, nanospheres and nanotubes, are employed. Due to their physio-chemical characteristics, nanomaterials have several uses in industries like food preservation, water treatment and medicine [13, 14].

Due to their effectiveness in eliminating heavy metal ions and other impurities from industrial effluents, nanotechnology applications have been used extensively in this decade. Nanomaterials are microscopic particles that have been designed to possess special physio-chemical characteristics that only exist at the nanoscale. When matter is modified at the atomic level to create discrete particles, it gains novel and useful qualities that would be impossible in bulk materials. Medical and environmental cleanup are only two of the numerous fields that can benefit from the technology's ability to direct particles down a predetermined path [15].

3 Noble Metal Nanoparticles

Some transition metals, including Gold (Au), Silver (Ag), Platinum (Pt), and Palladium (Pd), were referred to as noble metals. Due to their small atom size and strong ionisation energy, they often have low oxidation potential. However, their ionisation energy and oxidation potential significantly changed at the nanoscale, making a variety of unique reactions with noble metal possible [16].

In order to produce noble metal nanoparticles, it is normally necessary to reduce the corresponding metal salts and use a stabilising agent to regulate the growth of nanocrystals. Noble metal nanoparticles can also be used to absorb contaminants and remove bacteria in addition to for pollution monitoring [17].

When waterborne microorganisms like *Escherichia coli* (*E.coli*) came into contact with silver nanoparticles, their biocidal activity was used to disinfect the water. The cellular membrane may be harmed by direct contact with Ag nanoparticles, and the size and crystal structure of the particles affect how effectively they inhibit bacteria. Better antibacterial action is correlated with higher atom density. Surgical masks, textile fibres and even mouthwash are now frequently disinfected with the help of silver nanoparticles. Using noble metal nanoparticles, different water contaminants like pesticides, dyes and halogenated organics were also being photo-catalytically degraded [18].

4 Removal of Contaminants

4.1 Contaminants Removed by Nanoadsorbents

Toxic and non-toxic metal ions, radionuclides, organic and inorganic substances (such as oil, dyes, phosphorous, nitrate and sulphur), sediments, particles and pathogenic microbes are some of the numerous types of contaminants found in effluents. A number of hazardous metals, including Pb(II), As(III), build up in food chains and are harmful to human health. These dangerous metals can impair a variety of body organs, including the brain, kidneys, lungs and central nervous system. They also have negative effects on the environment and cannot be broken down by microbes. For instance, Cr(VI) is extremely poisonous, has high mobility and has a negative effect on human health. Moreover, Cr(VI) and U(VI) display much increased carcinogenicity and toxicity compared to Cr(III) and U(IV), respectively [19, 20]. Figure 1 shows the various methods to remove different pollutants in wastewater.

Carbon nanotubes (CNTs) are a type of nanomaterial with radii in the nanometer range and lengths from a few nanometres to several centimetres. These CNTs' performance can be considerably enhanced through functionalization with acids or alkalis, which gives their surfaces a negative charge. This enables the CNTs to interact with the contaminants through electrostatic contact. As a result of its tests using both functionalized and unfunctionalized CNTs, it has established the following hierarchy of heavy metal adsorption. Heavy metal adsorption is ranked as follows: $Pb^{2+} > Ni^{2+} > Zn^{2+} > Cu^{2+} > Cd^{2+}$, with the highest amounts seen on surface-oxidised CNTs [22].

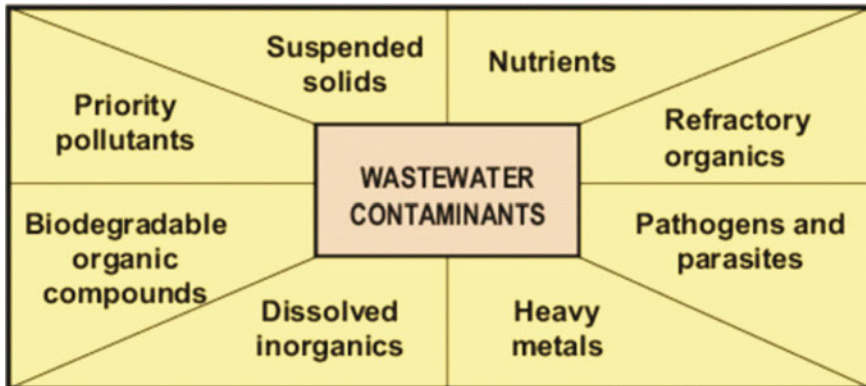


Fig. 1 Different types of pollutants in wastewater (Adapted from Gavrilescu [21])

4.2 Removal of Mercury Contaminants

Mercury (Hg) contamination is pervasive and challenging to handle effectively, and has drawn growing attention worldwide. Fast-evolving nanotechnology has just given heavy metal contamination treatment, a new option and opportunity. The potential for Hg remediation of contaminated soil and water is also greatly increased by the significant advantages of many nanomaterials. Many artificial nanomaterials have been created to date that are very good at detecting and removing mercury. These materials are especially helpful in Hg-polluted water systems [23].

5 Water Treatment

5.1 Groundwater Treatment

Groundwater serves as a vital water source, particularly in places without any perennial streams or rivers. Rainfall or water bodies seeping into the earth are the main sources of groundwater replenishment. But groundwater is most susceptible to contaminating effects of human activity.

Untreated surface pollutants, like dye, metallurgical furnace sludge, untreated petrochemical wastes, pharmaceutical waste and biohazardous waste, will always seep into the earth and end up in the groundwater. These substances may be toxic and render water unfit for human consumption when they seep into the ground. Because it is largely inaccessible when it is inside of natural aquifers, treating groundwater presents the major obstacle. With the help of agriculture, people can feed vast populations as well as themselves on a regular and predictable basis, which makes agriculture essential to our modern society [24].

5.2 Water Treatment Using Nanomaterials as Adsorbents

Nanoscale particles made of organic or inorganic materials are known as nanoadsorbents and have a strong propensity to adsorb substances. As a result of their high porosity, small size and active surface, nanoadsorbents are able to efficiently digest source materials without releasing their dangerous payload. Nanoadsorbents have efficient pollutant-binding capabilities and operate quickly. Furthermore, once depleted, they can be chemically recycled [25]. Due to these factors, interest in nanotechnology among academics has been rising quickly all around the world. At the nanoscale, materials display unique characteristics due to their small size, including a large surface area and a high “surface area-to-volume” ratio. These qualities increase the nanoparticles’ ability to adsorb material. These particles have unusual qualities, such as strong reactivity and a catalytic potential, in addition to their huge surface

area, making them superior adsorbing materials than typical materials. The increased number of active sites for interacting with different chemical species is due to the huge surface area of nanoparticles. Nanoparticles are a promising new technology for treating wastewater, with the aim of increasing the efficiency with which toxins are removed [26, 27].

Figure 2 shows that many different methods have been used to treat the contaminants and remove organic and inorganic pollutants. While carbon nanotubes are widely used as an adsorbent in water filtration systems, concerns have been raised concerning their potential harm [29–31]. In order to properly understand the type and quantity of carbon nanotubes being used, it is necessary to know their composition [32, 33]. The carbon nanotubes have been functionalized and purified by a number of researchers using various techniques. Carbon nanotubes' ability to adsorb heavy metals could be greatly improved proper surfaces and surface charges. These nanoparticles can be very effective purifiers for turning wastewater into drinkable water when used in conjunction with the right functionalization agent [34–37].

The use of composite and hybrid materials with carbon nanotube (CNT) reinforcement has expanded the scope of photocatalytic and water pollutant splitting processes (Fig. 3). Carbon nanotubes (CNTs) improve the physical properties of photocatalytic nanoparticles like nano-TiO₂ and the catalyst's responsiveness to pollution mitigation. Doped CNTs have been used in a number of membrane engineering systems to desalinate brackish and seawater. They can be used as membranes on their own or as pores in membranes that have been specifically created by aligning them.

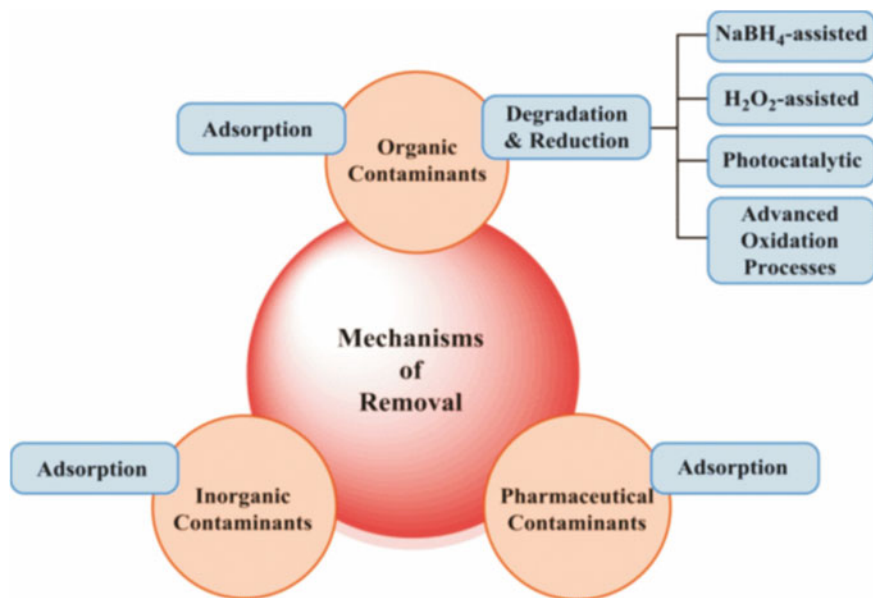


Fig. 2 Application of nanomaterials to the removal of contaminants (Adapted from Nasrollahzadeh et al. [28])

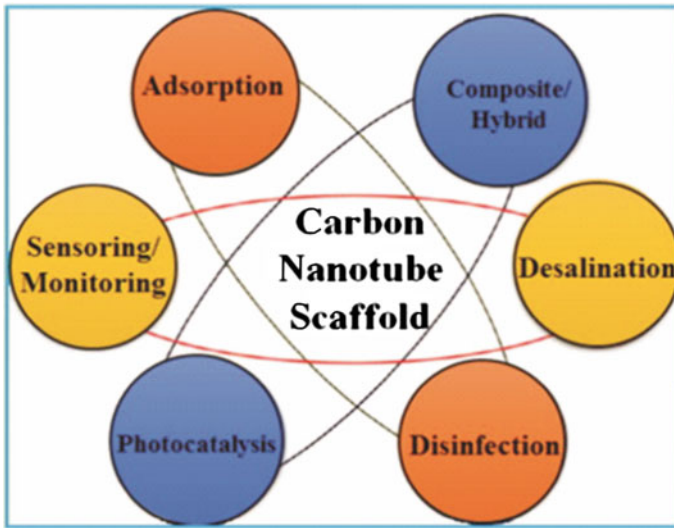


Fig. 3 CNT works as a scaffold to purify water (Adapted from Das et al. [38])

Carbon nanotubes (CNTs) are used in electrochemical sensor technology to detect and quantify pollutants, pathogens and complex wastewater matrices due to their high electrical conductivity.

The reverse osmosis (RO) water desalination process was discovered to be a perfect fit for these membranes. However, until the approach for constructing the membrane module arrangement is altered to reduce concentration polarisation and membrane fouling concerns are appropriately addressed, CNT membranes will likely save little energy. It has been proposed that a membrane made of carbon nanotubes might be used to desalinate and purify water, which would be a significant advancement over current water technology [39, 40].

6 Nanocomposites in Water Treatment

As nanoparticles are used widely in water treatment, there are several inherent technological problems that must be overcome, including aggregation and human health. A practical strategy for expanding the utilisation of nano-particulate materials is to incorporate them into host materials as nanocomposite materials [40]. Nanocomposites can also reduce environmental nanoparticle discharge and make nanotechnology more compatible with current infrastructure [41, 42]. The term “nanocomposite” is used to describe a wide variety of multiphase solid materials, such as porous media, colloids, gels and copolymers. In terms of nanoparticle dispersion, stability and recyclability, nanocomposites performed and were far more useful than free nanomaterials. Therefore, nanocomposite materials might connect the nanoscopic

and mesoscopic levels [43, 44]. Nanocomposites were thought to represent the best hope for bringing water nanotechnology out of the lab and into practical use.

7 Nanocomposites of Organic Supports

Due to their frequently changeable porosity architectures, superior mechanical attributes and chemically constrained functional groups, polymers make for particularly effective substrates for nanomaterials [45]. Materials for water and wastewater treatment that perform well are polymer-nanocomposites (PNCs). PNCs combine nanoparticles with polymeric matrix benefits. In situ synthesis and direct compounding are the two basic methods used to create different PNCs. The polymers with added functionality were created by grafting in functional nanoparticles. The addition of functional nanoparticles while monomers were being polymerized was another technique for in situ synthesis [46, 47].

8 Emerging Methods

8.1 Using Activated Carbon (AC)

The development of extremely selective adsorbent materials for target contaminants has been made possible by the incorporation of highly specialised chemical functionality at the AC surface. There is also a particle adsorbent system that combines the features of AC and Pt. Particle systems might not be useful for point-of-use (POU) water filtration, but they might be in facilities for water treatment where sedimentation and particle removal are feasible [48]. Figure 4 shows the transport of water molecules through CNT and graphene oxide.

Accessibility to safe, clean water is getting harder to come by every day, and it's expected to get worse in the coming years. Various technologies have been used to overcome this problem. The use of carbon nanotube (CNT) and graphene oxide (GO) membranes in the water purification industry has had a significant and far-reaching effect. The usage of CNTs and graphene oxide as reinforcement materials has improved the mechanical strength and fouling characteristics of polymer matrix.

8.2 Using Biologically Activated Carbon (BAC)

When particular microorganisms are added and get caught in the porous AC matrix, biologically activated carbon filters are created. The bacteria can then grow and colonise the surface of the AC under ideal circumstances and with the right organic

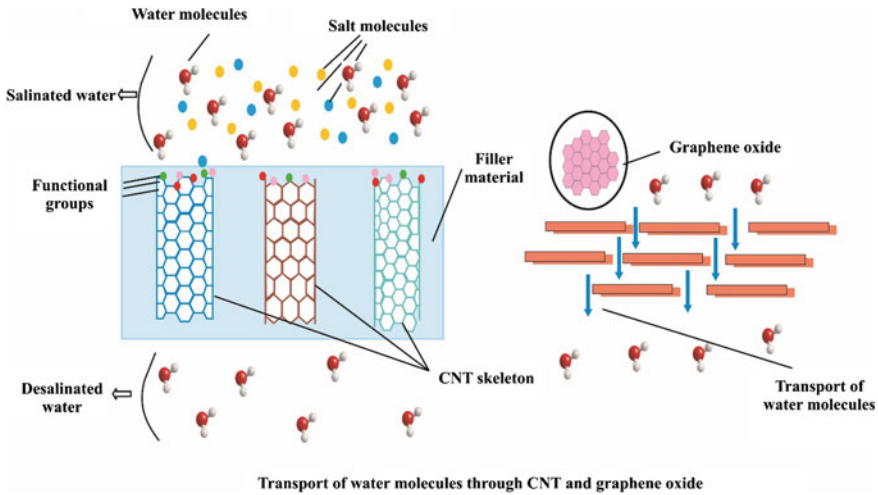


Fig. 4 Transport of water molecules through CNT and graphene oxide (Adapted from Sabir et al. [49])

ingredients. Then, it will be simple to remove these degradation products from the water by having them easily adsorb to the AC surface. Before BAC filtration, the dissolved contaminants are frequently treated with ozone or ultraviolet light. The organic compounds become more bioavailable and simpler for bacteria to degrade thanks to the process' generation of highly reactive species within them. Granular activated carbon that had been inoculated with various heterotrophic nitrifying bacterial strains performed better at removing ammonia than uninoculated granular activated carbon (GAC), increasing removal efficiency by 2.8–4-fold. The effectiveness of BAC filters for the removal of trihalomethanes (THMs) and haloacetic acids (HAAs) was determined by a pilot research conducted on a water treatment facility, with removal efficiencies of more than 45% and 80% for each substance, respectively. Additionally, it has been noted that BAC filters improve assimilable organic carbon removal, which may have an impact on how well microorganisms grow in water. The effectiveness of these materials is affected by a wide range of environmental factors, including temperature, pH and total DOM, which may limit their applicability in certain settings. One of the main drawbacks of BAC is the accumulation of biomass within the material, which must be routinely removed to ensure maximum function. While thermal treatment and several chemical techniques have proven successful in restoring the BAC, they come with a number of drawbacks, including the loss of the AC structure and the introduction of potentially harmful chemicals. Low-frequency ultrasound has been proposed as a workable substitute for BAC filter regeneration. With this method, the regenerated BAC regained its capacity to eliminate ammonia and dyes from aqueous solutions.

9 Toxic Potential of CNTs

A number of studies have shown that CNTs can damage the respiratory system and increase the risk of serious illnesses such as bronchitis, lung cancer, emphysema and asthma. Some industrial facilities appear to have more dust than others due to poor hygiene practises on the industrial level. An inhalation exposure could result from the usage of crushed CNTs or composite materials containing tiny CNT particles. The effects of CNTs on the pulmonary system have been studied in several laboratory studies on inhalation danger, which have helped to determine exposure limits. The recognised carcinogenic properties of CNTs can cause lung cancers. However, if the fibre length is shorter, the carcinogenicity of CNTs will decrease [50].

10 Conclusion

The appropriate treatment of contaminated water is essential for the environment and for general welfare. This wastewater treatment method can make use of cutting-edge technologies like nanotechnology and the elimination of dangerous substances that were previously untreatable. Nanotechnology offers the ability to provide these water-related requirements in underdeveloped countries with a flexible, affordable solution. To protect and improve water quality and quantity, it's crucial to take advantage of nanotechnology's opportunities for technological advancement. The unique properties of nanomaterials, such as a rapid response rate and surface-to-mass ratio, contribute to their better process efficiency. Despite the many benefits, there are a few issues that require prompt attention. Nanoparticle-based materials have the potential to be dangerous since they can be discharged into the ecosystem, where they may accumulate over time. Another drawback of technologies using nanomaterials for water treatment is that they are frequently unsuitable for widespread application and, in many cases, incompatible with currently available technology. However, nanotechnology offers a plethora of research possibilities in the realm of water treatment, especially for decentralised treatment systems, portable water treatment equipment and highly contaminated water.

References

1. Kunduru KR, Nazarkovsky M, Farah S, Pawar RP, Basu A, Domb AJ (2017) Nanotechnology for water purification: applications of nanotechnology methods in wastewater treatment. *Water Purif* 33–74
2. Adams LK, Lyon DY, Alvarez PJ (2006) Comparative eco-toxicity of nanoscale TiO₂, SiO₂, and ZnO water suspensions. *Water Res* 40(19):3527–3532
3. Harikrishnan S, Dhass AD, Oztop HF, Abu-Hamdeh N (2022) Measurement of thermophysical properties with nanomaterials on the melting/freezing characteristics of phase change material. *Measurement* 199:111477

4. Ahuja S (ed) (2014) Water reclamation and sustainability. Elsevier
5. Ahuja S (2022) Overview of separations of water pollutants with nanotechnology. In: Separation science and technology, vol 15, pp 1–11. Academic Press
6. Bhat SA, Sher F, Hameed M, Bashir O, Kumar R, Vo DV, Ahmad P, Lima EC (2022) Sustainable nanotechnology based wastewater treatment strategies: achievements, challenges and future perspectives. *Chemosphere* 288:132606
7. Khan NA, Khan SU, Ahmed S, Farooqi IH, Dhingra A, Hussain A, Changani F (2019) Applications of nanotechnology in water and wastewater treatment: a review. *Asian J Water Environ Pollut* 16(4):81–86
8. Harikrishnan S, Dhass AD (2020) Nanomaterials for latent thermal energy storage. *Handb Nanomater Nanocomposites Energy Environ Appl* 1–19
9. Ajith MP, Aswathi M, Priyadarshini E, Rajamani P (2021) Recent innovations of nanotechnology in water treatment: a comprehensive review. *Biores Technol* 342:126000
10. Fajardo C, Martinez-Rodriguez G, Blasco J, Mancera JM, Thomas B, De Donato M (2022) Nanotechnology in aquaculture: applications, perspectives and regulatory challenges. *Aquac Fish* 7(2):185–200
11. Pandi K, Prabhu SM, Choi J (2021) Fabrication of lanthanum methanoate on sucrose-derived biomass carbon nanohybrid for the efficient removal of arsenate from water. *Chemosphere* 262:127596
12. Qamar SA, Qamar M, Basharat A, Bilal M, Cheng H, Iqbal HMN (2021) Alginatebased nano-adsorbent materials–bioinspired solution to mitigate hazardous environmental pollutants. *Chemosphere* 132618. <https://doi.org/10.1016/j.chemosphere.2021.132618>
13. Deng H, Zhang Y, Yu H (2018) Nanoparticles considered as mixtures for toxicological research. *J Environ Sci Health C* 36(1):1–20
14. Dickinson E (2010) Food emulsions and foams: stabilization by particles. *Curr Opin Colloid Interface Sci* 15(1–2):40–49. <https://doi.org/10.1016/j.cocis.2009.11.001>
15. Mohanapriya V, Sakthivel R, Pham NDK, Cheng CK, Le HS, Dong TMH (2022) Nanotechnology-a ray of hope for heavy metals removal. *Chemosphere* 136989
16. Xie Y, Hu J, Esmaili H, Wang D, Zhou Y (2022) A review study on wastewater decontamination using nanotechnology: Performance, mechanism and environmental impacts. *Powder Technol* 118023
17. Jagessar RC (2022) Nanotechnology and treatment of Covid-19. *J Nanosci Res Rep.* 130(4):2–8. <https://doi.org/10.47363/JNSRR/2022>. (SRC/JNSRR-134)
18. Zhong Z, Zhang L (2021) Optimized rapid flame synthesis of morphology-controlled α -MoO₃ layered nanoflakes. *J Nanopart Res* 23(5):1–11
19. Khan I, Saeed K, Khan I (2019) Nanoparticles: properties, applications and toxicities. *Arab J Chem* 12(7):908–931
20. Ubaidullah M, Ahmed J, Ahamad T, Shaikh SF, Alshehri SM, Al-Enizi AM (2020) Hydrothermal synthesis of novel nickel oxide@ nitrogenous mesoporous carbon nanocomposite using costless smoked cigarette filter for high performance supercapacitor. *Mater Lett* 266:127492
21. Gavrilescu M (2010) Environmental biotechnology: achievements, opportunities and challenges. *Dyn Biochem Process Biotechnol Mol Biol* 4(1):1–36
22. Poornima S, Manikandan S, Karthik V, Balachandar R, Subbaiya R, Saravanan M, Pugazhendhi A (2022) Emerging nanotechnology based advanced techniques for wastewater treatment. *Chemosphere* 135050
23. Liu Y, Chen H, Zhu N, Zhang J, Li Y, Xu D, Zhao J (2022) Detection and remediation of mercury contaminated environment by nanotechnology: progress and challenges. *Environ Pollut* 293:118557
24. Cheemalamarry SK, Sharma V, Varun Y, Sreedhar I, Singh SA (2022) Recent advances of nanotechnology in water remediation. *Nano-Enabled Technol Water Remediat* 311–333
25. Santhosh C, Velmurugan V, Jacob G, Jeong SK, Grace AN, Bhatnagar A (2016) Role of nanomaterials in water treatment applications: a review. *Chem Eng J* 306:1116–1137

26. Gautam R, Chattopadhyaya MC (2016) Nanomaterials for wastewater remediation. Butterworth-Heinemann
27. Upadhyayula VK, Deng S, Mitchell MC, Smith GB (2009) Application of carbon nanotube technology for removal of contaminants in drinking water: a review. *Sci Total Environ* 408(1):1–13
28. Nasrollahzadeh M, Sajjadi M, Irvani S, Varma RS (2021) Green-synthesized nanocatalysts and nanomaterials for water treatment: current challenges and future perspectives. *J Hazard Mater* 401:123401
29. Zhou D, Kim D-G, Ko S-O (2015) Heavy metal adsorption with biogenic manganese oxides generated by *Pseudomonas putida* strain MnB1. *J Ind Eng Chem* 24:132–139
30. Zhuang Z, Huang L, Wang F, Chen Z (2015) Effects of cyclodextrin on the morphology and reactivity of iron-based nanoparticles using *Eucalyptus* leaf extract. *Ind Crops Prod* 69:308–313
31. Zinatloo-Ajabshir S, Salehi Z, Salavati-Niasari M (2018) Green synthesis and characterization of $Dy_2Ce_2O_7$ ceramic nanostructures with good photocatalytic properties under visible light for removal of organic dyes in water. *J Clean Prod* 192:678–687
32. Zinatloo-Ajabshir S, Morassaei MS, Salavati-Niasari M (2018) $Nd_2Sn_2O_7$ nanostructures as highly efficient visible light photocatalyst: green synthesis using pomegranate juice and characterization. *J Clean Prod* 198:11–18
33. Saleem H, Zaidi SJ (2020) Developments in the application of nanomaterials for water treatment and their impact on the environment. *Nanomaterials* 10(9):1764
34. Sun TY, Bornhöft NA, Hungerbühler K, Nowack B (2016) Dynamic probabilistic modeling of environmental emissions of engineered nanomaterials. *Environ Sci Technol* 50(9):4701–4711
35. Khosravi-Katuli K, Prato E, Lofrano G, Guida M, Vale G, Libralato G (2017) Effects of nanoparticles in species of aquaculture interest. *Environ Sci Pollut Res* 24(21):17326–17346
36. Brody JG, Tickner J, Rudel RA (2005) Community-initiated breast cancer and environment studies and the precautionary principle. *Environ Health Perspect* 113(8):920–925
37. Ecotoxicology OECD (2014) Environmental fate of manufactured nanomaterials: test guidelines, vol 40
38. Das R, Abd Hamid SB, Ali ME, Ismail AF, Annuar MSM, Ramakrishna S (2014) Multi-functional carbon nanotubes in water treatment: the present, past and future. *Desalination* 354:160–179
39. Burghard M, Balasubramanian K (2005) *Small* 1:180
40. Celik E, Park H, Choi H, Choi H (2011) *Water Res* 45:274
41. Zhang Y, Wu B, Xu H, Liu H, Wang M, He Y, Pan B (2016) Nanomaterials-enabled water and wastewater treatment. *NanoImpact* 3:22–39
42. Lau WJ, Gray S, Matsuura T, Emadzadeh D, Chen JP, Ismail AF (2015) A review on polyamide thin film nanocomposite (TFN) membranes: history, applications, challenges and approaches. *Water Res* 80:306–324
43. Li X-Q, Elliott DW, Zhang W-X (2006) Zero-valent iron nanoparticles for abatement of environmental pollutants: materials and engineering aspects. *Crit Rev Solid State Mater Sci* 31(4):111–122
44. Li QL, Mahendra S, Lyon DY, Brunet L, Liga MV, Li D, Alvarez PJJ (2008) Antimicrobial nanomaterials for water disinfection and microbial control: potential applications and implications. *Water Res* 42(18):4591–4602
45. Li Y, Peng X, Wang Z, Wang K, Zhang P, Du Q, Liu T, Xia Y, Zhang W, Zhu H (2011) Adsorption of fluoride from aqueous solution by grapheme. *J Colloid Interface Sci* 363(1):348–354
46. Li H, Shan C, Zhang Y, Cai J, Zhang W, Pan B (2016) Arsenate adsorption by hydrous ferric oxide nanoparticles embedded in cross-linked anion exchanger: effect of the host pore structure. *Appl Mater Interfaces* 8(5):3012–3020
47. Li J, Shi Y, Cai Y, Mou ACS S, Jiang G (2008) Adsorption of di-ethyl-phthalate from aqueous solutions with surfactant-coated nano/microsized alumina. *Chem Eng J* 140(1):214–220
48. Sweetman MJ, May S, Mebberson N, Pendleton P, Vasilev K, Plush SE, Hayball JD (2017) Activated carbon, carbon nanotubes and graphene: materials and composites for advanced water purification. *C* 3(2):18

49. Sabir A, Wasim M, Shafiq M, Jamil T (2019) Carbon nanotube and graphene oxide based membranes. In: *Nanoscale materials in water purification*, pp 361–381. Elsevier
50. Arora B, Attri P (2020) Carbon nanotubes (CNTs): a potential nanomaterial for water purification. *J Compos Sci* 4(3):135

Chapter 4

Adoption of the Green Energy Technology for the Mitigation of Greenhouse Gas Emission: Embracing the Goals of the Paris Agreement



Sarika, Abhishek Anand, Ramovatar Meena, Usha Mina, Amritanshu Shukla, and Atul Sharma

Abstract The greenhouse gases have the ability to trap heat in the Earth's atmosphere which is vital for keeping the planet at a habitable temperature. Effective climate change mitigation measures include reducing greenhouse gas concentrations to levels prior to the Industrial Revolution and restricting additional emissions from development activities, burning fossil fuels, agriculture, etc. This necessitates switching to non-fossil, renewable energy sources as well as installing various new technology for emitted gas collection, providing affordable carbon-free energy alternatives. Worldwide regional-level valuations help improve inventories at a national scale and build effective mitigation plans at manageable scales. Nonetheless, more innovation and policy changes are essential to adequately balance out the long-term economic benefits of development needs. A comprehensive strategy must be devised to persuade the public that prioritizing actions to reduce GHG emissions is critical if sustainable energy is to replace fossil fuels and avert a serious environmental catastrophe. The present chapter emphasizes the factors that contribute to greenhouse gas (GHG) emissions, GHG trends over time, and various mitigation tactics. It will also talk about the role and application of nanotechnology in solving various environmental problems and delivering efficient and cost-effective energy. It's a win-win to develop climate change adaptation and mitigation strategies that work together.

Sarika (✉) · R. Meena · U. Mina
Department of Environmental Sciences, Jawaharlal Nehru University, New Delhi, India
e-mail: sarika@atree.org

Sarika
Ashoka Trust for Research in Ecology and the Environment, Bangalore, India

A. Anand · A. Shukla · A. Sharma
Non-Conventional Energy Laboratory, Rajiv Gandhi Institute of Petroleum Technology, Jais, Amethi, India

A. Shukla
Department of Physics, University of Lucknow, Lucknow, India

Keywords Greenhouse gases · Mitigation · Emission trends · Nanotechnology · Development · Policy

1 Introduction

1.1 *“is the Mean Temperature of the Ground in Any Way Influenced by the Presence of Heat-Absorbing Gases in the Atmosphere?”—Svante Arrhenius, 1896*

The environmental conditions that we inhabit have endured for approximately 10,000 years. Throughout Earth’s history, the concentrations of greenhouse gases have experienced considerable fluctuations, leading to significant climatic changes during various periods (Canadell et al. 2021). Typically, greenhouse gas concentrations have been higher during warm periods and lower during colder epochs. Based on the evidence, it is highly probable that more than 50% of the observed increase in the world’s average surface temperature from 1951 to 2010 can be attributed to the combined effects of human-made factors such as anthropogenic increase in greenhouse gas concentrations (Hegerl et al. 2019).

According to recent reports, the concentrations of carbon dioxide (CO₂), methane (CH₄), and nitrous oxide (N₂O) have exceeded the maximum levels recorded in ice cores over the past 800,000 years (Change 2007). The average rates of growth in atmospheric concentrations during the previous century are also unparalleled in the last 22,000 years, with a high degree of certainty years (Stauffer et al. 2002; Krishnan et al. 2020). While natural phenomena such as tectonic activity, plant growth, soil, wetland, and ocean sources and sinks impact greenhouse gas concentrations over timescales ranging from millions of years to hundreds or thousands of years. Since the industrial revolution, various human activities, particularly fossil fuel burning, have been responsible for persistent increase in atmospheric concentrations of various greenhouse gases, including carbon dioxide, methane, ozone, and chlorofluorocarbons gases (Bernard Stauffer et al. 2002) [40]. Scientific evidence indicates that human activities are the primary cause of the global warming observed over the last 50 years, despite natural processes such as variations in the sun’s radiation, volcanic activity, Earth’s orbit, and the carbon cycle that can also impact Earth’s radiative balance (Mesarović 2019). Since the late 1700s, the concentration of greenhouse gases has increased steadily due to human activities, resulting in a warming effect and significant impacts on various climatic variables, such as surface air and ocean temperatures, precipitation, and sea levels (Ruddiman 2005; Salinger 2005) [17]. This climate change poses severe threats to human health, agriculture, water resources, forests, animals, and coastal regions, among others.

The Intergovernmental Panel on Climate Change (IPCC) reports that the Earth’s temperature has raised up by 0.85 degrees Celsius (1.53 degrees Fahrenheit) between 1880 and 2012, with human activities being a likely key contributor (Cellura et al.

2018; Mathez and Smerdon 2018). The average global temperature has been on a steady upward trend for decades, not just on land but also in the oceans. Although numerous factors contribute to this trend, anthropogenic greenhouse gas (GHG) emissions are the main cause, including activities like fossil fuel use, coal mining, and industrialization. The concentration of CO₂ has increased by 391 PPM over the past century, with alarming increase in CH₄ and N₂O levels [61]. Climate change will affect human livelihoods while increased GHG concentrations may benefit the economy, but they come at a high cost. The IPCC's fifth assessment report confirms that warming of the atmosphere and oceans, changes in the global water cycle, reductions in snow and ice, rising global mean sea level, and changes in certain climatic extremes are all linked to human activity. It is highly likely that human influence has been the primary driver of the observed warming since the mid-twentieth century.

The impact of greenhouse gases on global warming depends on three main factors [56]. The first factor is the current atmospheric concentration of the gas, which is measured in parts per million (ppm), parts per billion (ppb), or parts per trillion (ppt). For instance, a concentration of 1 ppm means that one molecule of the gas exists for every one million molecules of air. The second factor is the length of time that the gas remains in the atmosphere. The third factor is the gas's global warming potential (GWP), which is the amount of energy it can absorb over time (usually 100 years) in relation to carbon dioxide emissions, (Lashof and Ahuja 1990; Santero and Horvath 2009). The unique impact of each greenhouse gas on the Earth's climate depends on its chemical composition and atmospheric concentration, with gases that have high infrared radiation absorption or occur in large quantities having a greater impact than those with low absorption capacities or occurring in trace (Seinfeld and Pandis 2008; Karl and Trenberth 2003). The Intergovernmental Panel on Climate Change (IPCC) defines radiative forcing as the amount of radiant energy that greenhouse gases or other climate elements (such as solar irradiance or albedo) contribute to the energy balance of the Earth's surface. Each greenhouse gas has been assigned a forcing value (in watts per square meter) based on its contribution to global warming between 1750 and the present day (Schwartz 2004; Parrish 2005). Some greenhouse gases, such as carbon dioxide, are long-lived and persist in the atmosphere for many years, reflecting historical and current global contributions. Others, like tropospheric ozone, have a short lifespan (James Salinger 2005; Lacis et al. 2013).

Each year, the global production of greenhouse gases amounts to approximately 50 billion tons. Since 1990, the total greenhouse gas emissions have increased by 50% [24]. The totality of greenhouse gas emissions includes carbon dioxide, methane, and nitrous oxide, as well as trace gases such as hydrofluorocarbons and sulfur hexafluoride (SF₆) (Olivier et al. 2005a; Crippa et al. 2019). Carbon dioxide is the most significant source of greenhouse gas emissions, accounting for 74.4% of all emissions (Crippa et al. 2019). Methane contributes 17.3%, nitrous oxide 6.2%, and other pollutants (HFCs, CFCs, SF₆) make up 2.1% of the total emissions (Ehhalt and Prather 2001). Since the pre-industrial era, human activities have been the primary source of well-mixed greenhouse gas emissions, including carbon dioxide (CO₂), methane (CH₄), and nitrous oxide (N₂O). The amount of greenhouse gases that accumulate in the atmosphere is determined by a combination of physical and biogeochemical

processes on land and in the ocean, as well as emissions and removals by humans (Edmond Mathez and Smerdon 2019). This chapter provides a concise overview of the many potential roots of greenhouse gases (GHGs), including aspects such as the properties of GHGs, the assessment of atmospheric emissions, the lifespan of GHGs and their rising trends, the calculations of carbon dioxide-equivalents, and mitigation measures for the several key sectors using green nanotechnology. GHGs are an essential component of an ecosystem and are comprised of natural sinks such as terrestrial plants, soil, geological, biological, and stratospheric sinks. However, anthropogenic sinks are also accessible and may also perform the function of a sink. However, preventing or reducing GHG emissions is essential for adjusting to climate change. Mitigation involves employing new technology, making existing equipment energy efficient, using renewable energy, etc. This chapter contains various key concepts related to GHG emissions and various calculations related to its assessments along with GHG control approaches in various sectors to optimize emissions and limit global consequences.

1.2 Greenhouse Gases?

What do you mean by “greenhouse gases?” The transparent windows of a greenhouse (or a vehicle parked in the sun) transmit the sun’s warming visible rays, prevent the warm air from escaping, and therefore keep the interior of the building warmer than the outside (Victor et al. 2014; Sarkar 2009). Some trace gases in the Earth’s atmosphere collect infrared radiation from the planet’s sun-warmed surface and transport it to the many other molecules nearby. As a consequence, Earth’s temperatures are greater than they would be if these gases were not there. The atmospheric gases and greenhouse act in very different ways, but the end result, a higher temperature in both situations, has led to the term “Greenhouse Gases” being used to describe the atmospheric gases that cause the warming effect (Mitchell 1989; Darkwah et al. 2018). Despite the fact that this nomenclature is inaccurate, it is so widely used. Many chemicals in the atmosphere are greenhouse gases. Direct sunlight (relative shortwave energy) reaches the Earth’s surface. UV and visible light warm the surface, reradiating infrared energy (heat) into the atmosphere (Rosenberg et al. 1983; Boyd 2020). Greenhouse gases capture this energy, limiting heat loss into space. Natural gases including CO₂, methane, water vapor, and nitrous oxide are greenhouse gases. Industrial fluorocarbons include CFCs, HFCs, PFCs, and SF₆ (Chittapur et al. 2021). The industrial revolution boosted natural and man-made gas concentrations. Coal, oil, and natural gas use expanded along with the global population. Interfering with the carbon cycle (by burning forests or mining and burning coal) increases atmospheric concentrations [8].

1.3 Greenhouse Gas Properties

In relation to the greenhouse effect and its impact on global warming, three main characteristics of gas determine its contribution: its absorptivity for infrared radiation, its persistence in the atmosphere, and its concentration in the atmosphere (Ehhalt and Prather 2001) [25]. Gas is able to absorb infrared light only in specific energy bands, which are determined by the gas's physical or photochemical properties. However, in addition to this inherent quality of the gas, there is also competition among gases for the ability to absorb radiation in certain frequency ranges (band overlaps) (Chilingar et al. 2009b). As long as the preexisting constituents of the atmosphere are already absorbing most of the radiation in a certain band, incorporating a gas that absorbs in the same band will not significantly enhance the greenhouse effect (Chilingar et al. 2009b) [13]. In most cases, measurements of absorptivity represent the combined impacts of the gas's intrinsic features as well as the influences of the other constituents of the surrounding atmosphere. The second characteristic, lifespan, describes how long a gas will remain in the atmosphere once it has been released into the environment (Ehhalt and Prather 2001; Forster et al. 2007). This characteristic is regarded crucial in the context of global warming concerns because, if a gas is persistent, emissions into the atmosphere would cause global warming for many years, as opposed to emissions into the atmosphere from a gas that dissipates rapidly from the environment. This is reflected in the Global Warming Potential (GWP), which is a combination of the two qualities (Ehhalt and Prather 2001; Azar and Johansson 2012a).

The last characteristic is the concentration in the atmosphere. No matter how much or how long a gas absorbs Earth's heat, it isn't a significant greenhouse gas if it isn't present in adequate quantities or if it has the potential to attain significant concentrations in the atmosphere (Seinfeld and Pandis 2008; Heard and Saiz-Lopez 2012). This is the most challenging part of determining whether or not a gas may contribute to global warming. The term "scenarios" refers to projections of future concentrations based on assumptions that have been stated unambiguously. There is no way to identify how probable an event is just based on its likelihood (Maheshwari et al. 2018).

2 Greenhouse Gas Emission Calculation

To understand the impact of increasing concentrations of greenhouse gases on the Earth's temperature, it is necessary to develop an advanced holistic physicochemical theory that accounts for the redistribution of mass and energy among the Earth's systems. This theory must consider various factors, including the evolution of atmospheric composition, climatic and geological conditions, changing solar radiation, the Earth's revolution precession, oceanographic data, and the numerous feedback loops between the atmosphere and ocean. According to [25, 39], there are three

main characteristics of a gas that determine its contribution to global warming and the greenhouse effect. These characteristics include the gas's absorptivity of infrared radiation, which is often measured as radiative forcing; the length of time that the gas remains in the atmosphere, known as its lifespan; and the concentration or amount of the gas in the atmosphere.

2.1 Atmospheric Lifetime

The lifespan of a greenhouse gas is the estimated period required for the anthropogenic increase in the concentration of an atmospheric pollutant to return to its natural level, either by conversion to another chemical compound or removal from the atmosphere through a sink (Patel 2019). This time period is dependent on the source and sink of the pollutant, as well as its reactivity (Forster et al. 2007; Ramaswamy et al. 2001). A pollutant's lifespan is often compared to the mixing of pollutants in the atmosphere; a lengthy lifetime allows the pollutant to mix throughout the atmosphere. Average lives range from roughly a week to more than a century such as sulfate aerosols, carbon dioxide, etc. (Lacis et al. 2013) [8]. Water vapors have a half-life of about 9 days (Olivier 2022) and the major greenhouse gases are well mixed in the atmosphere and require several years to dissipate (Tuckett 2009). Although it is difficult to predict precisely how long greenhouse gases will remain in the atmosphere. This is a conservative estimation of the major greenhouse gases (Crippa et al. 2019).

2.2 Carbon Dioxide-Equivalents Calculation

The term “carbon dioxide-equivalents” refers to the standard unit of measurement for greenhouse gas emissions. The UN Framework Convention on Climate Change (UNFCCC) has approved this measure, and it is used in official GHG reporting and goal setting by nations and organizations throughout the world, as well as being the most extensively used metric in the scientific literature. Carbon dioxide (CO₂) is the most significant greenhouse gas, but it is not the only one—gases such as methane and nitrous oxide are also contributing to global warming in little amounts [15]. Carbon dioxide-equivalents (CO₂eq) are a measure of total greenhouse gas emissions that attempts to combine all of the warming effects of the various greenhouse gases into a single measure of total greenhouse gas emissions (Wiedmann and Minx 2008). To make matters more confusing, various gases have varying degrees of warming intensity, and gases remain in the atmosphere for varying lengths of time, depending on their composition (Houghton and Woodwell 1989; Karl and Trenberth 2003). Considering the mass (e.g., kilos of methane released) and multiplying it by the ‘global warming potential’ (GWP). GWP evaluates a gas's warming effect relative to CO₂; it assesses the gas's “strength” over time (Reisinger 2011). The standard

method is to analyze the GWP over 100 years (GWP100). The IPCC embraced GWP100 in inventory recommendations, while its Fifth Assessment Report (AR5) does not specifically endorse its usage. AR5 methane GWP100 is 28 (Or 34 if climate feedback processes are included) (Lynch et al. 2020).

In other words, one kilogram of methane causes 28 times more warming than one kilogram of CO₂. However, methane is considered a short-lived greenhouse gas, meaning its warming effect reduces over time [28]. In contrast, CO₂ can last for thousands of years. Therefore, using a measure called GWP100 to compare the warming effects of different gases may not accurately represent the impact of short-lived gases like methane (Özelsel et al. 2019). This is because GWP100 understates the short-term warming caused by methane, which is much higher than its GWP100 value of 28. To better account for short-term warming, some experts suggest using GWP20, which measures the warming potential over 20 years. The IPCC assigns methane a GWP20 value of 84 (86 with feedback included) (Azar and Johansson 2012b). This means that the warming effect of methane is much greater in the short term compared to the long term. As a result, the GTP (Global Temperature Potential) values of methane also vary significantly over time, with a GTP100 of 4 and a GTP20 of 67 (Cain et al. 2019). This complicates aggregating the warming consequences into a single statistic. Choosing a measure may influence how humans prioritize GHG reduction strategies: should they start with potent but short-lived gases like methane? A compelling argument if they have to worry about approaching temperature-induced tipping points? Or should only concentrate on the long-term CO₂ emissions that will generate long-term temperature impacts? Some researchers have created new ways to better portray the temperature response to various gases. The Martin School at Oxford University's Myles Allen and Michelle Cain conduct an investigation on climate pollution that directly sums this up (Allen et al. 2018; Maheshwari et al. 2017). Short-lived greenhouse gas emissions (GWP*) are a novel technique to characterize warming response (Stohl et al. 2015; Allen et al. 2022).

To compute CO₂-warming-equivalent emissions, GWP* implies that (a) growing methane emissions instantly raise global temperatures, (b) fast-dropping methane emissions immediately lower global temperatures, and (c) slow reductions in methane emissions stabilize world temperatures. In simulations (b) and (c), lowering CO₂ emissions causes future global temperature rises (only the rate of temperature increase slows) (Smith et al 2021; Lynch et al. 2020; Reisinger 2011). CO₂ emissions from fossil fuels and industries are simpler to assess than other greenhouse gases. Most CO₂ emissions originate from burning coal, oil, and gas. Researchers have comprehensive data on energy production and sources at the national, regional, and global levels (Olivier et al. 2005). They can estimate annual coal, oil, and gas use. Researchers know how much CO₂ is emitted when humans manufacture a unit (for example, a kilowatt-hour from coal). They compare "emission factors." They can calculate CO₂ emissions by multiplying the amount of energy generated by coal, oil, and gas by their emission factors (Parrish 2005; Julie Kerr Casper 2010a). Estimating other greenhouse gas emissions is more complicated. Notably, statistics on methane and NO_x emissions only go back to 1990 (Minx et al. 2019) [24]. An annual Global Carbon Project "Carbon Budget" on CO₂ emissions, natural sources, and sinks is

published. This budget is almost 50 years old. But it just recently issued its first Methane Budget (2020), and its first N₂O Budget was not yet ready (Friedlingstein et al. 2020; John Lynch et al. 2020).

Land usage and garbage contribute significantly to methane and nitrous oxide emissions. Obtaining reliable data for all nations and periods on livestock, soils, and land types is challenging (Oenema et al. 2005). In spite of typical emissions factors for greenhouse gases per unit of food (for example, per kilogram of rice), the amount produced by agriculture varies greatly depending on location, soil type, and agricultural techniques (Van Amstel and Swart 1994; Reay et al. 2012). The variations in emissions of various food kinds, e.g., beef produced in one region may emit up to ten times more than beef produced elsewhere. Unlike energy CO₂, agricultural and land use emission components are very changeable. This makes estimating long-term methane and NO_x emissions problematic (and other greenhouse gases which exist in lower concentrations). As a consequence, overall greenhouse gas emission estimates are generally less precise than CO₂ statistics (Deemer et al. 2016). Annual total emissions enable us to identify the world's top polluters in absolute terms. However, they often reflect a population narrative—China and India, for example, are among the top three emitters but are also the world's two most populated nations (Lamb et al. 2018; Olivier et al. 2005).

The adiabatic model is used to examine the relationship between atmospheric pressure and global temperature in the troposphere. It analyzes how changes in the atmosphere's mass and chemical composition affect temperature, with a focus on the impact of human-generated greenhouse gases but does not consider feedback between the atmosphere and oceans. The greenhouse gas emissions per capita are expressed in tons per person per year. Numerous smaller nations around the globe are the greatest polluters on a per capita basis. Guyana, Brunei, Botswana, the United Arab Emirates, and Kuwait are all major oil and/or gas producers (Coady et al. 2017). There are significant disparities in per capita emissions among the biggest emitters: the typical person in the United States emits more than 18 tons; in China, the average person emits less than half that much, at 8 tons; and in India, the average person produces roughly 2.5 tons (Ritchie and Roser 2020).

3 Greenhouse Gas Levels' Rising Trends

In the 165 years since 1850, the last four decades have been steadily warmer than the three preceding ones. For the first two decades of the twenty-first century (2001–2020), the average annual increase in the Earth's surface temperature was 0.99 [0.84–1.10] degree Celsius compared to the 1850–1900 average (Vornicu 2021). In the time between 2011 and 2020, the average temperature of the Earth's surface rose 1.09 [0.95 to 1.20] degree Celsius, with the rise being bigger over land (1.59 [1.34 to 1.83] degree Celsius) than it was over water (0.88 [0.68 to 1.01] degree Celsius) (Rupasinghe et al. 2022). Moreover, methodological advances and additional datasets contributed 0.1 °C to the AR6 report's warming estimate. Human activity has been

proven to be the cause of a worldwide rise in well-mixed quantities of greenhouse gases (GHGs) that has been observable since around 1750 (Hegerl et al. 2019). The atmospheric concentrations of carbon dioxide (CO₂), methane (CH₄), and nitrous oxide (N₂O) have all grown in the 5 years from 2011 (measurements reported in AR5), with 2019's annual averages at 410 ppm, 1866 ppb, and 332 ppm, respectively [61]. With some regional differences, land and ocean have absorbed an approximately constant percentage of CO₂ emissions from human activities over the last six decades (globally, around 56% every year) [40] (Andrew 2019).

The International Energy Agency reports that the global concentrations of well-mixed greenhouse gases (GHGs) such as carbon dioxide (CO₂), methane (CH₄), and nitrous oxide (N₂O) in 2019 are significantly higher than pre-industrial levels, with increase of approximately 47, 156, and 23%, respectively [24, 38]. According to recent studies by [24, 38], the current levels of these GHGs in the atmosphere are unprecedented. Methane concentrations have been rising rapidly, with an average annual increase of 7.6 parts per billion (ppb) in 2010 and a more recent increase of 9.3 ppb yr⁻¹ from 2014 to 2019 (Lashof and Ahuja 1990; Kirschke et al. 2013) [27].

Since 2007, the multi-decadal increasing trend (medium confidence) in atmospheric CH₄ has been driven mostly by emissions from fossil fuels and agriculture (mainly from cattle) (Chilingar et al. 2009a). Interannual fluctuation is driven by El Niño–Southern Oscillation cycles, although it is also influenced by factors including biomass burning, wetland emissions, and loss owing to interaction with tropospheric hydroxyl radical OH (James Salinger 2005) [55]. The atmospheric content of N₂O increased by 0.85 ppb year between 1995 and 2019, with an additional increase to 0.95 ppb annually in the most recent decade (2010–2019) (Ehhalt and Prather 2001; Olivier et al. 2005a) [38]. An additional 30% increase in human emissions during the 1980s has contributed to this rise in the most recent decade of monitoring (2007–2016). From 1980 to 2016, roughly two-thirds of the increase was caused by fossil fuels/industry, biomass burning, and wastewater treatment (Karl, science 2003; Torquati et al. 2010) [38].

3.1 The Permanence of Uncertainties

The global increase in greenhouse gas emissions is closely linked to five economic sectors: energy, industry, construction, transportation, and agriculture. These sectors continue to be driven by persistent underlying factors, with little indication of decreasing demand or transitioning to low-carbon and zero-carbon services. The decarbonization of Europe and North America's energy systems has been aided by the use of renewables and fuel switching [56]. In contrast, rapidly industrializing nations have continued to rely on fossil-based energy systems, which have only recently begun to slow down their expansion. The industrial, construction, and transportation sectors, especially in Eastern Asia, Southern Asia, and South-East Asia, have experienced increased emissions due to high demand for materials, energy services, floor space, and travel [1] Identifying and reversing the most pervasive and

climate-damaging patterns across sectors is a crucial research and policy challenge in the Anthropocene era. However, previous estimates of GHG emissions are uncertain due to the scarcity and ambiguity of underlying activity and inventory data, application of standard emissions factors, different interpretations of oxidation and combustion, and other factors (Crippa et al. 2019; Ehhalt and Prather 2001; Miodrag M. Mesarović 2019). The regulation of greenhouse gas emissions at various WWTPs (wastewater treatment plants) is now filled with challenges and difficulties. GHG emission estimation is difficult due to measurement errors and a lack of transposable data. To bridge this gap, mathematical models such as GHG modeling help improve the measurement of GHG emissions for different WWTP layouts and analyze the consequences of different operating circumstances [9].

4 Major Gases and Their Emission Sources

Currently, buildings and automobiles account for the majority of energy-related emissions. Road vehicles (12.5% of total emissions), residential structures (11.4% of total emissions), and business buildings all contribute to the majority of energy emissions (6.7% of total emissions) (Ritchie et al. 2022; LABARAN 2021) [55]. These activities generate emissions both directly from fossil fuel burning and indirectly via activities such as the usage of electricity. Apart from energy, significant drivers are livestock and manure (59.9%), other industries (4.5%), and agricultural soils (4.2%) (Hegerl et al. 2019; Law et al. 2017; Stephenson 2018). The category “other industry” encompasses any operations that do not line neatly into one of the other groups. As such, it encompasses a broad variety of operations, such as non-metallic metals, building, mining and quarrying, textiles and leather, wood and wood products, and transportation equipment (Hegerl et al. 2019).

The manufacturing of iron and steel contributes significantly to energy-related emissions, accounting for 7.2% of total emissions. This category also includes energy-related emissions from the production of fertilizers, medicines, refrigerants, and oil and gas extraction, which collectively make up 3.6% of emissions (Ji et al. 2018). Additionally, energy-related emissions from the production of tobacco products and food processing are responsible for 1% of total emissions. This includes the conversion of raw agricultural products into their final products, such as the transformation of wheat into bread (Coady et al. 2017). Metals other than iron and steel, such as brass, also contribute to emissions, with a total of 0.7% (Guruswamy 2015). These metals require a significant amount of energy to produce, resulting in pollution. The production of paper and pulp is another source of emissions, accounting for 0.6% of total emissions (Nyambuu and Semmler 2020). The manufacturing of equipment is also responsible for a portion of emissions, contributing 0.5% to the overall total. Finally, other industries, such as mining and quarrying, construction, textiles, wood products, and transport equipment, are responsible for a significant portion of emissions, accounting for 10.6% of total emissions. For instance, car manufacturing is included in this category (Boiangiu 2017; Guruswamy 2015; Urge-Vorsatz

et al. 2013). In summary, various industries contribute to energy-related emissions, and their collective impact on the environment cannot be ignored. However, with a concerted effort to reduce emissions across all sectors, nations should work toward creating a more sustainable future for planet Earth.

The two sectors responsible for emitting the largest amount of greenhouse gases are industry and transportation, with their emissions increasing rapidly over time. Since 1990, three industries have been responsible for the majority of greenhouse gas emission growth. Industrial processes have increased by a staggering 187%, while transportation (a subsector of energy) has increased by 79%, and manufacturing and construction (another subsector of energy) has increased by 56% (Ehhalt and Prather 2001; Ritchie et al. 2022; Nicholas J. Santero and Horvath 2009). It's not just CO₂ emissions contributing to the increase in industrial emissions, but also the rising usage of refrigeration and air conditioning. These processes produce hydrofluorocarbons (HFCs), which are extremely potent greenhouse gases (Guruswamy 2015). The primary reason for the increase in transportation emissions is automobile travel, which has grown exponentially over the years [32]. It's essential to recognize the significant role these industries play in the overall increase in greenhouse gas emissions. Without proper measures in place to mitigate their impact, the situation could continue to worsen. However, through collaborative efforts and innovative solutions can work toward a more sustainable future.

By contrast, emissions from the energy sector's biggest emitting subsector, electricity, and heat production surged by 78% between 1990 and 2013, but subsequently decreased by 2.4% between 2013 and 2016 (Ehhalt and Prather 2001; Yekini Suberu et al. 2014). The decline was attributed to a number of causes, including a move away from coal toward natural gas and an increasing reliance on renewable energy. However, the most recent carbon emission statistics indicate that emissions from this energy subsector increased by 1.3 and 2% in 2017 and 2018, respectively, while remaining stable at 0.06% in 2019 (Ehhalt and Prather 2001; Ritchie et al. 2022).

Nitrous oxide (N₂O), which is commonly referred to as "laughing gas," contributes to 5% of the greenhouse effect and is harmful to the ozone layer. It is produced by both human activities such as chemical industries, power plants, and fertilizers, and natural sources like microbial activity in the soil, particularly in humid zones [19, 52]. Significant amounts of CH₄ and N₂O can be detected in the small air bubbles that are trapped in ice cores and predate the industrial era [27]. These two gases are emitted naturally and their emission rates have fluctuated in response to climate changes throughout history. However, their atmospheric concentrations remained stable for centuries prior to the Industrial Revolution. Methane, a significant component of natural gas is responsible for approximately 16% of global warming (Reisinger 2011).

Although natural sources such as wetlands, termites, and marine microbes contribute to CH₄ emissions, human activities are responsible for 70% of CH₄ released into the atmosphere. These activities include fossil fuel production, livestock and manure management, wastewater treatment, and landfills [27]. Over thousands of years, rice farming in wetlands has also contributed significantly to CH₄ emissions, resulting in current levels that are 150% higher than pre-industrial revolution levels in landfills (Vergé, De Kimpe, and Desjardins 2007). With a global

warming potential 21 times greater than CO_2 , CH_4 poses a severe environmental threat (Ehhalt and Prather 2001; Reisinger 2011). Water vapor and clouds are also significant contributors to the greenhouse effect, with water vapor accounting for about 90–95% of the total greenhouse effect. CO_2 -induced warming of the Earth leads to increased water vapor molecules in the atmosphere. Water vapor has a high capacity to absorb and emit radiation at various wavelengths and is more abundant in the atmosphere compared to other greenhouse gases, making it a potent contributor to climate change [61]. Ozone is a critical protective layer in the stratosphere, shielding the Earth from harmful ultraviolet radiation. However, in the troposphere, it is considered an air pollutant, produced by the combustion of hydrocarbons. It is a significant contributor to urban smog, harmful to breathe and an important greenhouse gas that contributes to climate change. Tropospheric ozone is short-lived, and its levels vary by location and season [16, 59]. It is essential to understand the significant impact of these gases and pollutants on our environment and take collective action toward reducing their emissions to mitigate climate change.

CFCs, once used in a range of man-made products including foaming agents, insecticides, aerosols, fire extinguishers, and refrigerants (Bodansky 2001), were phased out by the Montreal Protocol and Clear Air Act Amendments of 1990 due to their role in depleting the polar ozone [32]. However, the replacement of CFCs with HFCs, PFCs, and sulfur hexafluoride has introduced a new set of challenges. These chemicals, while stable and resistant to atmospheric chemical processes, are potent greenhouse gases and released in industries such as aluminum and magnesium manufacturing, electrical transmission stations, and semiconductor factories (Myhre et al. 2021). Despite only accounting for 2% of total emissions, their global warming potential makes them a significant threat. These fluorinated gases have heat-trapping abilities ranging from 140 to 23,900 times more efficient than CO_2 , thus posing a considerable environmental hazard [38] (Sizirici et al. 2021).

Burning of biomass and fossil fuels produces black carbons that are considered a global atmospheric pollutant responsible for global warming. The presence of black carbon on clouds causes them to trap energy and generate heat instead of reflecting sunlight. This affects rainfall patterns and climate. When black carbon combines with other aerosols, it can create atmospheric brown clouds that absorb visible solar energy and dull the Earth's surface, ultimately impacting the hydrological cycle. In a study by Bauer et al. [4], Menon et al. [31] using a global climate model, the influence of aerosol black carbon on precipitation and temperature patterns in China and India was examined. Additionally, van Dorland, Dentener, and Lelieveld [12, 37] also suggest that black carbon, when scavenged by clouds, has a significant impact on climate.

5 Mitigating Greenhouse Gas Emissions

Climate change is one of today's most difficult topics. Climate change is accountable for various impacts including limited freshwater supplies, damage to the coastal system, and human health, and raises the question of food security. It has numerous elements—science, economics, society, politics, and moral and ethical issues—and will continue to exist for decades or centuries. Heat-trapping greenhouse gas carbon dioxide stays in the atmosphere for centuries, and the globe (particularly the seas) responds slowly to warming. Even if humans cease generating all greenhouse gases today, future generations will still be affected. Thus, mankind is “committed” to climate change.

How much warming? Our emissions and the climate system's response will decide that. Despite growing awareness of climate change, our greenhouse gas emissions continue to climb. For the first time in history, the daily atmospheric CO₂ concentration exceeded 400 ppm in 2013 (Canadell et al. 2021). About three to five million years ago, during the Pliocene Epoch, levels reached that high. Because the world is already committed to some degree of climate change, humans must react in two ways:

- reducing and stabilizing atmospheric levels of heat-trapping greenhouse gases (mitigation);
- adapting to impending climate change (adaptation).

High-level actions such as the creation of a circular economy and waste management, the adoption of sustainable production and consumption habits, and the use of renewable resources are all necessary for achieving these climate objectives. The fight against climate change demands a collaborative effort between the agricultural and financial sectors to implement effective mitigation measures. The financial sector must prioritize sustainable investment and support the execution of the Paris Agreement. The land use sector, represented by agriculture, plays a crucial role in aligning mitigation and adaptation strategies with the Sustainable Development Goals (SDGs) and other developmental objectives, to achieve a sustainable future by 2030. In order to address the challenges posed by climate change, it is crucial to limit global warming to below 2 degree Celsius, and preferably well below 1.5 degree Celsius, in accordance with the Paris Agreement, to avoid catastrophic consequences (Reisinger 2011).

Achieving this target would necessitate a complete overhaul of our economy and society, culminating in total decarbonization by the middle of this century. Sustainable transportation and urban design are only a few of the necessary actions that must be taken to combat climate change. Others include reducing reliance on climate-damaging fluorinated greenhouse gases (F gases) and extending the use of renewable energy sources [32]. The International Climate Initiative (IKI) assists partner nations and subnational entities in developing and implementing innovative greenhouse gas emission reduction strategies. The ultimate objective is to make economic and supply structures carbon-neutral [17]. The NDCs (nationally determined contributions) and

long-term strategies (LTSs) are key instruments for political governance. IKI also promotes the establishment of systems for measuring, reporting, and verifying greenhouse gas emissions, mitigation actions, climate finance, and adaptation measures [3, 32]. Many programs aim to raise public and private funding for climate change prevention.

To address climate change, it is crucial to implement measures aimed at reducing the release of heat-trapping greenhouse gases into the atmosphere. These efforts can be achieved by curbing the sources of these gases, such as reducing fossil fuel usage in electricity generation, heating, and transportation, or by enhancing the amount of “sinks” that accumulate and store these gases, including forests, oceans, and soil [5]. The primary objective of these mitigation efforts should be to stabilize greenhouse gas levels within a timeframe that facilitates the natural adaptation of ecosystems to climate change, safeguards food production, and promotes sustainable economic development. This aligns with the recommendations of the 2014 United Nations Intergovernmental Panel on Climate Change report on Mitigation of Climate Change, which stresses the need to prevent significant human intervention in the climate system. To address the existing or expected future climate, it is necessary to first comprehend climate change [3]. The ultimate goal is to reduce the sensitivity to the negative consequences of global warming such as rising sea levels, severe weather events, and food shortages. Additionally, it is essential to explore any potential benefits that may arise as a result of climate change, such as extended growing seasons or increased yields in some areas. The goal is to respond to climate change in a manner that maximizes the ability to adapt to its challenges while taking advantage of its opportunities.

At the beginning of the twentieth century, climate change was widely regarded as an academic investigation into theoretical scientific phenomena of uncertain origin. During the last few decades, nations have all agreed that they will work together to slow down global warming. Intergovernmental and international efforts to deal with environmental challenges were first put into action in the late twentieth century. Stockholm, Sweden hosted the first worldwide environmental meeting in 1972 [34]. As a result of this United Nations-sponsored meeting, worldwide environmental politics took an important step forward. Consequently, the UN Environment Programme (UNEP) was established, and worldwide promises to “promote sustainability” and “protect the environment” were made. Climate change, on the other hand, was just a side note at the Stockholm Conference (Bodansky 2001). Climate change was mostly thought of as a scientific issue, not a politically important one (Tesler 2018). In 1988, the WMO and UNEP agreed to collaborate on an intergovernmental evaluation of climate change research, consequences, and response options. For the purpose of conducting this assessment, the Intergovernmental Panel on Climate Change (IPCC) was founded [47]. The IPCC has since produced five complete assessments that have been subjected to rigorous review procedures (Arnall et al. 2014). Then, between this conference in 1972 and late in the 1980s, some politicians took note as scientists became more and more concerned about the risks of more greenhouse gas emissions (GHGs). Most governments and people throughout the globe now believe that global warming is a major danger to the future well-being of all people, and indeed

all living beings [27, 34]. They also believe that it is critical to reduce our carbon dioxide emissions in order to reduce CO₂ concentrations in the atmosphere. To stay below 1.5 °C, global greenhouse gas emissions must be decreased by 30 gigatons per year by 2030 (Pielke 2002; Grundmann 2007; Meyer-Ohlendorf et al. 2018).

5.1 Construction

Climate change is wreaking havoc on corporations, society, and individuals. It is becoming increasingly clear that a transition to a low-carbon economy is necessary (Deemer et al. 2016). The building and construction sector is critical to this transformation. The greenhouse gas (GHG) emissions from the sector account for around 40% of worldwide GHG emissions (WBCSD 2018; KRALJ 2008; Wang et al. 2016). The materials used in construction, as well as the heating, cooling, and lighting of buildings and infrastructure, are the primary sources of these emissions. Considerations for reducing GHG emissions in the construction industry (Ding 2013; Urge-Vorsatz et al. 2013):

- Reducing carbon output of construction supplies in upstream production.
- Energy efficiency and renewable energy consumption in residential housing and infrastructure are implemented (Sizirici et al. 2021).
- Recycling resources and controlled materials management during renovation and deconstruction.

Emissions can be regulated and decreased by maximizing the efficiency with which building resources are utilized (Ji et al. 2018). This involves making the most of available construction teams and resources in a way that decreases greenhouse gas emissions while keeping construction costs and duration to a bare minimum, among other things. Reducing CO₂ emissions from the construction industry can be achieved through implementing regulations and policies, undertaking impact assessments, and using low-carbon technologies. In order to minimize CO₂ emissions and contribute to combating climate change, all stakeholders must fulfill their responsibilities effectively (Ritchie et al. 2022). Regionally these strategies in construction industries can be implemented:

- Standards as well as policy and restriction strategy.
- Adopting low-carbon technology.
- Impact assessment of building process and materials (Cellura et al. 2018; Ding 2013).

5.2 Transportation

Transportation contributes about one-fifth of global GHG emissions, but close to 30% in most developed nations [61]. Transportation GHG emissions are rising faster

than any other industry globally. Most are linked with cars, although air travel is becoming more essential. Transportation GHG reductions are often more costly than other GHG reductions in cost-effectiveness studies (Tesler 2018). Weak demand for personal transportation, air travel, and commodities transport; difficulties adopting new low fossil energy and new fuel-efficient motor technology; declining quality of public transportation practically everywhere; and growing percentage of products transported by truck. Petroleum usage is also getting more carbon-intensive. Increasingly carbon-intensive and distant sources of carbon fuels are exploited, necessitating greater refining to improve fuel quality (Chilingar et al. 2009a; Ehhalt and Prather 2001). Considering the transportation sector in terms of global carbon emissions, it may be separated into two primary categories: civilian automobiles and commercial transport trucks. They account for approximately two-thirds of all greenhouse gas emissions associated with transportation. The following techniques for reducing greenhouse gas emissions in the transportation industry may be summarized (Luderer et al. 2019; Plambeck 2012; Rabie and Franck 2018):

- Encourage the use of public transportation, cycling, and walking for short-distance travel.
- Modal change and freight transportation improvement.
- Energy efficiency:
- Preference for more energy-efficient automobiles and use of low-carbon-intensive fuels.
- To phase out the oldest and least efficient automobiles.
- Driving license examinations have been toughened, which has the effect of lowering emissions and fuel consumption via less aggressive driving.
- Improved infrastructure: improved road connections reducing traffic congestion.

5.3 *Agriculture*

According to the United Nations Food and Agriculture Organization (FAO), between 40 and 50% of the world's land area is used for cropland management, permanent crops, such as agroforestry and bio-energy crops, and other uses (Bellarby et al. 2008; Torquati et al. 2010). Between 1990 and 2005, agricultural CH₄ and N₂O emissions increased by over 17% globally, or by around 60 MtCO₂-eq/yr on average (Van Amstel and Swart 1994; James Salinger 2005). The agriculture sector was accountable for around 60% of nitrous oxide emissions and roughly 50% of methane emissions (Weldeslassie et al. 2018). Carbon dioxide (CO₂) emissions were only about 0.04 GtCO₂/yr despite significant annual interactions between the atmosphere and agricultural land [36].

Methane and nitrous oxide emissions from agriculture are critical to mitigating and adapting to 1.5 °C or below, which is consistent with the Paris Agreement's temperature objective. Net zero carbon dioxide emissions and fuel consumption are also necessary [28, 36]. Modeled approaches that accomplish the necessary cutbacks in agricultural emissions do so through the use of agricultural emission pricing.

However, there is a significant disconnection between such model scenarios and reality in the agriculture industry [48]. Currently, no nation imposes a mandated carbon price on agricultural emissions, and current research indicates the substantial difficulty to apply other climate policies with equivalent rigor to agriculture. A more realistic perspective is required if we are to avoid modeled emission scenarios painting an excessively positive picture of agricultural sector mitigation possibilities [28]. A significant source of emissions, agriculture, has the potential to reduce its impact on the environment. Agriculture research is rarely highlighted as a mitigation option, despite the significant role it plays in shaping emissions through the transformation of native landscapes to food and biofuel crops (Boiangiu 2017) [28]. In the quest for a more sustainable and environmentally friendly future, agriculture has a crucial role to play in reducing greenhouse gas emissions. The crop and grazing lands, implementing improved agronomic methods, managing fertilizer use, and adopting effective livestock management practices (Julie Kerr Casper 2010). Livestock management techniques such as utilizing feed supplements and practicing rotational grazing can also help to store carbon in the soil. Proper management of manure is also crucial, as it can limit emissions of methane and nitrous oxide. This can be achieved by covering manure storage facilities and even capturing and burning methane from the storage [38, 11]. Additionally, recovering compost for crop production and rehabilitating degraded lands are popular options for reducing greenhouse gas emissions in agriculture. By implementing these solutions, society can work toward a more sustainable and environmentally friendly agricultural sector (Vasileiadou et al. 2011).

5.4 Energy Sector

The power industry will be a core concern of GHG reduction analyses in a large part of the world. Coal-burning power plants are the primary producer of CO₂, the most potent greenhouse gas (GHG). Net anthropogenic carbon emissions from the burning of fossil fuels range from 60 to 90% [40, 55]. Methane (CH₄) and nitrous oxide (N₂O) are both greenhouse gases (GHGs), and the energy industry is also a producer of additional GHGs, such as nitrogen oxides (NO_x), carbon monoxide (CO), and non-methane hydrocarbons (NMHC) [7] (Julie Kerr Casper 2010a). A fifth of the world's methane emissions are attributed to the production and transportation of fossil fuels including coal, oil, and natural gas [13] (Darkwah et al. 2018). Industry, commerce, transportation, and agriculture are some of the key sectors that use energy. The supply side of the energy sector includes the extraction, conversion, and distribution of generated electricity. GHG emissions may be mitigated at many stages in the supply chain, from extraction to usage, and there are a variety of ways to do so [7]. The UN Environment Program proposes a set of mitigation strategies for the power sector, including the promotion of ambitious renewable energy and efficiency initiatives (Luderer et al. 2019; Victor et al. 2014) [57]. The adoption of policies that encourage the use of clean, renewable energy, and the efficient use of existing resources is

also encouraged. To ensure that renewable energy and carbon reduction become a shared concern, organizations should work toward increasing reliance on clean energy sources, educating society about the importance of renewable energy, and individuals can contribute to this effort by decreasing their energy usage whenever possible and taking advantage of opportunities to use renewable energy.

5.5 Industrial and Manufacturing Sector

Almost one-fifth of the world's 2016 carbon dioxide (CO₂) emissions were attributed to the industrial and construction sectors. When electricity and heat emissions are broken down by end-use sector, it accounts for 36% of total emissions, making it the greatest emitter in this category (Frank et al. 2019; Lu 2017). Manufacturing industries and onsite energy outputs from the sector accounted for more than 20% of total greenhouse gas (GHG) emissions in 2014, an increment from 16% in 2000 (Sizirici et al. 2021). Even while large historical climate polluters have reduced their industrial emissions, industrial emissions have continued to expand at a rapid rate. As a result of the high temperature and other process requirements, the industrial and manufacturing sector is a particularly difficult sector to decarbonize; in addition, a fifth of the sector's CO₂ emissions come from processing rather than energy usage, and progress toward alternative processes is gradual (Nyambuu and Semmler 2020; Ritchie et al. 2022; Zeng et al. 2017).

6 Nano-Revolution: Advancements and Applications of Nanotechnology

Nanotechnology is a promising twenty-first-century technology, but its progress has been hindered by a lack of understanding of its risks and a shortage of policies to manage them. Researchers are still working to overcome these challenges, including funding, regulations, and technical issues. Green Nano requires an understanding of "Green Chemistry" and nanotechnology [53]. The goal of green chemistry is to redefine chemical use such that it is safer and more efficient. In recent years, the sustainability movement has been more involved with nanotechnology, and the terms sustainable and green chemistry have become ubiquitous as represented in Fig. 2. Green Nano has two primary goals: to create multifunctional nanomaterials for renewable energy generation, nanosensors for pollution detection and monitoring, green packaging, semiconductor photocatalysis for environmental remediation, and innovative membranes for efficient treatment and purification of wastewater [35].

Average temperature anomaly, Global

Global average land-sea temperature anomaly relative to the 1961-1990 average temperature.

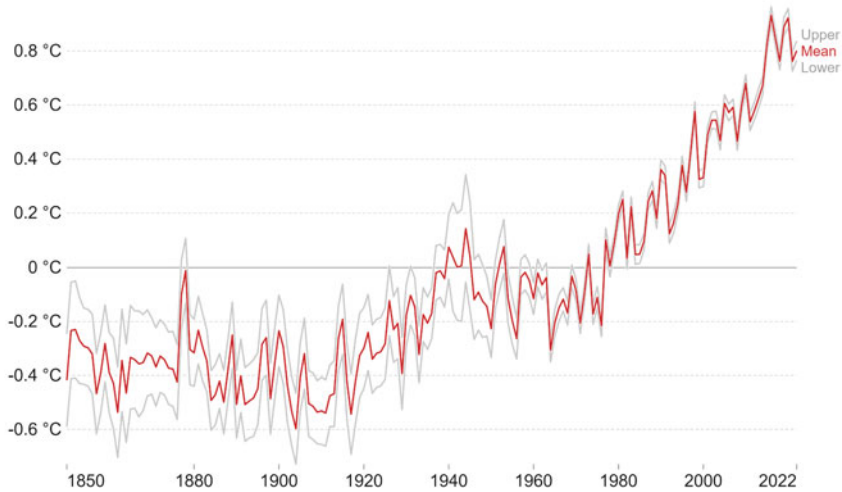


Fig. 1 Showing graphical analysis of global average temperature fluctuation from pre-industrial time to 2022. *Sources* [21]

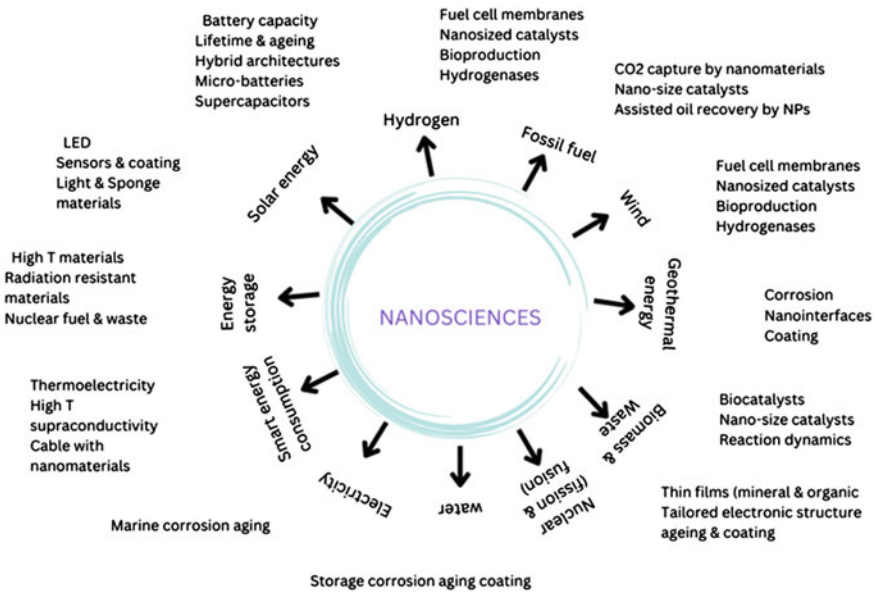


Fig. 2 Represented the range of nanomaterial application and requirements for future energy application. *Source* European GENNESYS project

6.1 Gases (Carbon and Methane)

Carbon sequestration involves capturing and storing carbon dioxide or other forms of carbon to mitigate global warming. Various methods of carbon separation technology, including chemical and physical absorption, adsorption, low-temperature distillation, and biomineralization, are used [57]. The ocean has the potential to act as a carbon sink, with direct injection and enhancing net oceanic uptake being two ocean carbon sequestration methods [8]. In terrestrial ecosystems, afforestation and natural biological processes, such as photosynthetic species and microbial communities, can effectively reduce atmospheric CO₂ [57]. Advanced chemical approaches and nanotechnology play a crucial role in developing new solvents, sorbents, and materials for CO₂ separation, storage, and transport. Methane, a component of biogas, is captured for fuel, and advanced materials such as metal–organic frameworks, nanoporous carbonaceous materials, and functionalized nanomaterials have been identified as potential candidates for the adsorption of natural gases [41].

Metal–organic frameworks, with their versatile pore sizes and shapes, are highly effective in adsorbing gas molecules and have been used in a range of applications, including gas storage and transport [46]. These frameworks are now being used in power generation plants to reduce carbon dioxide emissions through post-combustion capture, pre-combustion capture, and oxy-fuel combustion processes [7, 42]. To measure CO₂ adsorption, researchers have employed volumetric and gravimetric methods using Sievert's apparatus and microbalances, respectively [33]. Metal–organic frameworks (MOFs) can be surface-functionalized with high-affinity functional groups such as hydroxylamine, alkylamines, and mixed amines to increase their selectivity and capacity for CO₂ adsorption [46, 18]. Doping MOFs with metals like cobalt or incorporating them with carbon nanotubes and lithium ions can also enhance the uptake of gaseous molecules like H₂, CO₂, and CH₄ [20]. Additionally, electrostatic interactions between CO₂ molecules and extra framework metal ions in the pores of anionic MOFs can significantly enhance their CO₂ adsorption capacity [50]. Metal–organic frameworks (MOFs) are versatile materials also used for gas storage and transport, with specific functional groups and metals enhancing their adsorption capacity. Surface-functionalized MOFs with hydroxylamine, alkylamines, and mixed amines increase CO₂ adsorption (Subramanian et al. 2020b). Among the most promising MOFs for methane uptake are HKUST-1 and Ni-MOF-74. Zeolite imidazolate frameworks (ZIFs) have gained popularity for their gas-storage abilities [14]. MOF-177 has the highest adsorption capacity for CO₂ and CH₄, while heterobimetallic In(III)/Pd(II)-based MOF with square-octahedron topology has high CO₂/CH₄ selectivity [50]. The only drawback is the difficulty of packing their crystal structure in the adsorption column. The ability of nanoporous carbon materials, including CMK-1, CMK-3, and CMK-5, to capture and store natural gas, especially CO₂, has been reported [41, 49]. Open single-wall carbon nanostructures with interstitial channels were found to have a significant methane-storage capacity of 160 cm³/cm³ of nanocarbons at 3.5 MPa and 303 K [22, 60].

Carbon nanotubes (CNTs) have shown to be promising for CO₂ capture, with MWCNTs being more effective than SWCNTs in the uptake of CO₂ and CH₄ [29]. Modification with functional groups can make CNTs even more efficient for the adsorption of other gases. Graphene materials have also been used as sorbents for CO₂, biogas, and H₂S, with functionalization further enhancing adsorption and selectivity. While metal-decorated graphene is more commonly used for hydrogen storage, it shows potential for CO₂ and CH₄ adsorption [54]. Naturally occurring zeolites are less used due to the presence of impurities and structural defects, while synthetic zeolites are excellent choices for various applications such as adsorption, catalysis, and ion exchange [2]. Zeolites possess ideal characteristics such as polarity, reversibility, and selective adsorption capacity for the adsorption of gas molecules, especially CO₂ [50]. The interaction between the CO₂ molecular quadrupole moment and the electric field created by the charge distribution of the adsorbent material is responsible for CO₂ adsorption [51]. The adsorption of CO₂ on nano-zeolites is influenced by the charge density of exchangeable cations. Due to their molecular pore size distribution and highly selective adsorption at a wide range of pressure and temperature, zeolites have obtained the molecular sieving property [14]. Silica nanoparticles are utilized as a means of supporting regenerable CO₂ adsorbents that are effective in high-concentration streams, such as flue gases and natural gas wells [30]. Research indicates that polyethyleneimine (PEI) supported by silica nanoparticles has demonstrated the highest capacity for CO₂ sorption, reaching up to 202 mg CO₂/g adsorbent [29]. Additionally, silica nanofluids have been found to be efficient in the adsorption of natural gases and biogas.

6.2 Nanoparticle Innovations: Revolutionizing Clean Energy Production and Boosting Efficiency

Various types of nanoparticles, such as core-shell nanoparticles, alloy nanoparticles, and bimetallic nanoparticles, are utilized as anode catalysts. For instance, Cu-Pd bimetallic nanoparticles supported on carbon are used as anode electrocatalysts for direct borohydride-hydrogen peroxide fuel cells, which exhibited the highest catalytic activity [50]. Carbon nanomaterials, titanium oxide, lanthanide nanomaterials, and layered graphene/quantum dots are widely employed to fabricate photovoltaic cells [54, 45]. The integration of heterogeneous nano-catalysts has emerged as a promising solution for overcoming issues such as high mass transfer resistance, low efficiency, and fast deactivation in biofuel production. Studies have demonstrated that nanocatalyst CaO/CuFe₂O₄ significantly improves the yield of biodiesel from chicken fat, while biodiesel produced from Pongamia blended with diesel using cerium oxide nanocatalyst showed better performance in diesel engines with fewer emissions [44]. Polymer nanowires and thin nanofilms have proven to be a cost-effective and highly efficient approach to harvest electricity from mechanical energies in nanogenerators [26]. In addition, nanocoatings have been used as protective

materials to address issues of corrosion and scaling in seawater, and nano-zirconia-titania coatings have been found to provide non-corrosive coatings in geothermal systems [23]. Furthermore, nanotechnology has played a crucial role in developing sensors with self-diagnostic functionalities and providing real-time structural health monitoring in aircraft [10]. Nanoparticles are used to reduce friction and wear significantly, leading to lower fuel consumption in engines. For example, nano-lubricants dispersed with dodecylamine functionalized graphene (DAG) in commercial engine oil reduced the coefficient of friction by up to 40% compared to base engine oil [44].

To improve the efficiency of domestic refrigerators, alumina is used as a refrigerant, resulting in a 17.27% increase in the coefficient of performance and a 32.48% reduction in energy consumption [6]. The use of SiO₂ nanoparticles in heat transfer was investigated, and it was found that a maximum heat transfer coefficient of 163.2% could be obtained at a concentration of 0.4% [6]. Green synthesis methods are used to produce nanoparticles for a variety of applications, such as nano-catalysts for biofuel production, nano-lubricants, and nano-adsorbents for pollutants [45]. Innovative nanotechnology solutions have demonstrated their potential in the field of lubrication. Halloysite clay nanotubes, a natural, low-cost, and non-toxic nanoparticle, have shown promising results in reducing wear volume loss and friction coefficient by up to 70% as lubricant additives [50, 43]. Additionally, cellulose nanocrystals have been identified as green lubricant additives, with a concentration of 0.1% in base oil resulting in reduced friction and wear rate [51]. These eco-friendly and cost-effective alternatives offer a promising future in the field of lubrication.

7 Conclusion

Humans and their societies have had a mixed record of success when it comes to adapting to the weather and climatic changes. Particularly drought has been associated with the success or failure of civilizations. But, over the last 12,000 years, Earth's climate has been largely stable, permitting modern civilization and sustaining life. The existing way of life has been modified so that it is compatible with the weather patterns to which we are exposed and have been acclimated. Understanding the changing climate is necessary in order to respond to it. There is a direct correlation between the rate of climate change and the difficulty of adaptation. The rise of greenhouse gases from fossil fuels and industries has led to a substantial increase in global mean surface temperature. Fortunately, nanotechnology offers promising solutions to this problem by producing materials such as MOFs, nanoporous materials, nanocomposites, and nanopolymers that can help reduce GHGs in the atmosphere and combat global warming. Nanocatalysts, nanogenerators, and nanosensors have already shown their effectiveness in processes like biofuel and hydrogen production, as well as the development of fuel cells that can reduce our reliance on fossil fuels. With the potential for even more applications in the future, it's crucial to continue exploring and addressing research gaps in nanotechnology to unlock its full potential in fighting climate change.

Changes in the climate have far-reaching consequences, yet their effects are often noticed only on a smaller scale. That's why urban and municipal governments are leading the way in adapting to climate change. Cities and towns all across the globe have taken it upon themselves to tackle climate-related issues, in the lack of any coherent national or international climate policy direction. People are attempting to better manage floods and stormwater, enhance storage and utilization of existing water resources, and build flood defenses in anticipation of heat waves and greater temperatures. Thus, implementing sustainable practices and making conscious choices will be the possible solution to save planet Earth.

References

1. AHMETOĞLU S, TANIK A (2020) Management of carbon footprint and determination of GHG emission sources in construction sector. *Intern J Environ Geoinform* 7(2):191–204. <https://dergipark.org.tr/en/pub/ijegeo/issue/54146/726913> (September 22, 2022)
2. Akhmat G et al (2016) Does energy consumption contribute to environmental pollutants? Evidence from SAARC countries. *Springer* 21(9):5940–5951. <https://link.springer.com/article/>; <https://doi.org/10.1007/s11356-014-2528-1> (February 21, 2023)
3. Azar C, Johansson DJA (2012) On the relationship between metrics to compare greenhouse gases the case of IGTP, GWP and SGTP. *Earth Syst Dyn* 3(2):139–147. <https://esd.copernicus.org/articles/3/139/2012/> (September 20, 2022)
4. Bauer SE et al (2010) A global modeling study on carbonaceous aerosol microphysical characteristics and radiative effects. *Atmosph Chem Phys* 10(15):7439–7456. <https://acp.copernicus.org/articles/10/7439/2010/> (February 21, 2023)
5. Bhagwat SA et al (2012) A battle lost? Report on two centuries of invasion and management of lantana Camara L. in Australia, India and South Africa. *PLoS One* 7(3)
6. Bondre D et al (2019) Experimental performance and analysis of domestic refrigeration system using nano-refrigerants. *Springer*, pp 389–399. <https://link.springer.com/chapter/>; https://doi.org/10.1007/978-981-13-2490-1_35 (February 20, 2023)
7. Brear MJ, Baldick R, Cronshaw I, Olofsson M (2020) Sector coupling: supporting decarbonisation of the global energy system. *Elect J* 33(9). <https://www.sciencedirect.com/science/article/pii/S104061902030124X> (September 20, 2022)
8. Casper JK (2010) Greenhouse gases: worldwide impacts. In *Global Warming*, 1–287. [https://books.google.com/books?hl=en&lr=&id=A_48H1rBVJ4C&oi=fnd&pg=PP1&dq=11.%09Casper,+J.+K.+\(2010\).+Greenhouse+gases:+worldwide+impacts.+Infobase+Publishing.&ots=tejZCCChsh&sig=ILXmZe5UAG4n9I69YXUXW5pvigY](https://books.google.com/books?hl=en&lr=&id=A_48H1rBVJ4C&oi=fnd&pg=PP1&dq=11.%09Casper,+J.+K.+(2010).+Greenhouse+gases:+worldwide+impacts.+Infobase+Publishing.&ots=tejZCCChsh&sig=ILXmZe5UAG4n9I69YXUXW5pvigY) (September 20, 2022)
9. Chen S et al (2022) A critical review on deployment planning and risk analysis of carbon capture, utilization, and storage (CCUS) toward carbon neutrality. *Renew Sustain Energy Rev* 167. <https://www.sciencedirect.com/science/article/pii/S1364032122004373> (February 21, 2023)
10. Chow JC et al (2005) Nanoparticles and the environment. *J Air Waste Manag Assoc* 55(10):1411–1417. <https://www.tandfonline.com/doi/pdf/>; <https://doi.org/10.1080/10473289.2005.10464743> (February 21, 2023)
11. Cole CV (1996) Agricultural options for mitigation of greenhouse gas emissions. *Climate change 1995: Impacts, adaptation and mitigation of climate change: scientific technical analyses*, pp 745–71. <https://www.osti.gov/etdeweb/biblio/441904> (September 21, 2022)
12. van Dorland R, Dentener FJ, Lelieveld J (1997) Radiative forcing due to tropospheric ozone and sulfate aerosols. *J Geophys Res Atmosp* 102:28079–28100
13. Ehhalt D et al (1999) IPCC third assessment report - Chapter 4 - atmospheric chemistry and greenhouse gases. <https://orfeo.belnet.be/handle/internal/7978> (September 20, 2022)

14. Eskandari A, Jahangiri M, Anbia M (2016) Effect of particle size of NaX zeolite on adsorption of CO₂/CH₄. *Int J Eng Trans A: Basics* 29(1):1–7. https://www.ije.ir/article_72642.html (February 20, 2023)
15. Etminan M, Myhre G, Highwood EJ, Shine KP (2016) Radiative forcing of carbon dioxide, methane, and nitrous oxide: a significant revision of the methane radiative forcing. *Wiley Online Libr* 43(24):12, 614–12, 623. <https://agupubs.onlinelibrary.wiley.com/doi/abs/>; <https://doi.org/10.1002/2016GL071930> (September 20, 2022)
16. Eyring V et al (2010) Sensitivity of 21st century stratospheric ozone to greenhouse gas scenarios. *Geophys Res Lett* 37(16). <https://agupubs.onlinelibrary.wiley.com/doi/abs/>; <https://doi.org/10.1029/2010gl044443> (February 21, 2023)
17. Giorgetta MA et al (2013) Climate and carbon cycle changes from 1850 to 2100 in MPI-ESM simulations for the coupled model intercomparison project phase 5. *J Adv Model Earth Syst* 5(3):572–597
18. Govekar S, Kumar R, Suresh R, Sridharan K (2018) Nanotechnology to Sustain a Clean Environment 3–11. <https://link.springer.com/chapter/>; https://doi.org/10.1007/978-3-319-71327-4_1 (October 23, 2022)
19. Grosso D, Stephen J, Wirth T, Ogle SM, Parton WJ (2008) Estimating agricultural nitrous oxide emissions. *Eos* 89(51):529
20. Gurdal Y, Seda K (2016) A new approach for predicting gas separation performances of MOF membranes. *J Memb Sci* 519:45–54. <https://www.sciencedirect.com/science/article/pii/S0376738816304963> (February 21, 2023)
21. Hannah R, Max R, Pablo R (2022) ‘Energy’. Published Online at OurWorldInData.Org. 2022. https://scholar.google.com/scholar?hl=en&as_sdt=0%2C5&scioq=Nanotechnology+for+Mitigation+of+Global+Warming+Impacts&q=Hannah+Ritchie%2C+Max+Roser+and+Pablo+Rosado+%282020%29+ +%22CO2+and+Greenhouse+Gas+Emissions%22.+Published+online+at+OurWorldInData.org.+Retrieved+from%3A+%27https%3A%2F%2Fourworldindata.org%2Fco2-and-greenhouse-gas-emissions%27+&btnG= (February 21, 2023)
22. Hannig M, Hannig C (2012) Nanotechnology and its role in caries therapy. *Adv Dent Res* 24(2):53–57
23. Kannaiyan K, Reza S, Vignesh K (2019) Application of nanoparticles in clean fuels. Springer, pp 223–42. <https://link.springer.com/chapter/>; https://doi.org/10.1007/978-3-030-04500-5_9 (February 21, 2023)
24. Kaygusuz K (2009) Energy and environmental issues relating to greenhouse gas emissions for sustainable development in Turkey. *Renew Sustain Energy Rev* 13(1):253–270
25. Khalil MAK (1999) Non-CO₂ greenhouse gases in the atmosphere. *Annu Rev Energy Env* 24(1):645–661
26. Kumar S, Dinesha P, Bran I (2019) Experimental investigation of the effects of nanoparticles as an additive in diesel and biodiesel fuelled engines: a review. *Biofuels* 10(5):615–622
27. Kweku DW et al (2018) B. Greenhouse effect: greenhouse gases and their impact on global warming 17(6):1–9
28. Leahy Sinead, Harry Clark, Andy Reisinger (2020) Challenges and prospects for agricultural greenhouse gas mitigation pathways consistent with the Paris agreement. *Front Sustain Food Syst* 4
29. Lu C et al (2008) Comparative study of CO₂ capture by carbon nanotubes, activated carbons, and zeolites. *Ener Fuels* 22(5):3050–3056. <https://pubs.acs.org/doi/abs/>; <https://doi.org/10.1021/ef8000086> (February 21, 2023)
30. Mauter MS et al (2018) The role of nanotechnology in tackling global water challenges. *Nat Sust* 1(4):166–75. <https://www.nature.com/articles/s41893-018-0046-8> (February 20, 2023)
31. Menon S, Hansen J, Nazarenko L, Luo Y (2002) Climate effects of black carbon aerosols in China and India. *Science* 297(5590):2250–2253
32. Minx Jan C et al. (2021) A comprehensive and synthetic dataset for global, regional, and national greenhouse gas emissions by sector 1970–2018 with an extension to 2019. *Earth Syst Sci Data* 13(11):5213–5252. <https://essd.copernicus.org/articles/13/5213/2021/> (September 20, 2022)

33. Muhammad I et al (2013) Does environmental sustainability affect the renewable energy consumption? Nexus among trade openness, CO₂ emissions, income inequality, renewable energy. *Springer* 21(8):5427–5449. <https://link.springer.com/article/>; <https://doi.org/10.1007/s11356-022-22011-1> (February 21, 2023)
34. Najam A (2005) Developing countries and global environmental governance: from contestation to participation to engagement. *Intern Environ Agr Polit Law Econ* 5(3):303–21. <https://link.springer.com/article/>; <https://doi.org/10.1007/s10784-005-3807-6> (September 22, 2022)
35. Nazir R, Insha A (2021) Role of green nanotechnology in alleviating climate change. *Microbiom Glob Clim Change* 365–74. <https://link.springer.com/chapter/>; https://doi.org/10.1007/978-981-33-4508-9_19 (October 23, 2022)
36. Neeteson JJ, Verhagen A (2010) Climate change and agriculture: mitigation and adaptation. *Acta Horticult* 852:19–26. https://www.actahort.org/books/852/852_1.htm (September 21, 2022)
37. Novakov T, Menon S, Kirchstetter TW (2005) Aerosol organic carbon to black carbon ratios: analysis of published data and implications for climate forcing. *Wiley Online Libr* 110(21):21205. <https://agupubs.onlinelibrary.wiley.com/doi/abs/>; <https://doi.org/10.1029/2005JD005977> (February 21, 2023)
38. Panchasara H, Samrat NH, Islam N (2021) Agriculture, and undefined 2021. Greenhouse gas emissions trends and mitigation measures in Australian agriculture sector—a review. *mdpi.com*. <https://www.mdpi.com/966980> (September 21, 2022)
39. Prather M et al (2001) Atmospheric chemistry and greenhouse gases
40. Prentice IC et al (2001) The carbon cycle and atmospheric carbon dioxide
41. Rai M, Ingle A (2012) Role of nanotechnology in agriculture with special reference to management of insect pests. *Appl Microbiol Biotechnol* 94(2):287–293
42. Rehman Erum, Shazia Rehman (2022) Modeling the Nexus between carbon emissions, urbanization, population growth, energy consumption, and economic development in Asia: evidence from grey relational analysis. *Energy Rep* 8:5430–5442. <https://www.sciencedirect.com/science/article/pii/S235248472200734X> (February 21, 2023)
43. Roy K, Chandan KG (2017) Biological synthesis of metallic nanoparticles: a green alternative. In: *Nanotechnology: synthesis to applications*, pp 131–45. <https://www.sciencedirect.com/science/article/pii/S1549963409001154> (February 21, 2023)
44. Sekoai P T et al (2019) Application of nanoparticles in biofuels: an overview. *Fuel* 237:380–397. <https://www.sciencedirect.com/science/article/pii/S0016236118317435> (February 21, 2023)
45. Sharma S et al (2022) Recent developments in smart nano-agrochemicals: a promise for revolutionizing present-day agriculture. *Mater Today: Proce* 69:530–34. <https://www.sciencedirect.com/science/article/pii/S2214785322061235> (February 21, 2023)
46. Singh SP, Rathinam K, Gupta T, Agarwal AK (2021) Nanomaterials and nanocomposites for environmental remediation. *Energy Env Sustain* 1–4. <https://link.springer.com/chapter/>; https://doi.org/10.1007/978-981-16-3256-3_1 (October 23, 2022)
47. Speck DL (2010) A hot topic? Climate change mitigation policies, politics, and the media in Australia. *Human Ecol Rev* 17(2):125–34. <https://www.jstor.org/stable/24707660> (September 27, 2022)
48. Srivastava R (2019) Emerging trends of nanotechnology in environment and sustainability: a review based approach. Karthiyayini S (ed) *Australasian J Env Manag* 26(2):191–92. <http://link.springer.com/>; <https://doi.org/10.1007/978-3-319-71327-4> (October 23, 2022)
49. Stone V, Nowack B, Baun A, Van Den Brink N, von Der Kammer F, Dusinska M, Handy R, Hankin S, Hassellö VM, Joner E, Fernandes T (2010) F. Nanomaterials for environmental studies: classification, reference material issues, and strategies for physico-chemical characterisation. *Sci Total Env* 408(7):1745–54. <https://doi.org/10.1016/j.scitotenv.2009.10.035>
50. Subramanian KS, Karthika V, Praghadeesh M, Lakshmanan A (2020a) Nanotechnology for mitigation of global warming impacts. *Glob Clim Change: Resilient and Smart Agriculture* 315–336. <https://link.springer.com/chapter/>; https://doi.org/10.1007/978-981-32-9856-9_15 (October 23, 2022)

51. Subramanian KS, Karthika V, Praghadeesh M, Lakshmanan A (2020b) Nanotechnology for mitigation of global warming impacts. In *Global Climate Change: Resilient and Smart Agriculture*, Springer Singapore, pp 315–36
52. Syakila A, Carolien K (2011) The global nitrous oxide budget revisited. *Greenhouse Gas Measu Manag* 1(1):17–26. <https://www.tandfonline.com/doi/abs/>; <https://doi.org/10.3763/ghgmm.2010.0007> (February 21, 2023)
53. Thakur M, Sharma A, Chandel M, Pathania D (2021) Modern applications and current status of green nanotechnology in environmental industry. In: *Green Functionalized Nanomaterials for Environmental Applications*, pp 259–281, Elsevier
54. Thirumalaisamy R, Suriyaprabha R, Prabhu M, Sakthi Thesai A (2022) Role of nanomaterials in environmental remediation: recent advances—a review. In: *Strategies and Tools for Pollutant Mitigation*, pp 51–68, Springer International Publishing
55. Tubiello, Francesco N et al. (2013) The FAOSTAT database of greenhouse gas emissions from agriculture. *Environ Res Lett* 8(1):831–43. <https://iopscience.iop.org/article/>; <https://doi.org/10.1088/1748-9326/8/1/015009/meta> (September 21, 2022)
56. Tuckett R (2021) Greenhouse gases and the emerging climate emergency. In: *Climate Change*, pp 19–45
57. Ussiri DA, Lal R (2017) Carbon Sequestration for Climate Change Mitigation and Adaptation, pp 287–325. Berlin: Springer
58. Ussiri DAN, Lal R (2017) Carbon sequestration for climate change mitigation and adaptation *Carbon Sequestration for Climate Change Mitigation and Adaptation*. <https://link.springer.com/content/pdf/>; <https://doi.org/10.1007/978-3-319-53845-7.pdf> (September 20, 2022)
59. Wuebbles DJ (1995) Weighing functions for ozone depletion and greenhouse gas effects on climate. *Annu Rev Energy Env* 20(1):45–70
60. Zhang J et al (2020) Surface charge-dependent bioaccumulation dynamics of silver nanoparticles in freshwater Algae. *Chemosphere* 247:125936
61. Zhongming Z et al (2021) *Greenhouse Gas Bulletin: Another Year. Another Record*

Chapter 5

Prospects of Alcohols with Nanoparticles as an Alternative & Renewable Automotive Engine Fuels



Nitya Talwar, Gurtej Singh, Sumit Taneja, and Gurjeet Singh

Abstract Researchers worldwide are seeking alternative fuels due to the depletion of fossil fuel reserves and increasing pollution. In order to meet modern automobile emission standards, engineers are developing cleaner technologies and more efficient engines. To address both issues, current research focuses on using biofuel additives such as alcohols to compensate for fossil fuels in gasoline engines. Blending alcohol with exhaust gas recirculation (EGR) can improve the performance and emissions of spark-ignited (SI) engines. Methanol is a proven alcohol for blending in gasoline. Ethanol has recently become a more important fuel for automotive engines, as it reduces emissions and can be used in both SI and compression-ignited (CI) engines. Second-generation bioethanol, derived from bio-waste, can also be used as an alternative fuel for SI engines, leading to proper disposal of waste and a cleaner environment. Ethanol-gasoline blends can decrease CO and HC emissions, although NO_x emissions may increase. This article delves into detailed information about various alcohol fuels namely methanol, ethanol and butanol fuels, their synthesis, their utilization in SI engines & their impact on engine performance parameters and on the potential benefits of using various nanoparticles in the fuel blends.

Keywords Automotive fuels · Ethanol–gasoline blends · Exhaust emissions

1 Introduction

In the eighteenth century, the world had seen the revolutionary changes in the field of transportation, manufacturing and power sector. These revolutionary changes brought the changes in the life style of the people. With the time, advancement

N. Talwar · S. Taneja (✉)
Mechanical Engineering, Manipal University Jaipur, Jaipur, Rajasthan, India
e-mail: sumit4088@gmail.com

G. Singh · G. Singh
Mechanical Engineering, Punjab Engineering College, Chandigarh, India

© The Author(s), under exclusive license to Springer Nature Singapore Pte Ltd. 2023
D. Tripathi et al. (eds.), *Nanomaterials and Nanoliquids: Applications in Energy and Environment*, Advances in Sustainability Science and Technology,
https://doi.org/10.1007/978-981-99-6924-1_5

and improvement in the technologies revolutionized transportation by bringing rails and airplanes. Since the past three centuries, there were no drastic changes in the environment which were brought by the uncontrollable emissions in the field of transportation and power sector.

It was the mid of the twentieth century when the world started to realize the problems caused in the environment from the automobiles and power plants. As these automobiles and power plants largely depend on the use of fossil fuels for the energy, it also has raised the problem of fuel crisis in the future. Emissions from automobiles and power plants lead to phenomena like green-house effect and global warming. These problems have really caused an unbalance in the atmosphere, and can be sensed with the unpredictable climatic changes. One thing to be noted down is that exploitation of fossil fuels and environmental problems cannot be viewed separately because their existence is mutual to each other. Excessive exploitation of fossil fuels has led the world to face green-house effect and global warming. In order to rectify these problems, we need to reduce our large dependence on the fossil fuels and have to look after new resources of energy that must be eco-friendly and renewable in nature. Renewable sources of energy are clean in nature and their use can address many environmental problems in an effective manner.

Petrol and diesel are two important forms of fuel we obtain from crude petroleum. These are obtained by the fractional distillation of the crude petroleum. Today almost of the transportation sector heavily depend on these fuels. Unfortunately, scientists have estimated that petroleum sources would get depleted by the end of 2050. We are left with the approximate 35 years of the remaining petroleum. Such a situation looks heart-breaking in the times to come. We would be left with nothing in future if we do not make it today for the future. It is the only time to work on the combination of renewable sources with the petroleum products. Researchers have indicated many alternative fuels which are compatible with petrol and diesel, and research is already in the go-through phase.

Biofuels, which are harnessed from the biomass and biowaste, offer a number of advantages to meet the solution of environmental problems. A number of studies have shown that biofuels, when blended with petrol and diesel, bring a reduction in the pollutant emissions. Up to a certain limit, blending of biofuels with petrol and diesel can be done without the requirement of modifications in an engine.

Ethanol basically belongs to the class of hydrocarbon-based fuels which are synthesised from the biomass or the plant and food wastes. It has been attracting huge interest of the Renewable energy scientific community as it can be used as an alternative fuel in the spark ignition engines. Reduction in the net engine gives out emissions by burning ethanol compared to that of fossil fuels, Energy supply security is ensured by Ethanol and the economic growth of ethanol producing community and nation are the prime drivers which attract engineers towards ethanol. Globally, Brazil and USA are major ethanol producers and consumers. Ethanol is generally blended in gasoline from 5 to 50% in Europe for use in flexible fuel vehicles.

2 Rationale Behind the Present Study

Nowadays many people have become aware of the fact that the fossil fuels are a finite source of energy. As shown in the Fig. 1 it is estimated by the International Energy Agency, that the world production will peak in the year 2010–2020 and then it will start to decrease. Therefore finding alternatives to fossil fuel has now become a commercial priority. In the emerging economic powers such as India, China and Brazil, the demand for fuel is ever increasing. For instance between the year 1991 and 2006 China's demand grew at a phenomenal annual logarithmic rate of 7.2%. If we assume that the similar trend will continue then by the year of 2020 China would be consuming 20 million barrels per day (about as much as the U.S. is currently consuming), and by the year 2030 the amount would have doubled to nearly 40 million barrels per day [30].

Due to this there are many concerns over the increasing levels of greenhouse gases in the atmosphere and the potential for this to lead to a climate change with very serious consequences on society. Hence because of all these factors we have once again started to focus on ethanol. Ethanol has the capability to limit carbon dioxide emissions if the whole “well-to-wheel” cycle is considered (Fig. 2). The carbon dioxide which is emitted when ethanol is burned as a fuel in an engine, can be re-captured from the environment by growing crops that are then used in the production of ethanol, thus completing the cycle. It is clear that by using such a renewable cycle at least a part of the CO₂ emissions can be avoided, although the emissions associated with each stage and the net reduction compared to alternative energy source needs to be examined very carefully. Particularly after the 1973/74 fuel crisis there are many concerns about oil supply disruptions due to the unstable political situation in regions that export crude oil and thus increase in ethanol use has also been stimulated.

If we talk about the direct substitute for fossil fuels in the transport sector the best answer would be biofuels and the most commonly produced biofuel is ethanol. Also no major modifications are required today in the engines to use ethanol as a fuel. The low blended fuel can simply be used in unmodified engines whereas if we go for high blended fuels then some modifications may be required. Similar to ethanol, researchers have also diverted their efforts on the blending of butanol with petrol and diesel. Butanol possesses similar physical and combustive properties as that of ethanol.

3 Engine Emissions

Exhaust emissions and performance parameters are two important aspects in an engine, whether SI or CI engine. As discussed above that emissions from vehicles play a part to the green house effect and global warming. Therefore, the knowledge of these emissions is very much important before going deep into the topic. Emissions

in SI and CI engines are very much similar although their concentrations in the atmosphere generated are different. Emissions are given in detail in the next section.

Common engine emissions include:

- a. Unburned hydrocarbons
- b. Particulates
- c. Oxides of nitrogen
- d. Oxides of carbon
- e. Oxides of Sulfur

3.1 Unburned Hydrocarbons

Engine emissions depend upon the equivalence ratio which can be defined as the actual fuel/air ratio to the stoichiometric fuel/air ratio. When all the molecular oxygen which is present gets utilized during the combustion reaction, stoichiometric combustion is said to occur. The graphs for the emissions in SI and CI engines are different and depend on their respective equivalence ratio [31].

Unburned Hydrocarbons in an SI Engine

Presence of unburned fuel which does not undergo combustion in the combustion chamber results in the hydrocarbon emissions. Exhaust gases coming from combustion chamber contain up to 6000 ppm of unburned fuel, which accounts for about 2% of original fuel. Nearly 40% of this is unburned hydrocarbons of the fuel while the remaining hydrocarbons are obtained from the fuel whose structure was changed due to chemical reaction that did not finish. Remaining hydrocarbons are small non-equilibrium molecules which are produced when the large fuel molecules break up due to thermal cracking. About 9% of the fuel supplied does not get burned during the expansion stroke and about 2% fuel ends up in the exhaust whereas the rest of the fuel is used in the other three strokes.

As already mentioned in the above section, UHC emissions are a very strong function of the equivalence ratio. When the air-fuel ratio is high, there is not sufficient oxygen present around fuel molecules which results in improper combustion and higher UHC emissions. During starting, this can be noticed.

There are six reasons which are believed to be responsible for UHC emissions.

- (a) **Crevice:** The narrow regions in a combustion chamber are called crevices where flame cannot propagate because its size is quite less as compared to the quenching distance. Crevices are located around the piston, valve seats, spark plug and head gasket.
- (b) **Oil layers:** The piston ring cannot prevent migration of some of the oil into the cylinder. Hence an oil layer is formed within the combustion chamber that traps fuel.
- (c) **Deposits:** The deposits of carbon around the cylinder, piston crown and valves are much smaller in size than that of the quenching distance, making the fuel trapped in the deposits unburned.

- (d) Liquid fuel: Sometimes the liquid fuel which is introduced into the cylinder does not get vaporized and is absorbed by the deposits or crevices.
- (e) Flame-quenching—The flame travels very close to the walls and gets usually quenched which in turn leaves a small amount of unreacted fuel along with oxygen. The combustion process is slowed down due to the low pressure and temperature which is caused by the expansion of gases during the combustion process and the power stroke. Due to the slowdown of the combustion, the flame is quenched late in the expansion stroke.
- (f) Improper mixing—Due to heterogeneous mixing, the fuel molecules are not surrounded by the oxygen molecules properly resulting in incomplete combustion.

Hydrocarbon Emissions in a CI Engine

HC emissions in a Compression Ignition engine are quite less when compared to a Spark Ignition engine. This is because Compression Ignition engines operate with a lean air–fuel mixture. Diesel contains long chained hydrocarbons having higher molecular weights and hence higher condensing and boiling temperatures. In Compression Ignition engines carbon soot is formed. Some hydrocarbon molecules get condensed when these come in contact with the surface of carbon soot. These condensed molecules along with carbon soot come out as exhaust emissions from cylinder.

As the mixture in the combustion of a CI engine is non-homogeneous, some local spots are formed where the air–fuel mixture is too rich or too lean. This means, there are several flame fronts existing in the combustion chamber at the same time. In fuel rich local spots, there is no sufficient oxygen for combustion and the fuel does not get burned. Fuel is not burned in the spots where it is lean, as the combustion gets limited. As a result of overmixing, some of the fuel particles will get mixed with the already burned gases and hence will not combust totally.

3.2 Carbon Monoxide Emission (CO)

Carbon monoxide is generated when an engine is operating at an equivalence ratio which is fuel rich. In the absence of sufficient oxygen whole carbon is not converted to carbon dioxide. Some amount of the fuel is not burned which results in the formation of carbon monoxide. Carbon monoxide is considered as an undesirable emission for mainly two reasons.

Firstly, it is the loss of chemical energy as it is a combustible fuel which generated heat energy during its combustion. This heat can be supplied as an additional thermal energy. Secondly, carbon monoxide is a poisonous gas. It reacts with the hemoglobin present in the blood. It is too dangerous and affects the nervous system of the human body. The thing is that it has much greater affinity to the blood than that of oxygen. It is 1600 times highly reactive than oxygen with human blood.

Carbon monoxide generated is the maximum when an engine operates at fuel-rich equivalence ratio. During starting and accelerating under load, an engine requires rich fuel mixture resulting in higher generation of carbon monoxide. Poor combustion, improper combustion and local rich regions are also the reasons for carbon monoxide emissions. Compression Ignition engines operate with an overall lean mixture and produce very low carbon monoxide emissions.

3.3 Oxides of Nitrogen (NO_x)

Nitrogen oxides are considered very undesirable. A typical engine usually emits about 2000 ppm of nitrogen oxides. There is a small amount of nitrogen dioxide (NO_2) whereas there is a very large percentage of nitrogen oxide (NO). There are traces of other oxides of nitrogen which can also be observed. Government has continued to form strict policies and regulations to reduce NO_x emissions year by year. The thing is that the NO_x which is released, further results in the formation of ozone in the atmosphere and also forms photochemical smog when it comes in contact with fog in the presence of sunlight.

As nitrogen is in abundance in the atmosphere, NO_x is generated mostly from nitrogen present in the atmosphere. Fuel blends also contain oxygen and nitrogen, which react to form NO_x . The atmospheric nitrogen, which is a diatomic molecule, is very stable at low temperatures. However, during the combustion process in an engine very high temperatures occur. At these high temperatures, some of the nitrogen molecules break down to monoatomic or nascent nitrogen which is highly reactive. At higher temperatures in the combustion chamber, water vapors along with oxygen undergo dissociation. Diatomic oxygen molecules dissociate to produce nascent oxygen and water vapors into hydrogen. The products like nascent oxygen and hydrogen are highly reactive and are main for the generation of NO. As high combustion chambers temperatures are reached all of these react much further to the right. As the temperature of the combustion reaction keeps on increasing, the amount of nascent nitrogen generated goes up and hence the amount of NO_x formed also increases.

The factors other than high temperatures in the combustion chamber which affect the NO_x formation are combustion duration, pressure and air–fuel ratio. It is observed that less NO_x is generated in the engines with fast-burn combustion chambers. As CI engines have greater combustion temperature ranges for higher compression ratios, they produce higher levels of NO_x .

One of the most dangerous aspects of NO_x formation is observed as photochemical smog. Photochemical smog is formed in the atmosphere in the presence of sunlight due to the reaction between automobile exhaust and air. The reaction products are nascent oxygen and nitrogen oxide in addition to smog. As already mentioned, monoatomic oxygen is very reactive as it can initiate several different reactions. Monoatomic oxygen combines with the atmospheric oxygen to produce ozone in the atmosphere which is very near to the surface of the earth. Ozone not only causes

damage to the plants, trees and the crop yield but it is also very harmful for human lungs and other biological tissues.

3.4 *Oxides of Sulfur*

CI engine fuels contain small amount of sulfur in them. Sulfur after combustion comes out in the form of sulfur dioxide and sulfur trioxide as an exhaust emission. Unleaded gasoline may contain about 150–550 ppm sulfur by weight whereas the diesel fuels contain about 5500 ppm by weight. But in actual practice, these days sulfur content in CI engines has been reduced to one tenth of 5500 ppm in many developed countries. When the temperatures are quite high, sulfur reacts with oxygen and produces sulfur dioxide and it also reacts with hydrogen to produce hydrogen sulfide. Engine exhaust contains about 20 ppm of SO₂ which further reacts with atmospheric oxygen to form sulfur trioxide. Further, these combine with moisture present in the atmosphere to form sulfurous & dilute sulfuric acid which results in the formation of acid rain.

3.5 *Particulates*

Exhaust emissions of CI engines contains particulates relatively higher as compared to the exhaust emissions of SI engines. A very high concentration of particulate matter can result into a visible smoke in the exhaust gases. Particulates can be defined as a substance other than water that can be collected by filtering the exhaust. Types of particulates are as follows:

- a. solid carbon material or soot
- b. condensed hydrocarbons and their partial oxidation products

In a Compression Ignition engine carbon soot particles are produced. In CI engines, there are fuel-rich regions in the combustion chamber which result in the generation of soot particles. Maximum density of particulates can be observed when an engine is at WOT that is wide open throttle and under high load. At WOT, maximum amount of fuel is required to be injected to supply the maximum power output and the mixture required is fuel enriched.

Soot particles occur in forms of solid spheres. These are usually in the form of clusters and the diameters of these solid carbon spheres range from 9 to 90 nm. In absence of oxygen, in fuel-rich zones all the carbon is not converted into carbon dioxide and some of the carbon is formed as soot. Most of the components are continued to get mixed in the combustion chamber through turbulence and mass motion, majority of these soot particles find enough oxygen to get converted into carbon dioxide. Generally, around 25% of the carbon present in soot is due to the lubricating oil components which vaporize and then react during the combustion process and around 0.5% is due to the fuel.

In the Compression Ignition engines, the compression ratios are high and so the expansion stroke is large thus resulting in relatively low condensing temperatures at which gases are condensed. Due to this, the remaining high-boiling point hydrocarbons in the fuel and lubricants condenses on the surface of the carbon soot particles.

4 Global Warming and Carbon Dioxide Emission

The greenhouse gases are usually transparent to the high frequency of solar radiation that heat up the earth's surface, but they absorb the lower frequency radiation and therefore they result in global warming. The main cause responsible for global warming is carbon dioxide (CO_2) along with water vapor and methane. (Fig. 3).

The globally averaged concentration of carbon dioxide gas in the earth's atmosphere is currently 383 ppm by volume. About one-quarters, is due to deforestation and the main three quarters is due to the burning of fossil fuels. Due to transportation, there is around 14% of global greenhouse gas emissions and approximately 19% of CO_2 emissions. Since the beginning of the industrial revolution around the mid 1700's the atmospheric concentration of carbon dioxide has increased by about 31%.

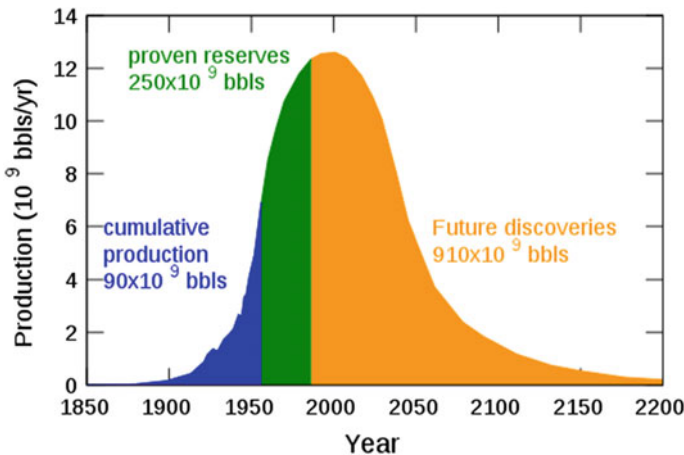


Fig. 1 Peak generation of fossil reserves per Year—an estimate by IEA [30]

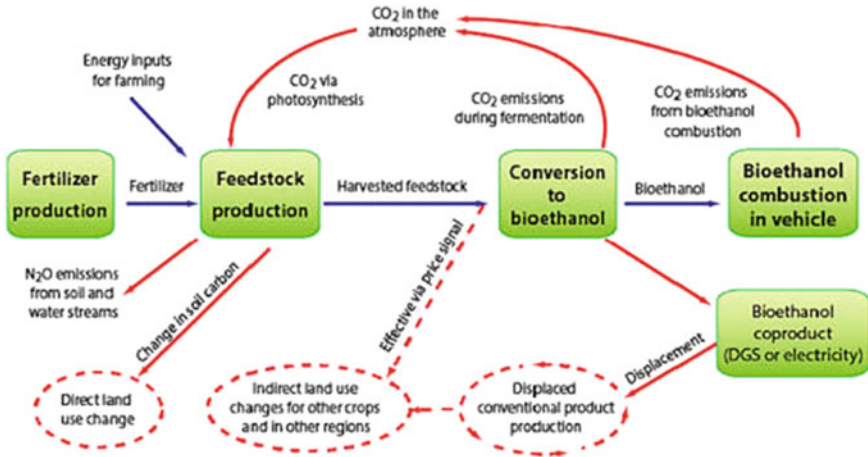


Fig. 2 Well-to-wheel CO₂ cycle for bioethanol as a fuel [30]

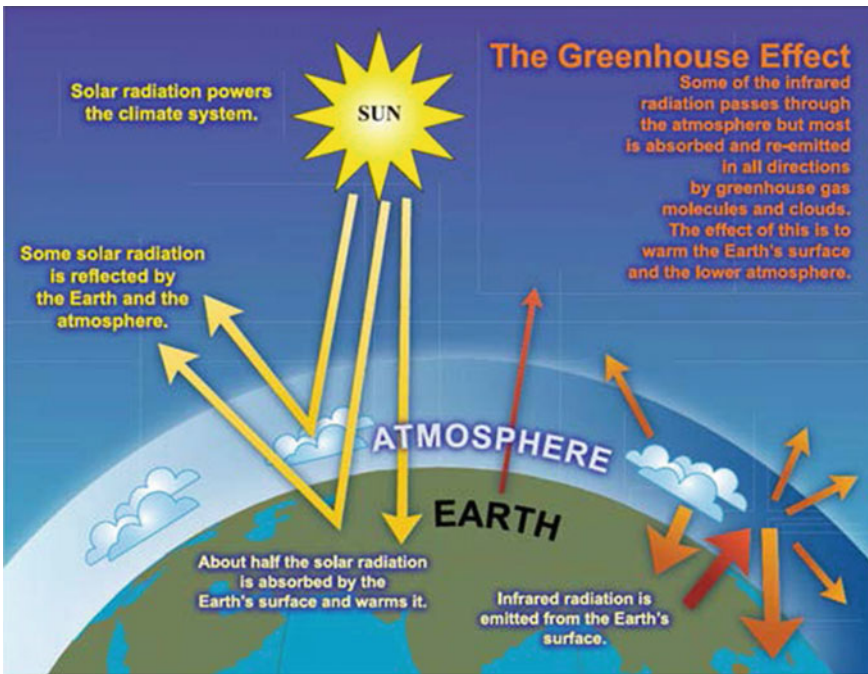


Fig. 3 Green house effect [31]

5 Emission Norms: European Union

Table 1 shows the present and proposed emissions level by the European Union in their respective years for light duty vehicles [32].

Table 1 EU present and proposed emission levels for light duty vehicles [32]

Euro standards	Year of implementation	CO (g/km)	HC (g/km)	NMHC (g/km)	NO _x (g/km)	HC + NO _x (g/km)
Diesel						
Euro I	1993	2.72	–	–	–	0.97
Euro II	1997	1.00	–	–	–	0.70
Euro III	2001	0.64	–	–	0.5	0.56
Euro IV	2006	0.50	–	–	0.25	0.30
Euro V	2010	0.500	–	–	0.180	0.230
Euro VI	2014	0.500	–	–	0.080	0.170
Petrol						
Euro I	1993	2.72	–	–	–	0.97
Euro II	1997	2.20	–	–	–	0.50
Euro III	2001	2.30	0.20	–	0.15	–
Euro IV	2006	1.00	0.10	–	0.08	–
Euro V	2010	1.000	0.100	0.068	0.060	–
Euro VI	2014	0.100	0.100	0.068	0.060	–

Table 2 Comparison of different alternate fuels [39]

	Gasoline	Methanol	Ethanol	Butanol
Chemical formula	C ₂ –C ₁₄	CH ₃ OH	C ₂ H ₆ OH	C ₄ H ₉ OH
H/C ratio	1.795	4	3	2.5
O/C ratio	00	0.7	0.5	0.2
Oxygen content (%)	00	50	34.7	21.6
Research octane number	95	129	106	96
Stoichiometric air/fuel ratio	15:1	6.5:1	9:1	11:1
LHV (MJ/kg)	43	20	27	29
Density@20 °C (kg/m ³)	744.6	792	791	810
Enthalpy of vaporization (kJ/kg)	373	1100	840	430
Boiling point (°C)	32.8	64.7	78.8	117

5.1 Emission Control Methods

To control the emissions from an engine, one needs to have complete knowledge of chemistry and dynamics of the combustion process which is taking place in the combustion chamber. Depending upon the various operating conditions of the engine the combustion process takes place in about 25–50 ms. After the combustion process has taken place, the partially burned constituents of exhaust gas continue to react in expansion stroke, exhaust process and exhaust blowdown. Approximately 95% of the unburned HC react during the time in cylinder in the exhaust manifold. Hydrocarbons and CO mix with oxygen to form carbon dioxide along with water vapor, thus reducing undesirable emissions. The secondary reactions which take place late in the exhaust manifold or in the exhaust stroke mainly depend on the temperature of the exhaust. If exhaust temperature is high, these reactions take place more and engines emissions will be lowered down. With the help of stoichiometric combustion, high engine speed, retarded spark and a low expansion ratio we can achieve a higher exhaust temperature. Some additional set-ups are required to reduce emissions in which these exhaust emissions are treated after the exhaust stroke.

Thermal Converters

Thermal converters are chambers through which exhaust is made to pass through. Actually, the thermal converters are kept at higher temperatures so that the exhaust emissions like carbon monoxide and unburned hydrocarbons can be oxidized. As already mentioned above these are secondary reactions.

The oxidation of carbon monoxide occurs at temperature nearly around 700 °C. To reduce hydrocarbons substantially into carbon dioxide and water vapor, the temperature needed is above 600 °C and the time needed is at least for 50 min to maintain this temperature. Therefore, a thermal converter must meet two essential requirements. Firstly, it should be maintained at a high temperature to work effectively. Secondly, it should provide adequate time to allow the secondary reactions occur completely. Hence, thermal converters have mainly a very large exhaust manifold which is thereby connected to the engine outside the exhaust ports. This enlarged section keeps the exhaust gases from cooling down to the non-reacting temperatures and also helps to minimize heat losses. There can also be a provision of additional oxygen supply in thermal converters. However, it makes a system complex, increases cost and size also. Although emissions like unburned HC and CO can be effectively oxidized through thermal converters but they are not found suitable for reducing NO_x emissions.

Catalytic Converters

Use of thermal converters gets limited by the fact they have to maintain higher temperatures. Catalytic converters facilitate the thermal converters by reducing these temperature ranges. The beauty of catalysts present in the converters is that they do not get consumed in the process and reduces the temperature required for the oxidation

of the carbon monoxide, unburned HC and NO_x . The temperature needed to sustain those oxidation process is reduced to 250–300° C by using certain catalysts [31].

Catalytic converters reduce the emissions of UHC, NO_x and CO, hence they are three-way convertors (Fig. 4). Along the exhaust pipe of the engine usually a stainless-steel container is mounted. Inside the stainless-steel container, there is a honeycomb ceramic structure with several flow passages. This ceramic structure is porous which allows the exhaust gases to pass through it. Some converters have loose granular ceramic structure inside the container. Volume of the ceramic structure is just half the displacement volume of the engine. The base material used for the ceramic structure is aluminum oxide. On the surface of the ceramic structures, catalytic materials are embedded that promote the oxidation of the secondary reactions. Rhodium, palladium, and platinum are the catalyst materials which are used for oxidation. Platinum and palladium help in the oxidation of UHC and CO. Rhodium promotes the reaction of NO_x in one or more of the following reactions. Sulfur and lead which are present in the exhaust are considered as poison because they inhibit the catalytic converter.

Some catalysts in the converter promote the oxidation of sulfur into sulfur dioxide and to sulfur trioxide also. Eventually sulfur trioxide gets converted into sulfuric acid or sulfurous acid which degrades the catalytic converter. Small amount of lead is always present in the fuel. It has been observed that the presence of lead in the fuel reduces HC emission reduction in the catalytic converters.

Exhaust Gas Recirculation

NO_x are the most dominant undesirable emissions in a compression ignition engine than in a spark ignition engine. Catalytic converters do not work efficiently

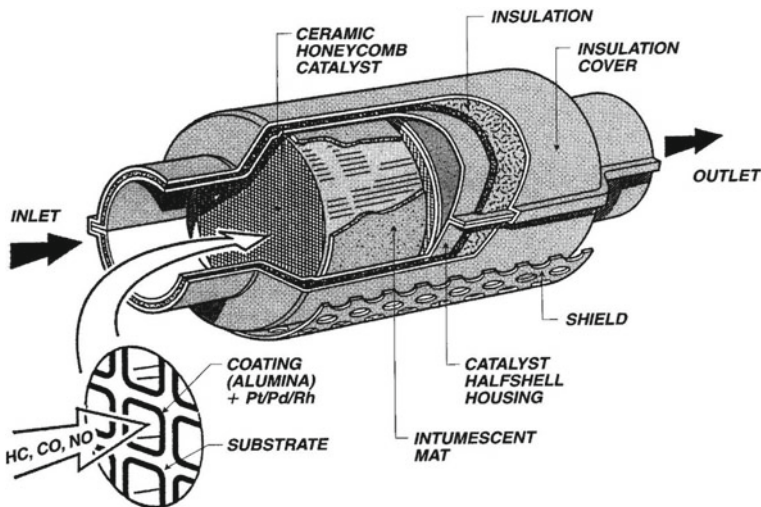


Fig. 4 Thermal catalytic converter [31]

with the compression ignition engines, because these engines operate with a lean mixture. NO_x can be reduced by using the EGR system in a CI engine. EGR is known as exhaust gas recirculation. As we know NO_x emissions are generated at high temperatures, therefore the maximum stress is given on the fact to reduce the maximum temperature.

In an EGR system combustion chamber is maintained at low temperatures. The principle of an EGR system is based on the reducing the maximum flame temperature inside the engine cylinder. For this exhaust gas, which is non-reacting with the other gases present in the combustion chamber, is mixed with the air–fuel mixture. The flame temperature is lowered down because the exhaust gases have larger specific heats as it absorbs the thermal energy during the combustion process.

In a CI engine, after the throttle valve some of the exhaust gas is ducted back into the intake system and hence EGR is set up. The adiabatic flame temperature and NO_x generation is reduced by the addition of exhaust gas to the air–fuel mixture. The flow of the exhaust gas back to the intake manifold is limited by many factors. Firstly, with EGR the adiabatic flame temperature gets reduced which in turn decreases the thermal efficiency of the engine. Secondly, due to an increase in EGR there are some cycle partial burns and if we consider the extreme conditions, it can also lead to total misfires in the engine. This increases the HC emissions. So, the use of EGR is also limited [31].

6 Alcohols as Alternative Fuels

Alcohols are a potential replacement for the crude oil and most of these are renewable too. Many countries have in fact already started blending these alcohols in gasoline to reduce emissions and dependence on fossils fuels. Major alcohols and their fuel characteristics are as below:

6.1 Methanol

Methanol, an alcohol, is a colorless, odorless, toxic liquid. By substituting one of the hydrogen atoms from the methane gas by the radical hydroxyl ion (OH), the methyl alcohol or methanol (CH_3OH) is formed. It is the simplest alcohol found or produced in nature. It can be obtained from natural gas, residual oil, biomass, or coal. Although methanol fuel (M100) is available and vehicles can be operated on this fuel, still a lot of practical work needs to be done on it. Methanol mixed with 25% gasoline is referred as M75 and is considered a more practically useful fuel for the real-life applications. No major changes in the fuel supply systems of an engine are required because methanol is a liquid fuel. But auto manufactures generally not make vehicles compatible with M75 fuel. M75 blend possesses low energy content per liter, thus the engine gives lower mileage. However, the power produced by

engine, payload capacity and the acceleration are close to pure gasoline. Also, M75 is costly as compared to other alcohol blends and cars using methanol need to use a special costly lubricant.

One major issue is that methanol in the M75 blend tends to combine with the available moisture present and then it separates from the petrol in localized zones, turning into a non-homogeneous mixture. Thus engine starts running erratically because of the significant difference in the air–fuel ratio of two fuels. Engine running on M10 fuel produces nearly same emissions as produced with pure gasoline. By using M75 fuel, there is a significant reduction in CO and HC emissions in exhaust. However, it is accompanied with a rise in oxides of nitrogen emissions.

6.2 Ethanol

For centuries, Ethanol has been used as a lamp fuel or spirit around the globe. Brazil was probably the pioneer, where in the early 1990s it started using ethanol as an automotive fuel. Gasohol is a mixture of 10% ethanol and 90% gasoline and has been sold for ages at the gas stations in America. Even Henry Ford's first car was designed to run on ethanol only.

Ethanol is a second derivative of the sugar. It is a clear and colorless liquid which is obtained by the fermentation process of sugar. These sugar or starch are found in grains like rice, wheat, corn and in urban wastes like potato wastes, crop residue, spoiled fruits and rice straw. Alcohols like ethanol can be produced from biomass by a number of processes. Most methods employ 'yeast' for fermenting the starch or sugar present in the feedstock into ethanol. A modern method applies enzymes for breaking down the cellulose or starch into fermentable sugar. This method allows to generate ethanol from crop residue or broken trees and biowaste materials also.

Gasoline having 10% ethanol, referred as E10, is recommended by environment protection agency, USA to meet the standards for ozone & carbon monoxide in certain urban zones. Ethanol possesses extra oxygen which oxidizes carbon monoxide into carbon dioxide and results in up to 25% lower CO emissions compared to pure gasoline. E10 is an alternate fuel blend that is fully compatible with pure gasoline SI engines with no additional retrofitting. Many countries have even adopted higher ethanol blends like E20 with minor engine modifications.

6.3 Butanol

Biobutanol is also an alternative fuel. Biobutanol has a higher calorific value to that of ethanol and can be used as additive to the gasoline. Moreover, butanol is non-hygroscopic which enables it not to soak water from the atmosphere which is not found in the case of ethanol. Ethanol being hygroscopic absorbs moisture and results in the poor performance of engine beyond a certain blending in gasoline.

Butanol has longer hydrocarbon chain which makes it non-polar and fairly similar to the gasoline, unlike ethanol. Butanol blends are found to work safely in vehicles designed for gasoline operation without any modifications. Butanol can be processed from fossil fuels and biomass also.

7 Production of Ethanol

Ethanol can be derived from carbohydrates. Carbohydrates are simply called sugars which exist in three forms—monosaccharide, disaccharides and polysaccharides. Monosaccharide contains a single sugar bound together with a general formula CH_2O_n . Disaccharides are formed when two monosaccharide bonds together after removal of one water molecule. Main disaccharides are sucrose, maltose and lactose. Polysaccharides are long chains of bonded monosaccharide. Polysaccharides made of similar sub-units are referred as polymers. Cellulose and Starch are the polymers made of the monomers of glucose. Lignocellulosic biomass is primarily made of lignin, hemi-cellulose and cellulose.

7.1 *Biomass-To-Ethanol Conversion Steps*

Biomass is prepared at the warehouse prior to delivery to the ethanol plant to ward off bacterial contamination and early fermentation. Most simple sugars firstly make pre-treatment of the carbohydrates available that are present in the biomass. Via reactions involving hydrolysis or other processes, disaccharides are transformed into monosaccharides, which are then fermented.

In the batch fermentation, yeasts and other ingredients are added to the hydrolysate from the beginning. Continuous processes are used in which inputs are constantly fed and products are removed from the fermentation vessels. Recycling or immobilizing the yeasts in the processes ensures the fermentation process to occur fast. The fermentation reactions occur at 25–30. The fermentation reactions last to 6–72 h depending on the cell density and activity of yeasts and composition of the hydrolysate. The broth contains 8–14% v/v ethanol. Above this concentration, inhibition of yeasts starts occurring. Distillation yields an azeotropic mixture (95.5% alcohol and 4.5% water).

7.2 *Disaccharides into Ethanol*

The most common disaccharide is sucrose for ethanol production. It is converted into glucose and fructose. The process requires the enzymatic hydrolysis of sucrose into glucose and fructose. The yeast invertase is an enzyme used for this purpose.

Then these simple sugars are fermented into ethanol through another enzyme called zymase which converts fructose and glucose.

7.3 Starch-To-Ethanol

Biomass consisting of plants has starch which is a polysaccharide. Starch contains long chains of alpha glucose, 1000 or more monomers for one amylose and 1000–6000 monomers for amylopectin. Starch is broken into glucose through a catalytic enzymatic hydrolysis reaction with an enzyme called gluco-amyase. The resulting product is known as dextrose which is an isomer of glucose. Then the fermentation of dextrose results in ethanol. Grains are main source of starch. Corn grain is the dominant feedstock.

7.4 Lignocellulose-To-Ethanol

Lignocellulose is the main component of the plant cell walls. It contains cellulose (40–60%), hemicellulose (20–40%) and lignin (10–25%). Cellulose molecules are long chain of beta glucose. Hemicellulose molecules can be xyloglucans or xylans depending on the types of plants. Lignins are phenolic compounds which are formed by the polymerization of three types of monomers. Lignocellulosic biomass comes from agricultural and forestry residues, plants and grass wastes, dedicated woody crops and industrial wastes. Lignocellulosic biomass is abundant in nature and has no competition with food.

Pre-treatment of lignocellulosic biomass is required before it is converted into the simple sugars. Lignin must be taken out of the feedstock during pre-treatment of lignocellulose to transform it into a more usable state. The most used techniques are enzymatic hydrolysis, followed by steam explosion and diluted acid pre-hydrolysis. The lignocellulosic materials are treated using a high-pressure saturated steam (0.69–4.83 MPa) at a high temperature (160–260 °C) for a short period of time to a few minutes in the steam explosion method. The explosion of the materials is then caused by an abrupt pressure break. During the procedure, most of the hemicellulose is solubilized. To enhance the solubilization of the hemicellulose, acid like sulfuric acid or CO₂ is typically used. Some limitations exist in the steam explosion method e.g.

- (a) A major part of xylan fraction gets destroyed.
- (b) lignin-carbohydrate matrix does not break fully.
- (c) Generation of degradation products, which lower the fermentation efficiency.

Dilute acid pre-hydrolysis is commonly used to break lignocellulosic biomass. In this method, a solution of Sulfuric acid with concentration of 0.5–1.0% is added to the lignocellulosic biomass at a temperature of 160–190 °C. This breaks down the

structure of lignocellulosic materials. Hemicellulose is largely hydrolyzed during this reaction producing different simple sugars like xylose, arabinose and mannose. The stream is then cooled. Part of the acetic acid, much of the Sulfuric acid and other inhibitors produced during the degradation process are removed. Then the stream is neutralized, and its pH is set to 10 before hydrolysis and fermentation.

Enzyme assisted hydrolysis of the cellulose and fermenting the simple sugars are the next steps in lignocellulose to ethanol conversion. Enzymatic hydrolysis of cellulose is obtained using cellulases. Cellulases are the group of enzymes such as endoglucanases, exoglucanases and B-glucosidases. They attack the crystalline structure of cellulose to produce glucose. Cellulases are produced by a breed of fungi, primarily the *Trichoderma reesei*. Efficiency of enzymatic hydrolysis of cellulose is greatly affected by the substrate to enzyme ratio, presence of inhibitors and cellulose dosage. High concentration of glucose inhibits the efficiency of the saccharification. To reduce the inhibition, reduced sugars are fermented along their release. Simultaneous saccharification and fermentation (SSF) method is used to achieve this. In this method, fermentation by yeasts and enzymatic hydrolysis are achieved in the same reactor at the same time. The main co-product of lignocellulose conversion to ethanol is energy [33].

8 Production of Butanol from Biomass

Barley straw, which is regarded as a lignocellulosic feedstock, may be effectively converted into biobutanol. The hemicellulose in barley straw was solubilized from cellulosic residues using a pretreatment with diluted sulfuric acid. In acetone-butanol-ethanol (ABE) fermentation, the pretreatment hydrolysate and biomass derived from starch were co-fermented. Two co-fermentation procedures were used: I) Barley grain and straw were combined, and the mixture was then pretreated with diluted acid. Pretreated barley straw hydrolysate and gelatinized barley grain slurry were mixed and fermented to produce biobutanol, which was made from the sugars primarily liberated from hemicellulose and starch in the mixture. Cellulases, xylanases, and surfactants worked in concert to efficiently hydrolyze the pretreatment solid residues, which were primarily composed of cellulosic biomass, into fermentable sugars for ABE fermentation. Additionally, research was done on the co-fermentation process using fresh barley silage as a source of biobutanol.

The best sugar that ferments yields were obtained by pre-treating a combination of barley straw and grain (process I) for 60 min at a pre-treatment condition of 1.5% sulfuric acid. The hydrolysate mixture (M1.0) had superior ABE fermentability after pre-treatment with 1.0% sulfuric acid than it had after 1.5% sulfuric acid, though. Although only 19% of the pentoses were used up during the fermentation of M1.0, 11.3 g/L ABE was generated. More ABE (13.5 g/L) was produced by fermentation of pre-treated straw hydrolysate and gelatinized grain slurry in process II than in process I, and 95% of the pentoses in the hemicellulose hydrolysate prepared with more severe conditions (1.5% sulfuric acid) were used. When ABE was fermented

using pre-treated hydrolysate, which is pre-treatment liquor made from both green and yellow barley silage and added to the gelatinized barley grain slurry, 9.0 g/L and 10.9 g/L of total ABE, respectively, were formed. In the hydrolysis of pre-treated solid residues by cellulase, the combined application of xylanase and PEG 4000 boosted the glucose and xylose yields, which were much larger than those produced with the application of any one of them alone. ABE output rose from 93.8 to 135.0 g/kg of pre-treated straw due to improved sugar production.

8.1 Selection of Ethanol and Butanol as Additives to Gasoline

Ethanol and butanol are clean sources of energy which can be harnessed from biomass. As the biomass is found in abundance produced from agricultural waste, ethanol and butanol can be regarded as renewable sources of energy. The physical properties allow ethanol and butanol to be used as additives to gasoline. The calorific values of ethanol and butanol are much higher than other conventional sources of energy. Further, the combustion of ethanol and butanol are characterized by higher flame propagation speed and higher oxygen content. Thus, these all properties make ethanol and butanol as an obvious option for gasoline additives (Table 2).

9 Ethanol Policy in India

With the GDP expanding at an average yearly pace of more than 7% since 2004, India is one of the world's fastest-growing economies. Energy inputs are a crucial part of the economy thus use of biofuels in place of fossil fuels is growing rapidly. Ethanol will be a potential renewable fuel in future.

To mandate a phased implementation of the program of ethanol blending in gasoline in various states, the Ministry of Petroleum and Natural Gas (MoPNG) published a notification in September 2002 for the mandatory blending of 5% ethanol in petrol in nine major sugar-producing states and four union territories beginning in 2003–04. Under the supervision of the Planning Commission, the Report of the Committee on Development of Biofuel advocated a phase-by-phase implementation schedule to blend biofuels with petrol and diesel in 2003. However, the ethanol-blending mandate was rendered optional in October 2004 due to a supply deficit from 2004 to 2005. However, it was reinstated in 20 states in October 2006 following a break in the mandate. With the exclusion of J&K, the Northeast, and island areas, the Indian government mandated the necessary 5% ethanol blend in petrol in October 2007. The National Biofuel Policy, which was launched by the Indian government in 2008, calls for the plan of ethanol blending in petrol to be implemented in various states in stages. It became necessary to blend 5% bioethanol with petrol starting in October 2008, and by 2025 the goal is to blend 20% bioethanol.

The Union Cabinet approved the new biofuel program in December 2009. The policy also suggested that the import price and real cost of production of bioethanol should drive the minimum purchase price (MPP) for bioethanol. Additionally, it was claimed that biodiesel is exempted from excise duty and that bioethanol already gets a concessional excise charge of 16%. To ensure that domestically generated biofuels are not more expensive than imported biofuels, duties and taxes would be placed on imports. The National Biofuel Policy's goal is to promote the Ethanol Blending Program (EBP) in the nation and promote domestic ethanol production. To purposefully avoid a potential conflict between food and fuel, India's approach to biofuels is centered on non-food feedstock. However, due to issues including ethanol shortages, state government tax structures and specific regulatory limitations, the introduction of the 5% EBP nationwide has been delayed actually [28].

10 Literature Survey

10.1 Based on Methyl Alcohol as Additives to Gasoline

Gautam et al. looked at the performance traits of C1-C5 alcohol-gasoline blends with equivalent oxygen contents in a single cylinder Spark Ignition engine. Each of the C1 through C5-carbonated alcohols was mixed with a specific amount of unleaded test fuel. The oxygen mass content was the same across each of the alcohol-gasoline mixtures. Only a single cylinder spark ignition engine was used to quantify the efficiency characteristics of the mixtures. Each (C1-C5) blend's working conditions were optimised for two different matched oxygen content values. Knock resistance was increased when lower alcohols (C1, C2, and C3) were added to UTG96. By increasing the fuel blend's oxygen percentage, further improvement was made. When compared to straight petrol, blends with higher alcohol content (C4, C5) demonstrated diminished knock resistance [12].

Demirbas et al. investigated the outcomes of blending bio-alcohols with petrol in the Otto engine. The goal of their work was to develop bio-alcohols as petrol substitutes that could improve engine performance while lowering pollutants. They offered methanol and ethanol as potential substitutes. Biofuels like ethanol and methanol offer petrol substitutes. They discussed how common and sustainable commodities including wheat, sugar beets, and maize are fermented to produce bioethanol. They noticed that automobiles may run on a 10% bioethanol/gasoline mixture without altering the engine or fuel parameters [1].

Demirbas and Demirbas (2010) studied if employing bio-alcohols in IC engines was technically and financially feasible. According to their investigation, blending methanol and ethanol with petrol increases its octane rating. As the proportion of methanol and ethanol in petrol rises, the octane number of the fuel also rises linearly. They discovered that ethanol increases gasoline's volatility, which causes more fuel to evaporate at a particular temperature. Bio-alcohol additions are used to enhance the

performance of petrol in automobiles and to lower particular pollutants. They consist of corrosion-inhibiting substances, detergents, and dyes, as well as oxygenates, antiknock chemicals, and octane enhancers [10].

10.2 *Based on Ethanol as an Additive to Gasoline*

Hsieh et al. investigated how ethanol-gasoline mixtures affected the operation and emissions of a SI engine. The New Sentra GA16DE, a 1600 cm³ multi-point injection petrol engine with cylinder bore and stroke measurements of 76.0 and 88.0 mm, respectively, and a compression ratio of 9.5, was the engine system employed in this experiment. The authors decided to use mixes with ethanol at five different percentages: 0%, 5%, 10%, 20%, and 30%.

The findings of their study indicated that as ethanol concentration in the blends increased, the octane number increased while the value of heating decreased. The engine test results showed that using ethanol-gasoline blended fuels resulted in slightly higher fuel consumption and torque output for the engine; lower CO and HC emissions due to the leaning effect of the ethanol addition; and higher CO₂ emissions due to improved combustion. Last but not least, it was mentioned that engine operating conditions, rather than ethanol content determine NO_x emission [23].

Al-Hasan (2003) investigated the effects of ethanol-unleaded gasoline blends on the performance and emissions in a spark ignition engine. A four stroke, four cylinder SI engine (type TOYOTA, TERCEL-3A) was used for conducting this study. The author performed the experiments with 10 test blends in which ethanol content was varied from 0 to 25%. There was an average increment of 2.5% of ethanol in every next blend used in the experiments. The engine performance and emissions tests were carried out at different engine speeds 1000, 2000, 3000 and 4000 rpm. The throttle opening was kept constant with 3/4 part of the wide-open throttle (WOT). The 20 vol.% ethanol in fuel blend gave the best results for all measured parameters at all engine speeds [11].

Ceviz and Yuksel (2005) concentrated on researching the impact of cyclic variability and emissions in a SI engine on ethanol-unleaded petrol mixes. The FIAT 1.801dm³ four-stroke SI engine was employed in the investigation. To create five test mixes that contained 0% to 20% ethanol with a 5% increment, ethanol was combined with unleaded petrol. 2000 rpm was the engine's operating speed.

The findings demonstrated that the use of ethanol-unleaded petrol blends as a fuel that reduced the factor of variation in indicated mean effective pressure, CO and HC emission concentrations, while increasing CO₂ concentration up to 10% ethanol in fuel mix. On the contrary hand, the above characteristics showed the opposite effect after this mix level. The fuel blends with 10% ethanol produced the best results [13].

Celik determined the high compression ratio in a petrol engine and the appropriate ethanol-gasoline blend rate experimentally. A steady 25% increment was added to the ethanol concentration with each subsequent blend, ranging from 0 to 100%. There were six to ten different compression ratios. Engine tests were carried out with a

steady load and speed. At full load and different speeds, the engine was tested with E0 fuel with the compression ratio of 6/1 and with E50 fuel at a compression ratio of 10/1 without experiencing any knock.

According to the experimental findings, using E50 fuel boosted engine power by roughly 29% when compared to using E0 fuel. Additionally, the amount of fuel used and the emissions of CO, CO₂, HC, and NO_x were reduced by 3%, 53%, 10%, 12% and 19%, respectively [12].

Koc et al. examined the impact of ignition timing and ethanol-unleaded petrol mixtures on engine output and exhaust emissions. A Hydra single-cylinder, spark-ignition, fuel-injection engine was used for the experimental study. Wide open throttle (WOT) was used to maintain a constant engine speed of 2000 rpm. Three alternative compression ratios (8, 9 and 10) with varying spark timing were used in the experiments. In the trials, five test fuels with ethanol content levels of 10%, 20%, 40%, and 60% each were used. According to the experimental findings, adding ethanol to unleaded fuel modestly enhanced brake torque while lowering carbon monoxide and hydrocarbon emissions [15].

Yousaf et al. examined bioethanol's effects as a potential replacement for petrol. For spark ignition engines using gasoline-ethanol mixes, they modified a quasi-dimensional SI engine cycle. They created a mathematical model in Matlab to forecast engine performance behaviour. The emissions were also examined using the model. They selected various ethanol concentrations for the petrol. They conducted engine tests using petrol with ethanol concentrations of 5, 10, 15, and 20. At various engine speeds, experiments were run.

The results indicated that adding more ethanol to petrol resulted in a small increase in engine torque and brake power. The scientists found that increasing the ethanol level up to 10% has reduced the brake-specific consumption when compared to pure petrol. Additionally, they discovered that adding 5% and 10% ethanol to petrol had improved the thermal and volumetric efficiency of the brakes. The levels of both unburned hydrocarbons and carbon monoxide in the exhaust engine emissions decreased, the authors discovered after analysing the data from the emission graphs. While employing ethanol-gasoline blends, the amount of carbon dioxide and nitrogen oxides in engine emissions rose. They owed a justification to ethanol as being an oxygenated fuel for the emissions [21].

10.3 Based on Butanol as an Additive to Gasoline

Dernotte et al. assessed the effects of butanol-gasoline blends in spark ignition engine. Five test mixes were employed in the investigation, starting with pure petrol and adding butanol in increments of 20% up to 80% in each blend, using a 4-cylinder, 16-valve, 1.6-L spark-ignition Honda engine, model D16Z6. Their study's key conclusions were as follows: 1) a 40% butanol/60% petrol blend by volume (B40) reduces HC emissions; 2) NO_x emissions were not significantly affected, with the

exception of the 80% butanol/20% petrol blend; and3) the specific fuel consumption of the B40 blend is within 10% of that of pure petrol for stoichiometric mixture [8].

Gu et al. studied the emission characteristics of a SI engine running on butanol-gasoline mixtures and exhaust gas recirculation. A three-cylinder, port fuel injection, spark-ignition engine with a 9.6 compression ratio was used in this study. This engine was operated with three distinct loads (low, part, and full) at a speed of 3000 rpm. Pure petrol, B10, B30, B40, and pure butanol were the five tested fuels.

According to the findings, HC, CO, and NO_x emissions were lower in gasoline-butanol blends than in pure gasoline. Compared to petrol, pure butanol produced more CO and HC emissions while producing less NO_x and particle concentration. The researchers discovered that in SI engines running on mixtures of petrol and butanol, EGR simultaneously decreased nitrogen oxides and particle number concentration [26].

Mittal et al. examined the butanol and gasoline-blended SI engine's performance and emission characteristics. For the investigation, a 10 HP single-cylinder, air-cooled, four-stroke SI engine made by Briggs and Stratton was chosen. By adjusting the torque while maintaining a steady engine speed, the engine performed under various brake loads. For testing, fuel mixtures with various volume ratios were utilised, such as 90% petrol + 10% butanol and 85% petrol + 15% butanol. The experiments were carried out while keeping the engine rpm at 3000, and variations in performance traits caused by changes in braking loads were recorded.

The findings demonstrated that CO and HC emissions dramatically decreased with an increase in butanol content in the blends. The higher petrol temperatures were the cause of the higher NO_x emission across all test fuels in engines. All of the test fuels' SFC dropped as a result of the higher combustion temperature, which had a beneficial impact on SFC [16].

Feng et al. carried out an experimental investigation on a SI engine running on a butanol-gasoline mixture with water addition. Using pure petrol and a 35% volume butanol-gasoline blend, the investigation was done on a single cylinder motorcycle engine for two operating modes: full load and partial load at 6500 rpm and 8500 rpm. In addition to optimising the engine ignition timing for a 35% volume butanol-gasoline blend, 1% volume H₂O was also added to the fuel.

The experimental findings demonstrated that, when 35% volume butanol and 1% H₂O addition were paired with adjusted ignition timing, engine torque, BSEC, CO emissions, and HC emissions were superior to those of pure petrol at both full load and partial load. However, NO_x and CO₂ emissions were higher than the original level [17].

Singh et al. assessed how a butanol/gasoline blend affected a SI engine's performance, emissions, and noise levels. A single-cylinder, forced air-cooled, spark-ignition engine running at a constant speed of 3000 rpm with 5.1 compression ratio. Three test fuels were used, including pure petrol. The other two blends, designated E10G and B10G, stood for 10% ethanol + 90% petrol and 10% butanol + 90% petrol, respectively. At various engine loads and for various test blends, the efficiency and emissions of SI engines were measured and expressed by means of engine brake power.

It was discovered that butanol-blended petrol provided engines with performance superior to ethanol-blended petrol and on par with petrol. With butanol-blended petrol, CO and HC tailpipe emissions were also significantly decreased. At all loads, NO emission levels were found to be somewhat lower than those of petrol. Additionally, petrol and petrol with ethanol blend had lower CO₂ emissions [5].

Elfasakhany examined how internal combustion engine performance and emissions are affected by gasoline and gasoline-butanol. An engine with a single cylinder and spark ignition was employed for the experiments. 65.1 mm bore, 44.4 mm stroke, 0.147 L swept volume, and 7 compression ratios were the engine's geometrical parameters. The engine speeds used for the experiments ranged from 2600 to 3400 r/min. Blends of n-butanol with petrol (10, 7 and 3 vol.% n-butanol in petrol) were made.

The findings of the engine test showed that using butanol-gasoline blended fuels resulted in a minor reduction in the engine's power, output torque, exhaust gas temperature, volumetric efficiency, and in-cylinder pressure due to the butanol's leaning effect. Because butanol has more oxygen than regular petrol, it improves combustion, which enables a partial reduction of CO and UHC emissions through the generation of CO₂. This results in lower CO, CO₂ and UHC emissions for fuel blends as opposed to petrol [4].

Feng et al. carried out research on motorbike engines running on a butanol-gasoline mixture. A single cylinder high speed spark ignition (SI) motorcycle engine was the subject of experimental tests using pure petrol, 30% and 35% volume butanol-gasoline mixes, and operating under full and partial load at 6500 and 8500 rpm. According to the findings, butanol-gasoline blends offered better knock resistance by advancing the ignition timing in petrol engines, which resulted in more effective combustion. Increased butanol blending leads to more complete combustion, which proves to be the best operating condition. The results also demonstrated that with the addition of 35% volume butanol and optimised ignition timing, brake-specific energy consumption, torque, engine power and HC, CO, and O₂ emissions were superior to those of pure petrol at full load. However, emissions of CO₂ and NO_x were higher than pure petrol [18].

10.4 Based on Comparison of Ethanol and Butanol as Additive

Keskin and Guru investigated how adding ethanol and propanol to unleaded fuel affected the sound and exhaust pollutants of a SI engine. For the preparation of the test fuels, unleaded petrol was combined on a volume basis with ethanol (C₂H₅OH) and propanol (C₃H₇OH). The test fuels had alcohol levels of 4, 8, 12, 16, and 20%. The test engine was operated under constant loads during the tests. At 800, 1,600, and 2,400 Watts, the test fuels were put to the test. Propanol-gasoline blends and ethanol-gasoline blends both reduced CO and HC emissions by 65.56 and 33.92%,

respectively. With the blend fuels, NO_x and CO_2 emissions exhibited an upward trend [2].

Faradke and Pathre examined how a SI engine would react to methanol, ethanol, and butanol mixtures. Greaves MK-25 engine was used for the experimentation. The load was changed from no load to full load while the engine was kept at a steady speed of 3000 rpm. The percentages of methanol, ethanol, and butanol added to the petrol were 10, 20, and 30 respectively.

The results demonstrated that butanol performed better than the other two alcohols with the same oxygen content when it was used to substitute petrol at a rate of 5%. As an outcome of complete combustion, oxygen-rich combustion produced lower CO and HC emissions and higher CO_2 emissions. Higher temperatures were also beneficial for NO emission, which produced higher CO_2 emissions [6].

Shashank et al. examined how ethanol and butanol blends compare to petrol. Different ethanol and butanol mixes (25%, 50%, 75%, and 100% by volume) are simulated with variable speeds under full load conditions. The simulation findings showed that, compared to petrol, higher concentrations of alcohol resulted in much lower emissions of NO_x , CO, and HC emissions [19].

Varol et al. compared the emissions produced when methanol, ethanol, and butanol were combined with petrol in a SI engine. The engine used for the experiments was a Ford Engine Company four-cylinder, four-stroke, water-cooled, spark-ignited engine. M10, E10, B10, and unleaded petrol were the four test fuels that were evaluated in the engine. The seven different engine test speeds ranged from 1,000 to 4,000 rpm with a 500 rpm interval. For each of the tested fuels, the throttle position was changed to keep the brake torque values constant at the specified engine speed.

Compared to B10, M10 and E10 had larger fuel consumption, hydrocarbon and CO_2 emissions but reduced carbon monoxide emissions. Blended fuels with various alcohols appeared to indicate a lower carbon monoxide content than unleaded petrol. Blended fuels with various alcohols in them appeared to have reduced hydrocarbon and carbon monoxide emissions compared to unleaded petrol, but had higher fuel consumption and CO_2 emissions [27].

Zhang et al. compared several petrol mixtures with a lot of alcohol in a SI engine. In this study, a port-injection spark-ignition engine was used to test three high-alcohol petrol blends (85% vol. of ethanol, butanol, and ABE, referred to as E85, B85, and ABE85, respectively). Acetone, butanol, and ethanol, also known as ABE, have a 3:6:1 ratio. The same testing parameters (1200 RPM, = 0.83–1.25, BMEP = 3 bar) were used for all fuels.

Under stoichiometric circumstances, all three of the alcohol-containing fuels showed slightly lower BTE and somewhat higher BSFC compared to pure petrol. Due to incomplete combustion brought on by insufficient butanol evaporation, B85 produced much more CO and HC emissions than all other fuels under stoichiometric circumstances. Due to the interaction of adiabatic flame temperature and heat capacity, E85, B85, and ABE85 exhibited lower NO_x emissions than petrol. Four fuels displayed behaviour that was remarkably similar as the equivalency ratio increased [9].

Gravolos et al. compared and analysed the emissions from a tiny, off-road spark-ignition engine using various alcohol-gasoline blend fuels. The experiment employed a total of 28 fuels. These eight fuels were 5% (ME5, ET5), 10% (ME10, ET10), 20% (ME20, ET20), and 40% (ME40, ET40) v/v, respectively, gasoline-methanol and ethanol blends. Twelve greater molecular mass alcohols were combined with petrol to make up the third group of fuels. These twelve fuels were gasoline-propanol, butanol, and pentanol mixtures that had 5%, 10%, 20%, and 40% (PR5, BU5, and PE5, respectively) v/v of propanol, butanol, and pentanol. A 56 mm bore and 58 mm stroke, four-stroke, air-cooled, SI non-road engine (type Bernard Moteures 19A) with 2.2 kW was used. While the compression ratio was 8:1.

As the total proportion of alcohol in the mix grew, high CO₂/NO_x and low HC/CO emissions were seen in exhaust gases that came from alcohol petrol test fuels. The combustion efficiency of methanol-gasoline mixes appeared to be great, but the engine needed a catalytic converter to combat significant NO_x emissions. In some instances, butanol-gasoline blends produced fewer emissions than petrol blends made with ethanol and propanol. Finally, the emission patterns of the pentanol-gasoline mixes were identical to those of neat petrol [7].

11 Benefits of Adding Nanoparticles in the Engine Fuel

A lot of research is currently going on to improve the performance of the engines, one such way is the addition of nanoparticles to engine fuel. This development could increase engine performance, lower pollutants, and improved fuel efficiency.

A practical substitute for fuel that can be produced from renewable resources like biomass is butanol, a four-carbon alcohol. In comparison to conventional fuels like petrol and diesel, it has several advantages, including a higher energy density, reduced volatility. To effectively utilise butanol as a fuel option, there are still obstacles to be addressed. Researchers hope to solve these problems and gain new advantages by adding nanoparticles in the butanol. Nanoparticles are often metal or metal oxide particles, such as cerium oxide, iron oxide, or platinum. At the nanoscale, these nanoparticles display special characteristics such as a large surface area, enhanced reactivity, and catalytic behaviour.

The performance of IC engines can benefit by adding nanoparticles to butanol blends in a number of ways. First, the nanoparticles function as catalysts, promoting more efficient fuel burning. They encourage the breakdown of fuel molecules, which improves air mixing and increases the effectiveness of combustion which leads to increased power output and decreased fuel consumption. In addition, the nanoparticles can lessen some butanol-related combustion problems. For example, butanol has a greater octane value than petrol, which may cause an engine knock and premature ignition. By changing the combustion parameters, nanoparticles reduce the possibility of knocking and allow for higher compression ratios in engines [35].

Additionally, nanoparticles can help lower hazardous pollutants. They aid in reducing the production of pollutants like unburned hydrocarbons, carbon monoxide,

nitrogen oxides by promoting better combustion. The oxidation of hazardous substances is made easier by the nanoparticle's catalytic characteristics, which further lowers emissions. The ability of nanoparticles to improve the thermal conductivity is an additional benefit. The engine's heat transfer is enhanced by the high surface area to volume ratios of nanoparticles. This characteristic promotes heat dissipation more effectively, avoiding overheating and enhancing overall engine toughness. Further research is required to determine the long-term impact of nanoparticles on engine parts and emissions [36].

The choice of the nanoparticle used depends on several factors such as their stability, catalytic activity, cost, compatibility with the fuel and engine system. Some of the prominent nanoparticles being used are:

- Platinum nanoparticle are the most abundantly used ones, these nanoparticles serve as catalysts and encourage fuel combustion by raising the reactivity. They promote butanol molecule oxidation, resulting in improved combustion and increased engine performance.
- Similarly, Iron oxide (FeO) nanoparticles, also have catalytic qualities and support fuel combustion. They accelerate the breakdown of fuel molecules, which improves air mixing and lowers the engine emissions.
- The use of Cerium oxide (CeO₂) nanoparticles as catalysts in a variety of processes, such as fuel combustion, has attracted extensive research. They improve the combustion process when added to butanol-gasoline fuel by promoting the oxidation of fuel molecules and limiting the production of hazardous pollutants.
- It is well known that Palladium (Pd) nanoparticles have strong catalytic abilities. They facilitate ignition and combustion when added to butanol fuel, which enhances engine performance and lowers pollutants.
- The catalytic and antibacterial abilities of Silver (Ag) nanoparticles have also been explored. They may increase the life of engines by enhancing combustion efficiency and decreasing the accumulation of deposits on engine parts when added to butanol blended fuel.
- Lastly if we talk about Titanium dioxide (TiO₂) nanoparticles, they have excellent photocatalytic abilities and a large surface area. Even though they are frequently used in other products like solar cells, they can help alcohol-based fuel burn more efficiently and emit less pollutants [37–39].

12 Conclusion

Following conclusions can be drawn from the above review-based study.

- Methanol is an efficient additive to gasoline, can be safely produced from coal etc. and gives reasonably lower emissions as compared to pure gasoline. But its water toxication property and rubber seals damaging behavior restricts its use to lower blending proportions in gasoline.

- Ethanol is an ideal alternative fuel produced from sugar rich feedstocks by fermentation and has properties very similar to gasoline. It can be safely blended into gasoline upto 10–15% without engine modifications. But higher blending necessitates certain hardware modifications which increases the cost of apparatus. Also, lower calorific value of ethanol reduces the engine performance with much lower emissions.
- Butanol is an even better candidate with higher calorific value than ethanol thus engine performance is much superior compared to ethanol blends however emissions are nearly comparable to ethanol blends. However, it has got great potential to be the next sustainable fuel for coming generations.
- The use of nanoparticles in fuel, offers a promising opportunity to enhance engine performance while minimising environmental pollution. This novel strategy could improve fuel economy, reduce emissions, and support the development of a more sustainable transportation industry. Future advancements in this field's research and development might make it possible for nanoparticles to be important in maximising the utilisation of alternative fuels.

13 Future Prospects

Even though many past studies give a positive view of alcohols blending in gasoline as an alternative sustainable fuel, but it needs more deliberations for mass adoption. Some future prospects are:

- Much higher level of alcohol blending can be experimented in future for the potential substitution of crude gasoline. But the hardware modification requirements of engine need to be further thoroughly investigated.
- The cost associated with this hardware modification needs to be estimated and the benefit versus cost analysis must be rigorously done to establish the advantage.
- An engine can be made to run on different fuels that is Gasoline with varying alcohol blending percentage. It would help the owner stay unbothered with the varying fuel quality. The fuel sensor would estimate the ethanol blending level in fuel and automatically adjust engine settings like spark timing etc. However, this approach called as Flex fuel vehicle, needs more vetting.
- Two alcohols say ethanol and butanol can be mixed in gasoline to see potential benefits of their interaction on engine power and emission vis a vis a single alcohol blend. This would also need more future research.
- Use of nanoparticles in alcohol-based gasoline blends can enhance the engine performance while minimising emissions. This novel strategy could improve fuel economy, reduce emissions, and can lead to the development of a more sustainable fuel. Future advancements in this field's research and development might facilitate higher utilisation of alternative alcohol based fuels.

References

1. Demirbas A (2009) Bioalcohols as alternatives to gasoline. *Energy Sources A* 31:1056–1062
2. Keskin A, Guru M (2011) The effects of ethanol and propanol additions into unleaded gasoline on exhaust and noise emissions of a spark ignition engine. *Energy Sources A* 33:2194–2205
3. Elfasakhany A (2014) The effects of ethanol-gasoline blends on performance and exhaust emission characteristics of spark ignition engines. *Int J Automot Eng Vol* 4(1)
4. Elfasakhany A (2014) Experimental study on emissions and performance of an internal combustion engine fuelled with gasoline and gasoline/n-butanol blends. *Energy Convers Manage* 88:277–283
5. Singh E, Shukla MK, Pathak S, Sood V, Singh N (2014) “Performance emission & noise characteristics evaluation of n-butanol/gasoline blend in constant speed SI Engine. Vol 3 (11): 2278–0181
6. Farkade HS, Pathre AP (2012) Experimental investigation of methanol, ethanol and butanol blends with gasoline on SI engine. Vol 2 (4): 2250–2459
7. Gravalos I, Xyradakis P, Kateris D, Gialamas T, Loutridis S, Tsiropoulos Z (2016) Comparison and analysis of the emissions of a small non-road spark-ignition engine operating under different alcohol–gasoline blended fuels. *Int J Sustain Energ* 35(3):258–266
8. Dernote J, Mounaim-Rousselle C, Halter F, Seers P (2010) Evaluation of butanol-gasoline blends in a port fuel-injection, spark-ignition engine. *Oil Gas Sci Technol—Rev IFP* 65(2):345–351
9. Zhang, J, Nithyanandan, K, Li, Y, Lee, C, Huang Z (2015) Comparative study of high-alcohol-content gasoline blend in an si engine. *SAE Technical Paper* 2015-01-0891
10. Demirbas K, Sahin-Demirbas A (2010) Gasoline fuel blends for otto engines and gasoline fuel additives. *Energy Sources B* 5:243–249
11. Al-Hasan M (2003) Effect of ethanol–unleaded gasoline blends on engine performance and exhaust emission. *Energy Convers Manage* 44:1547–1561
12. Bahattin Celik M (2008) Experimental determination of suitable ethanol–gasoline blend rate at high compression ratio for gasoline engine. *Appl Therm Eng* 28:396–404
13. Ceviz MA, Yuksel F (2005) Effects of ethanol–unleaded gasoline blends on cyclic variability and emissions in an SI engine. *Appl Therm Eng* 25:917–925
14. Ghazikhani M, Hatami M, Safari B, Ganji DD (2013) Experimental investigation of performance improving and emissions reducing in a two stroke SI engine by using ethanol additives. *Propulsion Power Res* 2(4):276–283
15. Koç M, Sekmen Y, Topgul T, Yucesu HS (2009) The effects of ethanol–unleaded gasoline blends on engine performance and exhaust emissions in a spark-ignition engine. *Renew Energy* 34:2101–2106
16. Mittal N, Athony RL, Bansal R, Kumar CR (2013) Study of performance and emission characteristics of a partially coated LHR SI engine blended with n-butanol and gasoline. *Alex Eng J* 52:285–293
17. Feng R, Yang J, Zhang D, Deng B, Fu J, Liu J, Liu X (2013) Experimental study on SI engine fuelled with butanol–gasoline blend and H₂O addition. *Energy Convers Manage* 74:192–200
18. Feng R, Fu J, Yang J, Wang Y, Li Y, Deng B, Liu J, Zhang D (2015) Combustion and Emissions study on motorcycle engine fuelled with butanol-gasoline blend. *Renewable Energy* 81:113–122
19. Shashank SN, Kumar GN (2013) Comparison of ethanol and n-butanol blends with gasoline: a computational study Vol 2(4): 2319–3182
20. Vadivel TS, Saravanan CG, Balashanmugam P (2014) Experimental investigation on the performance and combustion characteristics of a gasoline engine run with ethanol blend. *Int J Engg Sci* 3(4):25–32
21. Yusaf T, Najafi G, Buttsworth D (2009) Theoretical and experimental investigation of SI engine performance and exhaust emissions using ethanol-gasoline blended fuels. In: *Proceedings of ICEE 2009 3rd International Conference on Energy and Environment*

22. Topgul T, Yucesu HS, Cinar C, Koca A (2006) The effects of ethanol–unleaded gasoline blends and ignition timing on engine performance and exhaust emissions. *Renew Energy* 31:2534–2542
23. Hsieh WD, Chen RH, Wu TL, Lina TH (2002) Engine performance and pollutant emission of an SI engine using ethanol–gasoline blended fuels. *Atmos Environ* 36:403–410
24. Lin W, Chang Y, Hsieh Y (2009) Effect of ethanol-gasoline blends on small engine generator energy efficiency and exhaust emission. *J Air Waste Manage Assoc* 60:142–148
25. Wang X, Chen Z, Ni J, Liu S, Zhou H (2015) The effects of hydrous ethanol gasoline on combustion and emission characteristics of a port injection gasoline engine. *Case Stud Thermal Eng* 6:147–154
26. Gu X, Huang Z, Cai J, Gong J, Lee C (2012) Emission characteristics of a spark-ignition engine fuelled with gasoline-n-butanol blends in combination with EGR. *Fuel* 93:611–617
27. Varol Y, Öner C, Öztöp HF, Altun S (2014) Comparison of methanol, ethanol, or n-butanol blending with unleaded gasoline on exhaust emissions of an SI engine. *Energy Sources A* 36:938–948
28. http://icrier.org/pdf/Policy_Series_No_9.pdf
29. F. Ansari, A.P. Verma and A. Chaube; 2013; “Effect on Performance and Emissions of SI Engine Using Ethanol as Blend Fuel Under Varying Compression Ratio”; *International Journal of Engineering Research & Technology*, Vol 2 (12).
30. Alrayyes and Taleb; 2011; “The effect of ethanol-gasoline blends on SI engine energy balance and heat transfer characteristics”; PhD thesis; University of Nottingham.
31. Ganesan V (2008) *Internal Combustion Engines*. Tata McGraw Hills Publications
32. Ojapah MM (2014) Experimental studies of performance and emissions in a 2/4-stroke engine with gasoline and ethanol. PhD Thesis, School of Engineering, Brunel University London UK
33. Gnansounou E, Dauriat A (2005) Ethanol fuel from biomass: a review. *J Sci Ind Res* 64:809–821
34. M. Yang; 2014; “The use of lignocellulosic biomass for fermentative butanol production in biorefining processes”; *Dissertationes Forestales* 2022.
35. Aalam CS, Saravanan CG (2017) Effects of nano metal oxide blended Mahua biodiesel on CRDI diesel engine. *Ain Shams Eng J* 8(4):689–696
36. Taneja S, Singh P, Singh G (2018) “Comparative analysis of the performance and emission characteristics of ethanol-butanol-gasoline blends. *IOP Conf Ser: Mater Sci Eng* 310:012136. <https://doi.org/10.1088/1757-899X/310/1/012136>
37. Sivakumar M, Sundaram NS, Kumar RR, Thasthagir MS (2018) Effect of Aluminium oxide nanoparticles blended pongamia methyl ester on performance, combustion and emission characteristics of diesel engine. *Renew Energy* 116:518–526
38. Parmar A, Taneja S (2019) “Analysis of the engine characteristics of a variable compression ratio SI engine fueled with various gasoline-ethanol blends”. *AIP Conf Proc.* 2148:030056. doi: <https://doi.org/10.1063/1.5123978>
39. Taneja S, Singh P, Sharma A, Singh G (2021) “Use of Alcohols and Biofuels as Automotive Engine Fuel”; *Energy Systems and Nanotechnology, Advances in Sustainability Science and Technology*; Springer. Singapore 5:161–183. https://doi.org/10.1007/978-981-16-1256-5_10

Chapter 6

Battery Thermal Management (BTM) Using Hybrid Nanofluid and Porous Medium in the Cooling Channel



Fatih Selimefendigil, Aykut Can, and Hakan F. Öztop

Abstract In this study, battery thermal management (BTM) of Li-ion batteries is considered using nanofluid and porous media in the cooling channel. Hybrid nanofluid of water including Al₂O₃-Cu nanoparticles is used as the cooling medium while the cooling channel is considered to be porous. A numerical model based on finite element method is developed and the nanoparticle volume fraction of hybrid nanoparticles is used up to 2%. The permeability of the channel is considered between Darcy number of 10^{-5} and 10^{-1} . The maximum temperature drops when nanoparticle solid volume fraction and permeability of the medium are increased. When the lowest and highest values of permeability cases are compared, temperature drops of 1.25 K and 3 K are obtained for water and nanofluid with the highest loading of nanoparticles. At $Da = 10^{-1}$, the maximum temperature drop is 2.4 K while it is only 1 K at $Da = 10^{-5}$ when the cooling medium of water and nanofluid with the highest hybrid nanoparticle loading amount are compared. As Li-ion batteries is a promising way to energy storage issue, methods for thermal management designs such as those presented in this paper will be helpful for further performance optimization and system development.

Keywords Porous channel · Battery thermal management systems · Hybrid nanofluids · Energy storage

F. Selimefendigil

Department of Mechanical Engineering, College of Engineering, King Faisal University, Al Ahsa 31982, Saudi Arabia

F. Selimefendigil · A. Can

Department of Mechanical Engineering, Celal Bayar University, Manisa, Turkey

H. F. Öztop (✉)

Department of Mechanical and Nuclear Engineering, College of Engineering, University of Sharjah, Sharjah 27272, United Arab Emirates

e-mail: hfoztop1@gmail.com

Department of Mechanical Engineering, Technology Faculty, Firat University, Elazığ, Turkey

1 Introduction

Due to the latest advancements in electrical vehicles, renewable energy, and electronics, the storage of energy has become a crucial concern. Lithium-ion batteries (LiBs) are the most promising solution for dealing with energy storage in recent years, and many academic and industrial studies published on this topic [1–6]. Lithium-ion batteries are proposed for the storage of electrical energy with an electrochemical method [7]. Due to the electrochemical reaction being exothermic, batteries reveal heat at the positive electrode and negative electrode while their charge and discharge cycle. During these reactions, generated heat in battery cells brings thermal issues such as thermal runaway, low-temperature performance, temperature maldistribution, and degradation in performance. These thermal issues are sorted in [8]. Thermal runaway and temperature maldistribution in LiB packages could cause ineffectiveness and even explosions while operating. Also, heat distribution in the battery pack needs to be kept under 5 K to avoid explosion and supply a safe operation [9]. Due to the abovementioned reasons, a battery thermal management system (BTMS) is required [10]. Thermal management systems employ one or more cooling techniques such as passive cooling, active cooling, and hybrid cooling techniques in several studies [11–15]. Adding nanoparticles in fluids is a common methodology called nanofluids to increase the thermal conductivity of heat transfer fluid hence, the heat transfer rate [16–19]. Thermophysical properties of nanofluids could be determined and their behaviors predictable with mathematical models by the latest advancements [20–24]. Nanoparticles in base fluid could be single nanoparticle type and also nanofluids could contain more than one type which is called hybrid nanofluids. Hybrid nanofluids are superior when compared with other nanofluids and bring several advantageous [25–29]. Nanofluids are a promising technology and also for the thermal management of LiBs and many researchers have studied this topic and some of these studies reviewed in [30]. Al_2O_3 nanoparticles and Cu nanoparticles were used in many studies separately [31–33] and Al_2O_3 -Cu particles were combined to prepare a hybrid nanofluid [34, 35] to improve the cooling capacity of base fluid. These studies have presented the achievement in the cooling performance of BTMS. Applications of nanofluid flow in porous media including convective heat transfer applications were reviewed in [36]. Also, nanofluid flow regimes in porous media were briefly explained in [37]. Porosity and permeability are considered when convective heat transfer in porous media is utilized [38].

In the present study, battery thermal management system with Al_2O_3 -Cu hybrid nanofluid and porous channels was numerically studied. Different Al_2O_3 -Cu nanoparticle volume fractions and various Darcy numbers are used as parameters to observe the effect on temperature distribution and maximum temperature in the battery cell. Aluminum plates with porous channels are considered and placed between cells. Heat transfer enhancement with nanofluid volume fraction and Darcy number variance of porous media are discussed.

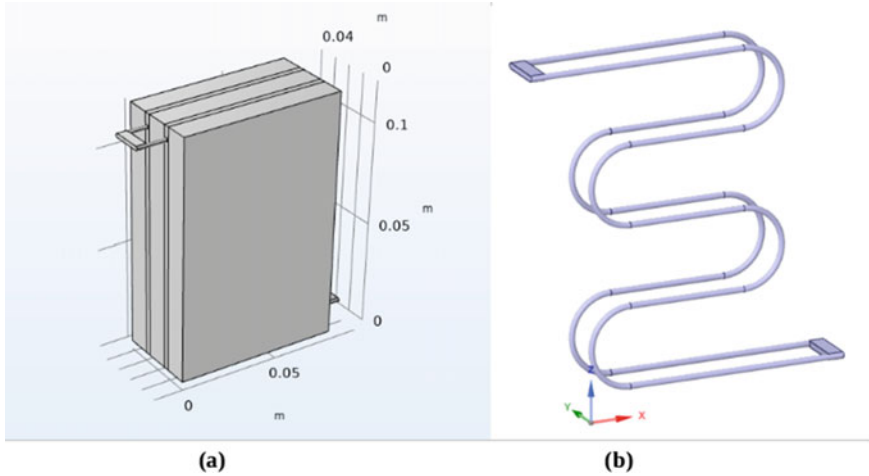


Fig. 7.1 **a** Battery arrangement, **b** porous cooling channels in the presented study

2 Numerical Modeling

In this study, three prismatic Li-ion battery cells cooled by Al_2O_3 -Cu hybrid nanofluid flow in porous channels are investigated numerically. Studied battery cells and battery thermal management system presented in Fig. 7.1. Dimensions of each battery cell are $120 \times 80 \times 12$ mm and the cooling plate thickness is 3 mm with a porous channel with a diameter of 2 mm is placed between battery cells. Three volumetric fractions ($\varphi = 0.1, 1, 2$) are designed and compared with pure water cooled at various Darcy numbers ($\text{Da} = 10^{-5}, 10^{-4}, 10^{-3}, 10^{-2}, 10^{-1}$) while Reynolds number and porosity are kept constant ($\text{Re} = 1000$ and $\varepsilon = 0.5$). Also, battery charge and discharge rate are used as 5C and modeled as 1 dimensional and the average temperature that batteries produce is calculated. Thermophysical properties are given in Table 7.1 and the equations to calculate hybrid nanofluids properties are presented in Table 7.2. Heat transfer fluid's temperature is considered as 298 K and fluid flow is assumed to be fully developed at the inlet of channel. Nanofluid is assumed incompressible and Newtonian.

Reynolds number and Darcy number are given as [39]:

Table 7.1 Thermophysical properties of hybrid nanoparticles and base fluid

Physical properties	Water	Cu	Al_2O_3
C_p [$\text{J kg}^{-1} \text{K}^{-1}$]	4179	385	765
k [$\text{W m}^{-1} \text{K}^{-1}$]	0.61	401	40
α [$\text{m}^2 \text{s}^{-1}$]	1.47×10^{-7}	1.11×10^{-4}	131.7×10^{-7}
ρ [kg m^{-3}]	997.1	8933	3970
μ [$\text{kg m}^{-1} \text{s}^{-1}$]	8.9×10^{-4}	—	—

The Brinkman-extended Darcy porous model is used [40]:

$$\nabla \cdot \mathbf{v} = 0 \quad (7.1)$$

$$\frac{\rho_{nf}}{\epsilon^2} (\mathbf{v} \cdot \nabla) \mathbf{v} = -\nabla P + \frac{\mu_{nf}}{\epsilon} \nabla^2 \mathbf{v} - \frac{\mu_{nf}}{\kappa} \mathbf{v} \quad (7.2)$$

$$(\mathbf{v} \cdot \nabla) T = \alpha_{nf} \nabla^2 T \quad (7.3)$$

$$Re = \frac{uDh}{\nu^2}, Da = \frac{\kappa}{Dh^2} \quad (7.4)$$

2.1 Li-Ion Battery Modeling

Li-ion batteries reveal heat due to exothermic reaction through the charge and discharge period. Produced heat and temperature distribution can be found with respect to the energy conservation law [41]:

$$\rho C_p \frac{\partial T}{\partial t} = \frac{\partial}{\partial x} \left(k_x \frac{\partial T}{\partial x} \right) + \frac{\partial}{\partial y} \left(k_y \frac{\partial T}{\partial y} \right) + \frac{\partial}{\partial z} \left(k_z \frac{\partial T}{\partial z} \right) + \dot{Q} \quad (7.5)$$

Energy accumulation in battery cells is represented at left-hand side in the equation and terms on the other side express, respectively, heat conduction in Cartesian coordinates and heat generation rate. The equation could be adjusted in polar coordinates for cylindrical battery cells as:

$$\rho C_p \frac{\partial T}{\partial t} = \frac{1}{r} \frac{\partial}{\partial r} \left(k_r r \frac{\partial T}{\partial r} \right) + \frac{1}{r^2} \frac{\partial}{\partial \theta} \left(k_\theta \frac{\partial T}{\partial \theta} \right) + \frac{\partial}{\partial z} \left(k_z \frac{\partial T}{\partial z} \right) + \dot{Q} \quad (7.6)$$

Overall effective battery thermal capacity is defined as below [42]:

$$\rho C_p = \frac{\sum \rho_i C_{p,i} V_i}{\sum V_i} \quad (7.7)$$

A battery cell is a combination of three different parts called a negative electrode, separator, and positive electrode that have thermal properties. Therefore, the thermal conductivity of the battery cell could be defined as [43]:

$$k_x = \frac{\sum L k_x}{\sum L} \quad (7.8)$$

Table 7.2 Thermal conductivity and viscosity of nanofluid at two different solid volume fractions

φ (%)	k [$\text{W m}^{-1} \text{K}^{-1}$]	μ [$\text{kg m}^{-1} \text{s}^{-1}$]
1	0.657	1.602×10^{-3}
2	0.685	1.935×10^{-3}

$$k_y = \frac{\sum L}{\sum L/k_y} \quad (7.9)$$

$$k_z = \frac{\sum Lk_z}{\sum L} \quad (7.10)$$

There are plenty of approaches to determine heat generation in Li-ion batteries because of their charge and discharge cycles. The complexity of these models increases the computational cost of modeling. A simplified electrochemical approach is used [44]:

$$\dot{Q} = I(U_{OC} - V) - I \left(T \frac{dU_{OC}}{dT} \right) \quad (7.11)$$

2.2 Nanofluid's Thermophysical Properties

Al_2O_3 -Cu nanoparticles and water base fluid employed as hybrid nanofluid and fluid flow modeled as single-phase flow. Base fluid and nanoparticle properties are given in Table 7.1.

Experimental data is used for the thermal conductivity and viscosity of hybrid nanofluid as available in Refs. [45, 46]. Table 7.2 shows these properties for hybrid nanofluid at a solid volume fraction of 1% and 2%.

3 Results and Discussion

In this study, the effect of hybrid nanofluid and porous channel on the cooling performance of battery cells is numerically investigated. Nanoparticle volumetric fractions of hybrid nanofluid are 0.1%, 1%, and 2% while Darcy number is changed from 10^{-5} to 10^{-1} . Battery cell dimensions are $120 \times 80 \times 12$ mm and porous channel's height is 2 mm. The porosity of the cooling channel is 0.5 and the inlet temperature of the heat transfer fluid is 298 K. Pure water was used and different volumetric fractions of Al_2O_3 -Cu/water hybrid nanofluid cases' maximum temperatures compared. when Reynold's number is 1000.

Fig. 7.2 Temperature contour of battery cell cooled by pure water without porous channel

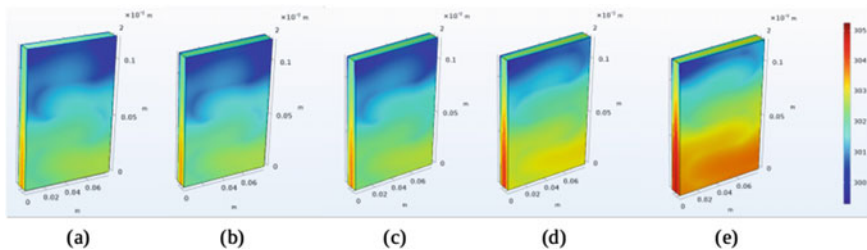
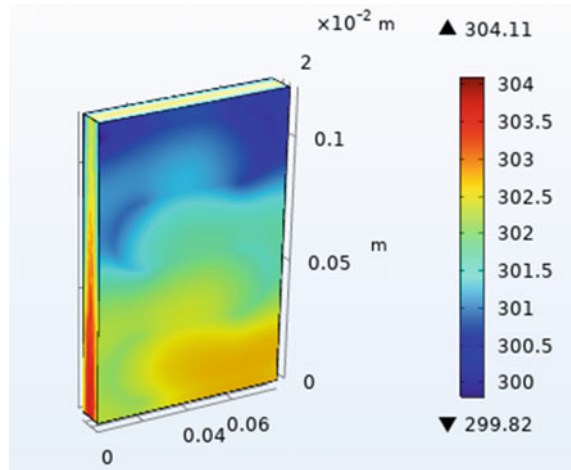


Fig. 7.3 Temperature contours of cooled battery by pure water at Darcy number **a** $1e-1$, **b** $1e-2$, **c** $1e-3$, **d** $1e-4$, **e** $1e-5$

Figure 7.2 shows the temperature contour of the battery cell cooled by pure water without a porous cooling channel when the charge and discharge rate is 5C. The maximum temperature is 304.11 K and the temperature difference is 4.29 K when the porous channel is not employed. Figure 7.3 shows the battery cell cooled by pure water flow in porous cooling channels with various permeability of the channel. At $Da = 10^{-1}$, the maximum temperature is 304.02 K while at $Da = 10^{-5}$, its value is 305.25 K. Using hybrid nanofluid with a loading amount of 0.1%, at permeabilities of $Da = 10^{-1}$ and $Da = 10^{-5}$, the highest temperature values are obtained as 303.66 K and 304.99 K (Fig. 7.4). At the highest nanoparticle volume fraction, the values become 301.56 K and 301.99 K. The permeability of the medium becomes significant when pure fluid is used as the heat transfer fluid while when nanofluid is used with higher nanoparticle loading, the impact of Da on the maximum temperature variation is less. However, using nanofluids for the same permeability of the channel is more effective in the thermal management (Fig. 7.5).

The uniformity in the temperature distribution is also established when nanofluid and medium with higher permeability are preferred. When pure water is used for

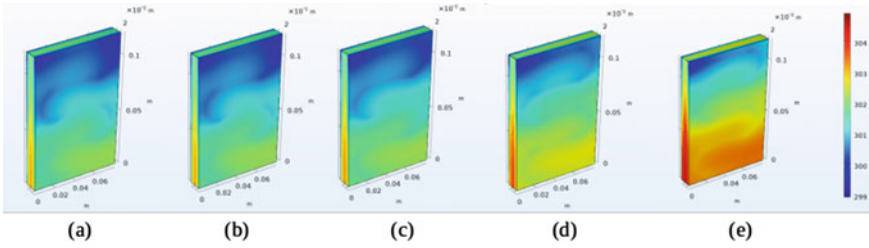


Fig. 7.4 Temperature contours of cooled battery by $\text{Al}_2\text{O}_3\text{-Cu}$ /water hybrid nanofluid ($\phi = 0.1$) at Darcy number **a** $1e-1$, **b** $1e-2$, **c** $1e-3$, **d** $1e-4$, **e** $1e-5$

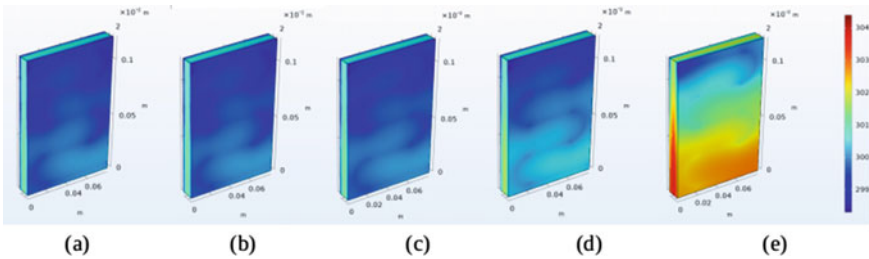


Fig. 7.5 Temperature contours of cooled battery by $\text{Al}_2\text{O}_3\text{-Cu}$ /water hybrid nanofluid ($\phi = 2$) at Darcy number **a** $1e-1$, **b** $1e-2$, **c** $1e-3$, **d** $1e-4$, **e** $1e-5$

heat transfer, the fluid temperature difference in the battery cell is 5.86 K at Darcy number 10^{-5} and 4.35 K at Darcy number 10^{-1} . With nano-enhanced cooling fluid at the highest loading, the value becomes 3.03 K at Darcy number 10^{-1} (Figs. 7.6 and 7.7)

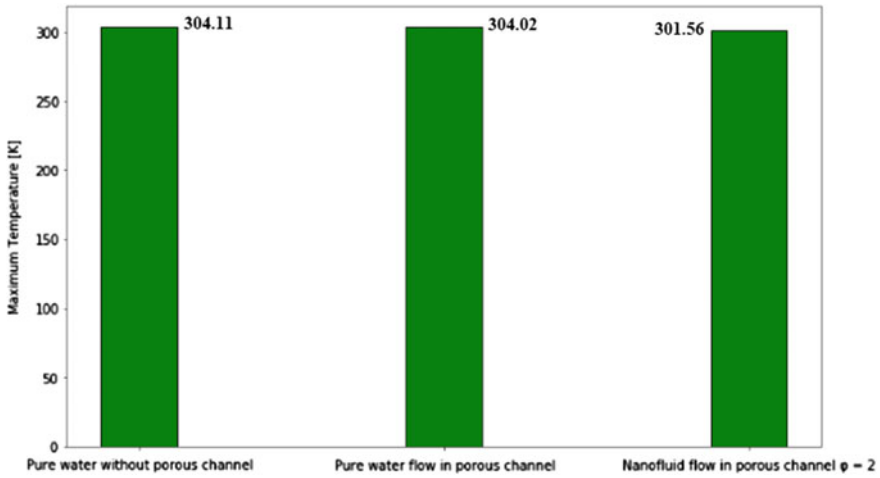


Fig. 7.6 Comparison of maximum temperature at different heat transfer fluids and channel zones

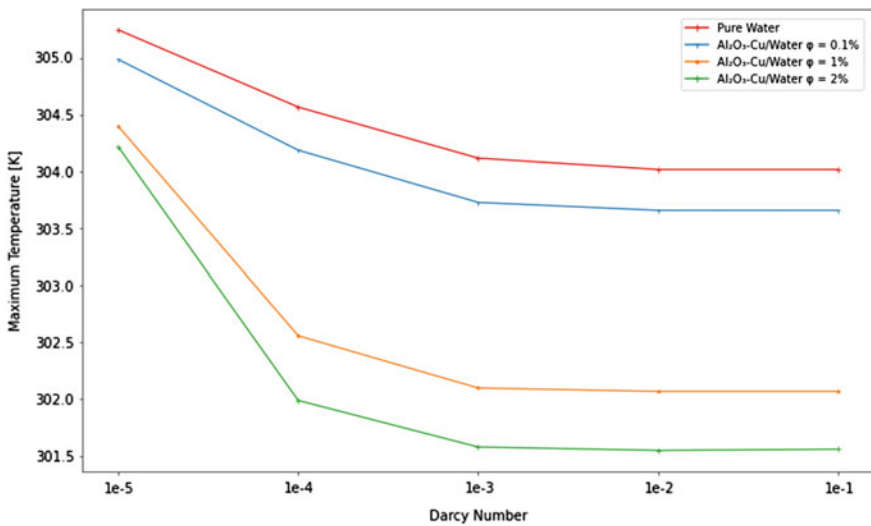


Fig. 7.7 Comparison of maximum temperature at different Darcy numbers (Re = 1000)

4 Conclusion

In this study, the maximum temperature, and temperature distribution of three prismatic lithium-ion batteries which are cooled by hybrid nanofluid flow in porous cooling channel are investigated numerically with various nanoparticle volume fractions and Darcy number at the constant Reynolds number and charge/discharge rate

of battery cells. The maximum temperature of the battery cell decreased with increment at the Al_2O_3 -Cu nanoparticle volume fraction in the base fluid. Increment in Darcy number also decreased the maximum temperature and temperature distribution in batteries. The lowest maximum temperature in the battery cell was observed with a 2% nanoparticle volume fraction and the highest permeability. A comparison of pure water and the highest volume fraction of 2% nanofluid cases shows that Al_2O_3 -Cu/water nanofluid provides a maximum temperature drop from 1 K to 2.46 K at a minimum and maximum permeability of porous channel.

References

1. Li H (2019) Practical evaluation of Li-ion batteries. *Joule* 3(4):911–914
2. Miao Y, Hynan P, Von Jouanne A, Yokochi A (2019) Current Li-ion battery technologies in electric vehicles and opportunities for advancements. *Energies* 12(6):1074
3. Tarascon JM (2020) Na-ion versus Li-ion batteries: complementarity rather than competitiveness. *Joule* 4(8):1616–1620
4. Xie L, Tang C, Bi Z, Song M, Fan Y, Yan C, Chen C (2021) Hard carbon anodes for next-generation li-ion batteries: review and perspective. *Adv Energy Mater* 11(38):2101650
5. El Kharbachi A, Zavorotynska O, Latroche M, Cuevas F, Yartys V, Fichtner M (2020) Exploits, advances and challenges benefiting beyond Li-ion battery technologies. *J Alloy Compd* 817:153261
6. Tian YF, Li G, Xu DX, Lu ZY, Yan MY, Wan J, Guo YG (2022) Micrometer-sized SiMgyOx with stable internal structure evolution for high-performance Li-ion battery anodes. *Adv Mater* 34(15):2200672
7. Zhou H, Zhou F, Xu L, Kong J (2019) Thermal performance of cylindrical Lithium-ion battery thermal management system based on air distribution pipe. *Int J Heat Mass Transf* 131:984–998
8. Bibin C, Vijayaram M, Suriya V, Ganesh RS, Soundarraj S (2020) A review on thermal issues in Li-ion battery and recent advancements in battery thermal management system. *Mater Today: Proc* 33:116–128
9. Behi H, Karimi D, Behi M, Ghanbarpour M, Jaguemont J, Sokkeh MA, Van Mierlo J (2020) A new concept of thermal management system in Li-ion battery using air cooling and heat pipe for electric vehicles. *Appl Therm Eng* 174:115280
10. Liao Z, Zhang S, Li K, Zhang G, Habetler TG (2019) A survey of methods for monitoring and detecting thermal runaway of lithium-ion batteries. *J Power Sources* 436:226879
11. Yang Y, Li W, Xu X, Tong G (2020) Heat dissipation analysis of different flow path for parallel liquid cooling battery thermal management system. *Int J Energy Res* 44(7):5165–5176
12. Xu Y, Li X, Liu X, Wang Y, Wu X, Zhou D (2021) Experiment investigation on a novel composite silica gel plate coupled with liquid-cooling system for square battery thermal management. *Appl Therm Eng* 184:116217
13. Qin P, Liao M, Zhang D, Liu Y, Sun J, Wang Q (2019) Experimental and numerical study on a novel hybrid battery thermal management system integrated forced-air convection and phase change material. *Energy Convers Manage* 195:1371–1381
14. Chen F, Huang R, Wang C, Yu X, Liu H, Wu Q, Bhagat R (2020) Air and PCM cooling for battery thermal management considering battery cycle life. *Appl Therm Eng* 173:115154
15. Zhou Z, Wang D, Peng Y, Li M, Wang B, Cao B, Yang L (2022) Experimental study on the thermal management performance of phase change material module for the large format prismatic lithium-ion battery. *Energy* 238:122081
16. Xuan Y, Li Q (2000) Heat transfer enhancement of nanofluids. *Int J Heat Fluid Flow* 21(1):58–64

17. Barber J, Brutin D, Tadrist L (2011) A review on boiling heat transfer enhancement with nanofluids. *Nanoscale Res Lett* 6(1):1–16
18. Senobar H, Aramesh M, Shabani B (2020) Nanoparticles and metal foams for heat transfer enhancement of phase change materials: A comparative experimental study. *J Energy Storage* 32:101911
19. Kumar N, Sonawane SS (2016) Experimental study of thermal conductivity and convective heat transfer enhancement using CuO and TiO₂ nanoparticles. *Int Commun Heat Mass Transfer* 76:98–107
20. Ali, N., Teixeira, J. A., & Addali, A. (2018). A review on nanofluids: fabrication, stability, and thermophysical properties. *Journal of Nanomaterials*, 2018.
21. Duangthongsuk W, Wongwises S (2008) Effect of thermophysical properties models on the predicting of the convective heat transfer coefficient for low concentration nanofluid. *Int Commun Heat Mass Transfer* 35(10):1320–1326
22. Babar H, Ali HM (2019) Towards hybrid nanofluids: preparation, thermophysical properties, applications, and challenges. *J Mol Liq* 281:598–633
23. Sezer N, Atieh MA, Koç M (2019) A comprehensive review on synthesis, stability, thermophysical properties, and characterization of nanofluids. *Powder Technol* 344:404–431
24. Dey D, Kumar P, Samantaray S (2017) A review of nanofluid preparation, stability, and thermophysical properties. *Heat Transfer—Asian Res* 46(8):1413–1442
25. Kiani M, Omiddezyani S, Houshfar E, Miremadi SR, Ashjaee M, Nejad AM (2020) Lithium-ion battery thermal management system with Al₂O₃/AgO/CuO nanofluids and phase change material. *Appl Therm Eng* 180:115840
26. Sidik NAC, Adamu IM, Jamil MM, Kefayati GHR, Mamat R, Najafi G (2016) Recent progress on hybrid nanofluids in heat transfer applications: a comprehensive review. *Int Commun Heat Mass Transfer* 78:68–79
27. Bhattach A, Sarkar J, Ghosh P (2018) Discrete phase numerical model and experimental study of hybrid nanofluid heat transfer and pressure drop in plate heat exchanger. *Int Commun Heat Mass Transfer* 91:262–273
28. Kiani M, Omiddezyani S, Nejad AM, Ashjaee M, Houshfar E (2021) Novel hybrid thermal management for Li-ion batteries with nanofluid cooling in the presence of alternating magnetic field: An experimental study. *Case Stud Thermal Eng* 28:101539
29. Abdelkareem MA, Maghrabie HM, Abo-Khalil AG, Adhari OHK, Sayed ET, Radwan A, Olabi AG (2022) Battery thermal management systems based on nanofluids for electric vehicles. *J Energy Storage* 50:104385
30. Kumar R, Mitra A, Srinivas T (2022) Role of nano-additives in the thermal management of lithium-ion batteries: a review. *J Energy Storage* 48:104059
31. Mashayekhi M, Houshfar E, Ashjaee M (2020) Development of hybrid cooling method with PCM and Al₂O₃ nanofluid in aluminium minichannels using heat source model of Li-ion batteries. *Appl Therm Eng* 178:115543
32. Yetik O, Yilmaz N, Karakoc TH (2021) Computational modeling of a lithium-ion battery thermal management system with Al₂O₃-based nanofluids. *Int J Energy Res* 45(9):13851–13864
33. Liao G, Wang W, Zhang F, Jiaqiang E, Chen J, Leng E (2022) Thermal performance of lithium-ion battery thermal management system based on nanofluid. *Appl Therm Eng* 216:118997
34. Dwivedi, A., Kumar, A., & Goel, V. (2022). Selection of nanoparticles for battery thermal management system using integrated multiple criteria decision-making approach. *Int J Energy Res*
35. El Idi MM, Karkri M, Tankari MA (2021) A passive thermal management system of Li-ion batteries using PCM composites: experimental and numerical investigations. *Int J Heat Mass Transf* 169:120894
36. Khanafer K, Vafai K (2019) Applications of nanofluids in porous medium. *J Therm Anal Calorim* 135(2):1479–1492
37. Esfe MH, Bahiraei M, Hajbarati H, Valadkhani M (2020) A comprehensive review on convective heat transfer of nanofluids in porous media: energy-related and thermohydraulic characteristics. *Appl Therm Eng* 178:115487

38. Bourantas GC, Skouras ED, Loukopoulos VC, Burganos VN (2014) Heat transfer and natural convection of nanofluids in porous media. *European Journal of Mechanics-B/Fluids* 43:45–56
39. Bitla, P., & Sitotaw, F. Y. (2022). Effects of Slip and Inclined Magnetic Field on the Flow of Immiscible Fluids (Couple Stress Fluid and Jeffrey Fluid) in a Porous Channel. *Journal of Applied Mathematics*.
40. Kasaeian A, Daneshzarian R, Mahian O, Kolsi L, Chamkha AJ, Wongwises S, Pop I (2017) Nanofluid flow and heat transfer in porous media: a review of the latest developments. *Int J Heat Mass Transf* 107:778–791
41. Chen X, Zhou F, Yang W, Gui Y, Zhang Y (2022) A hybrid thermal management system with liquid cooling and composite phase change materials containing various expanded graphite contents for cylindrical lithium-ion batteries. *Appl Therm Eng* 200:117702
42. Chen Y, Evans JW (1996) Thermal analysis of lithium-ion batteries. *J Electrochem Soc* 143(9):2708
43. Gu WB, Wang CY (2000) Thermal-electrochemical modeling of battery systems. *J Electrochem Soc* 147(8):2910
44. Lai Y, Du S, Ai L, Ai L, Cheng Y, Tang Y, Jia M (2015) Insight into heat generation of lithium ion batteries based on the electrochemical-thermal model at high discharge rates. *Int J Hydrogen Energy* 40(38):13039–13049
45. Suresh S, Venkataraj K, Selvakumar P, Chandrasekar M (2011) Synthesis of Al₂O₃–Cu/water hybrid nanofluids using two step method and its thermo physical properties. *Colloids Surf A* 388(1–3):41–48
46. Ghalambaz M, Mehryan SAM, Izadpanahi E, Chamkha AJ, Wen D (2019) MHD natural convection of Cu– Al₂O₃ water hybrid nanofluids in a cavity equally divided into two parts by a vertical flexible partition membrane. *J Therm Anal Calorim*, 138, 1723–1743

Chapter 7

Phenolic Effluent Treatment Using Advanced Nanomaterials



Baskaran Sivaprakash, Natarajan Rajamohan, Angeline Reshmi, and Vedula Sairama Srinivasa Phanindra

Abstract Nanomaterials are of distinct origin and can be procured as naturally occurring materials, from combustion reactions or by specific engineered methods depending on their application. Owing to the compatibility in production methods, nanomaterials find a broad spectrum of applications including healthcare, space research, cosmetics, communication, electronics, defense, coatings, genetic engineering and environmental preservations. The present book chapter deals with the application of nanomaterials for phenolic waste treatment with a special focus on metal oxides and carbon-based materials. This includes novel and eco-friendly synthesis methods of nanomaterials and their performance in phenol treatment, mechanism of action, kinetic studies and machine learning methods.

Keywords Nanomaterials · Effluent · Phenol · Metal oxides · Kinetics

Abbreviations

DEP	Diethyl phthalate
CNTs	Carbon nanotube
CNMs	Carbon nanomaterials
CNM-AP	Au–Pd alloyed nanoparticles
Me-GO	Mechanochemically synthesised graphite oxide
2D	Two-dimensional
CeO ₂ -NPs	Cerium oxide nanoparticles

B. Sivaprakash (✉)
Tamilnadu Government Polytechnic College, Madurai, India
e-mail: spshivbhaskar@gmail.com

N. Rajamohan
Chemical Engineering Section, Faculty of Engineering, Sohar University, Sohar 311, Oman

A. Reshmi · V. S. S. Phanindra
Department of Chemical Engineering, Annamalai University, Annamalainagar 608002, India

LDHs	Layered double hydroxides
M-LDHs	Metal layered double hydroxides
AOPs	Advanced oxidation process
NPs	Nanoparticles
CNM	Carbon nanomaterials
PNC	Polymer nanocomposites
CPNs	Clay-polymers nanocomposites
PMMA	Polymethyl methacrylate
Cryst-PPy	Conductive crystalline polypyrrole
Ni-PPy	Nickel-polypyrrole
Cu-PPy	Copper-polypyrrole
TNPs	Titanium oxide nanoparticles
ECRs	Electrocatalytic reactors
FBERs	Fixed -bed electrocatalytic reactors
ECMRs	Electrocatalytic membrane reactors
POSS-NH ₂	Polyhedral oligosiloxane
PC	Proanthocyanidins
FPN	Ferrous proanthocyanidins
LSMM	Hydrophilic surface modifying macromolecules
EAO	Electrochemical advanced oxidation

1 Introduction

The history of phenols dates back to the 1860s and it was mainly produced as an antiseptic. Since then, several derivatives of phenols have been formulated for usage as disinfectants, preservatives, plastics, explosives, dyes, and medicinal drugs. Due to multi-faceted applications of phenolic compounds, their requirement is projected to be 4.9% of the compound annual growth rate from 2022 to 2032. The corresponding market size measures between 25.6 and 41.4 billion USD. The pivotal factors for this accelerated growth projection are attributed to the usage of phenols in personal care products and household applications. Additionally, phenols serve as feedstock for a broad spectrum of compounds in several other industries [1]. These factors make phenol and phenolic derivatives inevitable compounds in process industries. The overuse of these components has led to their occurrence in water bodies beyond the permissible level, which is considered a major threat to the ecosystem. Petroleum refineries, steel mills, coke ovens, medicines, synthetic resins, coal gas, mine discharges, plywood industries, paper and pulp factories and pharmaceutical industries are some of the principal sources of phenolic effluents [2]. Since they are extremely hazardous to plants, animals and human beings even at extremely low concentrations, phenols are regarded as one of the main organic toxic contaminants found in wastewater. This class of organic contaminants in wastewater comprises phenol, bisphenol A, p-nitrophenol, pentachlorophenol, etc. Moreover,

the manufacture of dyestuffs and pesticides uses chemical intermediates including 4-amino-5-hydroxynaphthalene-2,7-disulfonic acid, DEP (diethyl phthalate) and 2-mercaptobenzothiazole. The molecular structures of phenols and chemical intermediates are aromatic and heteroatom based. These chemical substances are fatal to living organisms due to their extreme toxicity. It is the responsibility of the scientific community to protect the environment against these substances in a sustainable manner with cost-effectiveness [3].

To treat wastewater contaminated with phenolic ingredients, conventional treatment techniques like solvent extraction, distillation, membrane pervaporation, chemical oxidation, ion exchange, physical and chemical adsorptions, membrane–solvent extraction, photocatalytic degradation and electrochemical oxidation have been researched extensively [4, 5]. Nevertheless, three of these technologies, namely, adsorption, advanced oxidation and filtration are reported to give prospective results in terms of degradation efficiency, cost-effectiveness, real-time applications and versatility of materials utilised as remediating agents. The evolution of nanotechnology has evinced numerous game-changing approaches and milestones in the scientific world, with a special impact on environmental engineering applications. Nano-sized materials possess large surface-to-volume ratio, reactive sites, flexible size distribution, surface morphology, aggregation states, crystallinity, solubility, etc. that make them susceptible to be employed as promising agents in adsorption, oxidation and filtration. Development and application of carbon-based materials (biochar, graphene, MXenes), metal oxides and polymers of nano-configuration for abating phenolic contaminations in wastewater are detailed in this chapter along with the mechanism of action in each of the three methodologies [6–10].

2 Classification of Nanomaterials for Phenolic Waste Treatment

In the present chapter, three classes of nanoparticles, namely carbon-based, metal-ion-based and polymer-based materials are dealt with. These three classes are widely reported to yield sound results in the treatment of many organic and inorganic contaminations in wastewater streams. This section elaborates on the salient features, preparation methods and special properties of the aforesaid nanomaterials in phenolic waste treatment.

2.1 Carbon-Based Nanomaterials

There are tremendous types of processes available to remove phenol, many of which use nanoparticles based on different materials like carbon, metal and polymers. Carbon-based materials have very wide applications in treating heavy metals,

and organic and inorganic pollutants from wastewater using distinct technologies. Biochar, graphene, carbon nanotubes and MXenes are the present generation carbon materials reported to yield promising results in treating organic pollutants like phenols. Nanoparticles made from these materials integrated with metals and polymers to yield nanocomposites are also attracting more attention. Biochar is synthesised from several renewable and sustainable feedstocks by thermochemical methods. This is further processed to fabricate nano-structured composites with high performance in phenol degradation. The major highlight of this approach is that the spent biochar finds excellent application as fertiliser, thereby contributing to a circular economy. By coupling with other nanomaterial catalysts, biochar, a component of the carbon family, functions admirably as a photocatalyst. Biochar is a bioactive material rich in carbon source having multiple functional groups and a substantial number of pores. These functional groups are readily responsive to organic compounds offering a very high rate of degradation and very high adsorption due to the high surface area, increased porosity, and abundance of functional groups containing oxygen. Biochar serves as a support for a large number of nanoparticles. It can be prepared by thermochemical conversion of feedstocks like plant residue, animal manure, sludge, agro waste, residue, industrial bio waste and aquatic and micro-organisms. Graphene, being a pseudocapacitive substance possesses a large surface area and conducive mechanical properties and is regarded as the building element for many graphitic allotropes. Graphene-based carbon compounds are prepared by exfoliation (mechanical and electrochemical), solvothermal, chemical vapor deposition, etc. grouped under top-down and bottom-up methodologies [11].

Using industrial waste like jute fibres, a cost-effective nanocomposite with the ability to separate organic pollutants can be produced. A simple procedure was implemented to coat pre-treated carbonaceous industrial waste (jute fibres) with graphene oxide. In comparison to graphene oxide, the coated nanocomposites were reported to exhibit improved separation performance. The nanocomposite possesses the ability to perform adsorption at a wide variety of parameters which makes it a promising candidate for phenol removal. The challenging issue in this process is using powdered nanomaterials in large-scale water treatment. The smaller size of the nanoparticles complicates their separation from reaction mixtures after usage, which is a serious concern. Sea buckthorn stones, an agricultural waste, were used to make activated carbon, which was then magnetised using cobalt (magnetic metal nanoparticles). The results of the phenol desorption tests demonstrated that the reusability is outstanding, due to the magnetic features of the nanoparticles-coated magnetic cobalt. High-solid, grease- and oil-suspended sample contamination can be eliminated with the magnetic cobalt nanoparticles coated onto activated carbon [3, 12, 13].

Carbon nanotube (CNT) materials are effective agents for phenol adsorption from aqueous solutions. Prominent features of CNTs include high surface area, porosity and functional groups, which contribute to improvised adsorption efficiency. To further enhance the performance of the adsorbent, nanoparticles are often integrated with silica, carbon nanotubes and polymers. Polymeric nanocomposites are promising adsorbents for water treatment applications with good mechanical properties, large specific surface area, tuneable surface qualities and cost-effectiveness.

When nanoparticles are added to a polymer matrix to enhance the surface area of the sorbents it provides more active sites, which enhances the adsorption capacity of the selected nanoparticles. The main impediment to their widespread use is the laborious collection of carbon nanotube powder following the remediation process, which necessitates additional steps like centrifugation and filtration with membranes of nanometre-sized pores. An intriguing technique to improve the CNT powder's usage in wastewater treatment without sacrificing its chemical attraction to phenols is to fix it easily in a solid compact [14, 15].

Due to their exceptional chemical, mechanical and thermal stabilities and high surface-to-volume ratio, carbon nanomaterials (CNMs) have enormous potential as new-generation adsorbents. However, pristine CNMs are poorly soluble in most solvents, which limits the use of CNMs in practical applications. It is crucial to modify the surface of CNMs for wastewater treatment applications in order to increase their chemical stability, fouling resistance, effectiveness and solubility. Promising adsorbents for treating organic and inorganic wastewater contaminants include functionalised CNMs [16].

Graphene-based nanomaterials have high specific surface areas and large pore diameters. Mechanochemically synthesised graphite oxide (Me-GO) can be added in minimal doses, over a broad pH range and micropollutant concentrations in a treatment system for high removal efficiency. g-C₃N₄ exhibits a laminar structure with numerous nanopores (diameter: 1.48 nm) that can serve as water transport channels and provide a molecular sieving function. It is a type of two-dimensional (2D) nanomaterial with a visible-light response. In addition, g-C₃N₄ has several other benefits, including a conducive energy band, excellent physicochemical stability, non-toxicity, and ease of fabrication. As a result, it has enormous potential for membrane separation applications, particularly for photoactivity stimulated by visible light. Me-GO and g-C₃N₄-based material are effective adsorbents for removing phenolic, and reducing organic contaminants and dye chemicals in wastewater. The rate at which Me-GO regenerates frequently further implies that it has the potential to be used in a variety of applications. The challenging issue is to gather and renew the suspended g-C₃N₄-based powders for use in real-world applications [17, 18].

2.2 *Metal-Based Nanomaterials*

The fundamental units of nanotechnology are nanoparticles, which have distinct properties like increased surface area, precisely articulated shape and nanoscale dimensions. The distinctive properties include excellent biocompatibility towards the immobilisation of enzymes for the detection of particular biomolecules, changeable lattice and cell parameters due to structural changes, and easily tuneable electrochemical characteristics. These characteristic features make metal oxide nanoparticles occupy a dominating position in environmental remediation-based separation processes.

Owing to their environmentally friendly nature, affordability and renewability qualities, oil palm leaves have been extensively used in the research field to synthesise cerium oxide nanoparticles (CeO_2 -NPs). CeO_2 -NPs are gaining high interest in the scientific community when compared to other metal oxide nanoparticles because of their superior electrical, optical, eco-friendly and catalytic uses. CeO_2 has been produced using a variety of synthesis techniques, including hydrothermal, sol-gel, and photosynthesis. The photocatalytic degradation activities of the hydrothermal and sol-gel-based CeO_2 were relatively lower, reaching 80 and 72.10%, respectively. According to the type of industrial pollutants, the photosynthesis strategy can serve as an excellent method for producing CeO_2 -NPs, which reveal high photocatalytic potential for the elimination of various pollutants in the range of 92 to 99.6% [19].

Due to the synergistic interactions between ferrous and copper ions, copper ferrites that contain Cu^+ ions are regarded as highly efficient heterogeneous Fenton catalysts. Three distinct nano-spheric particles were formulated based on calcination temperature and ingredient compositions. The cuprite and cubic copper ferrite together present in the copper ferrite nanospheres is the reason for higher catalytic activity in the phenolic degradation process [20].

The benefits of employing layered double hydroxides (LDHs) exhibit many advantages, simpler and lower cost of preparation, homogenous atomic level diffusion of the metal ions, and the susceptibility to have customised metal layered double hydroxides (M-LDHs) with distinct compositions. Copper-containing 2D transition metal oxides can be created using two-dimensional (2D) layered double oxide made of magnesium chloride with aluminium chloride as a precursor and structural template. This approach results in the fabrication of copper nanosheets with a perfect support matrix. The resulting CuOx -based nanosheets were witnessed to possess inherent thickness and inner support matrix which effectively activated persulfate for quick phenol degradation [21].

Zirconia nanoparticles were electrolytically synthesised to improvise the degradation of phenol in aqueous solutions. In advanced oxidation processes (AOPs), photocatalysts including titanium dioxide (TiO_2), ZrO_2 , ZnO , Fe_2O_3 and ZnS have been utilised to cleanse water. Due to unique optical and electrical characteristics, thermal stability, high mechanical strength and the existence of acid-base and redox capabilities, ZrO_2 nanoparticles show significant potential for phenol degradation. ZrO_2 is likewise stable when exposed to light for catalysis and can function both as a catalyst or catalyst supporter. However, the zirconia material exhibits lesser photocatalytic activity towards phenol degradation than electrogenerated zirconia [22].

According to the Globally Harmonized System of Classification and Labelling of Chemicals, TiO_2 is a white metal oxide that is non-flammable, lesser soluble, thermally stable and non-toxic. TiO_2 is also regarded as one of the most promising photocatalysts due to its photostability, nontoxicity and energy efficiency. Recent advances in research demonstrate the effectiveness of metal oxides as photocatalysts, which include ZnO , CuO and SnO_2 . *Hibiscus rosasinesis* could improve the performance of the synthesising process because the phytochemicals in the extract are perceived to serve as a capping agent that stabilises the generated metal oxide

nanoparticles and inhibit agglomeration. TiO_2 photocatalyst was used in a controlled environment to degrade phenol solutions at various concentrations. This research outcome revealed that TiO_2 generated with *H. rosasinensis* leaves extract has the capacity to treat phenol contaminants in an appreciable manner [23]. By hydrolysing the TiCl_4 precursor in an aqueous solution with various amounts of glycerol followed by calcination, coloured titania nanoparticles were yielded. The primary cause of the colour of the synthetically produced titania, at the lowest level of the samples, is the presence of Ti^{3+} ions. The ability of the coloured titania to absorb visible light and perform photocatalysis is found to be considerably enhanced by these Ti^{3+} species' ability to produce mid-gap states in the bandgap. Within 180 min of exposure to visible light, treated palm oil mill effluent was reported to achieve the elimination of over 48.17% of phenolic compounds and 62.18% of colour removal [24].

Through the application of a conventional one-pot calcination method, Au/Pd bimetallic alloyed nanoparticles were successfully embellished on mesoporous silica-modified g- C_3N_4 (graphitic carbon nitride) nanosheets. Tandem reactions for the simultaneous oxidation of phenol and reduction of Cr were used to test the photocatalytic performance of the photocatalysts Cr(VI). The g- C_3N_4 /MCM-41 composite (CNM) has proven to be an effective photocatalyst for the elimination of pollutants in an aqueous medium, which serves as a good substrate for the loading of noble metal nanoparticles. g- C_3N_4 /MCM-41 nanosheets (CNM-AP) modified with bimetallic alloyed Au/Pd nanoparticles were created by in situ calcination followed by borohydride reduction. When compared to stabilising molecules utilised in the conventional colloid synthesis approach, the presence of silanol groups on CNM favoured the deposition of Au-Pd alloyed nanoparticles. In the mixed Cr(VI)/phenol reaction solution, the prepared photocatalyst (CNM-AP) exhibited superior photocatalytic performance, due to significantly improved visible light response, bimetallic co-effect, catalyses the reduction of Cr(VI) and oxidation of phenol [25].

Pristine nanoparticles are hard to separate, whereas magnetic nanoparticles have higher efficiencies in separation with enhanced adsorption capacity and significantly higher permanence in suspension medium. Iron-oxide-based nanomaterials have drawn relatively higher attention with promising magnetic properties because of their ease in magnetic separation from solutions and their biocompatibility. Nanomaterials can also be functionalised with polymeric molecules or inorganic materials surface to improve the surface reactivity for higher scale adsorption purposes. By increasing the magnetic nano powder's carbon content, methyl orange and phenol removal effectiveness were reported to be significantly improved [8]. Due to high catalytic effectiveness, low cost, physical and chemical stabilities and accessibility, FeTiO_3 is a well-recognised magnetic nanoparticle with a bandgap of 2.5–2.9 eV. The photocatalytic breakdown of organic molecules can be accomplished effectively using FeTiO_3 . Doping with metallic ions and non-metallic substances like carbon compounds has given prospective results to enhance FeTiO_3 's photocatalytic efficiency. These alterations aid in increasing the amount of light that can be absorbed in the visible spectrum and terminate the recombination of electron-hole pairs. Additionally, FeTiO_3 has proved to be still more effective under visible light with a lower bandgap energy when combined with graphene oxide [26].

2.3 *Polymer-Based Nanomaterials*

The removal of various contaminants including inorganic, organic and viscous pollutants from water, has been reported to be attained using various natural and synthetic polymer nanocomposites (PNC), clay, metal and carbon-based PNCs. Polymer nanocomposites are playing a pivotal role in environmental remediation applications attributed to the presence of functional materials and cost-effectiveness for efficient water purification systems. Designing materials with on-demand qualities for a variety of water treatment processes, including flocculation, coagulation, flotation, adsorption, degradation, reduction, and membrane systems, is greatly facilitated by both polymers and nanomaterials, which make up polymer nanocomposites. Many research advancements have aided the potential of PNCs' reusability and recyclability for abating the potential negative environmental consequences. Their life cycle assessment will undoubtedly be a significant step in understanding and resolving the difficulties associated with using these materials for water treatment applications [27].

Naturally occurring clay minerals have relatively lower surface area, and to replace them in environmental applications, polymeric resins have been used. However, factors like pH dependence, high cost, low water wettability and particle size sensitivity have prevented polymeric resins from being widely used in industries for water treatment. Organoclay is a kind of material that is yielded when organic molecules are added to clay minerals like palygorskite and montmorillonite. In synthesising clay-polymer nanocomposites (CPNs), organoclays preparation is the initial step. Hydrophilic clay minerals are found naturally, in which clay minerals are combined with quaternary ammonium, phosphonium, or sulfonium cations to create organoclays. Three major groups of clay-polymer layered composites are reported: Phase-separated micro composites, intercalated nanocomposites and exfoliated nanocomposites. Clay polymer nanocomposites find wide applications as a coagulant, catalytic agent, membrane, filter, adsorbents, etc. in wastewater treatment methods for eliminating organic and inorganic contaminants as well as dangerous bacteria. The effectiveness of CPNs for pollutant removal in aqueous systems gets increased by the appropriate incorporation of clay at optimal doses with numerous inorganic polymers and biopolymers in the nanometre range or nanoclay for the development of nanocomposites [28].

Varieties of source materials have been investigated as contaminant adsorbents, including clay minerals, modified clays, zeolites, activated carbon, polymeric resins, etc. The performance of polymeric materials can be improved by impregnating clay minerals for effluent treatments. With the proper synthesis procedures, CPNs may be made from a variety of polymers, including chitosan, polystyrene, polypropylene, polyesters, polyurethanes, epoxies and polyvinyl chloride. These engineered materials have been reported to be effective and affordable adsorbents for the eradication of organic and inorganic contaminants from water/wastewater [29].

The advantage of recovery of the nanoparticles after water treatment is provided by the incorporation of active TiO₂ nanostructures in polymethyl methacrylate

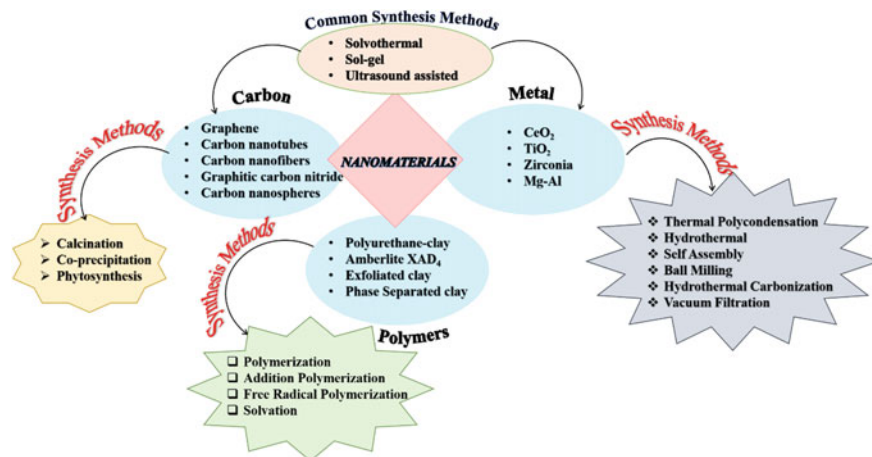
(PMMA). Moreover, by coupling single-walled carbon nanotubes, with electron acceptor TNPs, higher photocatalytic efficiency under UV irradiation can be achieved. These PMMA composites are reliable, safe, affordable and easily producible, allowing for prospective industrial use as effective tools for removing bacterial and organic pollutants from water [30].

Dimethylamine and trimethylamine were used to functionalise Amberlite™ XAD₄, a commercial styrenic polymer that is easier to manipulate physically and chemically. 1,2-dichloroethane was used to hyper-crosslink styrenic polymer. Due to the ability of selective deposition of specific amine groups onto surfaces that are otherwise devoid of functionalities, styrenic polymers offer a novel strategy for studying phenol adsorbent-adsorbate interactions. The polymer precursor used is Amberlite™ XAD₄, which is a commercially accessible substance with a track record of application in water treatment. The phenol adsorption capability of Amberlite™ XAD₄ increased significantly through physical and chemical modifications. 1,2-dichloroethane was used to hyper-cross-link XAD₄ in order to expand the size of the micropores and give more interaction sites. Dimethylamine and trimethylamine treatments were used to introduce tertiary and quaternary amine groups, respectively. As a result of the synergistic effects of increased surface affinity and micropore volume, the results demonstrated that the highest adsorption capacity was achieved when hyper-cross-linking and amination were combined. The development of physiochemically modified polymers with improved phenol adsorption capacity and regeneration efficiency is feasible by understanding the principles underlying phenol adsorption [31].

Using a chemical polymerisation technique in an aqueous solution, conductive crystalline polypyrrole (Cryst-PPy), nickel-polypyrrole (Ni-PPy) and copper-polypyrrole (Cu-PPy) hybrid materials were fabricated. Successful chemical synthesis of Cryst-PPy powder was accomplished using acetonitrile as the organic medium, polyethylene oxide as a stabilising agent and potassium peroxydisulfate as an oxidising agent. The chemical method from an organic medium was successfully used to create the Cryst-PPy, Ni-PPy and Cu-PPy hybrid materials. Using pure PPy, Ni-PPY and Cu-PPY electrodes, the electrochemical oxidation of phenol in an alkaline solution was investigated, wherein the obtained results show that, in order to increase the yield of phenol degradation at the alkaline solution, the type of the anode materials directly affecting the pace of the phenol electrochemical oxidation reaction needs appropriate alterations. The Cu-PPy electrode was reported to exhibit strong electrochemical oxidation ability for phenol degradation [32]. Table 1 elaborates on the salient features of the advanced nanomaterials used in phenolic wastewater degradation. An overview of the classification of nanomaterials along with their synthesis methods is portrayed in Fig. 1.

Table 1 Salient features of advanced nanomaterials derived from carbon, metal- and polymer-based substances

Characteristics	Carbon-based nanoparticles	Metal-based nanoparticles	Polymer-based nanoparticles
Electrical Conductivity	High electron mobility	High electron mobility	Good conductors of electricity—integrated polymer nanoparticles
Conductive properties	Large surface area, highly porous, better catalysing ability, stability, more functional groups and recoverability	Antimicrobial, magnetic, electronic and catalytic activity, highly active heterogeneous catalysts, good dispersion- metal film	Tensile strength, higher elastic modulus and high compression, adsorb a wide variety of organic compounds, high surface area, wide pore structure range, regenerated with no loss in their adsorption capacities
Mode of Treatment	Adsorption/ Advanced oxidation- photocatalytic degradation/ filtration	Advanced oxidation- photocatalytic degradation	Higher adsorption capacity-clay polymers/filtration
Economy	Cost efficient- biochar costlier- graphene based NPs	Non-toxic, stable, low-cost and abundant	High cost of filter repair and blocking- membrane film cheap- clay polymers

**Fig. 1** Fabrication methods of advanced nanomaterials of carbon, metal and polymeric origin for treatment of phenolic effluents

3 Methods of Treatment

The most common treatment methods of organic waste waters are adsorption, advanced oxidation followed by filtration. These physical, chemical and physio-chemical methods have been serving the environmental engineering treatment requirement successfully with a broad spectrum of remediating agents of distinct origin. The following section details the utility of nanomaterials for these three treatment methods.

3.1 Adsorption

Adsorption is a classical approach with a superior ability to abate varieties of pollutants in a cost-effective manner. The versatility of this method in phenol removal is attributed to the possibility of handling sorbate concentrations from trace to a pre-determined level. The possibility of producing adsorbents from green materials with versatile and flexible properties, regeneration of used adsorbents by simple physical and chemical methods for recycling have made this method a facile, eco-friendly and cost-effective one. One of the best adsorbents for wastewater treatment is CNMs, particularly carbon nanotube and graphene-based materials. Due to their exceptional chemical, mechanical and thermal stabilities and high surface-to-volume ratio, CNMs have enormous potential as new-generation adsorbents. However, pristine CNMs are poorly soluble in most of the solvents and hence their use in practical applications is still limited. Therefore, it is mandatory to modify the surface of CNMs before using them for wastewater treatment, which can still increase their solubility, chemical stability, fouling resistance and effectiveness [16]. The use of functionalised CNMs as highly promising adsorbents for treating organic and inorganic wastewater contaminants has been documented in numerous research. This section highlights and summarises the adsorptive treatment of phenol pollutants from wastewater utilising several types of functionalised CNMs [16].

The graphene-based nanomaterials exhibit good adsorption–desorption behaviour due to the high specific surface area and their ability to interact with the oxygen functional groups of phenolic compounds including bisphenol A. They were additionally reported to handle dyes like methylene blue and acid orange 7. Adsorption tests carried out in a batch setup by mechanochemically produced graphite oxide had strong adsorption capabilities for methylene blue, acid orange 7, bisphenol A and phenol, with maximal absorption of 288, 232, 110, and 68 mg g⁻¹ respectively [17]. CNT incorporated in a solid porous support of polydimethylsiloxane exhibit a strong removal ability of the phenolic chemicals from aqueous solutions. The oxidation and supporting approaches facilitate safer disposal and avoid expensive post-treatment processes. The adsorption investigations showed that the materials with various affinities for various phenolic compounds can effectively remove phenolic compounds from water. The results showed that the adsorption process was governed

by a two-step intraparticle diffusion model, in addition to Langmuir and Freundlich isotherms [14]. A hybrid adsorbent created by oxidising carbon nanotube and grafting polyethylene glycol is yet another promising remediating agent that was reported to yield 100% adsorption efficiency in 30 min under batch conditions for treating phenol contamination. Freundlich model is reported to exhibit a superior fit to the experimental results [15]. Graphene oxide was applied to a carbonaceous industrial waste with subsequent thermal activation at 800 °C and the graphene oxide coated biochar also enabled appreciable results in phenolic waste separation. The Langmuir isotherm fit indicated that the phenol separation was a monolayer surface adsorption, pseudo-second-order kinetics followed the phenol separation process. Thermodynamic observation reveals the endothermicity and spontaneity of the adsorption of phenols by graphene oxide and graphene oxide coated biochars [12].

A novel magnetic adsorbent made from activated carbon incorporated with magnetic cobalt nanoparticles is an example of carbon and metal-based nanocomposite that facilitates enhanced removal of phenol from industrial wastewater [13]. A similar adsorbent, magnetic iron oxide/carbon nanocomposites prepared by an one-step solvothermal method as nanopowders are highly effective in the elimination of phenol and methyl orange from aqueous solutions. The carbon content in the magnetic nanopowder largely influences the performance of this novel adsorbent with a discernible improvement in the removal efficiency for both the organic pollutants. The magnetic separation and tailored adsorption potential of this material offers appreciable performance in both single and binary solute systems, enabling multicomponent removal with higher regeneration ability of the adsorbent [8].

The potential of aqueous graphene oxide suspension from flake graphite synthesised through a facile oxidised chemical exfoliation method for removing phenols. This approach removed p-nitrophenol from aqueous solutions following Freundlich adsorption isotherm and pseudo second order model. The aqueous graphene oxide suspension has tremendous adsorption capacity, removal efficiency thus making it a promising candidate for adsorbing and removing organic contaminants from wastewater [34].

3.2 Advanced Oxidation

Advanced oxidation processes (AOPs) using nanomaterials are considered one of the promising techniques for pollutant removal than conventional chemical and biological treatments due to the synergistic effect of high surface area, higher stability, reusability, cost effectiveness, low toxicity and higher degradation capacity. In general, advanced oxidation process of phenolic compounds involves any of the three pathways, namely, hydrogen abstraction, electron transfer and radical addition. The underlying principle of AOPs are the generation of hydroxyl radicals, an authoritative transitory species using chemical or radiative modes facilitated by catalysts. Other active species reported are hydroperoxyl radical, sulphate radical, superoxide ion radical and the conjugate acid form of it. Several nanomaterials employed in

the removal of phenolic compounds in wastewater are TiO_2 , Mxene, CNT, graphitic carbon nitride ($\text{g-C}_3\text{N}_4$), graphene oxide (rGO) and biochar [21].

Pollutants like phenol and its derivatives emerging from industrial wastewater can be degraded effectively by the photocatalytic degradation process. The decomposition of phenol to CO_2 is reported to accomplish with the formation of nearly twenty intermediates including catechol, benzoquinone and hydroquinone at significant levels. Photocatalytic degradation enabled advanced oxidation process are the prominent technology for the degradation of phenolic pollutants from wastewater. Zirconia nanoparticles prepared by electrochemical synthesis termed electrocuted zirconia nanoparticles loaded with an aqueous solution containing phenol at optimal conditions ensured complete elimination of phenol in 1 h almost by photocatalytic degradation. The stability and activity of the catalyst were slightly decreased after repeated usage with no leaching effect and made itself one of the most promising photocatalysts for the removal of phenol as well as other pollutants [22]. Heminitite combined with graphene oxide (FeTiO_3/GO) catalyst prepared through an ultrasound-assisted technique exhibited high structural morphology and enhanced catalytic properties with low cost, high physical and chemical stability. Complete degradation was achieved within 150 min by photocatalytic degradation and the catalyst showed only a slight decrease in recyclability after repeated procedures which made it a highly stable photocatalyst [26].

Colored titania nanoparticles synthesised by a simple chemical precipitation method with the addition of glycerol solution yielded impressive results. Glycerol is an environment friendly, biodegradable, highly polar compound with a high boiling point and plays a major role in increasing the extent of reaction and specific surface area. Ti^{3+} ions induce the bandgap which enhances the photocatalytic performance for the removal of color and phenolic compounds. This is ascribed to a very high photocatalytic degradation efficiency of phenolic compounds under optimum conditions [24].

Fabrication of zinc oxide combined with Prussian blue ($\text{ZnO}@\text{FeHCF}$) by a green synthesis method using *A. indica* leaf extract is reported to be an effective remediating agent. The prepared nanocomposite is cheap and compatible with high recyclability and high photocatalytic efficiency. The prepared nanocomposite was used for the degradation of 3-aminophenol (3-AP) and 2,4-dinitrophenol (2,4-DNP) at optimum conditions. 3-AP showed a maximum removal efficiency followed by phenol and 2,4-DNP, which is because of the variation in basicity. The high stability of the $\text{ZnO}@\text{FeHCF}$ nanocomposite was observed after several repetitive usages through regeneration. The interaction of H_2O with its charge carriers produces OH. Radicals, which are responsible for phenol degradation under sunlight. Individual ZnO and FeHCF showed a minimum performance than the combined nanocomposite and it reduced the half-life period value significantly [35].

Degradation of phenol was accomplished using four different metal oxide nanomaterials namely TiO_2 , aluminium oxide (Al_2O_3), zinc oxide (ZnO) and copper oxide (CuO) by adsorption and photodegradation. In basic conditions, the adsorption capacity was superior to than in acidic conditions. Degradation efficiencies of 89% by TiO_2 , 70% by Al_2O_3 , 57% by ZnO, 61% by CuO were attained. TiO_2 produced

many intermediates compared to the other three metal oxides and proved to be the most effective nanocomposite among all four. Significant intermediates produced are resorcinol and hydroquinone which can further be converted to acetic acid [36].

Titanium oxide nanoparticles (TNPs) are a popular choice for photocatalysts due to their non-toxic nature, low cost, high activity and availability in various forms and sizes. The effectiveness of TNPs can be improved by increasing hydroxyl radicals and reducing the recombination of photogenerated electron–hole pairs. Special focus is given by the scientific community to explore the use of green-synthesised nanocomposites for the photocatalytic degradation of phenol in wastewater. Green electro-synthesised TNPs were used in combination with hibiscus leaf extract as an electrolyte to achieve maximum possible degradation under optimal conditions which revealed prospective outcomes [24]. Another study examined the photocatalytic degradation of phenol using TiO₂ nanorods aligned with silver (Ag) nanoparticles coated with magnesium oxide using atomic layer deposition. The presence of Ag nanoparticles facilitated light absorption and transfer of photo-induced electron–hole pairs, resulting in enhanced photocatalytic activity. The study also discusses the use of copper, chromium and vanadium-impregnated TiO₂ for the photocatalytic degradation of phenol under UV–vis irradiation, which was found to be energy efficient and chemically and mechanically stable. Cu-impregnated photocatalyst has the fastest degradation rate compared to the other two catalysts [37–39].

3.3 *Filtration*

Filtration-aided separation of phenolic contaminants use ultrafiltration and nanofiltration membranes and their potentials are influenced by the membrane morphology, molecular weight cut off and the operating conditions like feed rate, temperature and pressure. Nanomembranes are fabricated from organic polymers and silica nanoparticles usually with 100 nm thickness. The layer-by-layer method of nanofiller fabrication aids in prompt control of the plane composition of the membrane material and the integration of several components onto them. These are essential to tuning their optical, electronic and mechanical properties [40].

A nano-MnOx-loaded porous titanium membrane was used as an anode in electrocatalytic reactors for the treatment of synthetic phenolic wastewater. The performances of fixed-bed electrocatalytic reactors (FBERs) and electrocatalytic membrane reactors (ECMRs) were investigated by varying the operating voltage, residence time and reaction stage. The FBER under certain conditions showed the best electrochemical degradation performance. The phenol and COD removal rates of the FBER were higher in the eight-stage setup than in the one-stage setup. The reaction rate constant of the FBER enhanced with an increase in the number of stages. The ECMRs and FBERs exhibited high electrocatalytic reaction efficiency due to the synergistic effect of electrocatalytic oxidation and enhanced mass diffusion [41].

A novel strategy used to develop silica nanoparticles modified with choline chloride-ethylene glycol DES (or ethaline) as additives for PI UF membranes

showed promising results. The successful immobilisation of the DES on the surface of nanosilica particles was confirmed through spectroscopy and electron microscopy characterisation measurements. The original microstructure and spherical morphology of the nanofillers were preserved even after their incorporation inside the PI matrix. Silica-based nanofillers had an impact on the surface morphology, porosity characteristics, wetting and permeation properties of the UF membranes. The pH and concentration-dependent studies showed that ethaline contributed to the composite membranes' unparalleled efficiency for phenol elimination through cooperative hydrogen bonding and Lewis acid–base interactions over a wide pH range [6].

Superhydrophilic and underwater superoleophobic membranes have gained significant interest due to their unique properties in treating oily wastewater with phenolic content. The hydrophilic hierarchical structure using amino-functionalised polyhedral oligosiloxane/proanthocyanidins (POSS-NH₂/PC) surface coating synthesised with a combination of iron and PC networks (FPN) and combined with polyvinylidene fluoride microfiltration membrane exhibits robust superhydrophilicity and underwater superoleophilicity, making it highly efficient for separating oil-in-water emulsion in extreme environments with huge oil rejections. Moreover, the membrane has demonstrated good antifouling performance even after three cycles of oil/water separation. The incorporation of FPN further enhances the stability of the microfiltration membrane [42].

Graphitic carbon nitride (g-C₃N₄) based hybrid membranes that combine membrane filtration and photocatalytic technology have emerged as a promising solution in phenol-contaminated wastewater. Polyethersulfone (PES) membranes with hydrophilic surface modifying macromolecules (LSMM) and oxygen-doped g-C₃N₄ can provide more available active sites to the light source, improving the photocatalytic performance of the hybrid membrane. It was shown that LSMM enhances the light absorption capacity, which in turn improves the photodegradation through a g-C₃N₄ hybrid membrane instead of physical sieving when exposed to UV irradiation [18].

Electro-conductive membranes such as titanium oxide (Ti₄O₇) is a prominent example for one-pot membrane-electrochemical advanced oxidation (EAO) coupling for wastewater treatment. The use of filtration mode in the membrane-EAO system provides increased mass transfer rates compared to the traditional method and hence enhances the degradation performance of phenol, oily wastewater and humic acid. The mechanism of the membrane-EAO coupling process involves the formation of reactive oxygen species, such as hydroxyl radicals, on the surface of the conductive membrane electrode through electrochemical reactions, which then react with organic pollutants to promote degradation [43, 44]. Table 2 presents the performance level of the advanced nanomaterials by adsorption, advanced oxidation and filtration for the elimination of phenolic contaminations.

Table 2 Examples for carbon, metal and polymer-based advanced nanomaterials used in adsorptive, photocatalytic and filtration methods for the treatment of phenolic wastewater

Mode of action	Types of nanomaterials	Removal/uptake of phenol	References
Adsorption	Mechanochemically prepared graphite oxide- Me-GO	110 mg/g—Bisphenol 68 mg/g	[17]
	Carbon nanotubes	96%—4-nitrophenol 98%	[14]
	Polyethylene glycol- carbon nanotubes	≈100%	[15]
	Magnetic iron oxide/carbon nanocomposites	42.34 mg/g	[8]
	Graphene oxide/ Al ₂ O ₃ composite membrane	99.9%	[16]
	Graphene oxide -coated biochar	23.47 mg/g	[12]
	Magnetic cobalt nanoparticles-coated activated carbon (MCAC)	91.7%	[13]
	Nano- montmorillonite	99.6%—trinitrophenol	[29]
	Humic acid-modified bentonite	95.2 mg/g 2,4-dichlorophenol	[28]
Advanced oxidation	Cerium oxide nanoparticles	92.24%	[19]
	CuO ₂ -based nanosheets	96.4%	[21]
	Au/Pd alloyed nanoparticle	85%	[25]
	Zinc oxide doped Prussian blue nanocomposite	97%	[35]
	Ag/TiO ₂ nanocomposite	95%	[38]
	Copper ferrite nanosphere composites		[20]
	Glycerol-mediated titania nanoparticles (TiO ₂)	48%	[24]
	CuO metal oxides	61%	[36]
	Commercially prepared TiO ₂	99.4%	[37]
Filtration	Ultrafiltration (UF)- nanofiltration (NF), and reverse osmosis (RO)	94.9%	[40]
	TiO ₂ /carbon electrocatalytic membrane	99.4%	[41]
	Potassium-doped graphitic carbon nitride (g-C ₃ N ₄)	96%	[18]

4 Mechanism

Phenolic compounds consisting of carboxyl groups are considered as aromatic acids with widespread applications. The oxygen and hydrogen bond in the phenolic ring display electronegativity due to electron shift towards oxygen, the hydrogen atom can be separated as a proton making it a suitable base [45]. For the adsorption of phenolic compounds, intermolecular forces and hydrogen bonding between the phenol particles and the adsorbent play an important role. Numerous studies have shown that electrostatic attraction, hydrogen bonds and stacking interactions play a major role in the adsorption mechanisms of functionalised adsorbents for binding organic pollutants. Most of the nanomaterials exhibit intraparticle diffusion kinetics confirming the diffusion of phenolic compounds into the adsorbent layers. The adsorption is attributed to both monolayer and multilayer phenomena fitting the Langmuir and Freundlich isotherm models. Van der Waals force, π - π interactions, coordinate covalent bond formation, etc. are several other factors that are found to work with enhanced potentials in the nanomaterials of carbon and metal bases when compared to the conventional non-nanomaterials [46]. Pseudo-second-order kinetics is found to represent the nano-adsorbent's sorption kinetics predominantly. The performance of the regenerated adsorbents depends on the structural stability, regeneration of active sites and functional groups to offer all those mechanistic and chemical properties in the elimination of phenolic contaminants.

Of the various chemical degradation methods of phenol, advanced oxidation techniques have unique features that facilitate effective degradation. Various methods of oxidation and oxidising species can be utilised to break the complex structure of phenol. The oxidation includes the formation of different active radicals which is governed by the redox reaction of oxidising species [47, 48]. Commonly in photocatalytic degradation of phenol, there will be generation of hydroxyl, oxygen and superoxide radicals in which the most active species will lead to better cleavage of the phenol ring. To identify the most active species several scavengers are used, which detect the formation of active species for better degradation of the organic pollutant. The greater the redox reaction rate, the more will be the generation of electron-hole pairs. Increased electron-hole pairs will lead to generation of distinct active radicals. In a typical photocatalytic removal of phenols, two phases, namely, decomposition and mineralisation are reported widely. The decomposition phase involves the formation of hydroxylated compounds like benzoquinone and catechol including complex compounds comprising two benzene rings. The second phase incurs mineralisation of the hydroxylated compounds into short-chain organics like oxalic acid, formic acid, glycerol, etc. by ultraviolet energy, hydrogen and hydroxyl radicals. This, in turn, facilitates the cleavage of the simpler hydrocarbon chains to yield carbon dioxide and water [49].

The nanofiltration-based membrane technology, though reported in relatively lesser levels compared to adsorption and AOPs, has also proved to be an efficient method for the treatment of phenol-contaminated wastewater. The removal of phenol is reported to be achieved effectively by various types of carbon-based membranes

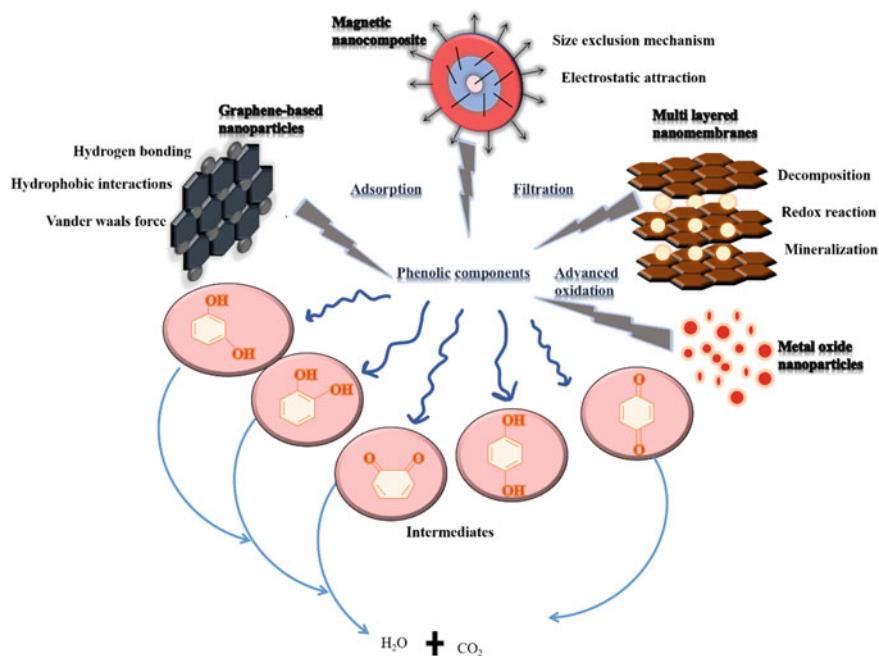


Fig. 2 Mechanism and pathways of degradation/removal of phenolic compounds by adsorption, advanced oxidation and filtration by advanced nanomaterials

and polymer-based nanomembranes [50]. The rejection of phenol is mainly due to the size exclusion mechanism in which the pollutant is allowed to capture in the pores. The mesh-like structure allows the pollutant to settle in which the finer mesh structure allows better capture of phenol. The filtration mechanism also depends on the contact of filter media with contaminated water. A sufficient flow velocity of the solution will establish the physical forces of pollutants with a filter mesh. Properties like cohesion and electrostatic attraction can be attributed if better contact is done, which ultimately provides better interaction of phenol particles with filter mesh. However, the biggest challenge usually faced by this methodology is the membrane fouling at higher pollutant concentrations. The mechanisms and degradation pathways of phenolic compounds degradation by adsorption, advanced oxidation and filtration by advanced nanomaterials are elucidated in Fig. 2.

5 Conclusion

The ubiquitous presence of phenolic compounds in water bodies poses a serious threat to aquatic species. Industrialisation has paved a way for the emanation of organic pollutants into clean water bodies, among which phenols, belonging to a highly

toxic class of pollutants are discarded in larger quantities. They also enter water bodies by natural phenomenon through decomposition of dead animal and plant matters. The phenolic compounds reported from petroleum refineries (biphenyls, naphthalene, benzene, toluene), petrochemicals (butadiene, heptane's, resorcinol), coal refineries (catechol, cresols, hydroquinone), tannery (catechin, nitrophenol, chlorophenol, tannin) and pharmaceutical industries (phenylacetic acid, ether, benzyl alcohol) are known to be poisonous and have negative effects on both people and animals that are severe and long-lasting. The abatement of phenol contamination is accomplished by several conventional wastewater treatment plants, but they demand high cost and energy requirements for smoother performance. Currently, different physio-chemical and chemical methods are used in which nanotechnology proves to be an efficient feedstock for the removal of such pollutants. This chapter portrays insight into various types of tailored nanomaterials derived from green compounds, chemicals, metal oxides for application as adsorbents, photocatalysts and membrane technology for efficient separation of phenolic substance from water. Carbon and metal oxide based nano sorbents show high potential for the capture of phenolic compounds. The nanoparticles drastically improve the pore size distribution, surface area and active sites for the sorption of phenol. However, the smaller sized sorbent is rather difficult to recover and reuse. To counteract this issue, magnetic nano sorbent is adopted in which different metal ions are coupled with the nano sorbent for easy detection and recovery of the sorbent. Chemical degradation is another strategy to remove phenol compounds from water bodies. Generation of oxidising species in a typical redox reaction can lead to the degradation of such pollutants. Such types of redox reactions are instances of advanced oxidation processes in which the degradation of pollutants is achieved by generating reactive species. The complex phenolic compounds get decomposed and mineralised by several mechanisms into simpler minerals that are less toxic or non-toxic. As far as the nano-filters are concerned, the structure and material of the nanomaterial influence the performance of the membrane. Carbon based, polymer or ceramic membrane display excellent filtration property in which the small pore size of these mesh can separate phenol compounds with minimal liquid flow velocity. Prolonged use of such membrane can cause membrane fouling as the separation is based on the size exclusion mechanism. However, these techniques are not commercially used as they are very energy-intensive and sensitive processes.

References

1. Sahoo TR, Prelot B (2020). Adsorption processes for the removal of contaminants from wastewater: the perspective role of nanomaterials and nanotechnology. In *Nanomaterials for the detection and removal of wastewater pollutants*. Elsevier, pp. 161–222. <https://doi.org/10.1016/B978-0-12-818489-9.00007-4>
2. Akash S, Sivaprakash B, Rajamohan N, Govarathanan M, Elakiya BT (2022) Remediation of pharmaceutical pollutants using graphene-based materials—a review on operating conditions, mechanism and toxicology. *Chemosphere* 135520. <https://doi.org/10.1016/j.chemosphere.2022.135520>
3. Ahmaruzzaman M (2021) Biochar based nanocomposites for photocatalytic degradation of emerging organic pollutants from water and wastewater. *Mater Res Bull* 140:111262. <https://doi.org/10.1016/j.materresbull.2021.111262>
4. Sivaprakash B, Rajamohan N, Reshmi A, Annadurai A, Varjani S (2022) Applications of submerged and staged membrane systems for pollutant removal from effluents and mechanism studies—a review. *Chemosphere* 134747. <https://doi.org/10.1016/j.chemosphere.2022.134747>
5. Akash S, Sivaprakash B, Rajamohan N, Pandiyan CM, Vo DVN (2022) Pesticide pollutants in the environment—A critical review on remediation techniques, mechanism and toxicological impact. *Chemosphere* 134754. <https://doi.org/10.1016/j.chemosphere.2022.134754>
6. Ali JK, Chabib CM, Abi Jaoude M, Alhseinat E, Teotia S, Patole S, Qattan I (2021) Enhanced removal of aqueous phenol with polyimide ultrafiltration membranes embedded with deep eutectic solvent-coated nanosilica. *Chem Eng J* 408:128017. <https://doi.org/10.1016/j.ccej.2020.128017>
7. Khan N, Anwer AH, Ahmad A, Sabir S, Sevda S, Khan MZ (2019) Investigation of CNT/PPy-modified carbon paper electrodes under anaerobic and aerobic conditions for phenol bioremediation in microbial fuel cells. *ACS Omega* 5(1):471–480. <https://doi.org/10.1021/acsomega.9b02981>
8. Istratie R, Stoia M, Păcurariu C, Locovei C (2019) Single and simultaneous adsorption of methyl orange and phenol onto magnetic iron oxide/carbon nanocomposites. *Arab J Chem* 12(8):3704–3722. <https://doi.org/10.1016/j.arabjc.2015.12.012>
9. Berslin D, Reshmi A, Sivaprakash B, Rajamohan N, Kumar PS (2022) Remediation of emerging metal pollutants using environment friendly biochar—Review on applications and mechanism. *Chemosphere* 290:133384. <https://doi.org/10.1016/j.chemosphere.2021.133384>
10. Monisha RS, Mani RL, Sivaprakash B, Rajamohan N, Vo DVN (2022) Green remediation of pharmaceutical wastes using biochar: a review. *Environ Chem Lett* 1–24. <https://doi.org/10.1007/s10311-021-01348-y>
11. Ajala OJ, Tijani JO, Bankole MT, Abdulkareem AS (2022) A critical review on graphene oxide nanostructured material: Properties, Synthesis, characterization and application in water and wastewater treatment. *Environ Nanotechnol Monitor Manag* 18:100673. <https://doi.org/10.1016/j.enmm.2022.100673>
12. Manna S, Prakash S, Das P (2019) Synthesis of graphene oxide nano-materials coated biochar using carbonaceous industrial waste for phenol separation from water. *Colloids Surf, A* 581:123818. <https://doi.org/10.1016/j.colsurfa.2019.123818>
13. Mohammadi SZ, Darijani Z, Karimi MA (2020) Fast and efficient removal of phenol by magnetic activated carbon-cobalt nanoparticles. *J Alloy Compd* 832:154942. <https://doi.org/10.1016/j.jallcom.2020.154942>
14. Turco A, Monteduro AG, Mazzotta E, Maruccio G, Malitesta C (2018) An innovative porous nanocomposite material for the removal of phenolic compounds from aqueous solutions. *Nanomaterials* 8(5):334. <https://doi.org/10.3390/nano8050334>
15. Bin-Dahman OA, Saleh TA (2020) Synthesis of carbon nanotubes grafted with PEG and its efficiency for the removal of phenol from industrial wastewater. *Environ Nanotechnol, Monitor Manag* 13:100286. <https://doi.org/10.1016/j.enmm.2020.100286>

16. Jun LY, Mubarak NM, Yee MJ, Yon LS, Bing CH, Khalid M, Abdullah EC (2018) An overview of functionalised carbon nanomaterial for organic pollutant removal. *J Ind Eng Chem* 67:175–186. <https://doi.org/10.1016/j.jiec.2018.06.028>
17. Mahmoud AED (2020) Graphene-based nanomaterials for the removal of organic pollutants: insights into linear versus nonlinear mathematical models. *J Environ Manage* 270:110911
18. Li X, Huang G, Chen X, Huang J, Li M, Yin J, Li Y (2021) A review on graphitic carbon nitride (g-C₃N₄) based hybrid membranes for water and wastewater treatment. *Sci Total Environ* 792:148462. <https://doi.org/10.1016/j.scitotenv.2021.148462>
19. Ahmad T, Iqbal J, Bustam MA, Zulfiqar M, Muhammad N, Al Hajeri BM, Ullah S (2020) Phytosynthesis of cerium oxide nanoparticles and investigation of their photocatalytic potential for degradation of phenol under visible light. *J Mol Struct* 1217:128292. <https://doi.org/10.1016/j.molstruc.2020.128292>
20. Moreno-Castilla C, López-Ramón MV, Fontecha-Cámara MÁ, Álvarez MA, Mateus L (2019) Removal of phenolic compounds from water using copper ferrite nanosphere composites as fenton catalysts. *Nanomaterials* 9(6):901. <https://doi.org/10.3390/nano9060901>
21. Guo S, Jiang Y, Li L, Huang X, Zhuang Z, Yu Y (2018) Thin CuO x-based nanosheets for efficient phenol removal benefitting from structural memory and ion exchange of layered double oxides. *J Mater Chem A* 6(9):4167–4178. <https://doi.org/10.1039/C7TA10877J>
22. Hanafi MF, Sapawe N (2019) Electrogenenerated zirconia (EGZrO₂) nanoparticles as recyclable catalyst for effective photocatalytic degradation of phenol. *Mater Today: Proc* 19:1537–1540. <https://doi.org/10.1016/j.matpr.2019.11.180>
23. Zamri MSFA, Sapawe N (2019) Kinetic study on photocatalytic degradation of phenol using green electrosynthesized TiO₂ nanoparticles. *Mater Today: Proc* 19:1261–1266. <https://doi.org/10.1016/j.matpr.2019.11.131>
24. Nawaz R, Kait CF, Chia HY, Isa MH, Huei LW (2019) Glycerol-mediated facile synthesis of colored titania nanoparticles for visible light photodegradation of phenolic compounds. *Nanomaterials* 9(11):1586. <https://doi.org/10.3390/nano9111586>
25. Patnaik S, Sahoo DP, Parida KM (2020) Bimetallic co-effect of Au-Pd alloyed nanoparticles on mesoporous silica modified g-C₃N₄ for single and simultaneous photocatalytic oxidation of phenol and reduction of hexavalent chromium. *J Colloid Interface Sci* 560:519–535. <https://doi.org/10.1016/j.jcis.2019.09.041>
26. Moradi M, Vasseghian Y, Khataee A, Harati M, Arfaeina H (2021) Ultrasound-assisted synthesis of FeTiO₃/GO nanocomposite for photocatalytic degradation of phenol under visible light irradiation. *Sep Purif Technol* 261:118274. <https://doi.org/10.1016/j.seppur.2020.118274>
27. Khodakarami M, Bagheri M (2021) Recent advances in synthesis and application of polymer nanocomposites for water and wastewater treatment. *J Clean Prod* 296:126404. <https://doi.org/10.1016/j.jclepro.2021.126404>
28. Mukhopadhyay R, Bhaduri D, Sarkar B, Rusmin R, Hou D, Khanam R, Ok YS (2020) Clay-polymer nanocomposites: Progress and challenges for use in sustainable water treatment. *J Hazard Mater* 383:121125. <https://doi.org/10.1016/j.jhazmat.2019.121125>
29. Amari A, Mohammed Alzahrani F, Mohammedsalem Katubi K, Salem Alsaiani N, Tahoon MA, Ben Rebah F (2021) Clay-polymer nanocomposites: preparations and utilization for pollutants removal. *Materials* 14(6):1365. <https://doi.org/10.3390/ma14061365>
30. Cantarella M, Sanz R, Buccheri MA, Ruffino F, Rappazzo G, Scalse S, Privitera V (2016) Immobilization of nanomaterials in PMMA composites for photocatalytic removal of dyes, phenols and bacteria from water. *J Photochem Photobiol, A* 321:1–11. <https://doi.org/10.1016/j.jphotochem.2016.01.020>
31. Ghafari M, Cui Y, Alali A, Atkinson JD (2019) Phenol adsorption and desorption with physically and chemically tailored porous polymers: Mechanistic variability associated with hyper-cross-linking and amination. *J Hazard Mater* 361:162–168. <https://doi.org/10.1016/j.jhazmat.2018.08.068>
32. Seid L, Lakhdari D, Berkani M, Belgherbi O, Chouder D, Vasseghian Y, Lakhdari N (2022) High-efficiency electrochemical degradation of phenol in aqueous solutions using Ni-PPy and Cu-PPy composite materials. *J Hazard Mater* 423:126986. <https://doi.org/10.1016/j.jhazmat.2021.126986>

33. Wang Y, Yang C, Mai YW, Zhang Y (2016) Effect of non-covalent functionalisation on thermal and mechanical properties of graphene-polymer nanocomposites. *Carbon* 102:311–318. <https://doi.org/10.1016/j.carbon.2016.02.069>
34. Sandhya PK, Sreekala MS, Padmanabhan M, Jesitha K, Thomas S (2019) Effect of starch reduced graphene oxide on thermal and mechanical properties of phenol formaldehyde resin nanocomposites. *Compos B Eng* 167:83–92. <https://doi.org/10.1016/j.compositesb.2018.12.009>
35. Rani M, Shanker U (2020) Sunlight assisted degradation of toxic phenols by zinc oxide doped prussian blue nanocomposite. *J Environ Chem Eng* 8(4):104040. <https://doi.org/10.1016/j.jece.2020.104040>
36. Zhan H, Jiang Y (2016) Metal oxide nanomaterials for the photodegradation of phenol. *Anal Lett* 49(6):855–866. <https://doi.org/10.1080/00032719.2015.1079211>
37. Zulfiqar M, Samsudin MFR, Sufian S (2019) Modelling and optimization of photocatalytic degradation of phenol via TiO₂ nanoparticles: An insight into response surface methodology and artificial neural network. *J Photochem Photobiol, A* 384:112039. <https://doi.org/10.1016/j.jphotochem.2019.112039>
38. Scott T, Zhao H, Deng W, Feng X, Li Y (2019) Photocatalytic degradation of phenol in water under simulated sunlight by an ultrathin MgO coated Ag/TiO₂ nanocomposite. *Chemosphere* 216:1–8. <https://doi.org/10.1016/j.chemosphere.2018.10.083>
39. Belekbir S, El Azzouzi M, El Hamidi A, Rodríguez-Lorenzo L, Santaballa JA, Canle M (2020) Improved photocatalyzed degradation of phenol, as a model pollutant, over metal-impregnated nanosized TiO₂. *Nanomaterials* 10(5):996. <https://doi.org/10.3390/nano10050996>
40. Obotey Ezugbe E, Rathilal S (2020) Membrane technologies in wastewater treatment: a review. *Membranes* 10(5):89. <https://doi.org/10.3390/membranes10050089>
41. Hui H, Wang H, Mo Y, Yin Z, Li J (2019) Optimal design and evaluation of electrocatalytic reactors with nano-MnOx/Ti membrane electrode for wastewater treatment. *Chem Eng J* 376:120190. <https://doi.org/10.1016/j.cej.2018.10.127>
42. Zhao Y, Zhang Y, Li F, Bai Y, Pan Y, Ma J, Shao L (2021) Ultra-robust superwetting hierarchical membranes constructed by coordination complex networks for oily water treatment. *J Membr Sci* 627:119234. <https://doi.org/10.1016/j.memsci.2021.119234>
43. Pan Z, Song C, Li L, Wang H, Pan Y, Wang C, Feng X (2019) Membrane technology coupled with electrochemical advanced oxidation processes for organic wastewater treatment: Recent advances and future prospects. *Chem Eng J* 376:120909. <https://doi.org/10.1016/j.cej.2019.01.188>
44. Yang Z, Zhang Y, Wang X, Tian Z, Yang W, Graham NJ (2020) Efficient adsorption of four phenolic compounds using a robust nanocomposite fabricated by confining 2D porous organic polymers in 3D anion exchangers. *Chem Eng J* 396:125296. <https://doi.org/10.1016/j.cej.2020.125296>
45. Said KAM, Ismail AF, Karim ZA, Abdullah MS, Hafeez A (2021) A review of technologies for the phenolic compounds recovery and phenol removal from wastewater. *Process Saf Environ Prot* 151:257–289. <https://doi.org/10.1016/j.psep.2021.05.015>
46. Dehmani Y, Dridi D, Lamhasni T, Abouarnadasse S, Chtourou R, Lima EC (2022) Review of phenol adsorption on transition metal oxides and other adsorbents. *J Water Process Eng* 49:102965. <https://doi.org/10.1016/j.jwpe.2022.102965>
47. Motamedi M, Yerushalmi L, Haghghat F, Chen Z (2022) Recent developments in photocatalysis of industrial effluents: A review and example of phenolic compounds degradation. *Chemosphere* 133688. <https://doi.org/10.1016/j.chemosphere.2022.133688>
48. Yadav G, Ahmaruzzaman M (2022) New generation advanced nanomaterials for photocatalytic abatement of phenolic compounds. *Chemosphere* 135297. <https://doi.org/10.1016/j.chemosphere.2022.135297>
49. Dang TTT, Le STT, Channei D, Khanitchaidecha W, Nakaruk A (2016) Photodegradation mechanisms of phenol in the photocatalytic process. *Res Chem Intermed* 42:5961–5974. <https://doi.org/10.1007/s1164-015-2417-3>

50. Rameetse MS, Aberefa O, Daramola MO (2020) Effect of loading and functionalization of carbon nanotube on the performance of blended polysulfone/polyethersulfone membrane during treatment of wastewater containing phenol and benzene. *Membranes* 10(3):54. <https://doi.org/10.3390/membranes10030054>

Chapter 8

Nanoparticles and Nanocomposites for Heavy Metals Removal



**Gopalakrishnan Sarojini, P. Kannan, Natarajan Rajamohan,
and Manivasagan Rajasimman**

Abstract Contamination of heavy metals in water is of great concern. Nanomaterials owing to their smaller size and higher surface area exhibit unique physico-chemical characteristics that enable potential application in the removal of heavy metals. Nanoparticles and nanocomposites find a major application in heavy metals due to their tunable properties, facile synthesis and stability. This chapter gives an overview of the application of nanoparticles and nanocomposites in the removal of heavy metals from wastewater. Nanomaterials-assisted techniques in the removal of heavy metals include adsorption, membrane separation and photocatalysis. Nanostructured materials in the form of nanoadsorbents, nanomembranes and nanophotocatalyst provide higher reactivity and show specific affinity to targeted heavy metals. Several nanoparticles exhibit strong antimicrobial properties.

Keywords Nanomaterial · Heavy metal · Adsorption · Membrane · Nanosorbents

1 Introduction

Hygienic water is essential for the survival of lives on earth. Lack of drinking water remains a major issue today. Although three-fourths of the earth's surface is covered by water, resources of freshwater are tremendously deteriorating. Increasing

G. Sarojini (✉)

Department of Food Technology, Dhanalakshmi Srinivasan College of Engineering, Coimbatore, India

e-mail: grsarojini@gmail.com

P. Kannan

Department of Chemistry, V.S.B College of Engineering Technical Campus, Coimbatore, India

N. Rajamohan

Chemical Engineering Section, Faculty of Engineering, Sohar University, Sohar, Oman

M. Rajasimman

Department of Chemical Engineering, Annamalai University, Annamalai Nagar, India

industrial activities, rapid population growth, change in lifestyle and climate change have decreased the accessibility of freshwater resources. Volcanic eruptions, modern farming and mining activities produce hazardous pollutants including organics, pharmaceutical products, pathogens and heavy metals in the aquatic environment. Among all pollutants, the presence of heavy metals remains a prime concern due to their non-degradability, toxic and carcinogenic nature. Heavy metals are defined as metals having a density greater than 4000 kg/m^3 . Chromium (Cr), cadmium (Cd), zinc (Zn), lead (Pb), mercury (Hg), copper (Cu), nickel (Ni) and arsenic (As) are a few examples of soluble forms of heavy metals and are considered to be an emerging pollutant [1]. These heavy metals are essential in most of the industrial and biological activities. Metallurgical, metal plating, electroplating, leather tanning, batteries, fertilizers and machinery manufacturing industries are responsible for heavy metal contamination as they release enormous amount of wastewater containing heavy metals [2]. Many regulatory bodies impose maximum permissible limits for the discharge of heavy metals in wastewater. However, most of the industrial effluent does not meet the standard permissible limits proposed by environmental and human organizations. The heavy metals laden polluted water is discharged into water sources and remains in soil, surface and groundwater. Intake of these heavy metals causes a severe threat to human health. Nevertheless, the presence of heavy metals beyond the acceptance level results in environmental health hazard both to marine and land living creatures [3]. Heavy metals accumulate inside the human body through the food chain and produce major health disorder. These heavy metals are non-persistent and cannot be decomposed or metabolized naturally [4]. The sources, maximum permissible limit given World Health Organization (WHO), and health issues associated with heavy metals are provided in Table 1.

Elimination of heavy metals remains a challenging issue and it is mandatory to reduce or prevent their toxic effects on living bodies [1]. Currently, nanotechnology finds its wide application in all branches of science and technology. The tendency to fabricate and formulate the particles with specific structures and functional groups by means of nanosized elements encouraged nanotechnology as a great resource. Recognizing the scope and utilities of nanotechnology and understanding the importance of water quality, scientists have attempted the usage of nanotechnology in wastewater remediation. In wastewater treatment, nanotechnology is being incorporated along with conventional methods to improve the efficiency of the process. Various researchers have identified several nanomaterials and found their efficacy in the removal of heavy metals. In this chapter, the application of different nanoparticles and nanocomposites and technologies implied for the removal of heavy metals has been discussed.

Table 1 Heavy metals, maximum permissible limit in drinking water, health issues and sources

Heavy metals	Maximum permissible limit	Health issues	Sources	References
Cr (VI)	0.01 mg/L	Haemorrhage, hemolysis, acute renal failure	Electroplating industries	[5]
Cd (II)	0.003 mg/L	Affects kidney, lungs, skeleton system and liver	Battery, alloys, electroplating industries	[6]
Zn (II)	5 mg/L	Causes anaemia, vomiting, nausea, stomach upset and skin irritation	Insecticides, fungicides, pipes, galvanic and paint industries	[7]
Pb (II)	0.01 mg/L	Produces nephritic syndrome, hepatitis, anaemia and lead poisoning affects the nerves, bones and brain	Oil extraction, lead extraction, batteries, ceramic, glass	[8]
Hg (II)	0.001 mg/L	Vomiting, fever, diarrhea, caustic gastroenteritis	Mining operations, electroplating industries	[9]
Cu (II)	0.01 mg/L	Headache hemorrhage, hemolysis,	Household plumbing and battery applications	[10]
Ni (II)	0.07 mg/L	Dermatitis and hair loss	Alloys and nickel plating industries	[7]
As (V)	0.01 mg/L	Nausea, vomiting, painful neuropathy	Paints, agricultural applications, mining and smelting industries	[11]

2 Conventional Methods for Heavy Metal Removal

In the present scenario, there is a vast demand for pure water. It is mandatory to eliminate all heavy metals present in industrial wastewater before their discharge into the aquatic ecosystem. The most common methods employed in the removal of heavy metals are chemical precipitation, ion exchange, solvent extraction, chemical leaching, photoelectrocatalysis, reverse osmosis, membrane technology and adsorption [12]. Several techniques available for the removal of heavy metals for the past decades are provided in Table 2.

Most of the techniques remain ineffective in the treatment of the large volume of solution of less concentration of heavy metals. However, some of the techniques are effective, but face the problem of the generation of secondary waste. Effectiveness, operation cost, long-term sustainability and energy consumption are the major issues associated with all technologies. Very few of them are difficult to implement at an industrial scale. The negative impact of heavy metals on the environment paves

Table 2 Conventional techniques for the removal of heavy metals associated with advantages and disadvantages

Technique	Advantages	Disadvantages	References
Chemical precipitation	Effective and easy to operate for a broad range	Formation of secondary pollutants	[13]
Coagulation-flocculation	Effective in the removal of microorganisms	High cost	[14]
Ion exchange	Effective and applicable to inorganic/organic pollutants	High cost and be applicable for small scale	[15]
Precipitation	Easy applicable	Secondary pollution	[14]
Membrane technology	Applicable to inorganic pollutants	Energy intensive	[16]
Electrochemical treatment	Very effective in the removal of heavy metals	Requires large investment and energy intensive	[17]
Adsorption	Simple and economical	Hazardous by-products	[18]

the way to finding an economical, effective and eco-friendly technology. Recently, nanotechnology has gained much attraction in liquid waste treatment and they are recognized as high-performance technology.

3 Role and Properties of Nanoparticles and Nanocomposites

Nanomaterials are a new class of emerging engineering material. Nanoparticles (NPs) are nanomaterials having a size in the range of 1–100 nm on at least one dimension. Nanoparticles are highly specific in nature and they differ from bulk materials owing to large surface area, higher stability and greater resistance. These features allow them to find vast application in wastewater remediation, particularly in the removal of heavy metals [19]. Nanomaterials exhibit unique and amazing properties. For instance, gold nanoparticles get converted into liquid form at room temperature, silver nanoparticles display excellent antimicrobial activities, platinum nanoparticles acts as a superior catalyst and aluminum nanoparticles turn off into combustible ingredient. Thus, these newly created properties offered by nanoscale materials find their application in heavy metals removal.

Nanocomposite is a composite material in which at least one of the components should dimension in the range of nanometers (10–100 nm). Nanocomposites are formulated by incorporating fine species onto a large solid matrix to conquer the restrictions of nanoparticles [20]. To remove heavy metals from contaminated water, several low cost, high efficiency and reusable nanoparticles and nanocomposites are being developed. Nanoparticles and nanocomposites find a major application in the field of adsorption, photocatalysis, membrane technologies and antibacterial agent.

3.1 Properties of Nanomaterials and Nanocomposites

Several properties listed below enable nanoparticles and nanoparticles to find a major potential in the removal of heavy metals [21]. Properties include:

- Increased surface-to-volume ratio
- Higher reactivity
- Higher adsorption capacity
- Higher dissolution activity
- Reduction in size: As the size of nanoparticles gets reduced, the proportion of atoms present on the surface of the particles increases, thus creating a more reactive surface
- Change in the reactive surface: Increased surface produced due to reduced particle size causes a change in surface free energy which in turn alters the chemical reactivity
- Change in atomic structure: As the size of the particle gets reduced, the defects may be produced on the surface
- Change in electronic structure: The smaller size of the particles produced lies in the lower energy state

3.2 Classification of Nanomaterials

Nanomaterials exist in different forms of structure namely nanotubes, nanorods and nanowires. Nanomaterials are classified into four types based on the nature of composite of the materials. They are as follows:

- (i) Carbon-based nanomaterials
- (ii) Metal-based nanomaterials
- (iii) Dendrimers
- (iv) Composites

3.2.1 Carbon-Based Nanomaterials

Carbon-based nanomaterials generally contain carbon as a main ingredient. These materials usually have the shapes of ellipsoids, hollow spheres and tubes. Elliptical and spherical shaped materials are called fullerenes whereas cylindrical form is referred to as nanotubes [22]. Most of carbon-based nanomaterials find application in electronic devices.

3.2.2 Metal-Based Nanomaterials

Noble metallic nanomaterials, metallic oxide nanomaterials including iron oxide, zinc oxide, titanium oxide and quantum dots come under the category of metal-based

nanomaterials. Quantum dot, a closely assembled semiconductor crystal, encloses billions of atoms and size is in the range of nanoscale. Metal-based nanomaterials are extensively used in cream application.

3.2.3 Dendrimers

Nanosized polymers fall under the category of dendrimers-based nanomaterials. Generally, the surface of these materials has several chain ends. Molecules containing several functional groups could be tailored to these end chains in order to a new nanomaterial. These materials are mostly used in catalysis and drug delivery.

3.2.4 Nanocomposites

Nanocomposite is a combination of nanomaterial with another nanomaterial or with bulky material. Nanoparticles especially nanosized clay, metals are added to a standard matrix in order to enhance the mechanical, thermal, optical and physical properties.

3.3 *Synthesis of Nanoparticles*

The synthesis technique adopted for the preparation of nanoparticles decides the final characteristics of nanoparticles. Top-down and bottom-up are the two methods commonly used for the synthesis of nanoparticles. The synthesis procedure controls the size, shape and structure of nanoparticles. Wet chemical synthesis, solvent combustion technique, hydrothermal technique, sol-gel technique and mechanical milling technique are the most commonly used methods for synthesizing nanoparticles [23]. Among all, wet chemical synthesis, sol-gel technique and hydrothermal technique are highly preferred because the process is easier, highly reproducible and requires less investment. Wet chemical synthesis otherwise known as the liquid phase synthesis technique is simple to operate. Different solutions of quantified morality are mixed under a controllable heat to begin the nanoparticle formation through precipitation [24]. Then the excess amount of solution is drained and precipitates are dried and grinded. This technique is operated usually at low temperatures and therefore saves energy. This technique has control in the stoichiometry of nanoparticles. This technique offers the advantage of control over the final characteristics of synthesized nanomaterial. Sol-gel is another popular and cheaper technique to synthesize nanoparticles. The nanoparticles produced by this technique are smaller in size and size distribution is narrow due to the linear growth of particles across the gel. This technique involves hydrolysis of precursors (metal alkoxides or metal chlorides) with water and alcohol. They are mixed to form a gel. They are then calcined to remove gel and nanoparticles are left behind [25]. Hydrothermal technique involves

the synthesis of nanoparticles at higher temperatures and pressures and in a closed atmosphere. This technique involves the mixing of precursor with strong alkali and allowed to react in a Teflon-lined autoclave. The synthesized nanoparticles are then washed with excess water to remove excessive alkali. Then the particles are dried and ground. This technique offers the advantages of easy preparation, larger yield and high controllability in size. Metallic and non-metallic hybrid nanoparticles could be synthesized by this method [26].

3.4 Techniques Associated with Nanostructured Materials in Heavy Metals Removal

Nanomaterials in the form of nanocomposites, nanoadsorbents, molecularly imprinted polymers, nanomembranes, nanocatalyst and bioactive nanoparticles find their application in wastewater remediation for the removal of toxic metal ions, pathogens, organic and inorganic pollutants from water [27]. Features especially paramagnetism, quantum captivity effect, and semiconducting attainment offer additional advantages to finding potential in heavy metals removal [28]. Various researches are focused on the fabrication of different new nanomaterials from different sources. However, main attention should be given to the usage cost of nanomaterial.

Various conventional methods including coagulation, chemical precipitation, photocatalysis, electrochemical treatment, adsorption and membrane processes are processed to remove heavy metals. Among all, three processes namely adsorption, membrane-based process [29] and photocatalytic reduction are mainly focused on heavy metals removal in large-scale applications. The application of nanoparticles and nanocomposites in heavy metal removal is given in Fig. 1.

3.4.1 Adsorption

Heavy metals are removed by means of adsorption where metal ions are held up on the surface of a nanomaterial. Compared with several conventional methods, adsorption remains an effective and efficient technique in the removal of heavy metals from wastewater. Easy accessibility, flexibility, high proficiency, simpler design, less space requirement and less capital investment offer additional advantages and researchers are focusing huge attention on the expulsion of heavy metals using adsorbents [30]. Adsorption of heavy metals on the surface of solids adsorbents is gaining importance. Usually, in the adsorption process, the desired quantity of nanomaterial is added to heavy metal laden water. Heavy metals diffuse onto the exterior surface of the nanoadsorbent, then diffuse into the interior pores and gets accumulated on the pores by means of physical or chemical forces. In case of polymer-based adsorbents, adsorption is usually via complex formation and electrostatic interaction.



Fig. 1 Application of nanoparticles and nanocomposites in heavy metals removal

3.4.2 Photo Catalysis

Photocatalysis emerges as one of the best processes in wastewater remediation techniques as it has a tendency to destroy or reduce the contaminant instead of separating it. Photocatalysis is a combination of light and catalytic reactions. Usually, semi-conducting materials act as photocatalyst. Here light is used to excite the electrons to produce electron-hole pairs. Semiconductors while being irradiated with light sources release oxidative free radicals which have a tendency to destroy organic pollutant and reduce heavy metal ions. While being irradiated with light, photons are produced and electrons get excited to a higher level creating electron hair poles on the surface of the semiconductors. Electron hair poles further produce free radicals mainly superoxide radical and hydroxyl radical which detoxifies heavy metals [31].

3.4.3 Membrane-Based Processes

Membrane separation is another budding technology in the removal of heavy metals. Integration of nanoparticles into membranes has enhanced the water permeability of membranes. In ordinary membrane separation, separation is achieved based on membrane pore size. Smaller particles pass through the pores of membranes whereas larger particles get retained on the surface of the pores. Major issue concerned with nanofiltration is that nanomembrane as its pore size is very small, and movement of water through is difficult which reduces membrane flux. The incorporation of nanomaterials in the membranes increases the permeation. Metal oxide nanoparticles, nanotubes, CNTs, polymer nanocomposites, etc. are coated on the surface of the membrane to improve the selectivity of membranes [32]. The addition of nanoparticles induces modification in the characteristics of the membrane, which produces better removal efficiency. These nanoparticles create a pathway for water

transport. Currently, adsorptive membranes have been fabricated for the removal of heavy metals. Adsorptive membranes have the potential to trap heavy metals in the membrane matrix as well as permit the passage of water thereby producing clean permeates. Generally, ultrafiltration membranes are employed as adsorptive membrane. However, to overcome the difficulty faced with low rejection of heavy metals, nowadays nanoparticles are incorporated into ultrafiltration membranes to achieve excellent heavy metal removal.

4 Nanoadsorbents in Adsorption

Generally, adsorbents should contain enormous active binding sites. Most of the conventional adsorbents suffer from several disadvantages including low adsorption capacity, lack of functional tenability, recyclability and reusability. Recently usage of nanoscale materials and nanocomposites as nanoadsorbents overcomes all those difficulties. Properties of nanoadsorbents, including the presence of a large number of binding sites, active functional groups, larger specific area and lower flocculent generation have attracted researchers to use nano-structured materials as appropriate adsorbents in the removal of heavy metals from contaminated [33]. Nanoparticles have a tendency to penetrate deep into a contaminant, which in turn increases the reactivity that could not be possible by conventional adsorbents [34]. Nanoadsorbents could be incorporated with prevailing treatment processes in columns or slurry reactors [35]. Carbon-based metals, bimetals, metal oxides, ferrite, magnetite, polymer based, chitosan and zeolites have been extensively employed in the removal of heavy metals. These nanostructured substances remove heavy metals by adsorbing them on their surface. Various nanoadsorbents used for the removal of heavy metals are listed in Table 3.

4.1 Carbon-Based Nanoadsorbents

Carbon-based nanomaterials provide unique physical and chemical features and emerge as the most appropriate nanoadsorbents. Numerous research including carbon-based nanocomposite, graphene and carbon nanotubes (CNTs) have been employed in the removal of various HMs. Carbon nanotubes (CNTs) is one of the eminent examples for carbon-based nanomaterial used for the elimination of HM from wastewater. CNTs are cylinder-shaped macromolecule rolled up in the form of tubes [36]. CNTs on the basis of the arrangement of graphene sheets are divided into two types, single-walled carbon nanotubes and multi-walled carbon nanotubes. Single-walled carbon nanotubes (SWCNTs) contain single graphene sheet rolled up whereas multi-walled carbon nanotubes (MWCNTs) contain multiple sheets of graphene roll-up. Tunable physical, chemical, electrical and structural properties enable it to find a wide application as adsorbent, membranes, catalyst and filters in

Table 3 Nanoadsorbents in the removal of heavy metal ions

S.No	Nanoadsorbents	Heavy metal removed	Removal efficiency or adsorption capacity	References
1	SWCNT	Hg ²⁺	4.16%	[53]
2	SWCNT	Ni ²⁺	9.22 mg/g	[54]
3	MWCNT	Mn ⁷⁺	71.5%	[55]
4	MWCNT	Ni ²⁺	7.53 mg/g	[54]
5	CNT-COO ⁻	Hg ²⁺	3.300 mmol/g	[56]
6	CNT-CONH ₂	Cd ²⁺	1.563 mmol/g	[56]
7	Porous graphene	As ³⁺	90%	[57]
8	rGO-Sulfophenylazo	Cd ²⁺	26.7%	[58]
9	-COOH functionalized GO	Hg ²⁺	12.2%	[59]
10	Amino functionalized mesoporous silica	Cr ⁶⁺	8.205%	[60]
11	Graphene Oxide (GO)	Pb ²⁺	35.6%	[61]
12	GO/Fe ₃ O ₄	Cu ²⁺	18.3 mg/g	[62]
13	Graphene nanosheets (GNs)	Pb ²⁺	22.4%	[63]
14	MnO ₂ /GNs	Hg ²⁺	10.8%	[64]
15	GO/Mn-doped Fe(III)oxide	Cd ²⁺ and Cu ²⁺	87.2 and 129.7 mg/g	[65]
16	Goethite (α-FeOOH)	Cu ²⁺	149.25 mg/g	[66]
17	γ-Fe ₂ O ₃	Cu ²⁺	26.8%	[67]
18	Amino functionalized silica gel in Tea Polyphenol extracts	Pb ²⁺	98.1%	[68]
19	Thiol and amino functionalized SBA-15 Silica	Hg ²⁺	29.2%	[69]
20	Ionic liquid-functionalized silica	Pb ²⁺	20.23%	[70]
21	Hematite-Magnetite hybrid	Pb ²⁺	97.67%	[71]
22	Hematite-Magnetite hybrid	Cr ³⁺	99.50%	[71]
23	Maghemite NP	As ⁵⁺	50%	[72]
24	Magnetite NP	Pb ²⁺	100%	[46]
25	Magnetite NP	Zn ²⁺	100%	[46]
26	Grafted silica (SiN ₂)	Pb ²⁺	0.184 mmol/g	[73]
27	Carboxyl functionalized magnetite NP	Cu ²⁺	98.3%	[74]
28	Chitosan-Fe ₀ nanoparticles	Cr ⁶⁺	60.2 mg/g	[75]
29	Highly mesoporous silica (containing nanospheres) anchored with 2,5-dimercapto-1,3,4-thiadiazole	Pb ²⁺	67.2 mg/g	[76]

(continued)

Table 3 (continued)

S.No	Nanoadsorbents	Heavy metal removed	Removal efficiency or adsorption capacity	References
30	ZnO nanoparticles	Cd ²⁺	387 mg/g	[77]
31	Resin supported nanoscale zerovalent iron	Cr ⁶⁺	84.4%	[78]
32	Humic acid coated Fe ₃ O ₄ magnetic nanoparticle	Pb ²⁺	92 mg/g	[79]
33	Fe@MgO nanocomposite	Pb ²⁺	147.64	[80]
34	Thiol-lignocellulose sodium bentonite (TLSB) nanocomposites	Zn ²⁺	35.72%	[81]
35	Silica-coated iron oxide magnetic nanocomposites (Fe ₃ O ₄ @SiO ₂)	Hg ²⁺	94.12	[82]
36	Polypyrrole-iron oxide-seaweed nanocomposite	Cr ⁶⁺	99.12%	[83]
37	Polypyrrole-iron oxide—seaweed nanocomposite	Pb ²⁺	99.54%	[84]

wastewater remediation. As CNTs are hydrophobic in nature, they usually aggregate in aqueous media forming grooves and spaces that aid in the adsorption of pollutants [37]. Active sites with high surface area and pore size enhance the adsorption capacity of CNTs in the removal of HMs. CNTs remove HMs through physical, chemical and electrostatic attraction [38].

Graphene, one of the carbon-based nanomaterials plays a vital part in wastewater remediation. The higher surface area with the presence of various characteristic functional groups enables graphene to find special attention in the removal of heavy metals [39]. Graphene oxide particularly plays a major role in the removal of many contaminants due to the presence of oxygen-derived derived functionalities [40]. The heavy metals are removed through complexation formation by means of adsorption of heavy metal ions on the active oxygen sites of graphene.

4.2 Metal- and Metal-Oxide-Based Nanoadsorbents

Metals and metal oxide nanoparticles served as active materials in the expulsion of heavy metals from wastewater. Metallic nanoparticles are unstable as they tend to agglomerate and find little application as adsorbents in the removal of heavy metals. Moreover, the separation of metallic nanoparticles is a tedious one. Among the metallic nanoadsorbents, zero-valent iron is the most commonly used metallic

nanoadsorbent as they are highly stable, less toxic and possesses a higher surface area and large adsorption capacity. Most heavy metals including chromium, arsenic, zinc, copper, etc. are removed by zero-valent iron. Bimetallic nanoparticles also remain an effective nanoadsorbent in the removal of heavy metals. Fe/Ni nanoparticles were used for the removal of copper and nitrate ions with a removal efficiency of 99.7 and 40.4% respectively [41]. Numerous researches have been carried out to make it obvious that metallic oxides could be used as nanoadsorbents. On the basis of magnetic property, metal oxide nanoadsorbents are classified as magnetic and non-magnetic metal oxide nanoparticles. Oxides of zinc, copper, manganese, cerium and aluminum fall under the category of non-magnetic metal oxide nanoadsorbents. CuO nanoparticles were effectively used for the removal of Cr (VI) and Pb (II) ions from contaminated water with adsorption capacities of 15.62 and 37.02 mg/g, respectively [42].

Apart from traditional metal oxide nanoparticles, alkaline metal oxide nanoparticles have also been applied in the removal of heavy metals. Comparatively, they are less toxic and environment friendly. Many researchers have explored the admirable features of MgO nanoparticles in the removal of heavy metals. MgO nanoparticles effectively removed Pb (II) and Cd (II) ions with adsorption capacity of 1980 and 1500 mg/g respectively. MgO nanoparticles are found to high surface area. Al₂O₃ nanoparticles are present in soils and remain a better nanoadsorbent owing to their higher stability. It has various structural phases including α , β , γ , θ and χ phases. Fascinating properties of strong interatomic bonding, electrical insulation, high thermal conductivity, greater compressive strength and corrosion resistance enable it to remain as a potential nanoadsorbent. Silica, an additional metal oxide nanoadsorbent has immense application in the removal of heavy metals as they possess tunable surface properties, characteristic pore-size and larger surface area [43]. Also nanosilica is non toxic.

Magnetic metal oxide nanoparticles play a vital part in current research, particularly in the removal of heavy metals as it has acquired the combined advantage of nanostructure and magnetic properties. Magnetic metal oxide nanoparticles could be easily separated under the application of an external magnet and they can be effectively reused [44]. Utilization of magnetic metal oxide nanoparticles in wastewater remediation enables the process efficient, profitable and reliable [45]. Compared with non-magnetic nanoparticles they have a higher surface area, are less toxic, ease of dispersion, biocompatibility and ease of separation. Researchers investigated several magnetic metal oxide nanoparticles in the removal of heavy metals. Iron oxide nanoparticles occupy an integral part in the removal of heavy metals. Also, they possess high adsorption capacity. Iron oxide exists in three forms namely magnetite (Fe₃O₄), maghemite (γ -Fe₂O₃) and haematite (α -Fe₂O₃). Magnetite and maghemite possess spinal structures. Haematite (α -Fe₂O₃) is non-magnetic in nature and has a corundum structure. Maghemite Fe₃O₄ nanoparticles are the most widely nanoadsorbent and have been used in the removal of Mn (II), Zn (II), Cu (II) and Pb (II), respectively. The adsorption capacity of synthesized Fe₃O₄ was higher compared with commercial Fe₃O₄ in the removal of As (II) and Cu (II) [46].

4.3 Polymer-Based Nanoadsorbents or Polymer Nanocomposites

Polymer-based nanoadsorbents or polymer nanocomposites remain ideal adsorbents in the removal of heavy metal as they have the higher specific surface area and adsorption capacity. To overcome the problem of agglomeration, nanoparticles are converted into polymer nanocomposites by impregnating nanoparticles on polymer skeleton [47]. Higher skeletal strength, easy degradability and tunable surface functional groups make polymer-based nanoadsorbents a perfect choice in heavy metal removal. The presence of specific functionalities including $-\text{NH}_2$, $-\text{COOH}$, $-\text{SO}_3\text{H}$ increased the selectivity toward specific metal and promoted adsorption capacity. These nanoadsorbents are classified on the basis of polymers used.

Chitosan is an eco-friendly, biocompatible, hydrophilic and non-toxic polymer. It is a commonly used polymer in wastewater treatment as it has the potential to form complexes with several heavy metals. The availability of amino groups enhances the interaction towards heavy metal ions through chelation. Adsorption capacity and selectivity of chitosan can be improved by chemical transformations. Dubey et al. investigated the adsorption performance of chitosan alginate nanoparticles in the removal of Hg (II) ions [48]. Saad et al. synthesized ZnO/chitosan nanoparticles and explored their efficiency in the removal of Cu (II), Cd (II) and Pb (II) [49].

Chitin, a natural polymer is also used in the removal of heavy metals. Liu et al. compared the adsorptive capacity of chitin nanofibrils with chitin microparticles in the removal of Cr (III), Zn (II), Ni (II), Cd (II), Cu (II) and Pb (II). The adsorption capacity of chitin nanofibrils is high compared with chitin micro particles due to the presence of a large surface area and pores [50].

Many polymers including cellulose, lignin, starch, conducting, non-conducting polymers and a variety of natural biopolymers are also used in the removal of heavy metals [51].

4.4 Zeolite-Based Nanoparticles

Zeolite in the form of nano-sized particles is extensively used in the removal of heavy metals as they are highly porous and have high surface activity. In one report, Deravanesian et al. explored the adsorption performance of alumina NPs immobilized zeolite in the removal of Pb (II) and Cr (III) and compared the adsorption efficiency with alumina nanoparticles and zeolite granules. The results showed that the efficiency of alumina NPs immobilized zeolite is higher than alumina nanoparticles and zeolite granules [52].

5 Functionalization of Nanoparticles

Usually, nanoscale adsorbents tend to agglomerate which makes them difficult to separation.

To overcome this difficulty, nanoparticles are functionalized. It offers higher adsorption capacity and facilitates separation easier. Functionalization could be achieved through coating with carbon, polymers, inorganic molecules, and biomolecules. Atoms present on the surface of the nanoparticles are mostly unsaturated and have a tendency to bind with other atoms easily [85]. Consequently, most of the nanomaterials are functionalized by surface modification. Also, surface modification improves the mechanical, magnetic, rheological, electrical and optical properties [86]. Suitable surface functionalization provided specific functional groups to expel targeted metal ions from polluted water. Normally, magnetic nanoparticles are functionalized with hydrophilic groups containing polyethylene glycol (PEG), polyvinyl alcohol (PVA) and polyvinyl pyrrolidone (PVP) to increase the surface volume ratio [87].

The surface of metal oxide has been modified by adding surfactant which in turn enhances the adsorption capacity. In one study, Pham et al. modified the surface of alumina with sodium dodecyl sulphate (SDS) in order to increase the removal efficiency of ammonium ions. The adsorption capacity of carbon nanotubes is enhanced by surface-modified functionalization of acid treatment and grafting techniques [88].

Nguyen et al. modified the surface of alumina particles by coating them with two surfactants namely sodium dodecyl sulphate (SDS) and sodium tetradecyl sulphate (STS) and compared their removal efficiency towards cadmium ions. The results showed that the removal efficiency increased from 67 to 95% on adding surfactants [89]. The surface of silica has been modified by incorporating amino and thiol functionalities to achieve better adsorption capacity. Li et al. 2019 modified the surface of silica with nitrilotriacetic acid and its adsorption capacity towards in removal of lead, cadmium and copper ions [90]. Kotsyuda et al. modified the surface of silica nanospheres with 3-aminopropyl and phenyl groups and studied its adsorption characteristics in the removal of Cu (II). The results revealed that adsorption capacity increases with an increase in amino groups [91].

6 Nanocomposites Membranes in Membrane-Based Processes

In nanocomposite membranes, addition of nanoparticles improves the properties of porosity, permeation, hydrophilicity, swelling, antifouling and mechanical strength [92]. Generally, ZnO, TiO₂, SiO₂, iron oxides, GO and CNTs are incorporated in the development of nanocomposite membranes. Multifunctional nanomaterial incorporated into the membrane matrix has been developed to improve the water permeability [93]. The nanocomposite membranes offer additional advantages of

Table 4 Nanocomposite membrane in the removal of heavy metal ions

S.No	Nanocomposite membranes	Heavy metal	Removal efficiency (%)	References
1	Activated bentonite clay nanoparticle imparted on polyetherimide membrane	Cu ²⁺	82.5	[96]
2	Fe ₃ O ₄ -talc nanocomposites incorporated in polysulfone membrane	Ni ²⁺	96.2	[97]
3	Chitosan membrane embedded with 1.25 wt% zeolite nanoparticle	As ³⁺	94.9	[98]
4	Poly(acrylonitrile)-co-poly(methylacrylate) copolymer-polyaniline nanocomposite	Cr ⁶⁺	99.3	[99]
5	Ceramic hollow fiber membrane (CHFM) derived from rice husk ash	Ni ²⁺	99.99	[100]
		Zn ²⁺	99.79	
		Pb ²⁺	99.99	

no sludge formation, single-step process, pretreatment is not required and could be reused. Sunil et al. fabricated an AlTi₂O₆ incorporated polysulfone (PSF) composite membrane and explored its improved hydrophilicity towards the removal of heavy metals [94]. Ghaemi et al. developed a PPy@Al₂O₃ polymeric nanocomposites membrane by adding PPy@Al₂O₃ into a polyether sulfone (PES) membrane matrix and explored its performance in removal of copper ions. The results showed that PPy@Al₂O₃ enhanced the water permeability, increased copper rejection and decreased membrane surface roughness [92]. In other reports, the performance of PES-based nanocomposite membrane incorporated with polyaniline-modified GO nanoparticles in the removal of lead ions was discussed. It was reported the addition of polyaniline-modified GO nanoparticles showed better removal efficiency and also decreased the viscosity of the membrane [95]. Few nanocomposites membranes used in the removal of heavy metals are provided in Table 4.

7 Bioactive Nanoagents

The most serious threat is infectious diseases caused by infectious microorganisms. Nano antimicrobials are used as antibiotics for effective treatment. Bacterial growth control remains a challenging task. Liu et al. explored the antibacterial activities of graphite, graphite oxide, graphene oxide and reduced graphene oxide using membrane and oxidative stress. *E. coli* as a model bacterium [101]. *E. coli* cells were incubated in an isotonic saline solution containing dispersions of graphite, graphite oxide, graphene oxide and reduced graphene oxide in the concentration range of 40 lg/mg. Bacterial cell death rate was evaluated by colony counting method. The difference in antibacterial activity was observed among the four substances. Graphene and graphene oxide exhibited higher bacterial inactivation percentages than graphite and

graphite oxide. The antibacterial activities of graphene-based materials are due to their size, oxidation capacity and dispersability. Shao et al. evaluated the antibacterial property of silver nanoparticle decorated graphene oxide (GO-Ag) nanocomposite by using Gram-negative *E. coli* ATCC 25,922 and Gram-positive *S. aureus* ATCC 6538. The antibacterial property of GO-Ag nanocomposite was determined by determining antibacterial ratios based on the number of bacteria colonies [102].

8 Nanophotocatalysts in Photocatalysis

Researchers have focused on the usage of lighter responsive semiconductive nanomaterials especially titanium dioxide (TiO_2) and zinc oxide (ZnO) in the removal of pollutants. However, less attention is paid to the removal of heavy metals using nanomaterials as photocatalysts as heavy metals are difficult to degrade. Meanwhile, nanoparticle photocatalysts could reduce the harmful effects of heavy metals by converting them into lesser harmful metals. For example, Cr (VI) is highly toxic compared with Cr (III). In most of the wastewater techniques, Cr (VI) is reduced to Cr (III). Based on this photocatalyst approach, Cr (VI) is also reduced to Cr (III). Usually, TiO_2 , MnO , Fe_2O_3 , CeO_2 , MgO , ZnO are commonly used photocatalysts in the removal of heavy metals.

Mayo et al. explored the adsorption behavior of magnetite nanoparticles in the removal of As (III) and As (V) and reported the relationship between size and removal efficiency. Kar et al. 2019 developed an iron oxide (II) bismuth carbonate hybrid photocatalyst and explored reduction behavior in the reduction of Cr (VI) reduced to Cr (III) [103]. Kumar et al. 2018 synthesized a hybrid WO_3 /reduced graphene oxide (rGO) nanocomposite photocatalyst to reduce of Cr (VI) to Cr (III). To overcome the large bandgap felt with traditional semiconducting photocatalyst, nanocomposite photocatalysts are produced by doping metallic non-metallic substances [104]. Froing the atom available on the surface of the nanocomposite photocatalyst reduces the bandgap, which in turn reduces the energy required to irradiate a photon. Various nanophotocatalysts used for the removal of heavy metals are listed in Table 5.

9 Conclusion

The present chapter has shown the potential application of nanoparticles and nanocomposite for the removal of heavy metals from wastewater. They are promising nanotools for the detoxification of heavy metals owing to their physicochemical properties of higher surface area, tunable by functionalization and reusability. Numerous research in the literature showed the applicability of nanoparticles and nanocomposites in the removal of various kinds of heavy metals and inferred that the removal of heavy metals depends on the affinity of heavy metals towards nanomaterials. Different studies described magnetic-based nanoparticles and nanocomposites as

Table 5 Nanophotocatalyst in the removal of heavy metal ions

S.No	Nanophotocatalyst	Heavy metal	Removal efficiency (%)	References
1	WO ₃	Cr ⁶⁺	90	[104]
2	TiO ₂	Cd ²⁺	98	[105]
		Pb ²⁺	99	
3	CdS/CuInS ₂ nanoplates	Cr ⁶⁺	100	[106]
4	Graphene-based TiO ₂	Zn ²⁺	100	[107]
5	CeO ₂ /SnO ₂ /rGO nanocomposites	Pb ²⁺	80	[108]
		Cd ²⁺	80	
6	Zirconium-selenophosphate nanocomposite	Pb ²⁺	100	[109]
		Zn ²⁺	95	

having a remarkable role in the removal of heavy metals and separation was easier. Several pioneering platforms have established the potential of nanoparticles and nanocomposites as eco-friendly materials in the removal of heavy metals. Current development in the synthesis and fabrication of nanoparticles and nanocomposites displays promising perspectives; nevertheless, practical applicability in real application remains challenging. An almost challenging issue in nanotechnology is the possible conversion of lab-scale research findings to commercial-scale application.

References

1. Ali H, Khan E, Ilahi I (2019) Environmental chemistry and ecotoxicology of hazardous heavy metals: environmental persistence, toxicity, and bioaccumulation. *J Chem* 2019:6730305. <https://doi.org/10.1155/2019/6730305>
2. Yari S, Abbasizadeh S, Mousavi SE, Moghaddam MS, Moghaddam AZ (2015) Adsorption of Pb (II) and Cu (II) ions from aqueous solution by an electrospun CeO₂ nanofiber adsorbent functionalized with mercapto groups. *Process Saf Environ Prot* 94:159–171. <https://doi.org/10.1016/j.psep.2015.01.011>
3. Vardhan KH, Kumar PS, Panda RC (2019) A review on heavy metal pollution, toxicity and remedial measures: current trends and future perspectives. *J Mol Liq* 290:111197. <https://doi.org/10.1016/j.molliq.2019.111197>
4. Le AT, Pung SY, Sreekantan S, Matsuda A, Huynh DP (2019) Mechanisms of removal of heavy metal ions by ZnO particles. *Heliyon* 5. <https://doi.org/10.1016/j.heliyon.2019.e01440>
5. Cervantes C, Campos-García J, Devars S, Gutiérrez-Corona F, Loza-Tavera H, Torres-Guzmán JC et al (2001) Interactions of chromium with microorganisms and plants. *FEMS Microbiol Rev* 25:335–347. <https://doi.org/10.1111/j.1574-6976.2001.tb00581.x>
6. Zhu X, Song T, Lv Z, Ji G (2016) High-efficiency and low-cost α-Fe₂O₃ nanoparticles coated volcanic rock for Cd (II) removal from wastewater. *Process Saf Environ Prot* 104:373–381. <https://doi.org/10.1016/j.psep.2016.09.019>
7. Chennaiah JB, Rasheed MA, Patil DJ (2014) Concentration of heavy metal ions in drinking water with emphasis on human health. *Int J Plant Anim Environ Sci*
8. Hasanzadeh R, Moghadam PN, Bahri-Laleh N, Sillanpaa M (2017) Effective removal of toxic metal ions from aqueous solutions: 2-Bifunctional magnetic nanocomposite based on novel

- reactive PGMAMAn copolymer@Fe₃O₄ nanoparticles. *J Colloid Interface Sci* 490:727–746. <https://doi.org/10.1016/j.jcis.2016.11.098>
9. Venkateswarlu S, Yoon M Surfactant-free green synthesis of Fe₃O₄ nanoparticles capped with 3,4-dihydroxy-phenethylcarbamide: stable recyclable magnetic nanoparticles for the rapid and efficient removal of Hg (II) ions from water. *Dalton Trans* 44:18427–18437. <https://doi.org/10.1039/c5dt03155a>
 10. Razzaz S, Ghorban L, Hosayni M, Irani, Aliabadi M (2016) Chitosan nanofibers functionalized by TiO₂ nanoparticles for the removal of heavy metal ions. *J Taiwan Inst Chem Eng* 58:333–343. <https://doi.org/10.1016/j.jtice.2015.06.003>
 11. Martín DM, Faccini M, García MA, Amanti D (2018) Highly efficient removal of heavy metal ions from polluted water using ions elective polyacrylonitrile nanofibers. *J Environ Chem Eng* 6:236–245. <https://doi.org/10.1016/j.jece.2017.11.073>
 12. Wadhawan S, Jain A Nayyar J, Mehta SR (2020) Role of nanomaterials as adsorbents in heavy metal ion removal from wastewater: a review. *J Water Process Eng* 33:101038. <https://doi.org/10.1016/j.jwpe.2019.101038>
 13. Burakov A, Galunin E, Burakova I, Memetova A, Agarwal S, Tkachev A, Gupta V (2017) Adsorption of heavy metals on conventional and nanostructured materials for wastewater treatment purposes: a review. *Ecotoxicol Environ Saf* 148:702–712. <https://doi.org/10.1016/j.ecoenv.2017.11.034>
 14. Amit C, Chandarana H, Kumar MA, Sunita V (2018) Nano-technological interventions for the decontamination of water and wastewater. In: Bui X-T et al (eds) *Water and wastewater treatment technologies, energy, environment, and sustainability*. Springer, Singapore, pp 487–499
 15. Lee IH, Kuan YC, Chern JM (2007) Equilibrium and kinetics of heavy metal ion exchange. *J Chin Inst Chem Eng* 38:71–84. <https://doi.org/10.1016/j.jcice.2006.11.001>
 16. Ghaemi N, Zereshki S, Heidari S (2017) Removal of lead ions from water using PES-based nanocomposites membrane incorporated with polyaniline modified GO nanoparticles: performance optimization by central composite design. *Process Saf Environ Prot* 111:475–490. <https://doi.org/10.1016/j.psep.2017.08.011>
 17. Jin W, Zhang Y (2020) Sustainable electrochemical extraction of metal resources from waste streams: from removal to recovery. *ACS Sustain. Chem. Eng* 8:4693–4707. <https://doi.org/10.1021/acssuschemeng.9b07007>
 18. Cruz-Olivares J, Martínez-Barrera G, Pérez-Alonso C, Barrera-Díaz, CE, Chaparro-Mercado, MdC, Ureña-Núñez F (2016) Adsorption of lead ions from aqueous solutions using gamma irradiated minerals. *J Chem* 8782469. <https://doi.org/10.1155/2016/8782469>
 19. Singh DK, Verma DK, Singh Y HSH (2017) Preparation of CuO nanoparticles using Tamarindus indica pulp extract for removal of As (III): optimization of adsorption process by ANN-GA. *J Environ Chem Eng* 2017(5):1302–1318. <https://doi.org/10.1016/j.jece.2017.01.046>
 20. Huang Q, Liu Y, Cai T, Xia X (2019) Simultaneous removal of heavy metal ions and organic pollutant by BiOBr/ Ti₃C₂ nanocomposite. *J Photochem Photobiol A: Chem* 375:201–208. <https://doi.org/10.1016/j.jphotochem.2019.02.026>
 21. Anjum M, Miandad R, Waqas M, Gehany F, Barakat MA (2016) Remediation of wastewater using various nano-materials. *Arab J Chem*. <https://doi.org/10.1016/j.arabjc.2016.10.004>
 22. Zeng T, Yu Y, Li Z, Zuo J, Kuai Z, Jin Y, Wang Y, Wu A, Peng C (2019) 3D MnO₂ nanotubes@reduced graphene oxide hydrogel as reusable adsorbent for the removal of heavy metal ions. *Mater Chem Phys* 231:105–108. <https://doi.org/10.1016/j.matchemphys.2019.04.019>
 23. Pareek V, Jain N, Panwar J, Bhargava A, Gupta R (2017) Synthesis and applications of noble metal nanoparticles: a review. *Adv Sci Eng Med* 9:527–544. <https://doi.org/10.1166/asem.2017.2027>
 24. Nikam AV, Prasad BLV, Kulkarni AA (2018) Wet chemical synthesis of metal oxide nanoparticles: a review. *Cryst Eng Comm* 20:5091–5107. <https://doi.org/10.1039/C8CE00487K>

25. Ahmed MA, El-Katori EE, Gharni ZH (2013) Photocatalytic degradation of methylene blue dye using Fe₂O₃/TiO₂ nanoparticles prepared by sol–gel method. *J Alloys Compd* 553:19–29. <https://doi.org/10.1016/j.jallcom.2012.10.038>
26. Subramaniam MN, Goh PS, Abdullah N, Lau WJ, Ng BC, Ismail AF (2017) Adsorption and photocatalytic degradation of methylene blue using high surface area titanate nanotubes (TNT) synthesized via hydrothermal method. *J. Nanopart Res* 19:220
27. Sarma G, Sen Gupta S, Bhattacharyya KG (2019) Nanomaterials as versatile adsorbents for heavy metal ions in water: a review. *Environ Sci Pollut Res* 26:6245–6278. <https://doi.org/10.1007/s11356-018-04093-y>
28. Parvin F, Rikta SY, Tareq SM (2019) Application of nanomaterials for the removal of heavy metal from wastewater. In: Ahsan A, Ismail AF (eds) *Nanotechnology in water and wastewater treatment*. Elsevier, Amsterdam, The Netherlands, pp 137–157. <https://doi.org/10.1016/B978-0-12-813902-8.00008>
29. Abdullah N, Yusof N, Lau WJ, Jaafar J, Ismail A (2019) Recent trends of heavy metal removal from water/wastewater by membrane technologies. *J Ind Eng Chem* 76:17–38. <https://doi.org/10.1016/j.jiec.2019.03.029>
30. Al-Senani GM, Al-Fawzan FF (2018) Adsorption study of heavy metal ions from aqueous solution by nanoparticle of wild herbs. *Egypt J Aquat Res* 44:187–194. <https://doi.org/10.1016/j.ejar.2018.07.006>
31. Yu T, Lv L, Wang H, Tan X (2018) Enhanced photocatalytic treatment of Cr(VI) and phenol by Monoclinic BiVO₄ with {010}-orientation growth. *Mater Res Bull* 107:248–254. <https://doi.org/10.1016/j.materresbull.2018.07.033>
32. Khulbe KC, Matsuur T (2018) Removal of heavy metals and pollutants by membrane adsorption techniques. *Appl Water Sci* 8:1–30
33. Yang J, Hou B, Wang J, Tian B, Bi J, Wang N, Li X, Huang X (2019) Nanomaterials for the removal of heavy metals from wastewater. *Nanomaterials* 9:424. <https://doi.org/10.3390/nano9030424>
34. Bystrzejewski M, Pyrzyńska K, Huczko A, Lange H (2009) Carbon encapsulated magnetic nanoparticles as separable and mobile sorbents of heavy metal ions from aqueous solutions. <https://doi.org/10.1016/j.carbon.2009.01.007>
35. Qu X, Alvarez PJJ, Li Q (2013) Applications of nanotechnology in water and wastewater treatment. *WaterRes* 47:3931–3946. <https://doi.org/10.1016/j.watres.2012.09.058>
36. Menezes BRCd, Rodrigues KF, Fonseca BCds, Ribas RG, Montanheiro TLdA, Thim GP (2019) Recent advances in the use of carbon nanotubes as smart biomaterials. *J Mater Chem B* 7:1343–1360. <https://doi.org/10.1039/C8TB02419G>
37. Bassyouni M, Mansi AE, Elgabry A, Ibrahim B.A, Kassem OA, Alhebeshy R (2019) Utilization of carbon nanotubes in removal of heavy metals from wastewater: A review of the CNTs' potential and current challenges. *Appl Phys A* 126:38. <https://doi.org/10.1007/s00339-019-3211-7>
38. Ihsanullah Abbas A, Al-Amer AM, Laoui T, Al-Marri MJ, Nasser MS, Khraisheh M (2016) Heavy metal removal from aqueous solution by advanced carbon nanotubes: critical review of adsorption applications. *Sep Purif Technol*. <https://doi.org/10.1016/j.seppur.2015.11.039>
39. Ali I, Basheer AA, Mbianda XY, Burakov A, Galunin E, Burakova I, Mkrtchyan E, Tkachev A, Grachev V (2019) Graphene based adsorbents for remediation of noxious pollutants from wastewater. *Environ Int* 127:160–180. <https://doi.org/10.1016/j.envint.2019.03.029>
40. Smith AT, LaChance AM, Zeng S, Liu B, Sun L (2019) Synthesis, properties, and applications of graphene oxide/reduced graphene oxide and their nanocomposites. *Nano Mater Sci* 1:31–47. <https://doi.org/10.1016/j.nanoms.2019.02.004>
41. Cai X, Gao Y, Sun Q, Chen Z, Megharaj M, Naidun R (2014) Removal of co-contaminants Cu (II) and nitrate from aqueous solution using kaolin-Fe/Ni nanoparticles. *Chem Eng* 244:19–26. <https://doi.org/10.1016/j.cej.2014.01.040>
42. Verma M, Tyagi I, Chandra R, Gupta VK (2017) Adsorptive removal of Pb (II) ions from aqueous solution using CuO nanoparticles synthesized by sputtering method. *J Mol Liq* 225:936–944. <https://doi.org/10.1016/j.molliq.2016.04.045>

43. Ahmad N, Sereshti H, Mousazadeh M, Rashidi Nodeh H, Kamboh MA, Mohamad S (2019) New magnetic silica-based hybrid organic-inorganic nanocomposite for the removal of lead (II) and nickel (II) ions from aqueous solutions. *Mater Chem Phys* 226:73–81. <https://doi.org/10.1016/j.matchemphys.2019.01.002>
44. Fan H, Ma X, Zhou S, Huang J, Liu Y, Liu Y (2019) Highly efficient removal of heavy metal ions by carboxy methyl cellulose immobilized Fe₃O₄ nanoparticles prepared via high-gravity technology. *Carbohydr Polym* 213:39–49. <https://doi.org/10.1016/j.carbpol.2019.02.067>
45. Tamjidi S, Esmaeili H, Kamyab MB (2019) Application of magnetic adsorbents for removal of heavy metals from wastewater: a review study. *Mater Res Express* 6:102004. <https://doi.org/10.1088/2053-1591/ab3ffb>
46. Giraldo L, Erto A, Carlos J, Piraján M (2013) Magnetite nanoparticles for removal of heavy metals from aqueous solutions: synthesis and characterization. *Adsorption* 19(2):465–474. <https://doi.org/10.1007/s10450-012-9468-1>
47. Kenawy IMM, Abou El-Reash YG, Hassanien MM, Alnagar NR, Mortada WI (2018) Use of microwave irradiation for modification of mesoporous silica nanoparticles by thioglycolic acid for removal of cadmium and mercury. *Microporous Mesoporous Mater* 258:217–227. <https://doi.org/10.1016/j.micromeso.2017.09.021>
48. Dubey R, Bajpai J, Bajpai AK (2016) Chitosan-alginate nanoparticles (CANPs) as potential nanosorbent for removal of Hg (II) ions. *Environ Nanotechnol Monit Manag* 6:32–44. <https://doi.org/10.1016/j.enmm.2016.06.008>
49. Saad AHA, Azzam AM, Wakeel SY, Mostafa BB, Latif MBA (2018) Removal of toxic metal ions from wastewater using ZnO@Chitosan core-shell nanocomposites. *Environ Nanotechnol Monit Manag* 12:67–72. <https://doi.org/10.1016/j.enmm.2017.12.004>
50. Liu D, Zhu Y, Li Z, Tian D, Chen L, Chen P (2013) Chitin nanofibrils for rapid and efficient removal of metal ions from water system. *Carbohydr Polym* 98:483–489. <https://doi.org/10.1016/j.carbpol.2013.06.015>
51. Tian YL, Deng PH, Wu YY, Ding ZY, Li GL, Liu J (2019) A simple and efficient molecularly imprinted electrochemical sensor for the selective determination of tryptophan. *Biomolecules* 9(7):294
52. Deravanesiyan M, Beheshti M, Malekpour A (2015) The removal of Cr (III) and Co (II) ions from aqueous solution by two mechanisms using a new sorbent (alumina nanoparticles immobilized zeolite): equilibrium, kinetic and thermodynamic studies. *J Mol Liq* 209:246–257. <https://doi.org/10.1016/j.molliq.2015.05.038>
53. Alijani H, Shariatnia Z (2018) Synthesis of high growth rate SWCNTs and their magnetite cobalt sulfide nanohybrid as superadsorbent for mercury removal. *Chem Eng Res Des* 129:132–149. <https://doi.org/10.1016/j.cherd.2017.11.014>
54. Lu C, Liu C (2006) Removal of nickel (II) from aqueous solution by carbon nanotubes. *J Chem Technol Biotechnol* 81:1932–1940. <https://doi.org/10.1002/jctb.1626>
55. Farghali AA, Abdel Tawab HA, Abdel Moaty SA, Khaled R (2017) Functionalization of acidified multi-walled carbon nanotubes for removal of heavy metals in aqueous solutions. *J Nanostruct Chem* 7:101–111. <https://doi.org/10.1007/s40097-017-0227-4>
56. Anitha K, Namsani S, Singh JK (2015) Removal of heavy metal ions using a functionalized single-walled carbon nanotube: a molecular dynamics study. *J Phys Chem* 119:8349–8358. <https://doi.org/10.1021/acs.jpca.5b03352>
57. Tabish TA, Memon FA, Gomez DE, Horsell DW, Zhang S (2018) A facile synthesis of porous graphene for efficient water and wastewater treatment. *Sci Rep* 8:1817. <https://doi.org/10.1038/s41598-018-19978-8>
58. Zhang CZ, Chen B, Bai Y, Xie J (2018) A new functionalized reduced graphene oxide adsorbent for removing heavy metal ions in water via coordination and ion exchange. *Sep Sci Technol* 53:2896–2905. <https://doi.org/10.1080/01496395.2018.1497655>
59. Awad FS, Abouzied KM, Abou El-Maaty WM, El-Wakil AM, Samy El-Shall M (2020) Effective removal of mercury (II) from aqueous solutions by chemically modified graphene oxide nanosheets. *Arab J Chem* 13:2659–267. <https://doi.org/10.1016/j.arabjc.2018.06.018>

60. Li X, Han C, Zhu W, Ma W, Luo Y, Zhou Y, Yu J, Wei K (2014) Cr (VI) removal from aqueous by adsorption on amine-functionalized mesoporous silica prepared from silica fume. *J Chem* 2014:765856. <https://doi.org/10.1155/2014/765856>
61. Lee YC, Yang JW (2012) Self-assembled flower-like TiO₂ on exfoliated graphite oxide for heavy metal removal. *J Ind Eng Chem* 18:1178–1185. <https://doi.org/10.1016/j.jiec.2012.01.005>
62. Li J, Zhang S, Chen C, Zhao G, Yang X, Li J, Wang X (2012) Removal of Cu (II) and fulvic acid by graphene oxide nanosheets decorated with Fe₃O₄ nanoparticles. *ACS Appl Mater Interfaces* 4(4):4991–5000. <https://doi.org/10.1021/am301358b>
63. Huang ZH, Zheng X, Lv W, Wang M, Yang QH, Kang F (2011) Adsorption of lead (II) ions from aqueous solution on low-temperature exfoliated graphene nanosheets. *Langmuir* 27:7558–7562. <https://doi.org/10.1021/la200606r>
64. Sreepasad TS, Maliyekkal SM, Lisha KP, Pradeep T (2011) Reduced graphene oxide–metal/metal oxide composites: facile synthesis and application in water purification. *J Hazard Mater* 186:921–931. <https://doi.org/10.1016/j.jhazmat.2010.11.100>
65. Nandi D, Basu T, Debnath S, Ghosh AK, De A, Ghosh UC (2013) Mechanistic insight for the sorption of Cd (II) and Cu (II) from aqueous solution on magnetic Mn-doped Fe (III) oxide nanoparticle implanted graphene. *J Chem Eng Data* 58:2809–2818. <https://doi.org/10.1021/je4005257>
66. Gross PR, Sparks DL, Ainsworth CC (1994) Rapid kinetics of Cu (II) adsorption/desorption on goethite. *Environ Sci Technol* 28:1422–1429. <https://doi.org/10.1021/es00057a008>
67. Hu J, Chen G, Lo I (2006) Selective removal of heavy metals from industrial wastewater using maghemite nanoparticle: performance and mechanisms. *J Environ Eng* 132:709–715. [https://doi.org/10.1061/\(ASCE\)0733-9372\(2006\)132:7\(709\)](https://doi.org/10.1061/(ASCE)0733-9372(2006)132:7(709))
68. Huang X, Wang L, Chen J, Jiang C, Wu S, Wang H (2020) Effective removal of heavy metals with amino-functionalized silica gel in tea polyphenol extracts. *J Food Meas Charact* 14:2134–2144. <https://doi.org/10.1007/s11694-020-00460-x>
69. Liu AM, Hidajat K, Kawi S, Zhao DY (2000) A new class of hybrid mesoporous materials with functionalized organic monolayers for selective adsorption of heavy metal ions. *Chem Commun* 1145–1146. <https://doi.org/10.1039/B002661L>
70. Wieszczycka K, Filipowiak K, Wojciechowska I, Buchwald T, Siwinska-Ciesielczyk K, Strzemieska B, Jesionowski T, Voelkel A (2021) Novel highly efficient ionic liquid-functionalized silica for toxic metals removal. *Sep Purif Technol* 265:118483. <https://doi.org/10.1016/j.seppur.2021.118483>
71. Ahmed MA, Ali SM, El-Den SI, Galal A (2013) Magnetite–hematite nanoparticles prepared by green methods for heavy metal ions removal from water. *Mater Sci Eng B* 178:744–751. <https://doi.org/10.1016/j.mseb.2013.03.011>
72. Tuutijärvi T, Lu J, Sillanpää M, Chen G (2009) As (V) adsorption on maghemite nanoparticles. *J Hazard Mater* 166:1415–1420. <https://doi.org/10.1016/j.jhazmat.2008.12.069>
73. Chiron N, Guilet R, Deydier E (2003) Adsorption of Cu (II) and Pb (II) onto a grafted silica: isotherms and kinetic models. *Water Res* 37:3079–3086. [https://doi.org/10.1016/S0043-1354\(03\)00156-8](https://doi.org/10.1016/S0043-1354(03)00156-8)
74. Shi J, Li H, Lu H, Zhao X (2015) Use of carboxyl functional magnetite nanoparticles as potential sorbents for the removal of heavy metal ions from aqueous solution. *J Chem Eng Data* 60:2035–2041. <https://doi.org/10.1021/je5011196>
75. Geng B, Ji Z, Li T, Qi X (2009) Kinetics of hexavalent chromium removal from water by chitosan-FeO nanoparticles. *Chemosphere* 2009(75):825–830. <https://doi.org/10.1016/j.chemosphere.2009.01.009>
76. Shahat A, Hassan HMA, Azzazy HME, El-Sharkawy EA, Abdou HM, Awual MR (2018) Novel hierarchical composite adsorbent for selective lead (II) ions capturing from wastewater samples. *Chem Eng J* 332:377–386. <https://doi.org/10.1016/j.cej.2017.09.040>
77. Sheela T, Nayaka YA, Viswanatha R, Basavanna S, Venkatesha TG (2012) Kinetics and thermodynamics studies on the adsorption of Zn (II), Cd (II) and Hg (II) from aqueous solution using zinc oxide nanoparticles. *Powder Technol* 217:163–170. <https://doi.org/10.1016/j.powtec.2011.10.023>

78. Fu F, Ma J, Xie L, Tang, Han W, Lin S (2013) Chromium removal using resin supported nanoscale zero-valent iron. *J Environ Manage* 128:822–827. <https://doi.org/10.1016/j.jenvman.2013.06.044>
79. Liu J, Zhao Z, Jian G (2008) Coating Fe₃O₄ magnetic nanoparticles with humic acid for high efficient removal of heavy metals in water. *Environ. Sci Technol* 42:6949–6954. <https://doi.org/10.1021/es800924c>
80. Ge L, Wang W, Peng Z, Tan F, Wang X, Chen J, Qiao X (2018) Facile fabrication of Fe@MgO magnetic nanocomposites for efficient removal of heavy metal ion and dye from water. *Powder Technol* 326:393–401. <https://doi.org/10.1016/j.powtec.2017.12.003>
81. Zhang W, An Y, Li S, Liu Z, Chen Z, Ren Y, Wang S, Zhang X, Wang X (2020) Enhanced heavy metal removal from an aqueous environment using an eco-friendly and sustainable adsorbent. *Sci Rep* 10:16453. <https://doi.org/10.1038/s41598-020-73570-7>
82. Hu H, Wang Z, Pan L (2010) Synthesis of monodisperse Fe₃O₄@silica core-shell microspheres and their application for removal of heavy metal ions from water. *J Alloy Compd* 492:656–661. <https://doi.org/10.1016/j.jallcom.2009.11.204>
83. Sarojini G, Venkateshbabu S, Rajasimman M (2021) Facile synthesis and characterization of Polypyrrole-iron oxide-seaweed (PPy-Fe₃O₄-SW) nanocomposite and its exploration for adsorptive removal of PB (II) from heavy metal bearing water. *Chemosphere* 278:130400. <https://doi.org/10.1016/j.chemosphere.2021.130400>
84. Sarojini G, Venkateshbabu S, Rajmohan N, Senthilkumar P, Rajasimman M (2021) Surface modified polymer-magnetic-algae nanocomposite for the removal of chromium-equilibrium and mechanism studies. *Environ Res* 201:111626. <https://doi.org/10.1016/j.envres.2021.111626>
85. Rahmani A, Mousavi HZ, Fazli M (2010) Effect of nanostructure alumina on adsorption of heavy metals. *Desalination* 253:94–100. <https://doi.org/10.1016/j.desal.2009.11.027>
86. Kango S, Kalia S, Celli A, Njuguna J, Habibi Y, Kumar R (2013) Surface modification of inorganic nanoparticles for development of organic-inorganic nanocomposites—a review. *Prog Polym Sci* 38(8):1232–1261. <https://doi.org/10.1016/j.progpolymsci.2013.02.003>
87. Madrakian T, Afkhami A, Zadpour B, Ahmadi M (2015) New synthetic mercaptoethylamino homopolymer-modified maghemite nanoparticles for effective removal of some heavy metal ions from aqueous solution. *J Ind Eng Chem* 21:1160–1166. <https://doi.org/10.1016/j.jiec.2014.05.029>
88. Pham TD, Tran TT, Le VA, Pham TT, Dao TH, Le TS (2019) Adsorption characteristics of molecular oxytetracycline onto alumina particles: the role of surface modification with an anionic surfactant. *J Mol Liq* 287:110900. <https://doi.org/10.1016/j.molliq.2019.110900>
89. Nguyen TT, Ma HT, Avti P, Bashir MJK, Ng CA, Wong LY, Jun HK, Ngo QM, Tran NQ (2019) Adsorptive removal of iron using SiO₂ nanoparticles extracted from rice husk ash. *J Anal Methods Chem* 2019:6210240. <https://doi.org/10.1155/2019/6210240>
90. Li Y, He J, Zhang K, Liu T, Hu Y, Chen X, Wang C, Huang X, Kong L, Liu J (2019) Super rapid removal of copper, cadmium and lead ions from water by NTA-silica gel. *RSC Adv* 9:397–407. <https://doi.org/10.1039/C8RA08638A>
91. Kotsyuda SS, Tomina VV, Zub YL, Furtat IM, Melnyk IV (2017) Bifunctional silica nanospheres with 3-aminopropyl and phenyl groups. Synthesis approach and prospects of their applications. *Appl Surf Sci* 420:782–791. <https://doi.org/10.1016/j.apsusc.2017.05.150>
92. Ghaemi N, Daraei P (2016) Enhancement in copper ion removal by PPy@Al₂O₃ polymeric nanocomposites membrane. *J Ind Eng Chem* 40:26–33. <https://doi.org/10.1016/j.jiec.2016.05.027>
93. Gholami A, Moghadassi AR, Hosseini SM, Shabani S, Gholami F (2014) Preparation and characterization of polyvinyl chloride based nanocomposite nanofiltration-membrane modified by iron oxide nanoparticles for lead removal from water. *J Ind Eng Chem* 20:1517–1522. <https://doi.org/10.1016/j.jiec.2013.07.041>
94. Sunil K, Karunakaran G, Yadav S, Padaki M (2018) Al-Ti₂O₆ a mixed metal oxide based composite membrane: A unique membrane for removal of heavy metals. *Chem Eng J* 348:678–684. <https://doi.org/10.1016/j.cej.2018.05.017>

95. Ghaemi N, Madaeni SS, Daraei P, Rajabi H, Zinadini S, Alizadeh A, Heydari R, Beygzadeh M, Ghouzivand S (2015) Polyethersulfone membrane enhanced with iron oxide nanoparticles for copper removal from water: application of new functionalized Fe₃O₄ nanoparticles. *Chem Eng J* 263:101–112. <https://doi.org/10.1016/j.cej.2014.10.103>
96. Hebbbar RS, Isloor AM, Ismail AF (2014) Preparation and evaluation of heavy metal rejection properties of polyetherimide/porous activated bentonite clay nanocomposite membrane. *RSC Adv* 4:47240–47248. <https://doi.org/10.1039/C4RA09018G>
97. Moradihamedani P, Kalantari K, Abdullah AH, Morad NA (2016) High efficient removal of lead (II) and nickel (II) from aqueous solution by novel polysulfone/Fe₃O₄-talc nanocomposite mixed matrix membrane. *Desalin Water Treat* 57:28900–28909. <https://doi.org/10.1080/19443994.2016.1193449>
98. Mukhopadhyay M, Lakhotia SR, Ghosh AK, Bindal RC (2019) Removal of arsenic from aqueous media using zeolite/chitosan nanocomposite membrane. *Sep Sci Technol* 54:282–288. <https://doi.org/10.1080/01496395.2018.1459704>
99. Sankir M, Bozkir S, Aran B (2010) Preparation and performance analysis of novel nanocomposite copolymer membranes for Cr (VI) removal from aqueous solutions. *Desalination* 251:131–136. <https://doi.org/10.1016/j.desal.2009.09.134>
100. Khadijah S, Ha M, Othman D, Harun Z, Ismail AF, Rahman MA, Jaafar J (2017) A novel green ceramic hollow fiber membrane (CHFM) derived from rice husk ash as combined adsorbent-separator for efficient heavy metals removal. *Ceram Int* 43:4716–4720. <https://doi.org/10.1016/j.ceramint.2016.12.122>
101. Liu S, Zeng TH, Hofmann M, Burcombe E, Wei J, Jiang R, Kong J, Chen Y (2011) Antibacterial activity of graphite, graphite oxide, graphene oxide, and reduced graphene oxide: membrane and oxidative stress. *ACS Nano* 5:6971–6980. <https://doi.org/10.1021/nn202451x>
102. Shao W, Liu X, Min H, Dong G, Feng Q, Zuo S (2015) Preparation, characterization and antibacterial activity of silver nanoparticle-decorated graphene oxid nanocomposites. *ACS Appl Mater Interfaces* 7:6966–6973. <https://doi.org/10.1021/acsami.5b00937>
103. Kar P, Jain P, Kumar V, Gupta RK (2019) Interfacial engineering of Fe₂O₃@BOC heterojunction for efficient detoxification of toxic metal and dye under visible light illumination. *J Environ Chem Eng* 7:102843. <https://doi.org/10.1016/j.jece.2018.102843>
104. Kumar KVA, Chandana L, Ghosal P, Subrahmanyam C (2018) Simultaneous photocatalytic degradation of p-cresol and Cr (VI) by metal oxides supported reduced graphene oxide. *Mol Catal* 451:87–95. <https://doi.org/10.1016/j.mcat.2017.11.014>
105. Barati R, Gilan N, Yousefi N, Ghasemi S, Ahmadian M, Moussavi S, Rahimi S, Fatehizadeh A, Rahimi K, Reshadat S (2014) Photocatalytic removal of cadmium (II) and lead (II) from simulated wastewater at continuous and batch system. *Int J Environ Health Eng* 3:31. <https://doi.org/10.4103/2277-9183.139756>
106. Deng F, Lu X, Luo Y, Wang J, Che W, Yang R, Luo X, Luo S, Dionysiou DD (2019) Novel visible-light-driven direct Z-scheme CdS/CuInS₂ nanoplates for excellent photocatalytic degradation performance and highly-efficient Cr (VI) reduction. *Chem Eng J* 361:1451–1461. <https://doi.org/10.1016/j.cej.2018.10.176>
107. Kumordzi G, Malekshoar G, Yanful EK, Ray AK (2016) Solar photocatalytic degradation of Zn²⁺ using graphene based TiO₂. *Sep Purif Technol* 168:294–301. <https://doi.org/10.1016/j.seppur.2016.05.040>
108. Priyadharsan A, Vasanthakumar V, Karthikeyan S, Raj V, Shanavas S, Anbarasan PM (2017) Multi-functional properties of ternary CeO₂/SnO₂/rGO nanocomposites: visible light driven photocatalyst and heavy metal removal. *J Photochem Photobiol A Chem* 346:32–45. <https://doi.org/10.1016/j.jphotochem.2017.05.030>
109. Kaur K, Jindal R (2018) Synergistic effect of organic-inorganic hybrid nanocomposite ion exchanger on photocatalytic degradation of Rhodamine-B dye and heavy metal ion removal from industrial effluents. *J Environ Chem Eng* 6:7091–7101. <https://doi.org/10.1016/j.jece.2018.09.065>

Chapter 9

Advances in Solar Desalination System by the Application of Nanotechnology



Rahul Agrawal, Kshitij Yugbodh, and Abhishek Shrivastava

Abstract Desalination, which makes up 1% of the world's total water use, requires a lot of energy, and energy costs make up the majority of operational costs. However, at the moment, a sizeable amount of the energy is produced by conventional fossil-fuel-fired power plants, which offer a serious environmental danger due to the greenhouse gas emissions produced during the production of the energy as well as the discharge of concentrated brine. Because of their advantageous thermo-physical and optical properties, nanofluids have been extensively exploited recently to enhance the performance of several energy systems. Nanofluid technology has helped solar distillation in particular as an economical and dependable method of providing fresh-water. The current developments and use of nanofluids in solar distillers have been the main focus of the review. A thorough conclusion has been reached, along with some suggestions for a futuristic strategy.

Keywords Desalination · PCM · Nanotechnology · Water · Energy · Exergy

1 Introduction

Everyone agrees that one of the most important elements on earth is water. A significant amount of water is consumed by a number of human activities, including agriculture, the production of power, sanitization, drinking, and many more. About 0.014% of the earth's water, which covers around 75% of it, is directly useable by humans. In fact, the majority of the water in the world (up to 97.5% of the total water on the planet) is preserved as salty seawater. It is thought that this extremely modest

R. Agrawal (✉) · K. Yugbodh

Department of Mechanical Engineering, Sagar Institute of Science, Technology and Research,
Sikandarabad, Ratibad, Bhopal, Madhya Pradesh, India
e-mail: rahulagrawal@sistec.ac.in

A. Shrivastava

Department of Mechanical Engineering, VIT Bhopal University, Bhopal-Indore Highway,
Kothrikalan, Sehore, M.P, India

ratio is sufficient to meet the demands of all the many forms of life and plants on our planet. But as the world's population grows quickly and unchecked (the average daily amount of drinking water is 5 L), the amount of freshwater accessible is decreasing while demand for it is rising sharply as a result of climate change, higher living standards, water source pollution, and the huge economic cycle.

While nearly 41% of the world's population lives in coastal regions with plenty of access to saltwater water, freshwater sources are scarce and there is a significant water deficit affecting more than 1 billion people [1]. It focuses mostly on the methods to recover freshwater [2]. Many attempts have been made to supply fresh drinkable water for drinking and other applications. Desalination is a popular method that turns salty water into fresh water, making it one of the practical ways to get fresh water [3]. As of now, the global desalination scope is around 67.6 million m³/d, and it is predicted to increase to over 100 million m³/d [4].

Saudi Arabia, with a total desalination capacity of 17.4%, the United States, with 16.2%, the United Arab Emirates, with 14.7%, Spain, with 6.4%, and Kuwait, with 5.8% are the nations with the highest capacity of desalination plants [5].

Desalination is a process used to make polluted or salty water suitable for drinking and other applications. It involves the use of a thermal, electrical, or membrane technology to remove dissolved contaminants from the water.

Phase transformation and continuous phase processes are the main components of desalination technology. Saline water was purified using heat energy during the phase change process. Phase change, which depends on the distillation process, is one of the traditional desalination methods. They are primarily divided into three categories: There are three different types of distillation: multi-effect distillation (MED), multi-stage flash distillation (MSF), and vapour compression (VC), which can be mechanical or thermal. Temperature and pressure reduction techniques are effectively included into MSF and MED processes. The MSF technique depends on the abrupt drop in pressure that happens when saline water is introduced into the evacuated chamber, which results in the production of water vapour. At a lower pressure, these actions are continually repeated. More steam is frequently required, typically at a temperature of around 100 °C. In MED, evaporation results from saline water absorbing heat energy (Fig. 1).

Solar desalination could be a practical solution in areas with a lot of natural sun radiation but unusable water for drinking and other purposes. Solar stills have cheap operating and maintenance costs, but their main disadvantage is that they produce little freshwater. Because of its exclusive dependence on solar energy and lack of reliance on other energy sources like gasoline and electricity, it may thus be utilised for water systems with lower capacity requirements that are also self-sustaining. With the exception of a few chilly and cloudy days, India has a hot climate and gets sun radiation for the majority of the year. As a result, it may be utilised for more than 80% of the 365 days in a year. Solar distillation utilise abundantly accessible solar radiation energy, but new emerging media, like nanotechnology/nanofluids, are needed to enhance their performance and applicability. The productivity improvement in solar still brought about by the association of nanotechnology is highlighted in the current

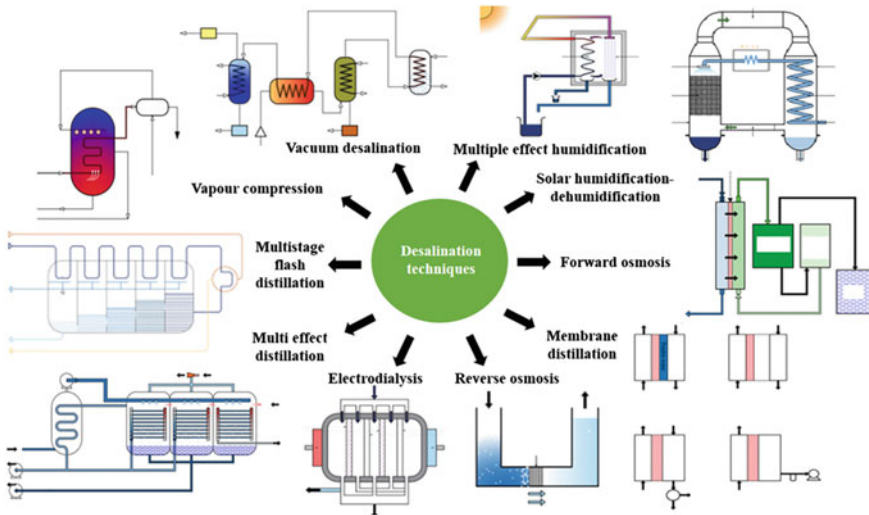


Fig. 1 Various types of desalination techniques [6–8]

research, and recommendations for the correct way to wrap up the ongoing work are also discussed.

2 Nanotechnology in Desalination

On the other side, nanotechnology interacts with a variety of material properties and basic concepts at the nanometre scale (10^{-9} m). When a material has at least one dimension that falls under the 1–100 nm range, it is referred to be “nano” [9]. Moreover, modifying materials to the nanometer range in an effort to create nanomaterials is included in the definition of nanotechnology. The two top-down and bottom-up techniques can be used to accomplish this [10]. In order to manage their assembly, smaller devices must be established using the top-down strategy, which involves breaking down larger ones. In contrast, complex assemblies are created using the bottom-up approach by organising smaller parts [11]. Since its inception in the 2000s, nanotechnology has been extensively used in countless applications. In underdeveloped nations, where this sort of nanotechnology is referred to as nanomedicine, it is utilised to prevent health problems and treat illnesses [12–14]. Nanotechnology is also used to create biosensors, and nanoceramic particles are now included in many consumer items to create smoother, heat-resistant surfaces and coatings [15].

Also, a lot of study publications have been published recently on different nanotechnologies created for desalination, but no researchers have shown the applications of many kinds of nanocomposites that have been created from distinct nanomaterials. This chapter discusses several nanotechnologies in terms of nanocomposites

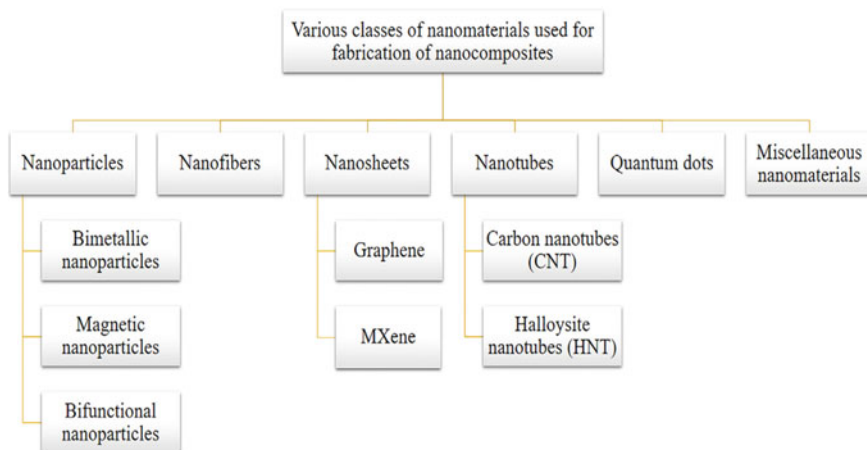


Fig. 2 Several kinds of nanoparticles used to make nanocomposites

that have recently been combined with conventional desalination methods to provide improved results. Several kinds of nanoparticles used to make nanocomposites are shown in Fig. 2.

3 Nanofluid Theory

The term “nanofluid” was originally used in 1995 by Choi [16]. It is simply described as a combination of basic fluids such as oil, water and ethylene glycol with solid metallic or metallic oxide nanoparticles. Due to their improved thermal characteristics, nanofluids represent a new generation of sophisticated fluids that improve heat transmission. As a result, they have been employed in several industrial and technical applications [17]. Researchers’ main focus throughout the first decade of nanofluids was on figuring out the thermophysical characteristics of these materials [18]. High thermal conductivity levels and effective radiation absorption are two characteristics of nanofluids. The diameter of nanoparticles is very small; typically, it falls within the range of 1–100 nm [19]. It is not advised to add large sized (greater than 100 nm) to the basic fluids since doing so would have a lot of negative effects.

4 Application of Nanofluid and Nanoparticles Solar Stills

In addition to research on improving the thermal characteristics of nanofluids for CSP power production, researchers have also thought about using nanofluids for effective thermal desalination procedures. In their trials, Sharshir et al. [20] employed

nanofluids to improve the productivity of three different solar stills. The concentrations of micro flakes in nanofluids varied from 0.125 to 2% at basin depths between 0.25 and 5 cm. Copper oxide and graphite micro-flakes had typical particle sizes of 1 μm and 1.2–1.3 μm , respectively. In comparison to standard models, the performance of the system was enhanced by 53.95% and 44.91%, respectively, by using CuO and graphite microparticles with glass cooling. The authors sought to increase production by altering the concentration of nanofluids, and they saw encouraging results, which are shown in Fig. 5.

Figure 3 shows that production is proportionally impacted by the weight concentration of the micro-flakes. Also, because graphite has a greater thermal conductivity than copper oxide, the graphite-based nanofluid solution increases productivity more than the copper oxide-based solution. Increased solar radiation absorption results from better thermal conductivity, which increases the thermal energy available for desalination. By dispersing Fe₃O₄-modified Multi-Walled Carbon Nanotubes (MWCNTs) nanoparticles in saline water, Chen et al. [21] created varied amounts of nanofluids. Inspired by the work of Manlin Wang and Lang Shao et al. [22, 23], MWCNTs of 8–15 nm diameter and 95% purity were modified to add magnetic characteristics. A two-step procedure was used to create the nanofluids at a variety of concentrations from 0 to 0.04 wt%. Also, the zeta potential of nanofluids was measured, and the results showed that while solutions had outstanding stability in pure water, they decreased when the water contained salt.

The experiment was carried out by considering dual slope solar still associated with different types of nanofluid such as water with a combination of copper oxide, aluminium oxide and titanium oxide nanoparticles as shown in Fig. 4 [13]. With a maximum efficiency of 50.34%, this model performs better when Al₂O₃ based on water is combined [24].

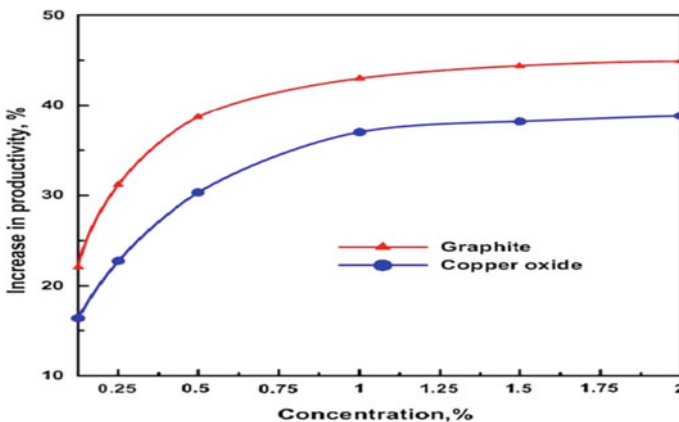


Fig. 3 The increase in productivity of solar stills with different nanofluid concentrations is shown [20]

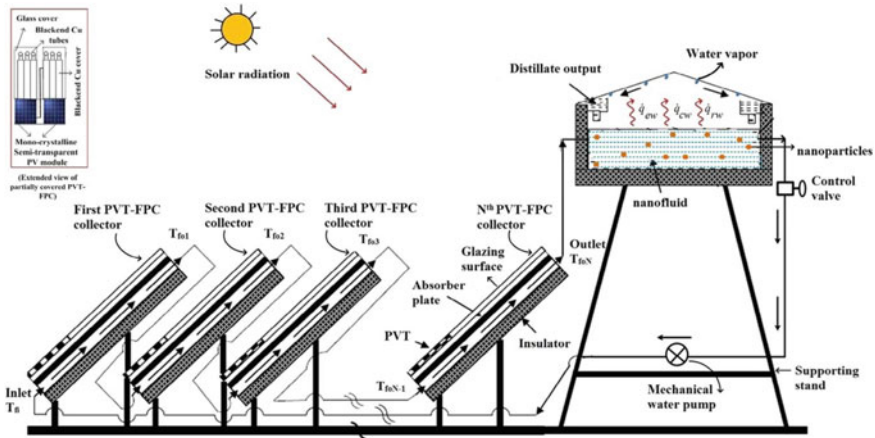


Fig. 4 Line diagram of an active double slope still using nanofluids without HHE [24]

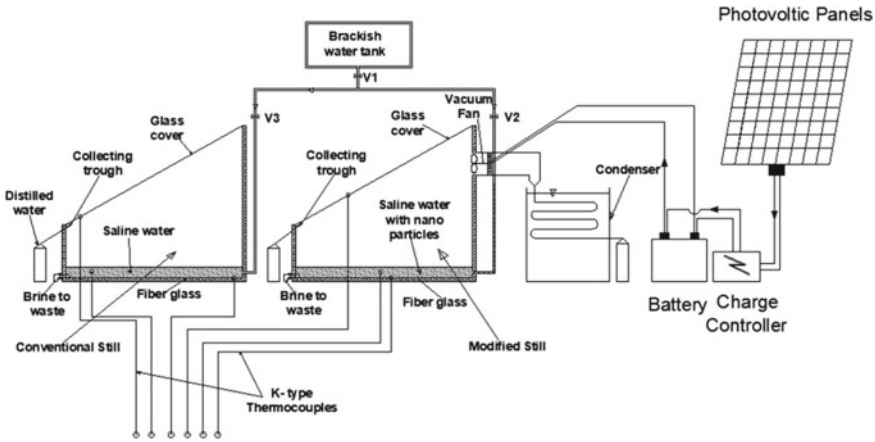


Fig. 5 Schematic representation of solar still associated with nanofluid and condenser [25]

Kabeel et al. in their experiment incorporated nanofluid (water + aluminium oxide) and condenser to enhance the productivity of solar still as shown in Fig. 5. The outcome is stated as a 53.2% improvement in freshwater yield with nanofluids only, while a 116% rise in yield is seen with an extra condenser [25].

Titanium oxide was employed by Panitapu et al. [26] as a nanomaterial in a solar still to increase its performance. According to their findings, employing nanofluid significantly raised the basin temperature over time compared to utilising merely water, as seen in Fig. 6. Also, they came to the conclusion that adding nanofluid to the still's basin raised the temperature of the water and glass cover temperature (Fig. 7).

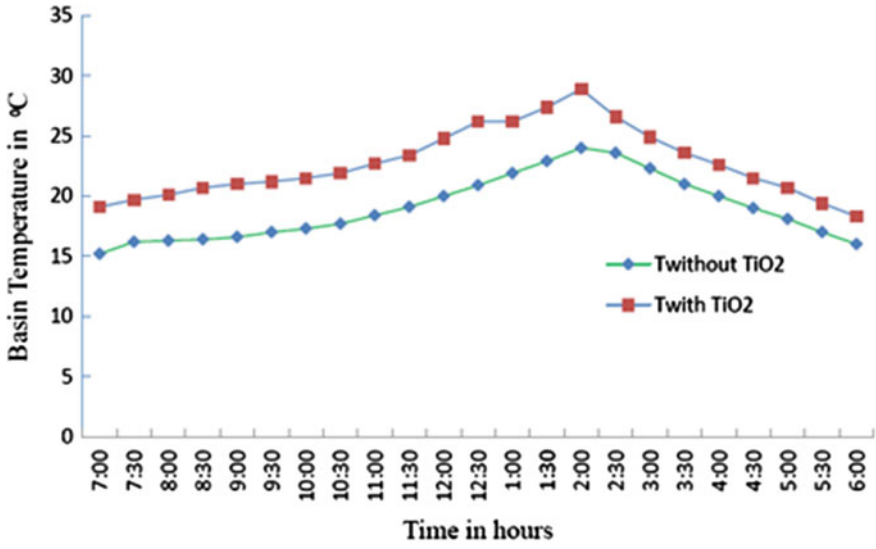


Fig. 6 Temporal fluctuation of the basin temperature of both cases [26]



Fig. 7 Image of the experimental setup of solar still [27]

Elango et al. [27] carried out an investigation study to examine the comparative analysis of solar still using water nanofluids of different types. As a basin fluid, four different types of nanofluids—zinc oxide/water, aluminium oxide/water, iron oxide/water and tin oxide/water—were used. They noted that stills filled with nanofluid made of tin oxide and zinc oxide produced 18.63% and 12.67% more than stills filled with regular water, respectively, while stills filled with aluminium oxide/water nanofluid suggested a greater production (29.95%) (Fig. 9).

By using phase (PCM), glass cover cooling and flake graphite nanoparticles (FGN), Sharshir et al. [28] improved the productivity of a typical solar still (Fig. 8). They found that when the three preceding improvements were used combined, productivity rose by roughly 73.8% as compared to the traditional still.

Theoretical research by Sahota and Tiwari [29] examined the impact of aluminium oxide nanoparticles at varying mass fractions of (0.04, 0.08, and 0.12%) on the productivity of solar still. In their analysis, two alternative water mass values were employed (35 and 80 kg). The findings showed that when the quantity of nanoparticles grew, the distillate yield also increased.

Using the aluminium oxide–water nanofluid shown in Fig. 9, Kabeel et al. [25, 30] made an experimental attempt to increase productivity by merging the still with an external condenser. According to their findings, adding the external condenser boosted the output by 53.22%. Whereas employing nanofluid raised this sort of stills' production by roughly 116%.

For design and operational parameters, Methre [31] carried out an exergy study of solar stills combined with NPCM. In melting paraffin wax, aluminium nanomaterials

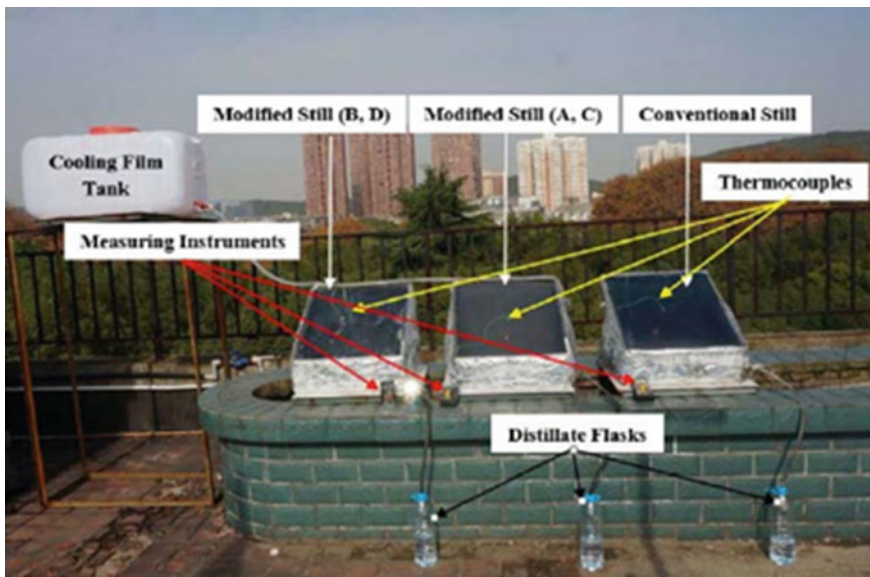


Fig. 8 Experimental setup of modified solar still [28]



Fig. 9 Image of the traditional and developed stills [25, 30]

(50 nm) are disseminated by weight ratio. The greatest instantaneous total energy and exergy efficiency, as well as the hourly output, were found to be 49.29, 9.48%, and 0.69 L/m², respectively. It is discovered that the daily averages for energy efficiency, productivity, and exergy are 30.42, 4.93% and 4.17 L/day, respectively [31].

Dsilva studies how NPCM affects the productivity and operation of solar stills. TiO₂, CuO and GO nanoparticles were each independently impregnated at 0.3 weight percent in paraffin. Four solar stills (CSS)—paraffin (PSS), paraffin-TiO₂ (PSS-1), paraffin-CuO (PSS-2) and paraffin-GO (PSS-3)—were used in the experiments. CSS, PSS-1, PSS-2 and PSS-3 produced 3.83, 4.83, 5.17, and 3.54 l/m²/day, respectively. This translates to 26 and 35% productivity gains over CSS for PSS-1 and 2 [32].

5 Conclusion

The following findings are derived from the overall assessment of solar distillation systems combined with nanofluids in the current study:

- When compared to traditional desalination systems, the overall performance of solar distiller units containing nanofluids is consistently shown to be superior.
- In comparison to active single slope solar stills with external condenser, active single solar distillation systems with flake nanoparticles, phase change material and thin film cooling perform better.

- By adding nanoparticles to the water, it is feasible to raise the solar still's output from 50 to 70%.
- More research is needed to determine whether using nanofluids in solar stills is reliable from an economic and environmental standpoint.

References

1. Kabeel AE, Hamed MH, Omara ZM, Sharshir SW (2014) Experimental study of a humidification-dehumidification solar technique by natural and forced air circulation. *Energy* 68:218–228. <https://doi.org/10.1016/j.energy.2014.02.094>
2. Velmurugan V, Gopalakrishnan M, Raghu R, Srithar K (2008) Single basin solar still with fin for enhancing productivity. *Energy Convers Manage* 49:2602–2608. <https://doi.org/10.1016/j.enconman.2008.05.010>
3. Nijmeh S, Odeh S, Akash B (2005) Experimental and theoretical study of a single- basin solar still in Jordan. *Int Commun Heat Mass Transfer* 32:565–572. <https://doi.org/10.1016/j.icheatmasstransfer.2004.06.006>
4. Government of India (2006) Report of the working group on water resources for the XI five year plan (2007–2012). Ministry of Water Resources Government of India, New Delhi, India
5. Rabiee H, Khalilpour KR, Betts JM, Tapper N (2019) Energy-water nexus: renewable integrated hybridized desalination systems. *Polygener Polystorage Chem Energy Hubs* 409–458. <https://doi.org/10.1016/b978-0-12-813306-4.00013-6>
6. Hussien AA, Abdullah MZ, Al-Nimr MA (2016) Single-phase heat transfer enhancement in micro/mini channels using nanofluids: theory and applications. *Appl Energy* 164:733–755. <https://doi.org/10.1016/j.apenergy.2015.11.099>
7. Hai F, Nguyen L, Nghiem L, Liao BQ, Koyuncu I, Price W (2015) Trace organic contaminants removal by combined processes for wastewater reuse, pp 1–39. https://doi.org/10.1007/698_2014_318
8. Abu-Zeid MAE, Zhang Y, Dong H, Zhang L, Chen HL, Hou L (2015) A comprehensive review of vacuum membrane distillation technique. *Desalination* 356:1–14. <https://doi.org/10.1016/j.desal.2014.10.033>
9. Stanford BD, Leising JF, Bond RG, Snyder SA (2010) Chapter 11 inland desalination: current practices, environmental implications, and case studies in Las Vegas, NV. *Sustain Water Futur Water Recycl Desalin* 327–350. [https://doi.org/10.1016/s1871-2711\(09\)00211-6](https://doi.org/10.1016/s1871-2711(09)00211-6)
10. Schummer J (2004) Multidisciplinarity, interdisciplinarity, and patterns of research collaboration in nanoscience and nanotechnology. *Scientometrics* 59:425–465. <https://doi.org/10.1023/B:SCIE.0000018542.71314.38>
11. Brady PV, Mayer T, Cygan RT (2011) Nanotechnology applications to desalination: a report for the joint water reuse & desalination task force. Office of Scientific and Technical Information. <https://doi.org/10.2172/1011669>
12. Kostoff RN, Koytcheff RG, Lau CGY (2007) Global nanotechnology research literature overview. *Technol Forecast Soc Chang* 74:1733–1747. <https://doi.org/10.1016/j.techfore.2007.04.004>
13. Kostoff RN, Stump JA, Johnson D, Murday JS, Lau CG, Tolles WM (2005) The structure and infrastructure of the global nanotechnology literature. Defense Technical Information Center. <https://doi.org/10.21236/ada435984>
14. Jayasena B, Subbiah S (2011) A novel mechanical cleavage method for synthesizing few-layer graphenes. *Nanoscale Res Lett* 6:95. <https://doi.org/10.1186/1556-276X-6-95>. (PubMed: 21711598)
15. Crandall BC, Lewis J (1992) *Nanotechnology: research and perspectives*. The MIT Press. <https://doi.org/10.7551/mitpress/4838.001.0001>

16. Choi S (1995) Enhancing thermal conductivity of fluids with nanoparticles. In: ASME international mechanical engineering congress and exposition. San Francisco, USA, pp 99–105
17. Chand R, Rana G, Hussein AK (2015) On the onset of thermal instability in a low Prandtl number nanofluid layer in a porous medium. *J Appl Fluid Mech* 8:265–272. <https://doi.org/10.18869/acadpub.jafm.67.221.22830>
18. Kasaiean A, Toghi Eshghi A, Sameti M (2015) A review on the applications of nanofluids in solar energy systems. *Renew Sustain Energy Rev* 43:584–598
19. Kolsi L, Hussein AK, Borjini MN, Mohammed HA, Aïssia HB (2014) Computational analysis of three-dimensional unsteady natural convection and entropy generation in a cubical enclosure filled with water- Al_2O_3 nanofluid. *Arab J Sci Eng* 39:7483–7493. <https://doi.org/10.1007/s13369-014-1341-y>
20. Sharshir SW, Guilong P, Lirong W, Nuo Y, Essa FA, Elsheikh AH, Mohamed SIT, Kabeel AE (2017) Enhancing the solar still performance using nanofluids and glass cover cooling: experimental study. *Appl Therm Eng* 113:684–693
21. Chen W, Zou C, Li X, Liang H (2017) Application of recoverable carbon nanotube nanofluids in solar desalination system: an experimental investigation. *Desalination*
22. Wang M, Fang G, Liu P, Zhou D, Ma C, Zhang D, Zhan J (2016) Fe_3O_4 @ β -cd nanocomposite as heterogeneous Fenton-like catalyst for enhanced degradation of 4-chlorophenol (4-CP). *Appl Catal B* 188:113–122. <https://doi.org/10.1016/j.apcatb.2016.01.071>
23. Shao L, Wang XF, Ren YM, Wang SF, Zhong JR, Chu MF, Tang H, Luo LZ, Xie DH (2016) Facile fabrication of magnetic cucurbit [6]uril/graphene oxide composite and application for uranium removal. *Chem Eng J* 286:311–319. <https://doi.org/10.1016/j.cej.2015.10.062>
24. Sahota L, Shyam GN, Tiwari GN (2017) Analytical characteristic equation of nanofluid loaded active double slope solar still coupled with helically coiled heat exchanger. *Energy Convers Manage* 135:308–326. <https://doi.org/10.1016/j.enconman.2016.12.078>
25. Kabeel AE, Omara ZM, Essa FA (2014) Enhancement of modified solar still integrated with external condenser using nanofluids: an experimental approach. *Energy Convers Manage* 78:493–498. <https://doi.org/10.1016/j.enconman.2013.11.013>
26. Panitapu B, Koneru V, Sagi S, Parik A, Solar distillation using nanomaterial. *Int J Sci Eng Technol* 3:583–587
27. Elango T, Kannan A, Kalidasa Murugavel K (2015) Performance study on single basin single slope solar still with different water nanofluids. *Desalination* 360:45–51. <https://doi.org/10.1016/j.desal.2015.01.004>
28. Sharshir SW, Peng G, Wu L, Essa FA, Kabeel AE, Yang N (2017) The effects of flake graphite nanoparticles, phase change material, and film cooling on the solar still performance. *Appl Energy* 191:358–366. <https://doi.org/10.1016/j.apenergy.2017.01.067>
29. Sahota L, Tiwari GN (2016) Effect of Al_2O_3 nanoparticles on the performance of passive double slope solar still. *Sol Energy* 130:260–272. <https://doi.org/10.1016/j.solener.2016.02.018>
30. Kabeel A, Omara Z, Essa F (2013) Enhancement of modified solar still integrated with external condenser using nanofluids: an experimental approach. In: Seventeenth international water technology conference (IWTC17), vol 89. Istanbul, Turkey, pp 1–9
31. Methre VK, Eswaramoorth M (2015) Exergy analysis of the solar still integrated nano composite phase change materials. *Appl Solar Energy* 99–106:51
32. Rufuss DW, Suganthi L, Iniyan S, Davies PA (2018) Effects of nanoparticle-enhanced phase change material (NPCM) on solar still productivity. *J Clean Prod* 9–29:192

Chapter 10

Mixed Convective Flow on Nanoparticle Shape Effects Over a Stretching Sheet



R. Hemalatha, Peri K. Kameswaran, and P. Sibanda

Abstract The main objective of the present investigation is the theoretical study of the impact of nanoparticle shapes on mixed convective flow on a stretching sheet. In this study, the incorporated nanoparticles and their shapes are SiO_2 , TiO_2 and these are platelet and cylindrical shaped, respectively. The basic equations are solved using the shooting method. For some special cases, we denoted similarities between the current results and the accessible findings in the literature. The influence of the shapes of the nanoparticles on the flow of the fluid, heat transfer, and temperature is presented and discussed.

Keywords Casson fluid · Mixed convection · Nanoparticles · Nanoparticle shape effect

1 Introduction

An analysis of the two-dimensional boundary layer flow over a stretching surface plays a significant role in other processes, the cooling of a metal plate in a bath, glass fiber production, melt-spinning, oil product transportation, and polymer processing. Muthukumaran and Bathrinathan [1] analyzed mixed convection near a stagnation point flow for both aiding and opposing flows. In both assisting and opposing flows, increasing the Prandtl number leads to an increase in the rate of heat transfer. In

R. Hemalatha

Department of Mathematics, Siddhartha Institute of Science and Technology, Puttur 517583, India

P. K. Kameswaran (✉)

Department of Mathematics, School of Advanced Sciences, Vellore Institute of Technology, Vellore 632014, India

e-mail: perikamesh@gmail.com

P. Sibanda

School of Mathematics, Statistics and Computer Science, University of KwaZulu-Natal, Private Bag X01 Scottsville 3209, Pietermaritzburg, South Africa

e-mail: sibandap@ukzn.ac.za

aiding flow, the skin friction decreases with an increase in the Prandtl number. In opposing flow, the skin friction increases with the Prandtl number. The magneto-hydrodynamic nanofluid flow on a stretching sheet with heat and mass transfer was analyzed by Nandeppanavar and Mahantesh [2]. They investigated the temperature profile, nanoparticle volume fraction on the flow field subjected to velocity slip, a magnetic field, and particle thermophoresis. Khan and Pop [3] investigated thermophoresis and Brownian motion effects on a stretching sheet in a nanofluid flow. They obtained the results that showed that for each dimensionless number, there is a reduction in the Nusselt number. When the Prandtl number increases, there is an enhancement in the Sherwood number. Ishak et al. [4] explored the flow of a fluid and temperature near a stagnation point. They obtained a unique solution for the aiding flow, for the opposing flow they obtained dual solutions, and for different parameters the heat transfer rate was calculated.

Vajravelu et al. [5] analyzed mixed convective flow in a non-Newtonian fluid. They analyzed the properties of the Casson fluid and determined the effects of the mixed convection parameter, velocity exponent parameter, and thermal conductivity parameter on the fluid flow structure. The heat and mass transfer in the convective boundary flow with the Hall effect was analyzed by Ashraf et al. [6]. They obtained results that showed that the flow of the fluid and the momentum boundary layer thickness reduces in the opposing flow and the contrary is observed in the aiding flow. Mahanta and Shaw [7] examined the properties of a three-dimensional Casson fluid over a porous medium. They found that the velocity profiles decreased with the Casson fluid parameter, magnetic field, and porosity parameters. The increase in the Casson fluid parameter reduces the skin friction which, however, increased with the stretching ratio parameter. Mustafa and Khan [8] studied Casson fluid with magnetic field effects. They showed that the Casson fluid has relatively higher skin friction coefficients as compared with a Newtonian fluid. The magnetic field enhances the skin friction coefficient leading to a decrease in the flow velocity. The transfer of heat and mass in Casson fluid flow was studied by Kameswaran et al. [9]. They reported that when the Soret number increases, the concentration boundary layer thickness also increases. For the Casson parameter, the mass transfer and skin friction increase.

Narayana et al. [10] analyzed Jeffrey fluid flow on a porous medium and calculated the changes in the temperature and velocity profiles. They noted that the thermal boundary layer and temperature increase with increases in viscous dissipations.

In the presence of a chemical reaction, mass transfer, and boundary layer flow were analyzed by Bhattacharyya [11]. The result showed that the first solution has a thinner boundary layer thickness as compared to the second solution. When there is an enhancement in the Schmidt number, then the boundary layer thickness decreases. Hemalatha and Kameswaran [12] examined the effect of the shapes of nanoparticles in flow over an impermeable wall. They found that aluminium-oxide blade-shaped nanoparticles have broader velocity profiles as compared to ferrous-oxide-, brick- and blade-shaped nanoparticles. The entropy generation and heat transfer in silver nanofluid were studied by Rashid et al. [13]. They noted a temperature enhancement for lamina-shaped particles and the opposite for sphere-shaped particles in flow with entropy generation. The platelet-, cylindrical-, blade-, and brick-shaped effects of

Al_2O_3 and Cu nanoparticles are examined by Gireesha and Archana [14]. They showed that the fluid temperature is lower in the case of cylindrical-shaped particles than the platelet-shaped particles. The Al_2O_3 nanoparticles gave less prominent temperature profiles as compared with Cu nanoparticles. The influence of nanoparticle shapes on non-Darcy flow with variable permeability was analyzed by Hemalatha and Kameswaran [15]. They observed that the ferrous oxide sphere-shaped particles are more efficient in transferring heat and in increasing the velocity than Cobalt disc-shaped particles. Using the nanoparticles Cu, TiO_2 , Ag, Al_2O_3 , Fe_3O_4 and the base fluid $\text{C}_2\text{H}_6\text{O}_2$ and H_2O , the impact of the different shapes of nanoparticles was studied by Gul et al. [16]. When there is an increase in the nanoparticle volume fraction leads to a decrease in velocity. The flow of the fluid is more vigorous for brick- and blade-shaped particles as compared with platelet- and cylindrical-shaped nanoparticles.

Building on the limited number of studies in the literature that have explored, the impact of nanoparticle shape on the flow behavior and structure, in this article we explore the shape effect of nanoparticles near the stagnation point flow of a stretching/shrinking sheet with a heat source/sink.

2 Mathematical Model

In this problem, we considered steady, incompressible two-dimensional Casson fluid flow near the stagnation point over a stretching sheet. The components of the fluid velocity in the x and y -directions are defined as u and v , respectively. The flow is generated by the stretching sheet, due to the application of two equal forces along the x -axis. The origin is fixed, by assuming a linear velocity $u_e(x) = a_0x$ the surface is stretched, where a_0 is a constant for the stretching sheet and $a_0 > 0$ (Fig. 1).

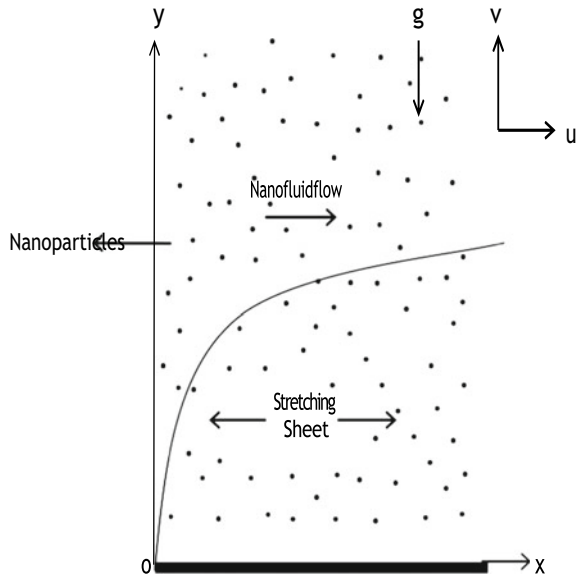
The rheological equation of state for an isotropic and incompressible Casson fluid can be written as

$$\tau_{ij} = \begin{cases} (\mu_B + \tau_y \sqrt{2\pi}) 2e_{ij}, & \pi > \pi_c \\ (\mu_B + \tau_y \sqrt{2\pi_c}) 2e_{ij}, & \pi < \pi_c \end{cases} \quad (1)$$

where μ_B is the plastic dynamic viscosity of the Casson fluid, τ_y is the yield stress, π is the product of the component of deformation rate, namely $\pi = e_{ij}e_{ij}$, e_{ij} is the (i, j) th component of the deformation rate, and π_c is the critical value of π . By using the above assumptions, the Navier–Stokes equations and the boundary conditions can be written as (Ishak et al. [17])

$$\frac{\partial u}{\partial x} + \frac{\partial v}{\partial y} = 0, \quad (2)$$

Fig. 1 Geometry of the problem



$$u \frac{\partial u}{\partial x} + v \frac{\partial v}{\partial y} = u_e \frac{du_e}{dx} + \frac{\mu_{nf}}{\rho_{nf}} \left(1 + \frac{1}{\beta} \right) \frac{\partial^2 u}{\partial y^2} + \frac{\phi \rho_s \beta_s + (1 - \phi) \rho_f \beta_f}{\rho_{nf}} g (T - T_\infty), \tag{3}$$

$$u \frac{\partial T}{\partial x} + v \frac{\partial T}{\partial y} = \frac{k_{nf}}{(\rho C_p)_{nf}} \frac{\partial^2 T}{\partial y^2} + \frac{Q}{(\rho C_p)_{nf}} (T - T_\infty). \tag{4}$$

$$u = u_w(x) = cx, \quad v = 0, \quad T = T_w(x) = T_\infty + b_1 x, \quad \text{at } y = 0,$$

$$u \rightarrow u_e(x) = a_0 x, \quad T \rightarrow T_\infty, \quad \text{at } y \rightarrow \infty, \tag{5}$$

Equation (2) is satisfied by defining the stream function $\psi(x, y)$, such that

$$u = \frac{\partial \psi}{\partial y} \quad \text{and} \quad v = -\frac{\partial \psi}{\partial x}.$$

where $\psi = (a_0 v_f)^{\frac{1}{2}} x f(\eta)$, $f(\eta)$ is the dimensionless stream function and $\eta = \left(\frac{a_0}{v_f}\right)^{\frac{1}{2}} y$.

The velocity and temperature components are given by

$$u = a_0 x f'(\eta), \quad v = -(a_0 v_f)^{\frac{1}{2}} f(\eta), \quad T - T_\infty = \Delta T \theta(\eta). \tag{6}$$

The effective thermal conductivity and the dynamic viscosity of the nanofluid are (Hamilton and Crosser [18])

$$k_{nf} = k_f \left[\frac{k_s + (n-1)k_f + (n-1)(k_s - k_f)\phi}{k_s + (n-1)k_f - (k_s - k_f)\phi} \right] \quad (7)$$

$$\mu_{nf} = \mu_f (1 + a\phi + b\phi^2) \quad (8)$$

Here, a and b are the nanoparticle shape constants, k_s , k_f , μ_f are the thermal conductivity of the solid nanoparticles, base fluid, and dynamic viscosity of base fluid, ϕ is the nanoparticle volume fraction of the fluid (Table 1) and the empirical shape factor is $n = -\frac{3}{\psi_0}$, where ψ_0 represents the sphericity (Table 2).

By applying Eqs. (6)–(8), Eqs. (2)–(5) were converted into the two-point boundary value problem.

$$(1 + a\phi + b\phi^2) \left(1 + \frac{1}{\beta} \right) f''' + A_2 \lambda \theta + A_1 f f'' - A_1 f'^2 + A_1 = 0 \quad (9)$$

$$\theta'' + Pr \left(\frac{k_f}{k_{nf}} \right) [(f\theta' - f'\theta)A_3 + \beta_1 \theta] = 0 \quad (10)$$

$$f(0) = 0, \quad f'(0) = \frac{c}{a_0}, \quad f'(\infty) \rightarrow 1, \quad (11)$$

$$\theta(0) = 1, \quad \theta(\infty) \rightarrow 0. \quad (12)$$

The primes denote differentiation in terms of η . Equations (9) and (10) contain non-dimensional constants. The mixed convection parameter is λ , the heat source/sink parameter is β_1 , and the Prandtl number Pr

where

$$\lambda = \frac{g\beta_f b_0}{a_0^2}, \quad \beta_1 = \frac{Q}{(\rho C_p)_f a_0}, \quad Pr = \frac{v_f (\rho C_p)_f}{k_f}$$

$$A_1 = 1 - \phi + \phi \left(\frac{\rho_s}{\rho_f} \right), \quad A_2 = 1 - \phi + \phi \left(\frac{\rho_s \beta_s}{\rho_f \beta_f} \right), \quad A_3 = 1 - \phi + \phi \left(\frac{(\rho C_p)_s}{(\rho C_p)_f} \right) \quad (13)$$

Table 1 Thermophysical properties of water, silicon dioxide and titanium oxide, Giressha and Archana [14]

Property	Water	SiO ₂	TiO ₂
ρ	997.1	2220	4250
C_p	4179	745	686.2
k	0.613	1.4	8.9538
β	21×10^{-5}	5.5×10^{-6}	0.9×10^{-5}

Table 2 For the different nanoparticle shapes, the sphericity and empirical shape factor are taken from Giressha and Archana [14]

Model	Platelet	Cylinder
a	37.1	13.5
b	612.6	904.4
ψ_0	0.52	0.62

2.1 The Skin Friction Coefficient

Skin friction C_f is the quantity of practical interest in this investigation. The skin friction coefficient is

$$C_f \text{Re}_x^{\frac{1}{2}} = \left(1 + \frac{1}{\beta}\right) f''(0), \tag{14}$$

where $\text{Re}_x = \frac{xu_e(x)}{\nu_f}$ and $\beta = \left(\mu_B + \frac{\tau_y}{\sqrt{2\pi c}}\right)$.

2.2 Coefficient of Heat Transfer

The dimensionless Nusselt number is expressed as

$$\frac{Nu_x}{\sqrt{\text{Re}_x}} \left(\frac{k_f}{k_{nf}}\right) = -\theta'(0) \tag{15}$$

3 Validation of Results

The system of ODEs (9)–(10) with respect to boundary conditions (11)–(12) were solved numerically using the MATLAB bvp4c solver. The results obtained are similar to the results obtained by Kameswaran et al. [9], Bhattacharyya [11], Ishak et al. [17] in the absence of certain parameters. The validation of the current results in relation to the literature is shown in Table 3 when $\beta = \lambda = 0$.

Table 3 Comparison of $f''(0)$ values with Kameswaran et al. [9], Bhattacharyya [11], Ishak et al. [17] for $Pr = 6.2, \lambda = 0, \beta = 10^8, \beta_1 = 0$

c/a	Present	Kameswaran et al. [9]	Bhattacharyya [11]	Ishak et al. [17]
-0.25	1.4022408	1.4022408	1.4022405	1.402241
-0.50	1.4956698	1.4956698	1.4956697	1.495670
-0.75	1.4892982	1.4892982	1.4892981	1.489298
-1.00	1.3288169	1.3288169	1.3288169	1.328817
-1.15	1.0822312	1.0822312	1.0822316	1.082231
-1.20	0.9324734	0.9324734	0.9324728	0.932474
-1.2465	0.5842817	0.5842817	0.5842915	0.584295

4 Discussion of the Results

Figures 2 and 3 show the velocity profiles using TiO_2, SiO_2 nanoparticles with platelet and cylindrical shapes. In Fig. 2, the TiO_2 platelet-shaped particles at the mixed convection parameter 2.0 show a velocity slightly higher than for the cylindrical-shaped particles, and the same phenomena is observed in the case of SiO_2 nanoparticles in Fig. 3. It is clear that the flow of the fluid is faster for increasing the values of the mixed convection parameters, the same result was observed by Ellahi et al. [19].

Figures 4 and 5 depict the fluid properties with respect to the effects of the nanoparticle volume fraction and shape factor for the TiO_2 nanoparticles. It is observed that the velocity is slightly higher for platelet-shaped particles when the volume fraction is 0.1 than is the case for cylindrical-shaped particles. The flow of the fluid

Fig. 2 Effect of mixed convection and nanoparticle shape factor on the flow of the fluid for titanium dioxide, when $\beta = 3.1, Pr = 6.2, \beta_1 = 0.2, c/a = 1.25, \phi = 0.01$

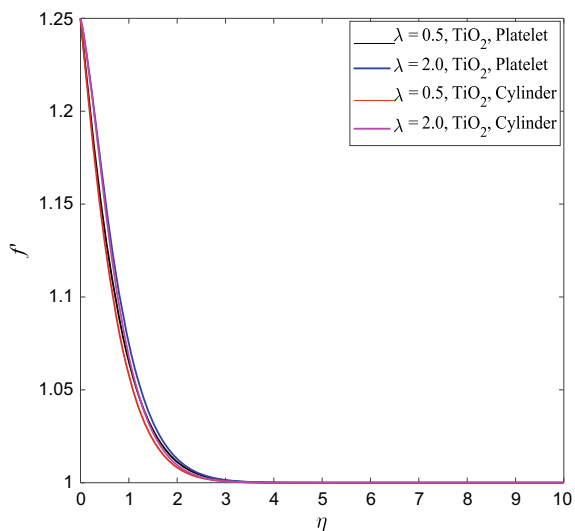
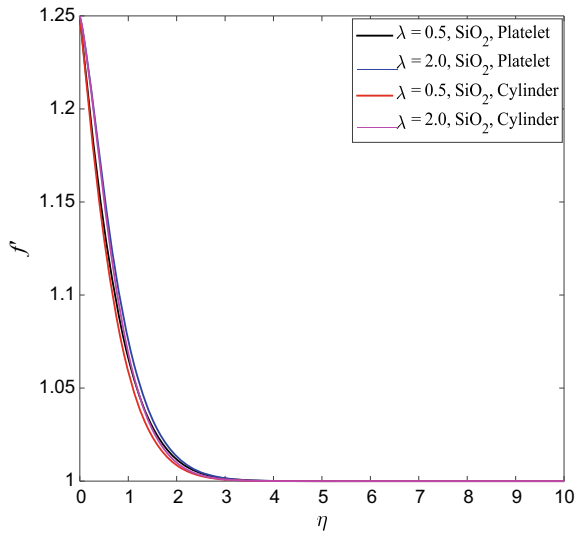


Fig. 3 Effect of mixed convection and nanoparticle shape factor on the velocity profile for silicon dioxide, when $\beta = 3.1$, $Pr = 6.2$, $\beta_1 = 0.2$, $c/a = 1.25$, $\phi = 0.01$



velocity increases with the nanoparticle volume fraction, with a slight increment in the velocity for platelet-shaped particles. The temperature is enhanced in the case of TiO_2 platelet-shaped particles than for the cylindrical-shaped particles. It can be practically explained that the suspension of nanoparticles in a base fluid leads to an enhancement in thermal conductivity. So, with an increase in the volume fraction, the temperature rises.

Fig. 4 Velocity profile for nanoparticle shape factor and volume fraction effects for the titanium dioxide nanoparticle, when $\beta = 3.1$, $Pr = 6.2$, $\beta_1 = 0.2$, $c/a = 1.25$, $\lambda = 2$

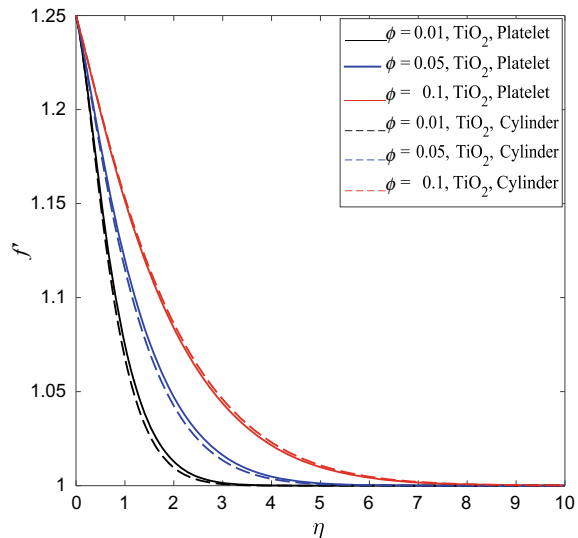


Fig. 5 Nanoparticle shape factor and volume fraction effects on the temperature distribution for titanium dioxide nanoparticle, when $\beta = 3.1$, $Pr = 6.2$, $\beta_1 = 0.2$, $c/a = 1.25$, $\lambda = 2$

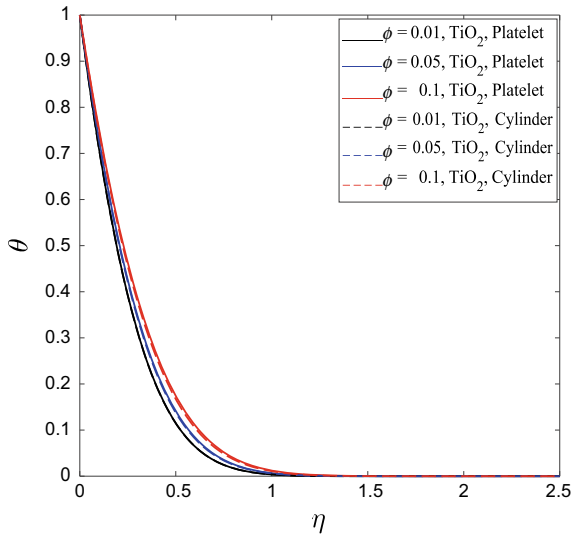


Figure 6 describes the velocity with changes in the shape factor and volume fraction for SiO₂ nanoparticles. It is clear that increasing the volume fraction of both platelet- and cylindrical-shaped particles leads to higher flow velocities compared with smaller volume fractions, the same result was reported by Ali et al. [20] for the secondary velocity. A slight enhancement of velocity is observed in the case of cylindrical shape.

Fig. 6 Nanoparticle shape factor and volume fraction effects on the velocity profile for Silicon dioxide nanoparticle, when $\beta = 3.1$, $Pr = 6.2$, $\beta_1 = 0.2$, $c/a = 1.25$, $\lambda = 2$

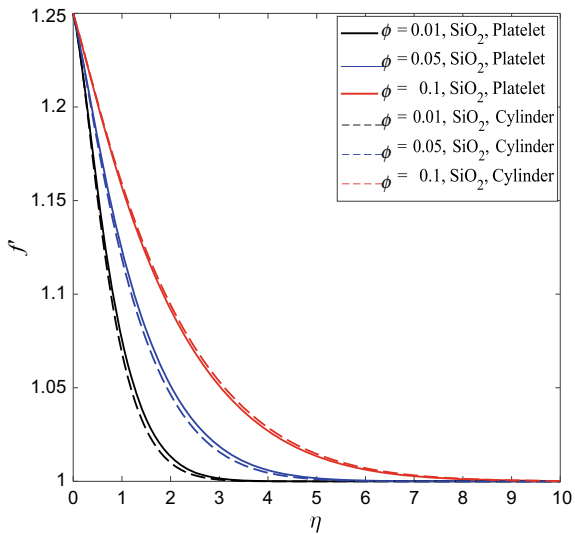
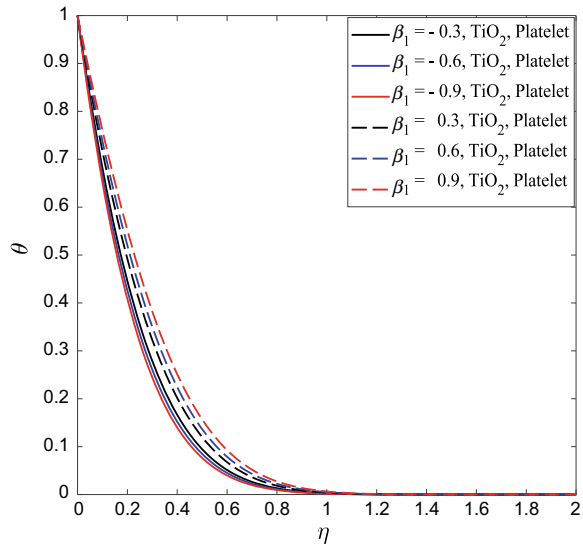


Fig. 7 Variations of temperature for different heat source/sink parameters β_1 , when $\lambda = 2$, $\beta = 3.1$, $Pr = 6.2$, $c/a = 1.25$, $\phi = 0.01$



The effect of the shape factor and the heat source parameter on temperature in the case of TiO_2 particles is described in Figs. 7 and 8. It is observed that for both the platelet- and cylindrical-shaped particles there is a high temperature in the case of positive values of the heat source parameter. In the sink case, the temperature is low for both shapes of the TiO_2 nanoparticles. It is well understood that a positive heat source directly increases the temperature, so as the strength of the heat source increases the temperature is expected to increase. The same phenomena are observed in the case of SiO_2 nanoparticles as shown in Figs. 9 and 10.

Figures 11 and 12 describe the velocity profiles for the TiO_2 and SiO_2 platelet and cylindrical nanoparticles with the variation in the Casson parameter. It is observed that for increasing values of the Casson parameter, the velocity decreases. Increasing the Casson parameter produces resistance in the flow of the fluid. The platelet-shaped particles show a higher enhancement in velocity than the cylindrical-shaped particles due to their elongated and thin shape.

The variation in skin friction coefficient with the different volume fractions and heat source/sink parameter for the TiO_2 nanoparticles is described in Figs. 13 and 14. It is observed that for the sink parameter the skin friction increases regardless of the shapes of nanoparticles. By increasing the nanoparticle volume fraction the fluid density increases, which leads to a decrease in fluid velocity. With an increase in the velocity, the drag force also increases. So, for increasing values of the sink parameter the skin friction increases. For the source parameter, the velocity is low as compared to the sink parameter which leads to the lower performance in skin friction. The same phenomenon is observed in the case of SiO_2 nanoparticles.

The variation in heat transfer coefficient for different volume fractions and heat source/sink parameter for TiO_2 platelet and cylindrical nanoparticles is depicted in Figs. 15 and 16. It is noticed that for increasing values of sink parameter the

Fig. 8 Variations of temperature for different heat source/sink parameters β_1 , when $\lambda = 2$, $\beta = 3.1$, $Pr = 6.2$, $c/a = 1.25$, $\phi = 0.01$

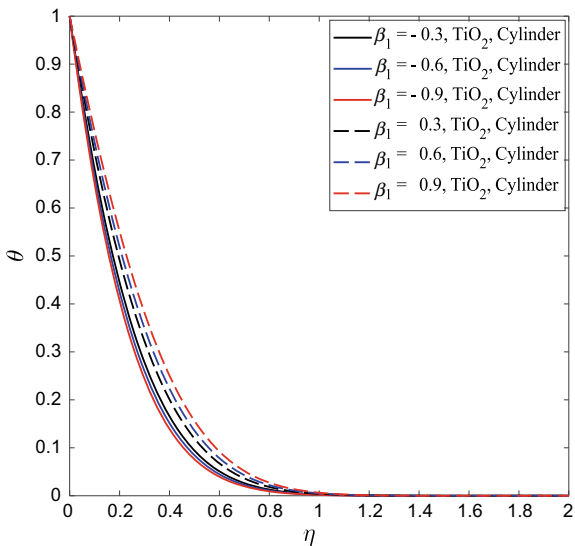
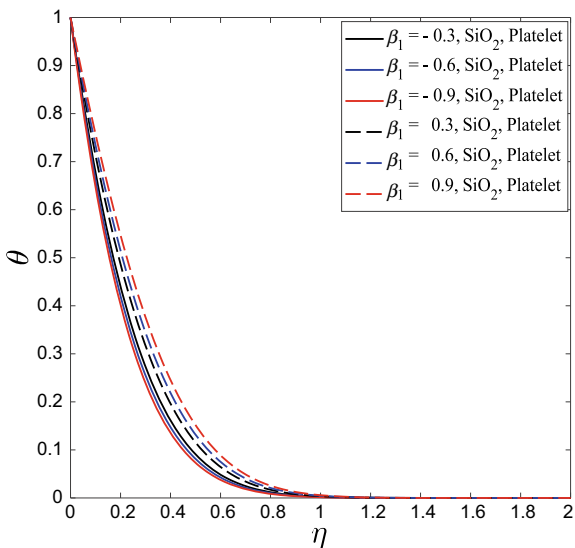


Fig. 9 Variations of temperature for different heat source/sink parameters β_1 , when $\lambda = 2$, $\beta = 3.1$, $Pr = 6.2$, $c/a = 1.25$, $\phi = 0.01$



heat transfer rate increases. For increasing nanoparticle volume fraction there is a reduction in heat transfer due to the increase in density. The same results are observed for SiO_2 platelet- and cylindrical-shaped nanoparticles.

The variation in skin friction coefficient for various volume fractions and Casson parameter for TiO_2 platelet- and cylindrical-shaped particles is shown in Fig. 17. We note that, for increasing values of the Casson parameter the skin friction increases. The variation in heat transfer for the TiO_2 platelet- and cylindrical-shaped particles

Fig. 10 Variations of temperature for different heat source/sink parameters β_1 , when $\lambda = 2$, $\beta = 3.1$, $Pr = 6.2$, $c/a = 1.25$, $\phi = 0.01$

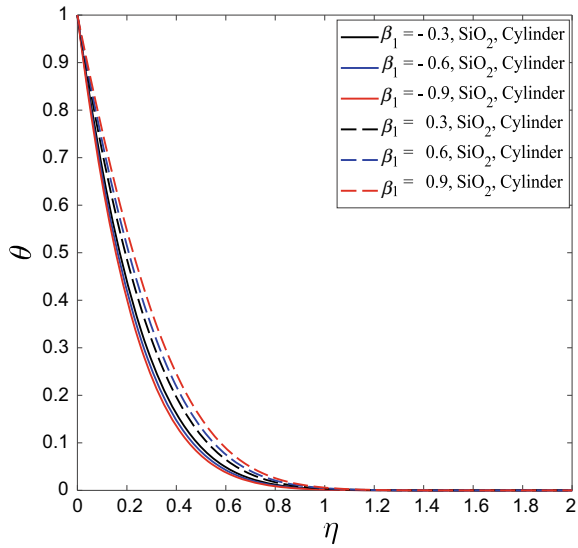
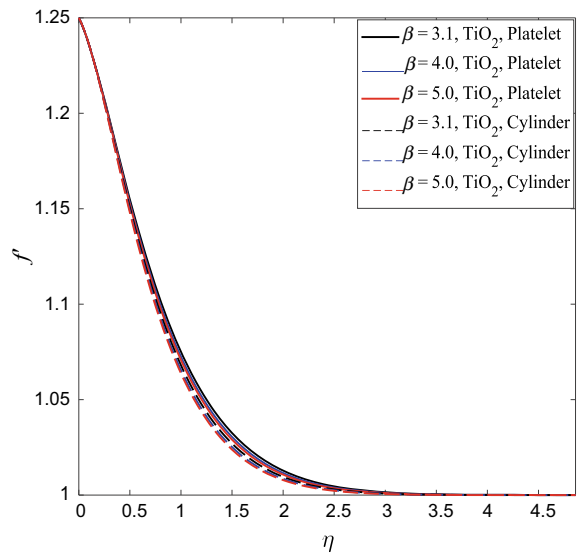


Fig. 11 Variations of velocity for Casson parameter β and nanoparticle shapes, when $\lambda = 2$, $\beta_1 = 0.2$, $Pr = 6.2$, $c/a = 1.25$, $\phi = 0.01$



are depicted in Fig. 18. The cylindrical-shaped particles show a better heat transfer rate than the platelet-shaped nanoparticles and also, there are no significant changes in the heat transfer for increasing values of the Casson parameter. The same results are observed for SiO₂ nanoparticles for the skin friction and the heat transfer as shown in Figs. 19 and 20, respectively.

Fig. 12 Variations of velocity for Casson parameter β and nanoparticle shapes, when $\lambda = 2, \beta_1 = 0.2, Pr = 6.2, c/a = 1.25, \phi = 0.01$

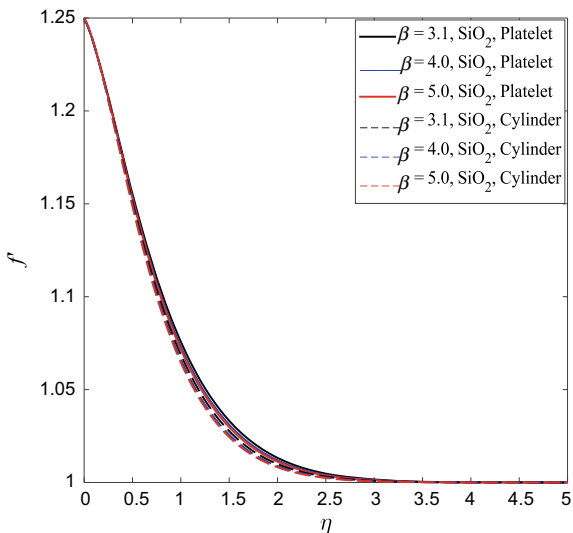


Fig. 13 Variations of skin friction coefficient for different volume fractions and heat source/sink parameters for TiO_2 nanoparticles, when $\lambda = 2, \beta = 3.1, Pr = 6.2, c/a = 1.25$

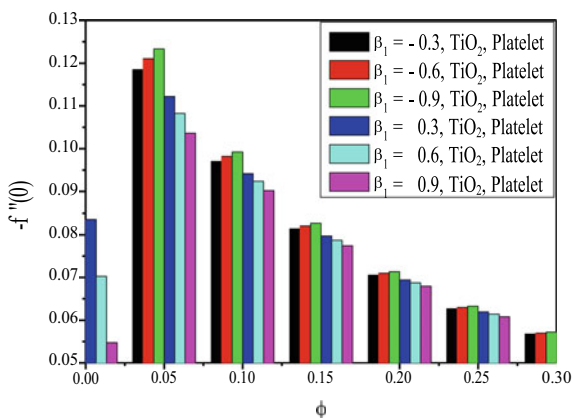


Fig. 14 Variations of skin friction coefficient for different volume fractions and heat source/sink parameters for TiO_2 nanoparticles, when $\lambda = 2, \beta = 3.1, Pr = 6.2, c/a = 1.25$

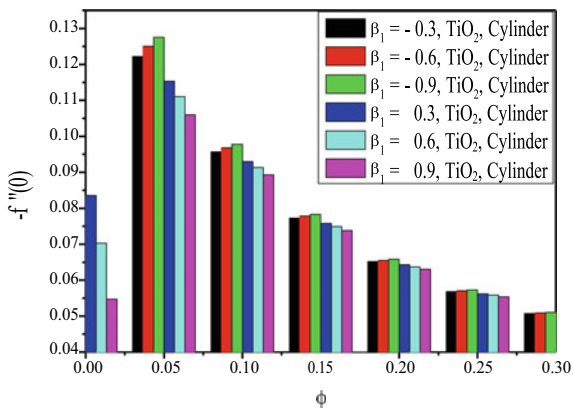


Fig. 15 Variations in heat transfer coefficient for different volume fractions and heat source/sink parameters for TiO₂ nanoparticles, when $\lambda = 2$, $\beta = 3.1$, $Pr = 6.2$, $c/a = 1.25$

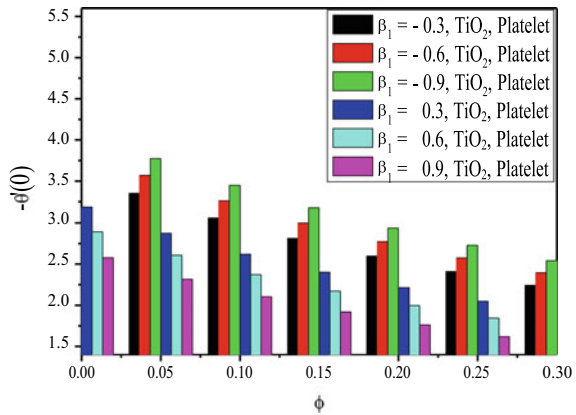


Fig. 16 Variations in heat transfer coefficient for different volume fractions and heat source/sink parameters for TiO₂ nanoparticles, when $\lambda = 2$, $\beta = 3.1$, $Pr = 6.2$, $c/a = 1.25$

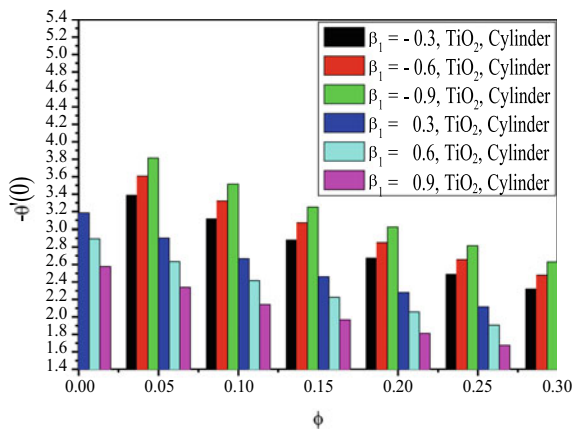


Fig. 17 Variations of skin friction coefficient for different volume fractions and Casson parameter for TiO₂ nanoparticles, when $\lambda = 2$, $\beta_1 = 0.2$, $Pr = 6.2$, $c/a = 1.25$

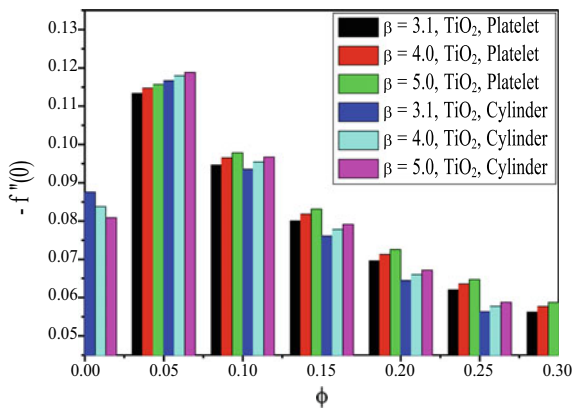


Fig. 18 Variations in heat transfer coefficient for different volume fractions and Casson parameter for TiO₂ nanoparticles, when $\lambda = 2, \beta_1 = 0.2, Pr = 6.2, c/a = 1.25$

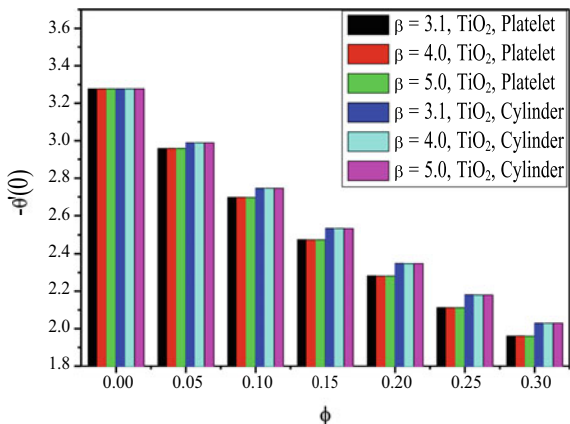


Fig. 19 Variations of skin friction coefficient for different volume fractions and Casson parameter for SiO₂ nanoparticles, when $\lambda = 2, \beta_1 = 0.2, Pr = 6.2, c/a = 1.25$

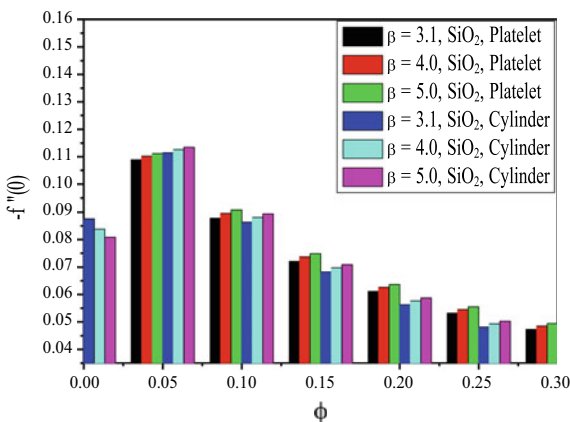
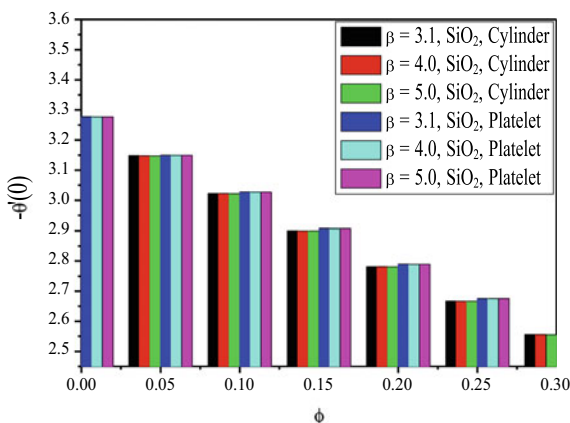


Fig. 20 Variations in heat transfer coefficient for different volume fractions and Casson parameter for SiO₂ nanoparticles, when $\lambda = 2, \beta_1 = 0.2, Pr = 6.2, c/a = 1.25$



5 Conclusions

In this study, we investigated the impact of the shape of nanoparticles on convective heat transfer in a Casson nanofluid flow. We have shown that the nanoparticle shape has an effect on the flow structure and fluid properties. The velocity profile is increased more for SiO₂ platelet-shaped nanoparticles as compared to TiO₂ nanoparticles. The TiO₂ platelet-shaped nanoparticles give high temperature profiles because of their elongated thin shape. For increasing the Casson parameter, there is a reduction in the fluid velocity for both TiO₂ and SiO₂ nanoparticles. In both nanoparticles, the skin friction coefficient increases with the sink parameter. The heat transfer rate is higher for the sink parameter than the heat source parameter for both the nanoparticles. By varying the Casson parameter, the skin friction coefficient is larger for increasing Casson parameter, but there are no significant changes in heat transfer while the Casson parameter increases.

References

1. Muthukumar C, Bathrinathan K (2020) Mathematical modelling of mixed convection boundary layer flows over a stretching sheet with viscous dissipation in presence of suction/injection. *Symmetry* 1(1):1754
2. Nandeppanavar M, Mahantesh M (2016) Mixed convection of MHD boundary layer flow of nanofluid due to a vertically stretching sheet with partial slip. *J Nanofluids* 5(3):416–422
3. Khan WA, Pop I (2010) Boundary layer flow of a nanofluid past a stretching sheet. *Int J Heat Mass Transf* 53(11–12):2477–2483
4. Ishak A, Nazar R, Pop I (2007) Mixed convection boundary layers in the stagnation point flow towards a vertical continuously stretching sheet. *J Heat Transfer* 129(8):1087–1090
5. Vajravelu K, Prasad KV, Vaidya H, Basha NZ (2017) C–O Ng., Mixed convective flow of a Casson fluid over a vertical stretching sheet. *Int J Appl Comput Math* 3:1619–1638
6. Ashraf MB, Hayat T, Alsaedi A (2017) Mixed convection flow of Casson fluid over a stretching sheet with convective boundary conditions and Hall effect. *Bound. Value Probl* 137:1–17
7. Mahanta G, Shaw S (2015) 3D Casson fluid flow past a porous linearly stretching sheet with convective boundary condition. *Alex Eng J* 54(3):653–659
8. Mustafa M, Khan JA (2015) Model for flow of Casson nanofluid past a non-linearly stretching sheet considering magnetic field effects. *AIP Adv* 5(7):077148
9. Kameswaran PK, Shaw S, Sibanda P (2014) Dual solutions of Casson fluid flow over a stretching or shrinking sheet. *Sadhana* 3(9):1573–1583
10. Satya Narayana PV, Harish Babu D, Sudheer Babu M (2019) Numerical study of a Jeffrey fluid over a porous stretching sheet with heat source/sink. *Int J Fluid Mech Res* 46(2):187–197
11. Bhattacharyya K (2011) Dual solutions in boundary layer stagnation-point flow and mass transfer with chemical reaction past a stretching/shrinking sheet. *Int Commun Heat Mass Transf* 38(7):917–922
12. Hemalatha R, Kameswaran PK (2022) Impact of nanoparticle shapes on non-darcy porous medium. *Int Commun Heat Mass Transf* 130:1–9
13. Rashid U, Baleanu D, Iqbal A, Abbas M (2020) Shape effect of Nano size particles on magneto-hydrodynamic nanofluid flow and heat transfer over a stretching sheet with Entropy Generation. *Entropy* 22(10):1171
14. Gireesha BJ, Archana M (2017) Study on shape effects in heat transfer phenomenon of Cu and Al₂O₃ nanoparticle in the presence of nonlinear thermal radiation. *JNNCE J Eng Manag (JJEM)* 1(2):1–7

15. Hemalatha R, Kameswaran PK (2022) Influence of nanoparticle shapes with variable permeability on non-darcy porous medium. *J Porous Media* 25(3):1–19
16. Gul A, Khan I, Shafie S, Khalid A, Khan A (2015) Heat transfer in MHD mixed convection flow of a Ferro fluid along a vertical channel. *PLoS ONE* 10:1–12
17. Ishak A, Nazar R, Pop I (2007) Mixed convection on the stagnation Point flow toward a vertical, continuously stretching sheet. *J Heat Transfer* 129:1087–1090
18. Hamilton RL, Crosser OK (1962) Thermal conductivity of heterogeneous two component systems. *I and EC Fundam.* 1(3):187–191
19. Ellahi R, Hassan M, Zeeshan A (2017) Shape effects of spherical and non-spherical nanoparticles in mixed convection flow over a vertical stretching permeable sheet. *Mech Adv Mater Struct* 24(15):1231–1238
20. Ali F, Aamina, Khan I, Sheikh NA, Gohar M, Tlili I (2018) Effects of different shaped nanoparticles on the performance of Engine-oil and Kerosene-oil: a generalized Brinkman-Type fluid model with Non-singular Kernel. *Sci Rep* 8:15285

Chapter 11

Entropy Generation Analysis During Heat Transfer by Darcy-Forchheimer Flow of Water-Based Al₂O₃ Nanofluid over a Curved Stretchable Surface



Kh. S. Mekheimer, M. A. Seddeek, R. E. Abo-Elkhair, Ahmed M. Salem, and Ayman A. Gadelhak

Abstract The objective of this study is to numerically investigate the heat and mass transfer characteristics of a nanofluid flow over a curved stretchable surface using the Darcy-Forchheimer model. Additionally, a comprehensive analysis of the entropy generation associated with the flow behavior will be conducted. It is widely recognized that entropy generation plays a vital role in reducing the energy demands of a system. The influence of Lorentz force due to the magnetic field and radiation caused by high temperatures near the surface are considered while modelling the problem. Along with the Hamilton-Crosser model for effective thermal conductivity, calculations also consider the thermophysical characteristics of water and alumina nanoparticles. The model's governing equations are transformed into a system of linked nonlinear ordinary differential equations using an appropriate similarity transformation before being numerically solved using Mathematica's finite difference approach. The results are graphically displayed as the outcome of velocity, temperature, and concentration profiles in order to assess the influence of various emergent characteristics. One significant result reveals that the amount of entropy generation grows with the curvature parameter, whereas the Bejan number exhibits the opposite tendency.

Keywords Heat transfer · Darcy-Forchheimer · Entropy generation · Nanofluid · Finite difference method

Kh. S. Mekheimer (✉) · R. E. Abo-Elkhair
Department of Mathematic, Faculty of Science (Boys), Al-Azhar University, Cairo, Egypt
e-mail: kh_Mekheimer@azhar.edu.eg

R. E. Abo-Elkhair
e-mail: elkhair33@azhar.edu.eg

M. A. Seddeek · A. M. Salem · A. A. Gadelhak
Department of Mathematic, Faculty of Science, Helwan University, P.O. Box 11795, Cairo, Egypt

R. E. Abo-Elkhair
Department of Basic Sciences, October High Institute of Engineering and Technology-OHI, 2nd Neighborhood, 3rd District, 6th of October, Giza, Egypt

Nomenclature

κ	Thermal conductivity
c_p	Specific heat at constant P
D_m	Mass diffusivity
$f'(\eta)$	Fluid velocity (dimensionless)
T_ω, T_∞	Temperatures at the wall and far away respectively
P	Pressure
R_d	Radiation parameter
η	Similarity variable
φ	Volume fraction of nanoparticles
b	Constant related to stretching of the surface
B_0	Applied magnetic field
C_ω, C_∞	Concentration at the wall and far away, respectively
$g(\eta)$	Fluid temperature
$h(\eta)$	Fluid concentration
k	Surface curvature
p	Pressure (dimensional)
P_r	Prandtl number
q_R	Heat flux radiation
R	Radius of the curved surface
S_c	Schmidt number
T, C	Temperature and concentration of the fluid, respectively
u, v	S, r velocity components, respectively

1 Introduction

Thermal engineering, which deals with the generation, conversion, and exchange of thermal energy and heat among physical systems, focuses mainly on heat transmission. However, heat transfer processes are categorized using thermal conduction, radiation, convection, and phase-dependent energy transfer changes. Thermal radiation is created when heat from the movement of the substance charges is converted to electromagnetic waves. Mass transfer, on the other hand, is the general movement of mass from one place to another, frequently involving changes in stream, phase, fraction, or component. Among other processes, mass transfer includes absorption, evaporation, precipitation, membrane filtration, and distillation. Mass is transferred between various phases or components throughout these procedures. Thermophoresis and Brownian effects on the flow of a nanofluid due to a curved surface with thermal radiation studied by Naveed et al. [1] and Seddeek and Aboeldahab [2]. Also, Ramzan et al. [3] focused on investigating the characteristics of the slip flow of nanoparticles for a curved surface by considering an autocatalytic chemical reaction. Variable viscosity and thermal radiation on the free convective flow and mass transfer over a

stretching sheet with a chemical reaction investigated by Seddeek and Almushigh [4]. The investigation aimed to analyze how radiation and varying viscosity affect the flow and mass transfer properties in the system. Initial cooling in mass and heat transfer with natural convective conditions for cryogenic surfaces was investigated by Choi and Kim [5]. The numerical solution of the porous solar cavity for combined heat transfer was introduced by Shirvan et al. [6]. Hayat et al. [7] discussed three-dimensional MHD flow with nanoparticles over a convectively heated nonlinear velocity stretching surface.

Numerous scholars made significant efforts to increase the heat transfer rate using developments in thermal engineering and thermos science. By suspending micro/millimeter-sized particles, Maxwell [8] devised certain techniques in the 18th century to improve the ability of fluids like water and oils to transmit heat. The term “nanofluids” was first used by Choi and Eastman [9] at the end of the 19th century, and they hypothesized that the emission of solid nanoparticles in regular fluids significantly improves heat transfer performance. Xue [10] declared that for effective thermal conductivity, the H-C (Hamilton-Crosser) model is the most effective.

The influence of gold and copper nanoparticles, magnetic force, and nonlinear thermal radiation for a non-Newtonian fluid examined by Mekheimer et al. [11] and Abo-Elkhair et al. [12].

Heat flow through porous media is a crucial aspect of various environmental and industrial systems, such as geothermal energy systems, geophysics, heat exchanger design, and catalytic reactors. The non-Darcian formula model extends beyond the conventional Darcy model by incorporating inertia effects and boundary characteristics. This expanded model allows for a more comprehensive understanding of heat transfer in porous media. However, Darcy’s model fails when boundary and inertia features are taken into consideration. Forchheimer [13] examines the boundary and inertia features for a square velocity factor in the Darcian law. This factor is always applicable for high Reynolds numbers. Later, this factor was known as a Forchheimer term by Muskat [14]. Darcy–Forchheimer flow for different kinds of fluids can be found in [15–17].

Flow through a stretching sheet holds immense importance in various technical and industrial sectors. It has a wide range of captivating applications, such as the manufacturing of plastic and rubber sheets, metalworking procedures including hot rolling, aerodynamic plastic sheet extrusion, metal shaping through melt spinning, and the production of elastic polymer, paints, and glass fiber fabrication. These applications demonstrate the critical role of understanding and analyzing the flow behavior on a stretching sheet in facilitating advancements across multiple industries. By stretching an elastic sheet that flows in its own plane with a velocity that linearly varies with distance from a fixed point as a result of the application of a regular stress. Two-dimensional incompressible boundary layer flow was studied by Crane [18]. After Crane’s study, the flow over a stretching surface attracted a great deal of interest, leading to a sizable body of literature on the topic. The effects of Brownian motion and thermophores are considered for the case, where the fluid motion is caused by the stretching of a flat surface for non-Newtonian fluids [19–21].

John von Neumann played a significant role in introducing the concept of entropy in quantum statistical mechanics, leading to the development of von Neumann entropy, which is considered an extension of the classical Gibbs entropy in quantum mechanics. Entropy generation refers to the production of entropy during irreversible processes, including fluid flow through a resistance, heat transfer across thermal resistances, friction between solid surfaces, diffusion, Joule heating, and viscosity of the fluid within a system. Conversely, when nanofluid flows over a surface and undergoes multiple irreversible processes, an increase in the total entropy of the system can be observed. The concept of entropy generation allows us to identify and quantify the irreversibility within a system. Researchers in engineering and industrial applications strive to minimize entropy generation as it is a key factor in improving efficiency and performance. By reducing entropy generation, it is possible to enhance the overall system performance and achieve greater efficiency in various engineering and industrial applications. The concept of entropy generation associated with the dissipation of energy in convective flow was initially proposed by Bejan [22, 23]. The irreversibility in hybrid nanofluid flow is studied by Khan et al. [24]. In their study, Esfahani et al. [25] examined entropy generation in nanofluids flowing through a wavy channel with a heated plate in a heat exchanger setup. Their findings indicated that the amplitude of the wave and Reynolds number significantly influenced the thermal irreversibility, highlighting their impact on the overall entropy generation within the system. Ranjit and Shit [26] investigated the heat transfer irreversibility for electro-osmotic peristaltic flow pumping.

To the author's knowledge, no one considers this model of Darcy-Forchheimer Flow of water-based Al_2O_3 nanoparticles model over a curved stretchable wall using the H-C model. This study's main target is to show the impact of radius curvature and other physical problem parameters on the flow under consideration and to analyze the entropy generation of this physical system. We discuss the mathematical modeling and the similarity transformation of the problem in the first section. The results, both numerical and significant, are then explained for each of the key parameters.

2 Mathematical Modeling

Darcy-Forchheimer incompressible fluid of Al_2O_3 nanoparticles over a curved surface is investigated. The curved surface with a radius R (see Fig. 1) and with a velocity stretch $U_\omega(s) = bs$, where $b > 0$ is the stretchable constant. The r -direction magnetic field is exerted, where the induced magnetic field is negligible. In the process of convection, transferring heat, and thermal radiation are considered.

Fig. 1 Configuration flow problem

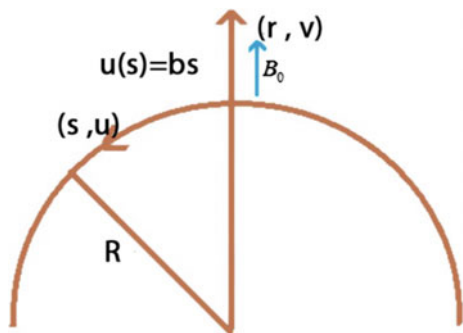


Table 1 The base fluid and alumina nanoparticles' thermophysical properties

Thermophysical properties	κ (W/mK)	σ (S/m)	$\beta \times 10^{-5}$ (K^{-1})	c_p (J/KgK)	ρ (Kg/m^3)
Water (H_2O)	0.612	55×10^{-7}	21	4181	996.5
Alumina (Al_2O_3)	40	3.5×10^7	0.85	765	3970

2.1 Thermophysical Properties

The thermophysical nanofluids properties are listed as (see Refs. [27, 28])

$$\left. \begin{aligned} \rho_{nf} &= \rho_{bf}(1 - \phi) + \phi\rho_{np}, \mu_{nf} = \mu_{bf}(1 - \phi)^{-2.5}, \sigma_{nf} = \sigma_{bf} \left(1 - \frac{3(1-\delta)\phi}{(2+\delta)+\phi(1-\delta)} \right) \\ (\rho c_p)_{nf} &= (1 - \phi)(\rho c_p)_{bf} + (\rho c_p)_{np}\phi, \frac{\kappa_{nf}}{\kappa_{bf}} = \frac{(\kappa_{np} + (n_p - 1)\kappa_{bf}) - \phi(n_p - 1)(\kappa_{bf} - \kappa_{np})}{(\kappa_{np} + (n_p - 1)\kappa_{bf}) + \phi(\kappa_{bf} - \kappa_{np})} \\ (\rho\beta)_{nf} &= (1 - \phi)(\rho\beta)_{bf} + \phi(\rho\beta)_{np}, \delta = \frac{\sigma_{np}}{\sigma_{bf}}, \end{aligned} \right\} \quad (1)$$

where ρ_{nf} is the density, μ_{nf} is the dynamic viscosity, σ_{nf} is the electrical conductivity, $(\rho c_p)_{nf}$ is the heat capacity, $\frac{\kappa_{nf}}{\kappa_{bf}}$ is the thermal conductivity of nonliquid, and $(\rho\beta)_{nf}$ is the thermal expansion coefficient of the nonliquid. The Al_2O_3 (alumina) nanoparticles and Al_2O_3 -water thermophysical properties are given in Table 1.

2.2 Problem Governing Equations

The nanofluid flow governing equations are presented as (see Ref. [28]):

Continuity equation:

$$\frac{\partial((r + R)v)}{\partial r} + R \frac{\partial(u)}{\partial s} = 0. \quad (2)$$

R-momentum equation:

$$\frac{u^2}{r+R} = \frac{1}{\rho} \frac{\partial p}{\partial r}. \quad (3)$$

S-momentum equation:

$$\begin{aligned} & \rho_{nf} \left(v \frac{\partial u}{\partial r} + \frac{R}{r+R} u \frac{\partial u}{\partial s} + \frac{uv}{r+R} \right) \\ &= -\frac{R}{r+R} \frac{\partial p}{\partial s} + \mu_{nf} \left(\frac{\partial^2 u}{\partial r^2} + \frac{1}{r+R} \frac{\partial u}{\partial r} - \frac{u}{(r+R)^2} \right) \\ & \quad - \sigma_{nf} B_0^2 u - \frac{v_{bf}}{K} u - Fu^2. \end{aligned} \quad (4)$$

Energy equation:

$$\begin{aligned} (\rho c_p)_{nf} \left(v \frac{\partial T}{\partial r} + \frac{Ru}{r+R} \frac{\partial T}{\partial s} \right) &= \kappa_{nf} \left(\frac{\partial^2 T}{\partial r^2} + \frac{1}{r+R} \frac{\partial T}{\partial r} \right) - \frac{1}{r+R} \frac{\partial[(r+R)q_r]}{\partial r} \\ & \quad + \left(\frac{\partial u}{\partial r} + \frac{u}{r+R} \right)^2 + \sigma_{nf} B_0^2 u^2. \end{aligned} \quad (5)$$

Concentration equation:

$$v \frac{\partial C}{\partial r} + \frac{Ru}{r+R} \frac{\partial C}{\partial s} = D_m \left(\frac{\partial^2 C}{\partial r^2} + \frac{1}{r+R} \frac{\partial C}{\partial r} \right). \quad (6)$$

The corresponding boundary conditions are:

$$\begin{aligned} u = U_\omega = bs, v = 0, T = T_\omega, C = C_\omega, \text{ at } r = 0, \\ \frac{\partial u}{\partial r} \rightarrow 0, u \rightarrow 0, T \rightarrow T_\infty, C \rightarrow C_\infty, \text{ as } r \rightarrow \infty. \end{aligned} \quad (7)$$

2.3 Nondimensional Similarity Transformations

The following similarity transforms are introduced:

$$v = -\frac{R}{r+R} \sqrt{bv_{bf}} f(\eta), u = bsf'(\eta), p = \rho_{bf} b^2 s^2 P(\eta),$$

$$g(\eta) = \frac{T - T_\infty}{T_\omega - T_\infty}, h(\eta) = \frac{C - C_\infty}{C_\omega - C_\infty}, \eta = \sqrt{\frac{b}{v_{bf}}} r. \tag{8}$$

After using Eq. (8) in Eqs. (2)–(7), we get:

$$P' = \frac{\Lambda_1}{\eta + k} f'^2 \tag{9}$$

$$\begin{aligned} \frac{2k}{\eta + k} P &= \Lambda_1 \left(-\frac{k}{\eta + k} f f'' + \frac{k}{\eta + k} f'^2 - \frac{k}{(\eta + k)^2} f f' \right) \\ &- \Lambda_3 \left(f''' + \frac{1}{\eta + k} f'' - \frac{1}{(\eta + k)^2} f' \right) + (\Lambda_6 M + \lambda) f' + F_r f'^2, \end{aligned} \tag{10}$$

$$\begin{aligned} R_d (3g'^2 (1 + (g_\omega - 1)\theta)^2 (g_\omega - 1)(\eta + k) + (1 + (g_\omega - 1)g)^3 ((\eta + k)g'' + g')) \\ + \Lambda_5 ((\eta + k)g'' + g') + P_r \Lambda_2 k f g' = 0, \end{aligned} \tag{11}$$

$$S_c k f h' + (\eta + k) h'' + h' = 0 \tag{12}$$

Eliminating the pressure (P) from Eqs. (9)–(10), we get

$$\begin{aligned} \frac{\Lambda_1 k}{\eta + k} \left(f' f'' - f f''' - \frac{1}{\eta + k} (f'^2 + f f'') + \frac{1}{(\eta + k)^2} f f' \right) \\ - \Lambda_3 \left(f^{(iv)} + \frac{2}{\eta + k} f''' - \frac{1}{(\eta + k)^2} f'' + \frac{1}{(\eta + k)^3} f' \right) \\ + (\Lambda_6 M + \lambda) \left(f'' + \frac{1}{\eta + k} f' \right) + F_r \left(2f' f'' + \frac{1}{\eta + k} f'^2 \right) = 0. \end{aligned} \tag{13}$$

where

$$\left. \begin{aligned} \Lambda_1 &= (1 - \phi) + \frac{\rho_{np}}{\rho_{bf}} \phi, \\ \Lambda_2 &= (1 - \phi) + \frac{(\rho c_p)_{np}}{(\rho c_p)_{bf}} \phi, \\ \Lambda_3 &= (1 - \phi)^{-2.5}, \\ \Lambda_4 &= (1 - \phi) + \frac{(\rho \beta)_{np}}{(\rho \beta)_{bf}} \phi, \\ \Lambda_5 &= \frac{(\kappa_{np} + (n_p - 1)\kappa_{bf}) - \phi(n_p - 1)(\kappa_{bf} - \kappa_{np})}{(\kappa_{np} + (n_p - 1)\kappa_{bf}) + \phi(\kappa_{bf} - \kappa_{np})}, \\ \Lambda_6 &= \left(1 - \frac{3(1 - \delta)\phi}{(2 + \delta) + \phi(1 - \delta)} \right). \end{aligned} \right\} \tag{14}$$

Along with transformed boundary conditions:

$$\begin{aligned} f(\eta) = 0, f'(\eta) = 1, g(\eta) = 1, h(\eta) = 1, \text{ at } \eta = 0, \\ f'(\eta) \rightarrow 0, f''(\eta) \rightarrow 0, g(\eta) \rightarrow 0, h(\eta) \rightarrow 0, \text{ as } \eta \rightarrow \infty. \end{aligned} \tag{15}$$

The expressions for parameters involved in the above equations are given as:

$$\begin{aligned}
 k &= \sqrt{\frac{b}{v_{bf}}} R, R_e = \frac{bs^2}{v_{bf}}, P_r = \frac{\mu_f (c_p)_{bf}}{\kappa_{bf}}, R_d = \frac{16\sigma^* T_\infty^3}{3\kappa^* \kappa_{bf}}, \\
 M &= \frac{\sigma_{bf} B_0^2}{\rho_{bf} b}, \lambda = \frac{v_{bf}}{Kb}, F_r = \frac{C_b}{\sqrt{K}}, S_c = \frac{v_{bf}}{D_m}.
 \end{aligned}
 \tag{16}$$

2.4 Analysis of Entropy Generation and Bejan Number

The analysis of entropy generation in a system is crucial for understanding the irreversibility of thermal energy within that system. The primary goal is to minimize entropy generation by controlling the problem parameters and leading to improved outcomes. The expression for entropy generation in terms of dimensional variables is:

$$\begin{aligned}
 E_G &= \underbrace{\frac{1}{T_\infty} \left(\kappa_{nf} + \frac{16\sigma^* T^3}{3\kappa^*} \right) \left(\frac{\partial T}{\partial r} \right)^2}_{\text{heas transfer irreo.}} + \underbrace{\frac{\mu_{nf}}{T_\infty} \left(\frac{\partial u}{\partial r} + \frac{u}{r+R} \right)^2}_{\text{viscous dissipation irrev.}} + \underbrace{\frac{\mu}{T_\infty} \left(\frac{u^2}{K} \right)}_{\text{porous medium irrev.}} \\
 &+ \underbrace{\frac{\sigma_{nf} B_0^2}{T_\infty} u^2}_{\text{joule hearing irrev.}} + \underbrace{\frac{RD}{C_\infty} \left(\frac{\partial C}{\partial r} \right)^2 + \frac{RD}{T_\infty} \left(\frac{\partial C}{\partial r} \frac{\partial T}{\partial r} \right)}_{\text{mass transfer irrev.}}.
 \end{aligned}
 \tag{17}$$

The entropy generation dimensionless can be written as:

$$N_G = \frac{E_G}{E_{G0}} = \frac{T_\infty^2 \left(\frac{y}{\eta} \right)^2}{\kappa_{nf} (T_\omega - T_\infty)^2} E_G,
 \tag{18}$$

where

$$E_{G0} = \frac{\kappa_{nf} (T_\omega - T_\infty)^2}{T_\infty^2 \left(\frac{y}{\eta} \right)^2}.$$

Introducing the similarity transformation, we get the reduced nondimensional entropy generation as follows:

$$N_G = \underbrace{\left[1 + R_d (g(g_\omega - 1) + 1) \right]^3}_{N_{GT}} g'^2$$

$$\begin{aligned}
 & + B_r \alpha_1 \underbrace{\left[\left(f'' + \frac{1}{\eta + k} f' \right)^2 + \left(\lambda + \frac{\Lambda_6}{\Lambda_3} M \right) f'^2 \right]}_{N_{GFF}} \\
 & + L \underbrace{\frac{\alpha_1}{\alpha_2} h'^2 + L g' h'}_{N_{GM}}.
 \end{aligned} \tag{19}$$

where B_r is the Brinkman number, α_1 and α_2 are the dimensionless temperature ratio and concentration ratio, respectively, and L is the diffusive variable. Here N_G denotes the system entropy generation, N_{GT} is the thermal irreversibility entropy number, N_{GFF} is the fluid friction irreversibility entropy number including the impact of magnetic field and porosity parameters. Finally, N_{GM} denotes the mass transfer irreversibility. Bejan number can be formulated mathematically as:

$$B_e = \frac{N_{GT}}{N_G} = \frac{N_{GT}}{N_{GT} + N_{GFFF} + N_{GM}} = \frac{\text{Heat transfer Entropy generation}}{\text{Total entropy generation}}. \tag{20}$$

It is clear that the ranges of the Bejan number can take values from 0 to 1. Entropy generation due to friction irreversibility dominates over heat transfer irreversibility for $B_e \ll 0.5$, while for $B_e \gg 0.5$, the entropy generation due to heat transfer irreversibility dominates over friction irreversibility. If the friction irreversibility and heat transfer irreversibility are equal, then $B_e = 0.5$.

2.5 Physical Quantities of Interest

The dimensionless form of the local Nusselt (Nu_s) number is:

$$R_e^{-\frac{1}{2}} Nu_s = -(\Lambda_5 + R_d g_w^3) g'(0). \tag{21}$$

The skin friction coefficient (C_f) in dimensionless form can be written as:

$$\frac{R_e^{-\frac{1}{2}} C_f}{2} = \Lambda_3 \left(f''(0) - \frac{f'(0)}{k} \right). \tag{22}$$

The dimensionless Sherwood number Sh_s is defined as:

$$R_e^{-\frac{1}{2}} Sh_s = -h'(0). \tag{23}$$

3 Results and Discussion

To explore the influence of problem parameters on flow behavior, we divided this section into five subsections, i.e., on heat and mass transport phenomenon over a curved stretchable surface. In the first, Figs. 2, 3, 4 and 5 are constructed to analyze the effects of the curvature parameter (k), magnetic field parameter (M), porosity parameter (λ), and the inertia coefficient parameter (F_r) on the velocity profile of the model problem. In the second, Figs. 6, 7, 8, 9, 10, 11 and 12 depict the nature of the temperature profile for several values of the curvature parameter (k), the magnetic parameter (M), the radiation parameter (R_d), the temperature ratio (g_ω), Eckert number (E_k), Prandtl number (P_r), and the nanoparticles volume fraction (ϕ). In the third, Figs. 13 and 14 are sketched to explain the nature of the concentration profile for several values of the curvature parameter (k) and Schmidt number (S_c), respectively. In the fourth, Figs. 15, 16, 17, 18, 19, 20, 21, 22, 23, 24, 25, 26, 27, 28, 29, 30, 31 and 32 describe how the Bejan number and entropy generation differ for different values of the magnetic parameter (M), the radiation parameter (R_d), the temperature ratio parameter (g_ω), the curvature parameter (k), the porosity parameter (λ), the diffusion parameter (L), Brinkman number (B_r), the temperature ratio parameter (α_1), and the concentration ratio parameter (α_2). Finally, Figs. 33, 34, 35, 36, 37, 38, 39, 40, 41, and 42 are sketched to explain the nature of physical parameters (Skin friction, Nusselt and Sherwood numbers) for several values of problem parameters.

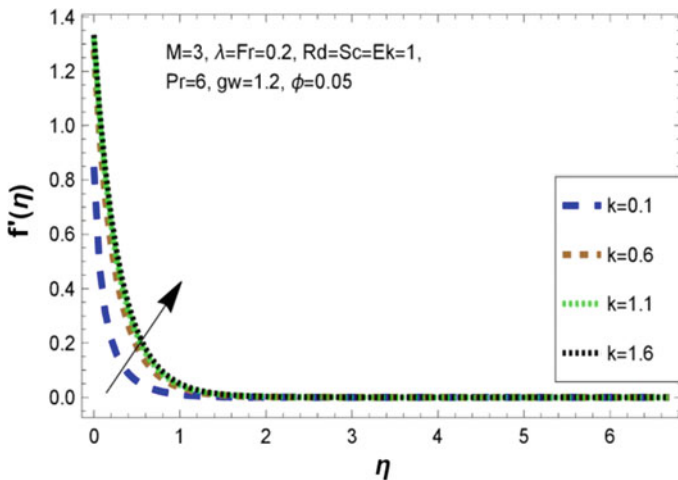


Fig. 2 Variation of velocity with k

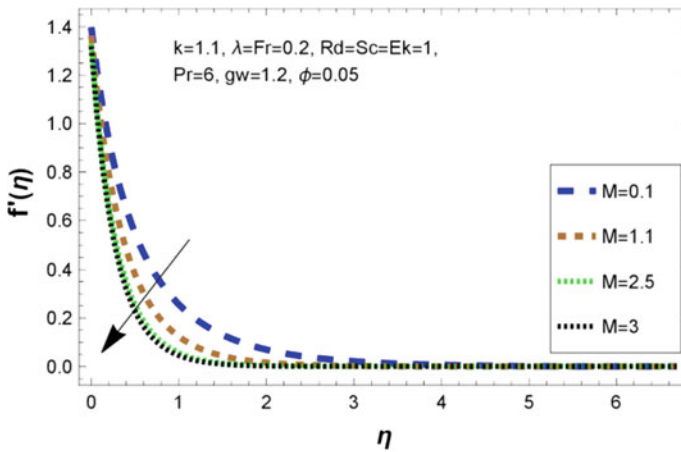


Fig. 3 Variation of velocity with M

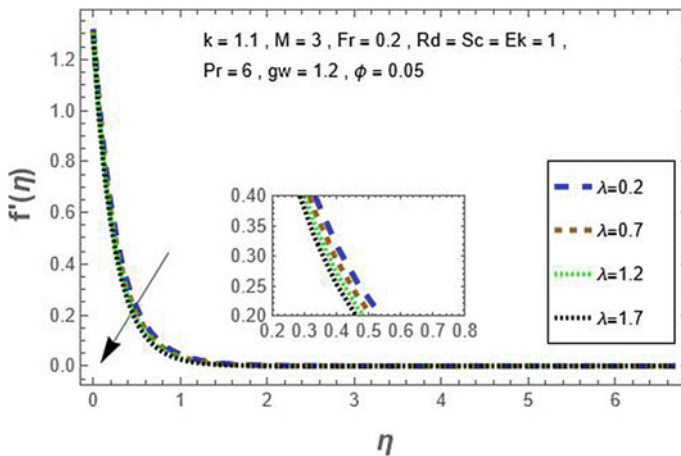


Fig. 4 Variation of velocity with λ

3.1 Velocity Profile

The influence of k (curvature parameter) on the velocity flow is illustrated in Fig. 2, it is clear that $f'(\eta)$ is an increasing function of k . Increased values of k , which corresponds to a larger radius of the curved surface enhance both the momentum and velocity layer thickness. For larger Lorentz force Fig. 3 depicts the behavior of the velocity profile, which is a decreasing pattern. Thus, reduction in the thickness of the momentum boundary layer according to the presence of a magnetic field, and this kind of reduction tends asymptotically to zero as the distance increases.

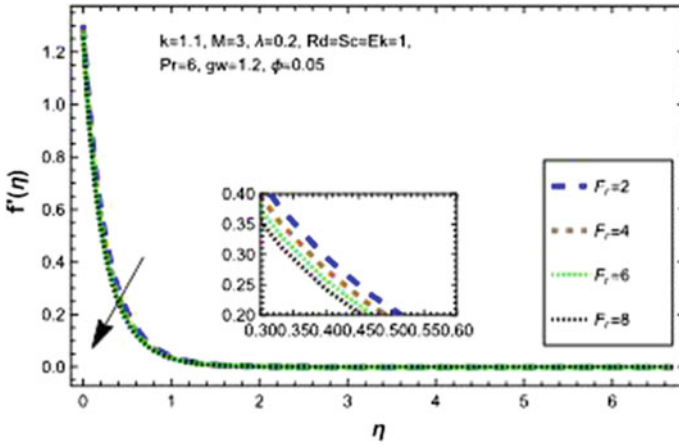


Fig. 5 Variation of velocity with F_r

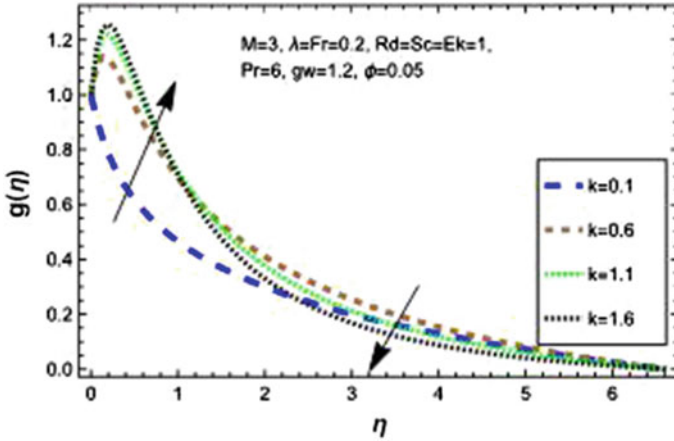


Fig. 6 Variation of temperature with k

Figure 4 shows the variation of velocity with the porosity parameter (λ), which is a diminishing effect in the velocity and momentum layer thickness. Similarly, Fig. 5 depicts the effect of inertia coefficient (F_r) on velocity, which is obvious to be a decreasing effect.

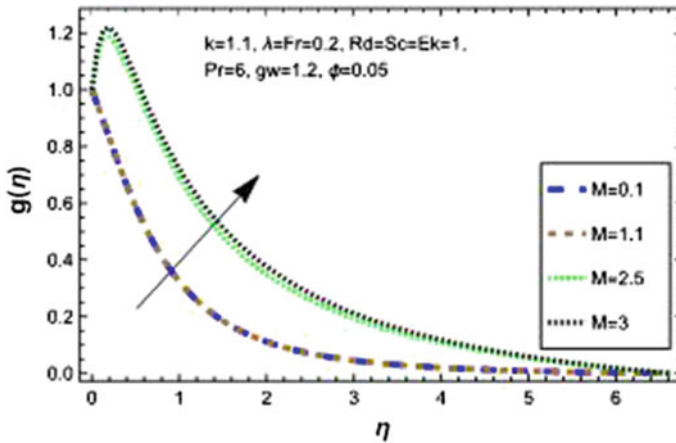


Fig. 7 Variation of temperature with M

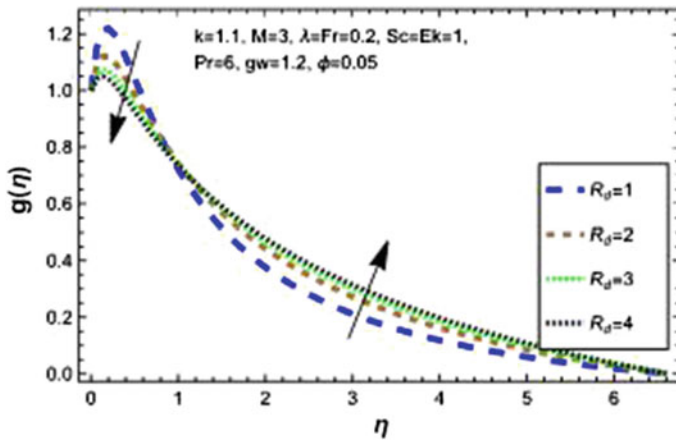


Fig. 8 Variation of temperature with R_d

3.2 Temperature Profile

Curvature parameter (k) effect on the temperature is shown in Fig. 6, it is apparent that $g(\eta)$ is enhanced near the curved surface, and then it dwindles far away from the wall surface of the boundary layer. Figure 7 is constructed to depict the temperature for higher values of M and it is clear that $g(\eta)$ is an increasing function of M .

The influence of (R_d) on the temperature is shown in Fig. 8, it is apparent that $g(\eta)$ is a decreasing function near the curved surface and after that, it increases away from the surface within the boundary layer. Figure 9 explores the variation in fluid temperature for higher values of (g_ω), it is clear that $g(\eta)$ is a decreasing

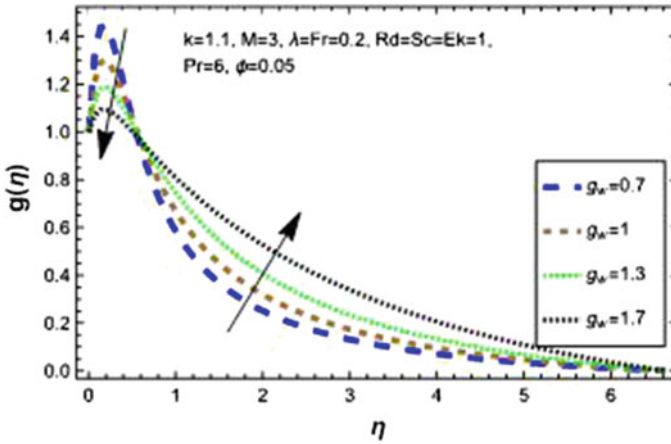


Fig. 9 Variation of temperature with g_w

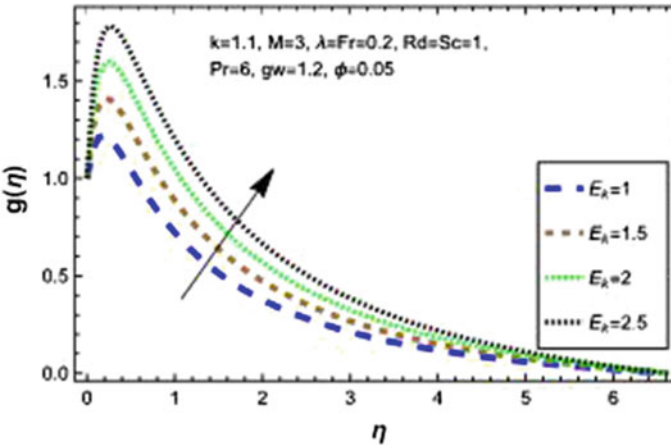


Fig. 10 Variation of temperature with E_k

function near the curved surface and after that, it increases away from the wall surface layer. Figure 10 is designed to investigate how the Eckert number varies with the temperature function $g(\eta)$ and it is obvious that it is an increasing function for higher values of E_k . In Fig. 11 we can see the effect of the Prandtl number on the temperature distribution, it is clear that $g(\eta)$ is an increasing function near the curved surface and after that, it diminishes away from the surface. Finally, Fig. 12 depicts the influence of the volume fraction of nanoparticles on the temperature distribution and it is obvious that it is an increasing pattern.

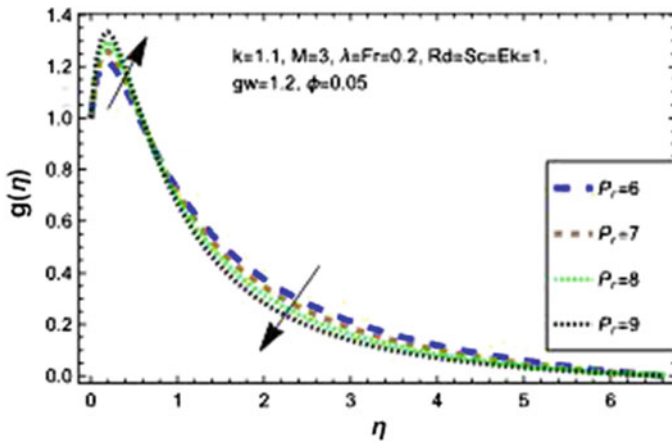


Fig. 11 Variation of temperature with P_r

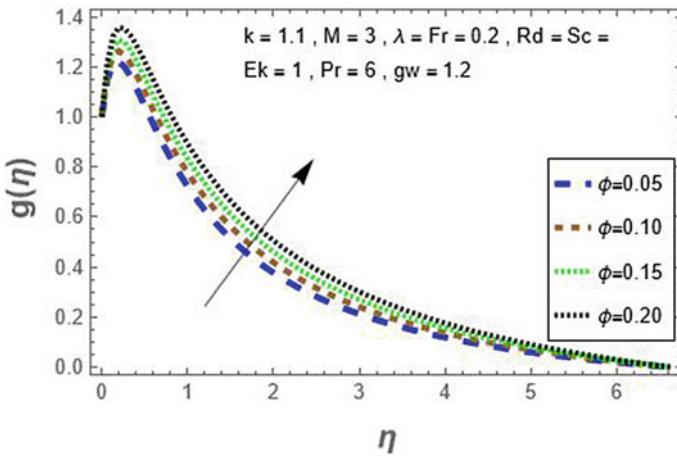


Fig. 12 Variation of temperature with ϕ

3.3 Concentration Profile

Figure 13 represents that the curvature radius impact on the concentration distribution is an increasing behavior. The concentration variation with η for different values of S_c number is shown in Fig. 14. We notice a decreasing concentration behavior. This is due to the fact that an increase in S_c lowers the rate of molecular diffusion while this increases the rate of viscous diffusion.

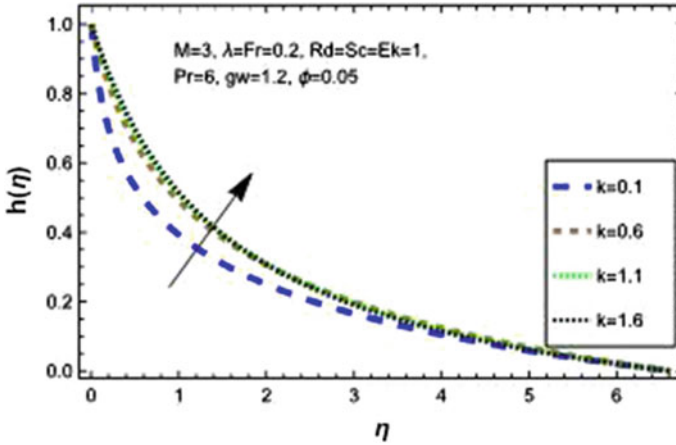


Fig. 13 Variation of concentration with k

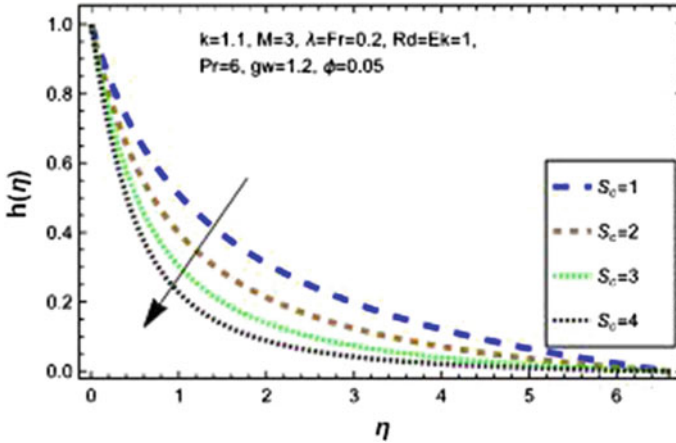


Fig. 14 Variation of concentration with Sc

3.4 Entropy Generation and Bejan Number

Figures 15 and 16 provide insights into the influence of M on entropy N_G and Bejan number B_e , respectively. Figure 15 reveals that initially, as M increases, there is a reduction in entropy near the sheet. However, beyond a certain point, the increment in the magnetic parameter leads to an enhancement of the entropy. In Fig. 16, the behavior of the Bejan number is observed. It can be seen that the Bejan number exhibits a consistent increasing pattern from the beginning to the end. This indicates that as the magnetic field increases, the Bejan number continues to rise throughout the range of the magnetic values. Based on Figs. 17 and 18, it is clear that a higher value

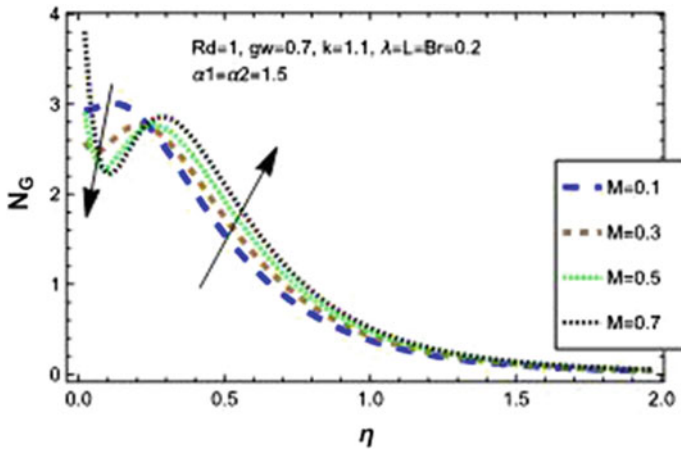


Fig. 15 Variation of N_G with M

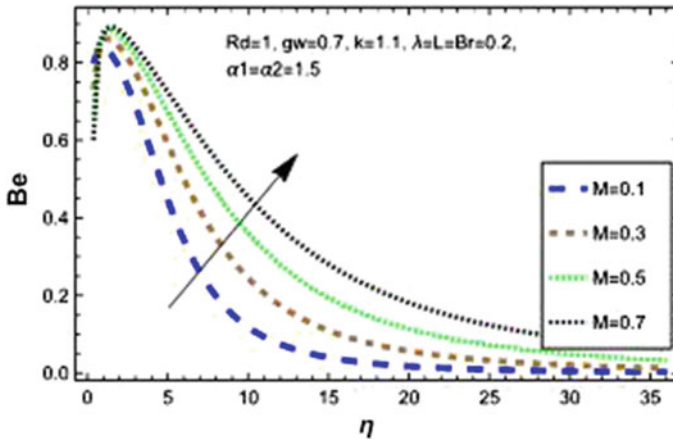


Fig. 16 Variation of Be with M

of R_d has a notable effect on entropy and the Bejan number. As R_d increases, there is an evident tendency for both the entropy and the Bejan to rapidly increase. This is attributed to the fact that with higher values of R_d , the temperature also increases, leading to an increment in entropy and the Bejan number. In this scenario, thermal irreversibility takes precedence and plays a dominant role in the overall entropy generation of the system. Based on Figs. 19 and 20, it can be clearly observed that a higher of g_ω has a tendency to increase both entropy and the Bejan number. As g_ω increases, there is a corresponding rise in temperature, which leads to an enhancement of entropy generation and the Bejan number. In this case, thermal irreversibility becomes dominant over the total entropy generation of the system

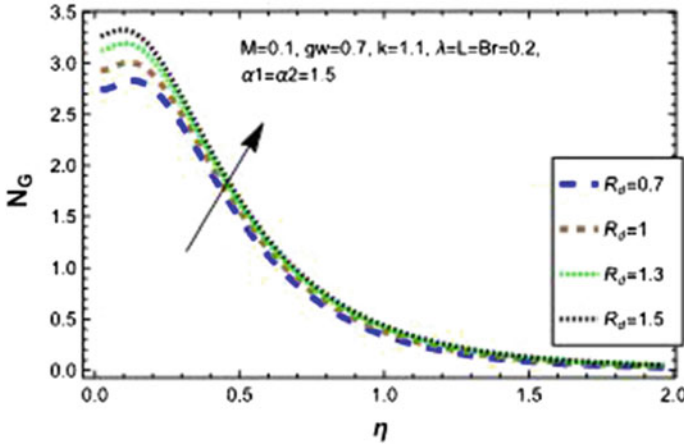


Fig. 17 Variation of N_G with R_d

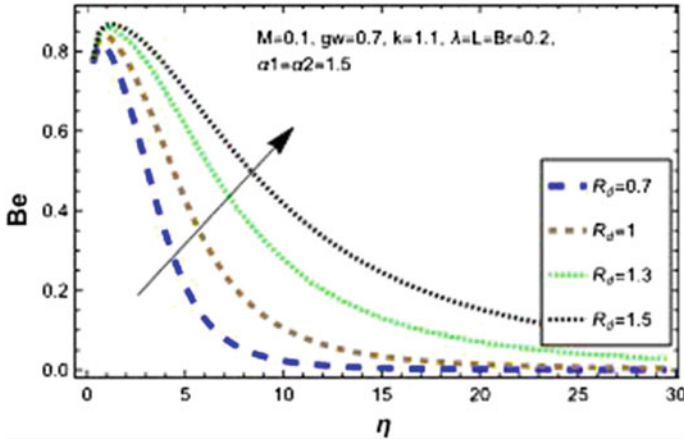


Fig. 18 Variation of B_e with R_d

due to the higher estimation of g_ω and its impact on temperature. For the curvature parameter effect, Figs. 21 and 22 show an enhancement in the entropy while the Bejan number shows a diminish, respectively. Figures 23 and 24 illustrate the impact of the porosity parameter λ on N_G and B_e . It is evident from these figures that as the porosity parameter λ increases, there is an increasing effect on N_G and B_e . This implies that higher values of λ lead to higher values of entropy generation and Bejan number. On the other hand, Figs. 25 and 26 examine the effect of the diffusivity parameter L on N_G and B_e . These figures reveal that as the diffusivity parameter L increases, there is an increase in entropy while the Bejan number decreases. This can be attributed to the fact that as L increases, the mass diffusivity of nanoparticles

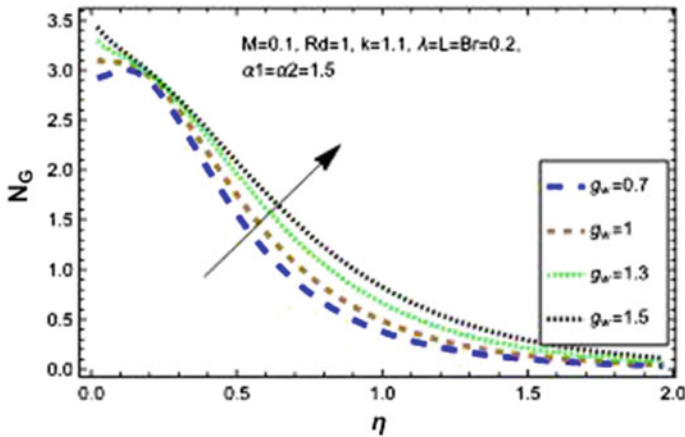


Fig. 19 Variation of N_G with g_ω

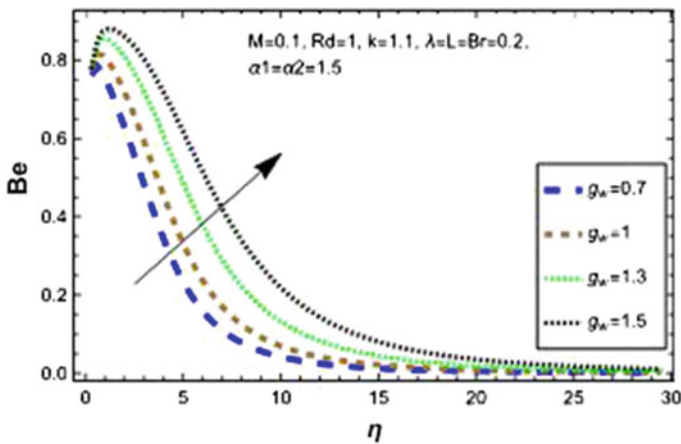


Fig. 20 Variation of Be with g_ω

also increases. This, in turn, results in an overall rise in entropy generation. From a physical perspective, the decrease in the Be_e can be explained by this increasing entropy generation associated with larger values of L . The impact of the Brinkman number appears in Figs. 27 and 28, physically increasing the B_r causes the conduction rate of heat generation by viscous dissipation to depreciate resulting in enhancing N_G and declining Be_e . For the temperature ratio parameter α_1 it is obvious from Figs. 29 and 30 that the N_G gets increased while Be_e gets decreased respectively for larger values of α_1 . Finally, Figs. 31 and 32 show that the concentration ratio parameter α_2 gives the inverse effect on both N_G and Be_e .

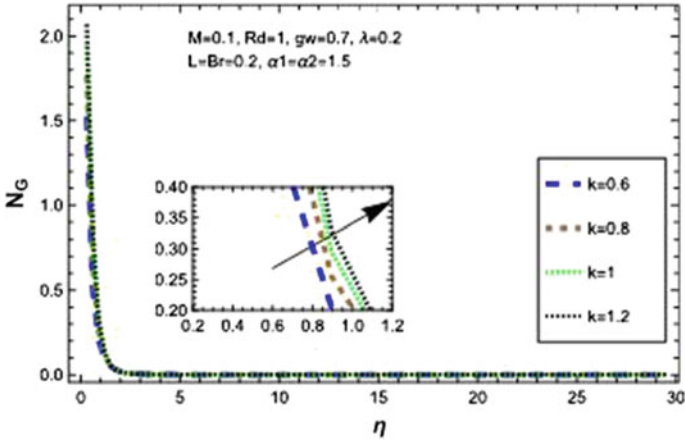


Fig. 21 Variation of N_G with k

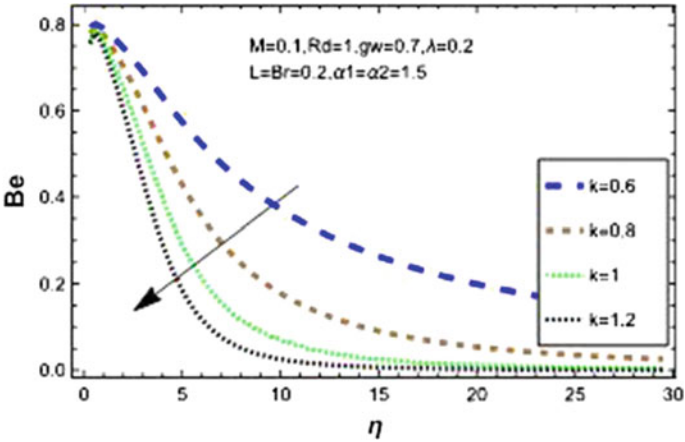


Fig. 22 Variation of B_e with k

3.5 Skin Friction, Nusselt Number, Sherwood Number, and Validation

For skin friction behavior Fig. 33 is designed to interpret the influence of k and we observe that an increase in curvature increases the skin friction of the system. Figures 34, 35 and 36 show the impacts of $M, \lambda,$ and F_r on skin friction, respectively, and they are a decreasing pattern. For Nusselt number behavior, Fig. 37 is constructed to show the influence of k and we observe that an increase in the curvature parameter increases the heat flux of the system. Figures 38, 39 and 40 show the impacts of $R_d, g_w,$ and P_r on Nusselt number, respectively, and they are an increasing pattern

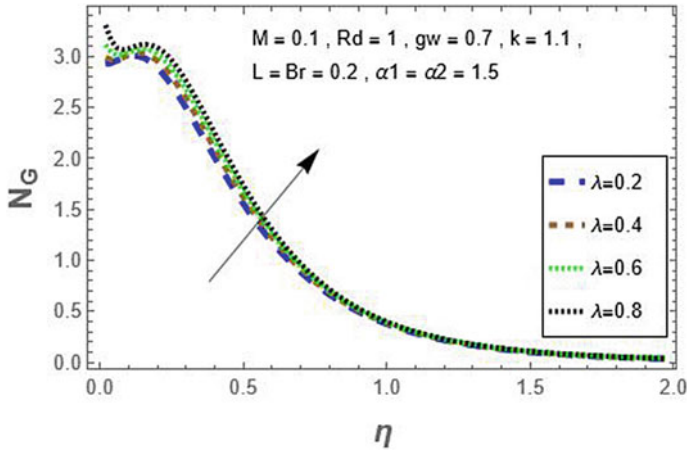


Fig. 23 Variation of N_G with λ

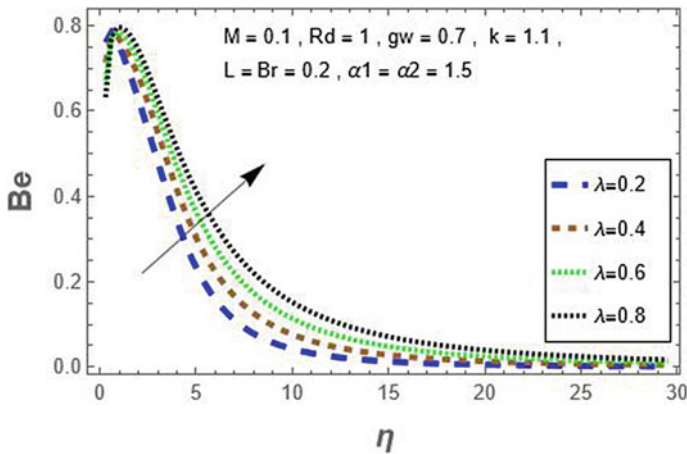


Fig. 24 Variation of Be with λ

also. Figure 41 shows the effect of k on the Sherwood number and it is an increasing pattern, while Fig. 42 explains the effect of S_c on the Sherwood number and it is also an increasing pattern. Our model can be compared with the pioneering work of Sajid et al. [29], since by neglecting the concentration equation and the energy equation and eliminating the Darcy-Forchhimer, magnetic effects, and thermo-physical properties (i.e. setting $\lambda = 0$, $F_r = 0$, and $\Lambda_1 = \Lambda_3 = 1$) we are left only with the momentum equation Sajid et al. [29]. Thus Table 2 shows our calculations of skin friction coefficient for different values of curvature parameters.

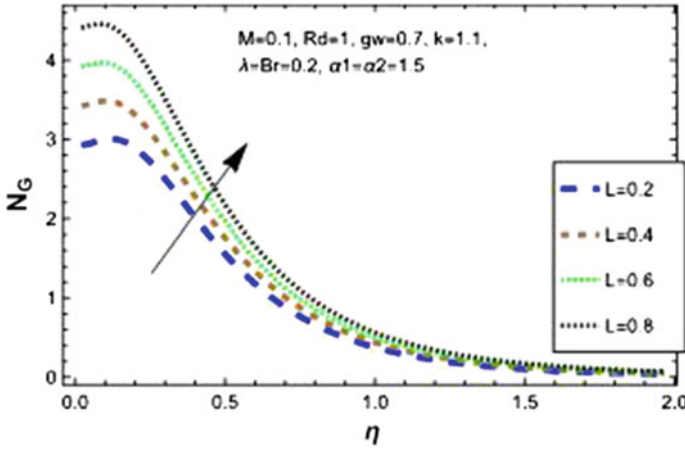


Fig. 25 Variation of N_G with L

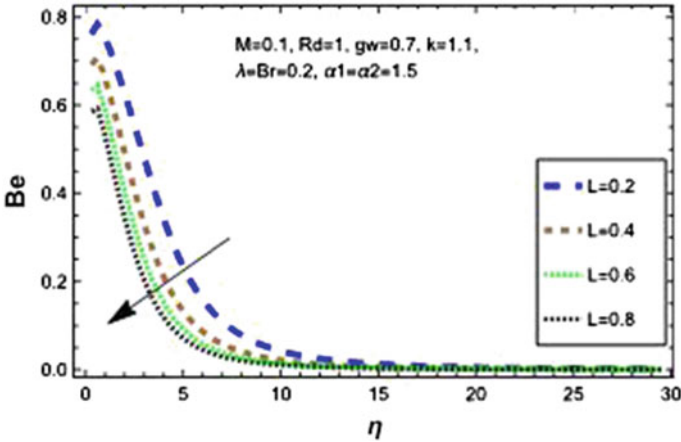


Fig. 26 Variation of B_e with L

4 Deductions

The model of a curvilinear coordinate system of Darcy-Forchheimer fluid with water-based Al_2O_3 nanoparticles and incorporated with the effects of thermal radiation above a curved surface with stretched velocity is utilized. The key findings of this research are as follows:

- The curvature parameter k enhances the flow velocity but it reduces with increasing the values of $M, \lambda,$ and $F_r,$ as these parameters effect increase the flow resistance.

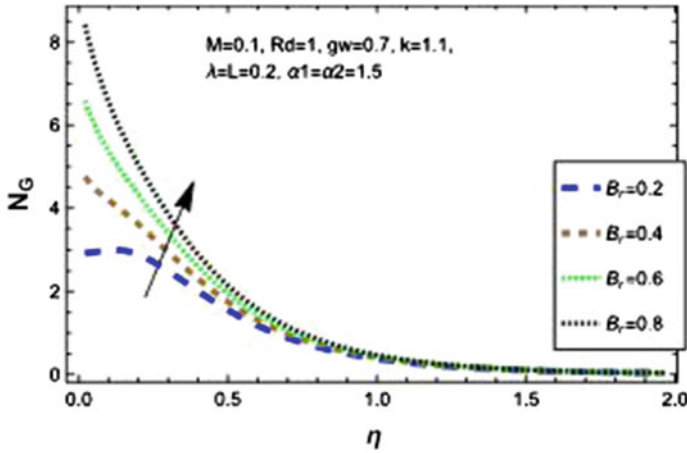


Fig. 27 Variation of N_G with B_r

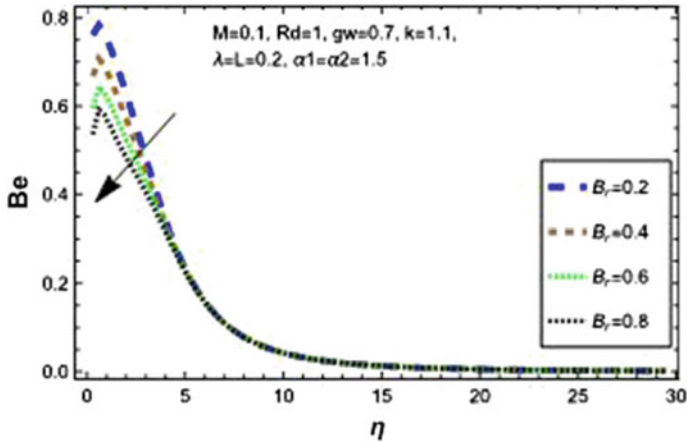


Fig. 28 Variation of B_e with B_r

- The temperature profile begins as an increasing function and as we get far from the sheet it starts decreasing for greater values of k while the reverse pattern is noticed for R_d , g_w , and P_r .
- The concentration behavior increases with k and decreases for higher values of S_c .
- The entropy generation gets higher values as M , R_d , g , w , k , λ , L , B_r , and α_1 increases but the reverse pattern is noticed for α_2 .
- The Bejan number increases as the parameters M , R_d , g , w , λ and α_2 increase, while it decreases as the parameters k , L , B_r , and α_1 increase.
- Skin friction expands with k and shrinks for M , λ , and F_r .

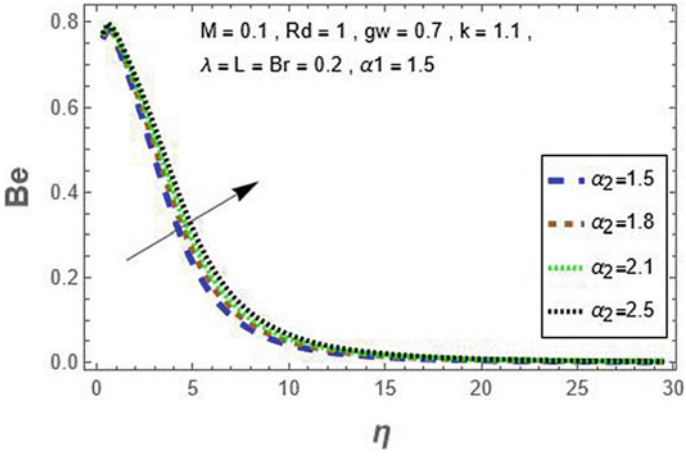


Fig. 29 Variation of N_G with α_1

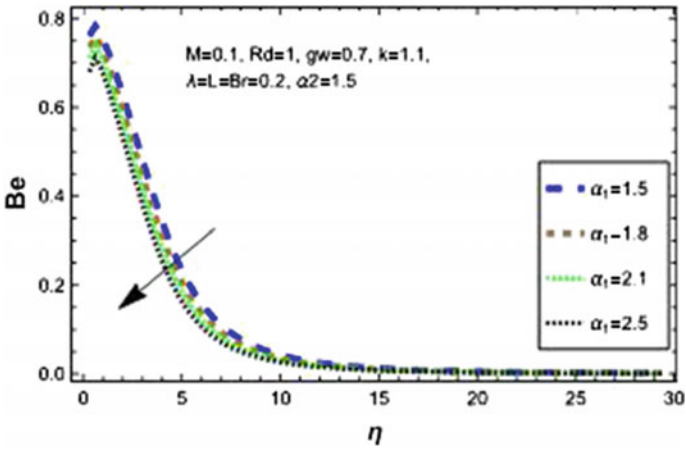


Fig. 30 Variation of B_e with α_1

- Heat flux increases with the values of $k, R_d, g_w,$ and P_r .
- Sherwood number increases as the values of k and Sc increase.

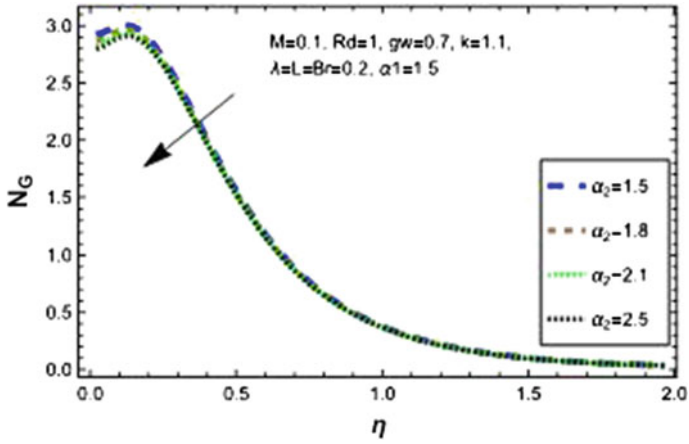


Fig. 31 Variation of N_G with α_2

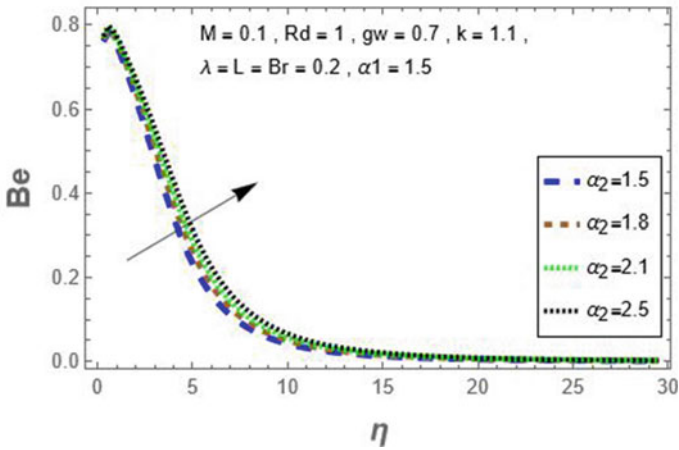


Fig. 32 Variation of B_e with α_2

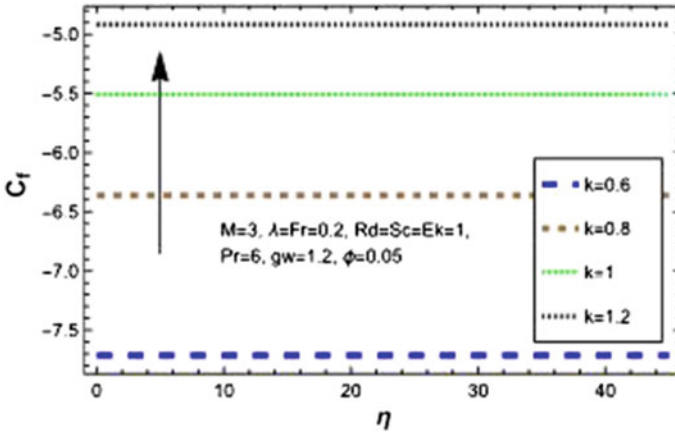


Fig. 33 Variation of skin friction with k

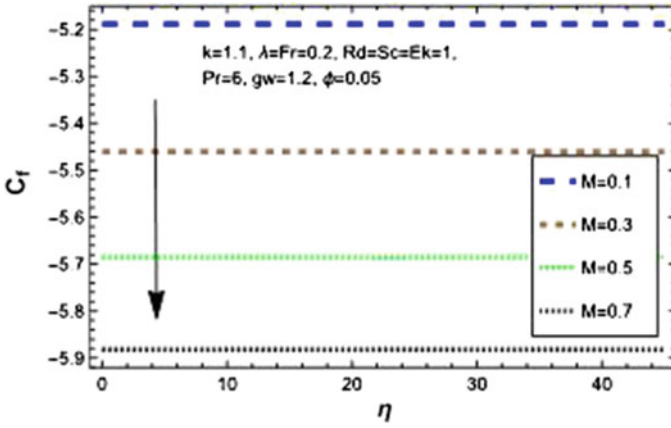


Fig. 34 Variation of skin friction with M

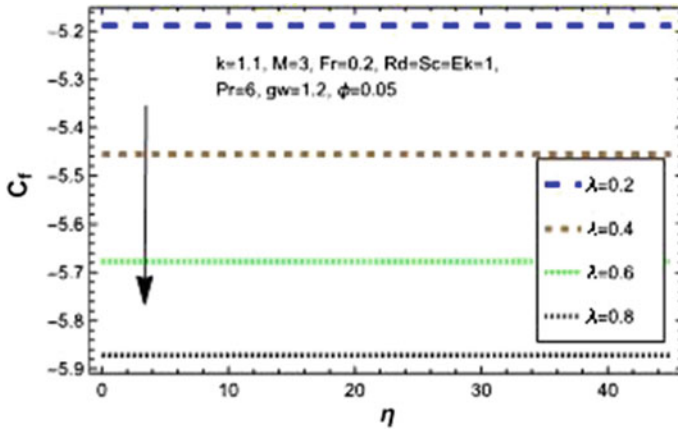


Fig. 35 Variation of skin friction with λ

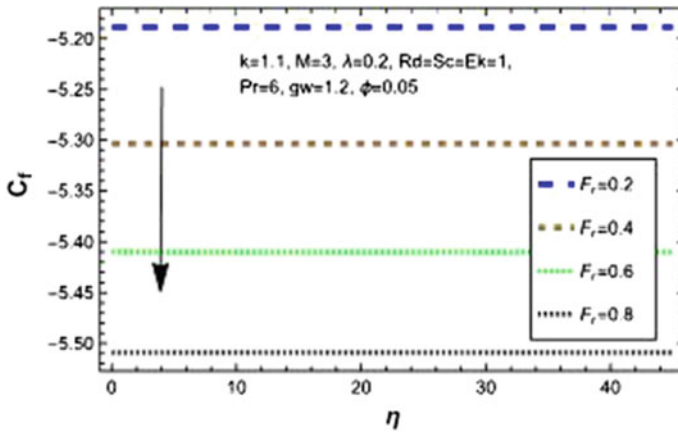


Fig. 36 Variation of skin friction with F_r

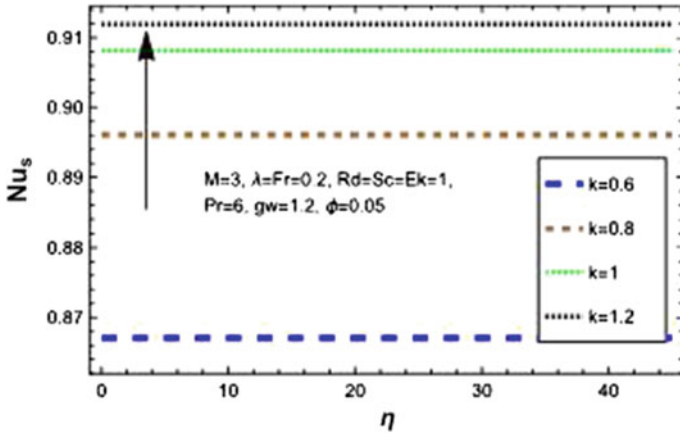


Fig. 37 Variation of Nusselt number with k

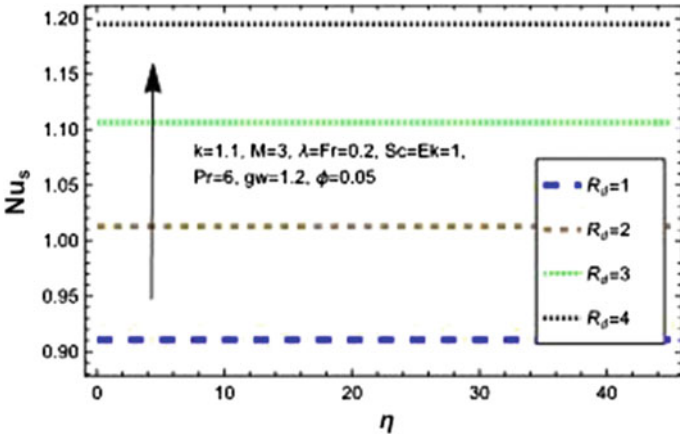


Fig. 38 Variation of Nusselt number with R_d

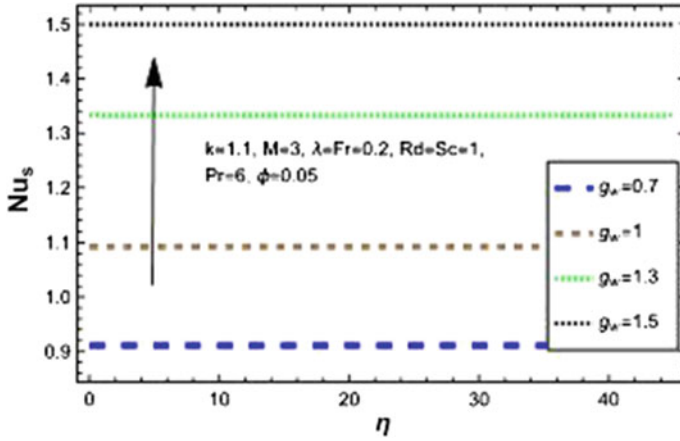


Fig. 39 Variation of Nusselt number with g_w

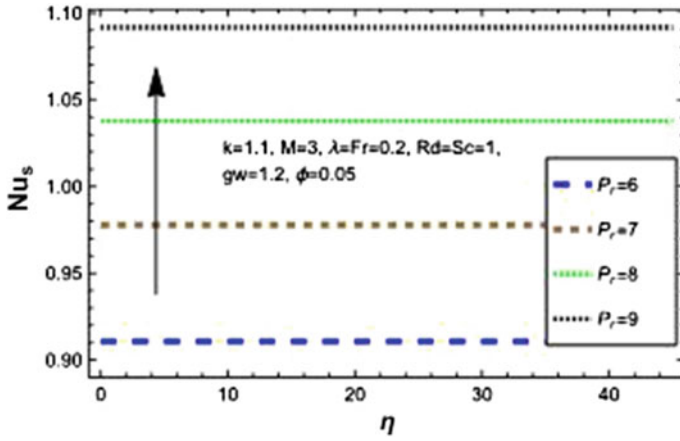


Fig. 40 Variation of Nusselt number with P_r

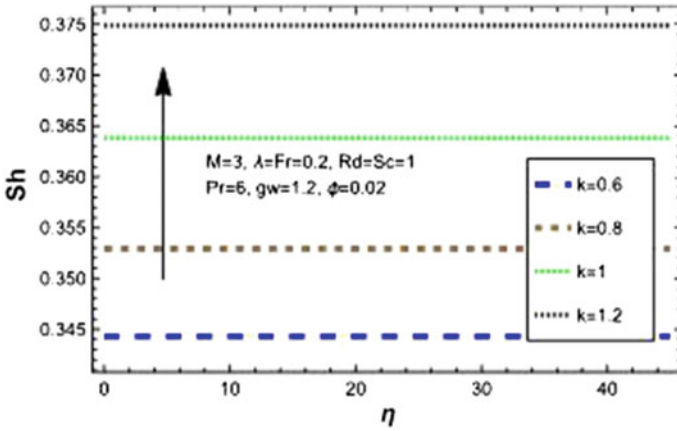


Fig. 41 Variation of Sherwood number with k

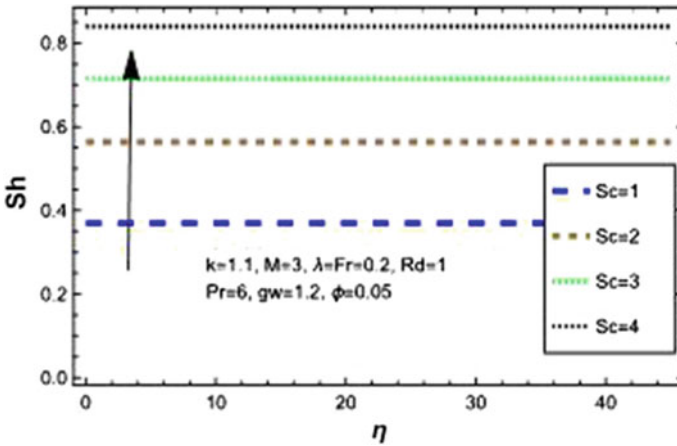


Fig. 42 Variation of Sherwood number with Sc_c

Table 2 Comparison of the reduced skin friction

k	Present results	Sajid et al. [29]
5	0.751742	0.75763
10	0.854923	0.87349
20	0.935188	0.93561
30	0.946698	0.95686
40	0.966111	0.96759
50	0.974039	0.97405
100	0.981571	0.98704

References

1. Naveed M, Abbas Z, Sajid M (2016) Thermophoresis and Brownian effects on the Blasius flow of a nanofluid due to a curved surface with thermal radiation. *Eur Phys J Plus* 131–214
2. Seddeek MA, Aboeldahab EM (2001) Radiation effects on unsteady MHD free convection with Hall current near an infinite vertical porous plate. *Int J Math Math Sci* 26(4):249–255
3. Ramzan M, Rafiq A, Chung JD, Kadry S, Chu YM (2020) Nanofluid flow with autocatalytic chemical reaction over a curved surface with nonlinear thermal radiation and slip condition. *Sci Rep* 10(1):1–13
4. Seddeek MA, Almushigh AA (2010) Effects of radiation and variable viscosity on MHD free convective flow and mass transfer over a stretching sheet with chemical reaction. *Appl Appl Math Int J (AAM)* 5(1):14
5. Choi S, Kim SJ (2017) Effect of initial cooling on heat and mass transfer at the cryogenic surface under natural convective condition. *Int J Heat Mass Transf* 112:850–861
6. Shirvan KM, Mamourian M, Mirzakhani S, Ellahi R, Vafai K (2017) Numerical investigation and sensitivity analysis of effective parameters on combined heat transfer performance in a porous solar cavity receiver by response surface methodology. *Int J Heat Mass Transf* 105:811–825
7. Hayat T, Aziz A, Muhammad T, Alsaedi A (2016) On magnetohydrodynamic three-dimensional flow of nanofluid over a convectively heated nonlinear stretching surface. *Int J Heat Mass Transf* 100:566–572
8. Maxwell JC (1873) *A treatise on electricity and magnetism*, vol 1. Clarendon Press
9. Choi SUS, Eastman J (1995) Enhancing thermal conductivity of fluids with nanoparticles. *ASME Publ Fed* 231:99–103
10. Xue QZ (2003) Model for effective thermal conductivity of nanofluids. *Phys Lett A* 307(5–6):313–317
11. Mekheimer KhS, Hasona WM, Abo-Elkhair RE, Zaher AZ (2018) Peristaltic blood flow with gold nanoparticles as a third grade nanofluid in catheter: application of cancer therapy. *Phys Lett A* 382(2/3):85–93
12. Abo-Elkhair RE, Bhatti MM, Mekheimer KhS (2021) Magnetic force effects on peristaltic transport of hybrid bio-nanofluid (Au–Cu nanoparticles) with moderate Reynolds number: an expanding horizon. *Int Commun Heat Mass Transfer* 123:105228
13. Forchheimer P (1901) Wasserbewegung durch boden. *Z Ver Dtsch Ing* 45:1782–1788
14. Muskat M (1946) *The flow of homogeneous fluids through porous media*. Edwards, MI
15. Saif RS, Hayat T, Ellahi R, Muhammad T, Alsaedi A (2018) Darcy–Forchheimer flow of nanofluid due to a curved stretching surface. *Int J Numer Methods Heat Fluid Flow*
16. Hayat T, Muhammad T, Al-Mezal S, Liao SJ (2016) Darcy-Forchheimer flow with variable thermal conductivity and Cattaneo-Christov heat flux. *Int J Numer Methods Heat Fluid Flow* 26(8):2355–2369
17. Muhammad T, Alsaedi A, Shehzad SA, Hayat T (2017) A revised model for Darcy-Forchheimer flow of Maxwell nanofluid subject to convective boundary condition. *Chin J Phys* 55(3):963–976
18. Crane LJ (1970) Flow past a stretching plate. *J Appl Math Phys (ZAMP)* 21:645–647
19. Khan WA, Pop I (2010) Boundary-layer flow of a nanofluid past a stretching sheet. *Int J Heat Mass Transf* 53(11–12):2477–2483
20. Wang CY (1984) The three-dimensional flow due to a stretching flat surface. *Phys Fluids* 27:1915–1917
21. Rajagopal KR, Na TY, Gupta AS (1984) Flow of a viscoelastic fluid over a stretching sheet. *Rheologic Acta* 23(2):213–215
22. Bejan A (1979) A study of entropy generation in fundamental convective heat transfer. *ASME J Heat Transf* 101:718–725
23. Bejan A (1980) Second law analysis in heat transfer. *Energy* 5:720–732
24. Khan MI, Alsaedi A, Hayat T, Khan NB (2019) Modeling and computational analysis of hybrid class nanomaterials subject to entropy generation. *Comp Methods Prog Biomed* 179:104973

25. Esfahani JA, Akbarzadeh M, Rashidi S, Rosen MA, Ellahi R (2017) Influences of wavy wall and nanoparticles on entropy generation over heat exchanger plat. *Int J Heat Mass Transf* 109:1162–1171
26. Ranjit NK, Shit GC (2017) Entropy generation on electro-osmotic flow pumping by a uniform peristaltic wave under magnetic environment. *Energy* 128:649–660
27. Hatami M, Jing D (2020) Nanofluids: mathematical, numerical, and experimental analysis
28. Reddy JVR, Sugunamma V, Sandeep N (2018) Dual solutions for nanofluid flow past a curved surface with nonlinear radiation, Soret and Dufour effects. *J Phys Conf Ser* 1000:012152
29. Sajid M, Ali N, Javed T, Abbas Z (2010) Stretching a curved surface in a viscous fluid. *Chin Phys Lett* 27(2):024703

Chapter 12

Numerical Modelling of Electromagnetohydrodynamic (EMHD) Radiative Transport of Hybrid $\text{Ti}_6\text{Al}_4\text{V-AA7075}/\text{H}_2\text{O}$ Nanofluids from a Riga Plate Sensor Surface



M. Ganeswara Reddy, D. Tripathi, O. Anwar Bég,
and Abhishek Kumar Tiwari

Abstract A Riga plate is a special electromagnetic magnetic sensor surface that can be exploited in numerous technologies including nuclear reactor heat transfer control. Although developed for conventional viscous fluids, the Riga plate system may be improved via the use of magnetic nanoliquids. Motivated by this, the current work examines the incompressible magnetohydrodynamic (MHD) $\text{Ti}_6\text{Al}_4\text{V-AA7075-H}_2\text{O}$ hybrid nanofluid two-dimensional boundary layer flow and heat transfer from a variable thickness vertical Riga plate is studied theoretically and numerically. Viscous dissipation, heat source and thermal radiation effects are included. The governing partial differential boundary layer equations are formulated by employing the mass, momentum and energy conservation laws, and they are simplified into a nonlinear system of coupled ordinary differential equations with associated wall and free stream boundary conditions via appropriate scaling similarity transformations. The transformed nonlinear coupled boundary value problem is solved computationally with the `bvp4c` numerical function in MATLAB. The physical impacts of key emerging

M. G. Reddy

Department of Mathematics, Acharya Nagarjuna University Campus, Ongole 523001, A.P, India

D. Tripathi (✉)

Department of Mathematics, National Institute of Technology, Uttarakhand, Srinagar 246174, Uttarakhand, India

e-mail: dtripathi@nituk.ac.in

O. A. Bég

Multi-Physical Engineering Sciences Group, Department of Mechanical and Aeronautical Engineering, Salford University, Manchester M54WT, UK

e-mail: O.A.Beg@salford.ac.uk

A. K. Tiwari

Department of Applied Mechanics, Motilal Nehru National Institute of Technology Allahabad, Prayagraj 211004, Uttar Pradesh, India

parameters on all key thermal and hydrodynamic characteristics, i.e. velocity, temperature, skin friction factor and reduced Nusselt number are computed, and the results are presented as graphs and tables. Validation is included for several special cases with earlier studies in the literature. The velocity of hybrid nanofluid $f'(\eta)$ is enhanced with an increment in modified Hartmann magnetic number Q . Hybrid nanofluid temperature is depleted with an increase in thermal Grashof number Gr . An augmentation of fluid temperature is observed with a boost in thermal radiation. In addition, the rate of heat transfer Nu_x of the unitary (mono) nanofluid is significantly lower than that obtained with the hybrid nanofluid. Hybrid nanofluids are demonstrated to achieve significant benefits in thermal management relevant to hybrid thermal reactors and advanced micro-coolers utilizing magneto-hydrodynamics.

Keywords Hybrid nanofluid model · EMHD · Thermal Radiation · Heat source · Riga electromagnetic sensor · Viscous dissipation · Numerical solution · Variable plate thickness

1 Introduction

Combined electro-magneto hydrodynamic (EMHD) phenomena are featuring increasingly in many novel emerging applications in modern engineering including electro-thermal reactors [1], micro-hybrid coolers and electro-dynamical systems [2]. In these designs, the regulation of heat and continuous monitoring of surface temperatures in addition to surface drag control is necessary for optimized performance. In this regard, electromagnetic sensors provide an excellent methodology for achieving this. A promising electromagnetic sensor design was introduced in 1961 by Gailotis [3] to reduce the drag by deploying a wall-parallel Lorentz magnetic body force and utilizing permanent magnets organized in series with aligned spanwise alternating electrodes. Lorentz force is generated parallel to the Riga sensor surface and decays exponentially in the direction normal to the surface. Although originally developed as an electromagnetic actuator for naval engineering flow control, the presence of crossed electric and magnetic fields that produce the wall-parallel Lorentz force has many possible applications in medicine, coating diagnostics, industrial heat transfer control, etc. Boundary layer flow characteristics can be successfully altered with modification in the applied electrical and magnetic field strengths on Riga plate sensors. Furthermore, different working fluids can be deployed and thermo-solutal (heat and mass transfer) phenomena can also be incorporated. This has mobilized considerable interest in recent years and a rich body of literature has emerged in applied mechanics which analyses the performance of Riga and other plate sensor flows with multi-physics effects. The combined impacts of magnetic and electric fields in a Riga plate have been examined by Avilov [4]. The natural convective EMHD transport in a Riga surface was addressed by Pantokratoras and Magyari [5]. Magyari and Pantokratoras [6] examined mixed convective flows from a Riga plate using a finite difference method (FDM) and noted that flow acceleration is

induced with the modified Hartmann (magnetic) number. EMHD characteristics for both Blasius and Sakiadis flows from a Riga plate sensor were scrutinized by Pantokratoras [7]. Farooq et al. [8] computed the phase change heat transport from a Riga plate of variable thickness with chemical reaction and viscous heating effects. High temperatures can often be generated in MHD systems owing to radiative heat transfer (nuclear reactors). The inclusion of thermal radiation heat transfer is, therefore, important in a more precise simulation of Riga sensor transport phenomena. This is usually achieved with some form of algebraic flux model to avoid having to solve the general integro-differential equation for radiative heat transfer, which is formidable even with advanced computational methods. The thermal radiation effects on viscoelastic hydromagnetic flow from a vertical Riga plate with Newtonian heating were, therefore, explored by Shafiq et al. [9]. They noted that temperature is strongly elevated with greater radiative flux; whereas, it is suppressed with higher values of modified Hartmann number. Anjum et al. [10] computed the non-Fourier thermal relaxation effects in non-Newtonian flow along a Riga plate with heat source/sink effects. They showed that momentum boundary layer thickness is decreased with a stronger modified Hartmann parameter. Nasir et al. [11] investigated the heat transfer in stagnation flow impinging on a stretching Riga plate with thermal radiative flux and hydrodynamic wall slip. Shamshuddin and Satya Narayana [12] have scrutinized the non-Fourier transport from a Riga surface with Ohmic and viscous heating effects, noting that temperature is an increasing function of the Eckert number. Mishra et al. [13] used the variational parameter method (VPM) to study the double-diffusive heat and mass transfer in squeezing flow on a Riga plate sensor with viscous heating, Ohmic dissipation and Cattaneo-Christov hyperbolic heat flux effects. Shamshuddin et al. [14] examined the influence of thermophoretic particle deposition and thermal/solutal stratification on convection from an exponentially stretching Riga plate sensor. All these investigations have confirmed the excellent range of advantages offered by Riga plates in fine-tuning flow properties for modern magnetic sensor design [15].

The idea of nanofluids was initiated in the mid-1990s by Choi [16] via carefully suspending material nanoparticles in a base fluid. This study along with other investigations [17, 18] confirmed via experiments that a superior thermal conductivity of nanofluid is achieved compared with regular fluids. This produces enhanced ballistic collisions of nanoparticles, exacerbates micro-convection, and thereby contributes to the enhancement of heat transfer. The transport characteristics of a nanofluid flowing from a Riga plate were first addressed by Ahmed et al. [19] by considering thermophoresis and Brownian motion via the Buongiorno nanoscale two-component formulation. Hayat et al. [20] computed the influence of variable wall thickness and convective wall conditions on the Riga plate sensor boundary layer flow. Both velocity and temperature were shown to be enhanced with greater wall thickness. Abbas et al. [21] conducted a second-law thermodynamic optimization study on nanofluid convection from a Riga plate. Bhatti et al. [22] have addressed the radiative flux impact on EMHD nanoliquid Riga plate flows. Ayub et al. [23] considered wall slip effects on a horizontal Riga plate using a shooting numerical technique. Ahmed

et al. [24] studied the mixed convective nanofluid flow in a heated Riga plate. Iqbal et al. [25] used a Keller-box finite difference method to simulate the micro-organism doped nanofluid convection from a Riga sensor. Non-Newtonian effects in Riga plate boundary layer flows were examined by Ramzan et al. [26] (using the Williamson viscoelastic model), Rasool and Zhang [27, 28] (using a Powell–Eyring model and Reiner–Rivlin second-grade model, respectively). EMHD flow of nanofluids with heat transfer along a Riga plate was examined by Abbas et al. [29]. Rooman et al. [30] have discussed the radiative hydromagnetic nanofluid with Bejan entropy generation minimization. Rasool et al. [31] have investigated the EMHD convective nanofluid from a Riga Plate with a revised version of Buongiorno’s nanoscale model. The heat transfer in Riga plate nanofluid flow with viscoelastic and radiative effects was examined by Shafiq et al. [32]. Bhatti et al. [33] have computed activation energy effects on micro-organism-doped nanofluid transport from a Riga plate nanofluid. Kayikci et al. [34] computed thermal relaxation and radiative heat flux effects on glycerine carbon nanotube (CNT)-water nanofluid dynamics from a Riga plate sensor using the homotopy analysis method (HAM). Shamshuddin et al. [35] analysed the heat and mass transfer from an exponentially stretching Riga surface with dual stratification, radiative heat transfer and chemical reaction.

A new subset of nanofluids has recently emerged, known as *hybrid nanofluids*, which are synthesized by suspending two (or more) distinct material nanoparticles in a single base fluid. Hybrid nanofluids have demonstrated a further enhancement in thermal conductivity compared with unitary nanofluids or regular fluids and many promising applications in renewable energy have been documented by Sarkar et al. [36]. Several investigators have recently explored the use of hybrid nanofluids in Riga plate sensors. Zaib et al. [37] computed the non-Newtonian TiO_2 /Kerosene-water hybrid nanofluid mixed convective transport along a Riga plate using the `bvp4c` function in MATLAB. SWCNT-MWCNT/ H_2O hybrid nanofluid micropolar flow along a Riga sensor was examined by Abbas et al. [38]. Hybrid Al_2O_3 -Cu -water nanofluid transport in Riga plates was theoretically investigated by Khashiie et al. [39]. Hybrid nanoparticle performance in a Riga plate was studied by Nadeem et al. [40], who observed a notable increase in temperatures with escalating solid volume fractions. A comparative study of mono-nanofluid and hybrid nanofluids in radiative convection from a Riga surface was conducted by Asogwa et al. [41]. These investigations all verified the considerable elevation in heat transfer performance with judicious combinations of hybrid nanoparticles in Riga sensor systems.

The above studies did not consider the performance of hybrid titanium alloy ($\text{Ti}_6\text{Al}_4\text{V}$) and aluminium alloy (AA7075) nanoparticles. These offer some advantages in modern sensor design systems [42] and are the focus of the present study. The base carrier fluid is considered as water (H_2O). A mathematical model is, therefore, presented for two-dimensional (2D) steady ternary hybrid nanofluid from a Riga vertical plate. Variable plate thickness, thermal radiation, thermal buoyancy, heat source and viscous dissipation effects are also included. The dimensionless ordinary differential boundary value problem is derived using similarity scaling variables and solved numerically with the `bvp4c` function in MATLAB. The results are compared

and validated against published studies for several special cases. Extensive visualization of the thermal and flow characteristics is included via graphs and tables. The current study constitutes a novel contribution to the scientific literature on Riga plate electromagnetic sensor transport phenomena utilizing hybrid nanofluids.

2 Formulation of the Problem

Steady, two-dimensional (x - y) electro-magneto hydrodynamic (EMHD) transport of hybrid magnetic nanofluid along a vertical Riga sensor plate is considered under the influence of thermal buoyancy, radiation, dissipation and heat source. The hybrid nanofluid comprises two non-identical nanoparticles, i.e. titanium alloy ($\text{Ti}_6\text{Al}_4\text{V}$) and aluminium alloy (AA7075) suspended in base carrier fluid of water (H_2O). The Riga plate consists of electrodes and magnets organized alternately on a surface that has variable thickness according to the relation, $y = A(x + b)^{\frac{1-n}{2}}$ along the x -axis with the y -axis directed normal to the plane surface. Here, the dimensional constant A is supposed to be very small. The physical configuration is depicted in Fig. 1a with the boundary layer regime illustrated in Fig. 1b. The Riga plate has a wall velocity $u_w(x) = U_0(x + b)^n$, here U_0, b is a positive constant and n is the velocity power index. Nanofluid temperature at the surface is T and ambient fluid temperature away from the surface is T_∞ . Hall current and Maxwell displacement currents are neglected as they are insignificant in Riga plate regimes. Rosseland's flux model is used for radiative heat transfer. Based on the afore-mentioned suppositions along with the Boussinesq approximation, the equations of continuity, momentum and energy for the regime with hybrid nanoparticles take the following form by amalgamating the models in Farooq et al. [8], Shamshuddin and Satya Narayana [12], Hayat et al. [20], Khashi'ie et al. [39]:

$$\frac{\partial u}{\partial x} + \frac{\partial v}{\partial y} = 0, \quad (1)$$

$$u \frac{\partial u}{\partial x} + v \frac{\partial u}{\partial y} = \nu_{hnf} \frac{\partial^2 u}{\partial y^2} + \frac{\pi J_0 M_0}{8 \rho_{hnf}} e^{-\frac{\pi}{a_1} y} + \frac{\beta_{hnf}}{\rho_{hnf}} g(T - T_\infty), \quad (2)$$

$$u \frac{\partial T}{\partial x} + v \frac{\partial T}{\partial y} = \frac{k_{hnf}}{(\rho c_p)_{hnf}} \frac{\partial^2 T}{\partial y^2} + \frac{16\sigma^* T_\infty^3}{3k^*(\rho c_p)_{hnf}} + \frac{Q_0}{(\rho c_p)_{hnf}} (T - T_\infty)$$

$$+ \frac{\mu_{hnf}}{(\rho c_p)_{hnf}} \left(\frac{\partial u}{\partial y} \right)^2, \quad (3)$$

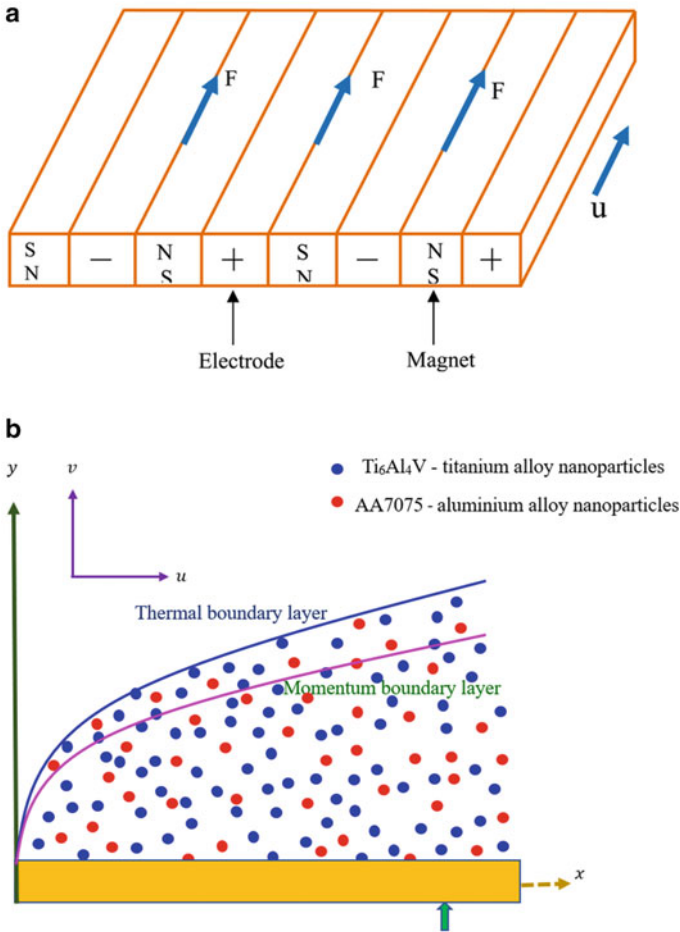


Fig. 1 a Riga plate b Boundary layer regime on the Riga sensor surface

The imposed boundary conditions are prescribed following Farooq et al. [8], Abbas et al. [21]:

$$\begin{aligned}
 u = u_w(x) = U_0(x + b)^n, v = 0, T = T_w at y = A(x + b)^{\frac{1-n}{2}}, \\
 u \rightarrow 0, T \rightarrow T_\infty as y \rightarrow \infty
 \end{aligned}
 \tag{4}$$

Here u and v are denoted the velocity components along the Cartesian co-ordinates, ϑ_{hnf} is the kinematic viscosity of hybrid nanofluid, J_0 is applied current density, ρ_{hnf} is the fluid density of hybrid nanofluid, M_0 is the magnetization of the permanent magnets, σ^* is the Stefan–Boltzmann radiation constant, k^* is the mean absorption coefficient, and Q_0 is heat generation coefficient. The properties of the nanoparticles and base fluid are given in Table 1.

Table 1 Thermo-physical characteristics of titanium alloy (Ti₆Al₄V), aluminium alloy (AA7075) and water (H₂O) [34]

Physical parameter	Nanoparticles		Base fluid
	Ti ₆ Al ₄ V	AA7075	H ₂ O
ρ	4420	2810	997.1
β	28.17×10^{-5}	29.64×10^{-5}	21×10^{-5}
k	7.2	173	0.613
c_p	0.56	960	4179

Table 2 The physical and thermal features of unitary nanofluid [27]

Properties	Hybrid nanofluid
Viscosity	$\frac{\mu_{nf}}{\mu_f} = \frac{1}{(1-\phi_1)^{2.5}}$
Density	$\frac{\rho_{nf}}{\rho_f} = (1 - \phi_1) + \phi_1 \frac{\rho_{s1}}{\rho_f}$
Thermal expansion	$\frac{(\rho\beta)_{nf}}{(\rho\beta)_f} = (1 - \phi_1) + \phi_1 \frac{(\rho\beta)_{s1}}{(\rho\beta)_f}$
Thermal conductivity	$\frac{k_{nf}}{k_f} = \frac{k_{s1} + 2k_f - 2\phi_1(k_f - k_{s1})}{k_{s1} + 2k_f + \phi_1(k_f - k_{s1})}$
Heat capacitance	$\frac{(\rho c_p)_{nf}}{(\rho c_p)_f} = (1 - \phi_1) + \phi_1 \frac{(\rho c_p)_{s1}}{(\rho c_p)_f}$

Table 3 The thermal and physical features of hybrid nanofluid [36, 37]

Properties	Hybrid nanofluid
Viscosity	$\frac{\mu_{hnf}}{\mu_f} = \frac{1}{(1-\phi_1)^{2.5}(1-\phi_2)^{2.5}}$
Density	$\frac{\rho_{hnf}}{\rho_f} = (1 - \phi_2) \left\{ (1 - \phi_1) + \phi_1 \frac{\rho_{s1}}{\rho_f} \right\} + \phi_2 \frac{\rho_{s2}}{\rho_f}$
Thermal expansion	$\frac{(\rho\beta)_{hnf}}{(\rho\beta)_f} = (1 - \phi_2) \left\{ (1 - \phi_1) + \phi_1 \frac{(\rho\beta)_{s1}}{(\rho\beta)_f} \right\} + \phi_2 \frac{(\rho\beta)_{s2}}{(\rho\beta)_f}$
Thermal conductivity	$\frac{k_{hnf}}{k_f} = \frac{k_{s2} + 2k_{nf} - 2\phi_2(k_{nf} - k_{s2})}{k_{s2} + 2k_{nf} + \phi_2(k_{nf} - k_{s2})}$
Heat capacitance	$\frac{(\rho c_p)_{hnf}}{(\rho c_p)_f} = (1 - \phi_2) \left\{ (1 - \phi_1) + \phi_1 \frac{(\rho c_p)_{s1}}{(\rho c_p)_f} \right\} + \phi_2 \frac{(\rho c_p)_{s2}}{(\rho c_p)_f}$

The formulations for mono-nanofluid and hybrid nanofluid are reported in Tables 2 and 3, respectively.

In Tables 2 and 3, ϕ_1, ϕ_2 are the volume fractions of Ti₆Al₄V and AA7075 nanoparticles, $\mu_{hnf}, \mu_{nf}, \mu_f$ are the dynamic viscosity of hybrid nanofluid, unitary nanofluid and base fluid, k_{hnf}, k_{nf}, k_f are the thermal conductivity of hybrid nanofluid, unitary nanofluid and base fluid, $(\rho c_p)_{hnf}, (\rho c_p)_{nf}, (\rho c_p)_f$ are the specific heat capacitance of hybrid nanofluid, unitary nanofluid and base fluid, respectively.

To simplify the primitive boundary layer flow model, we define the following scaling similarity transformations and non-dimensional physical parameters:

$$\begin{aligned} \psi &= \sqrt{\frac{2}{(n+1)}U_0} \vartheta_f(x+b)^{n+1} F(\eta), \quad \eta = y \sqrt{\frac{(n+1)U_0}{2} \frac{U_0}{\vartheta_f}}(x+b)^{n-1}, \\ v &= -\frac{\partial \psi}{\partial y} = \sqrt{\frac{(n+1)U_0}{2}} \vartheta_f U_0(x+b)^{n-1} \left(F(\eta) + \eta \left(\frac{n-1}{n+1} \right) F'(\eta) \right), \\ u &= \frac{\partial \psi}{\partial x} = U_0(x+b)^n, \quad Pr = \frac{\vartheta_f}{\alpha_f}, \quad Q = \frac{\pi j_0 M_0}{8 \rho_f U_0^2}, \quad \beta_1 = \frac{\frac{\pi}{a_1}}{\sqrt{\frac{(n+1)U_0}{2} \vartheta_f U_0(x+b)^{n-1}}}, \\ Rd &= \frac{4\sigma^* T_\infty^3}{kk^*}, \quad \lambda = \frac{Q_0(x+b)^{1-n}}{(\rho c_p)_f}, \quad \theta(\eta) = \frac{T - T_\infty}{T_w - T_\infty} \end{aligned} \tag{5}$$

where ψ is the dimensional stream function, F is the dimensionless stream function and θ is the non-dimensional temperature function.

By employing Eq. (5) in the Eqs. (1)–(4), the mass conservation Eq. (1) is automatically satisfied, and the momentum and energy equations are transformed to:

$$\frac{N_1}{N_2} F''' + F F'' - \frac{2}{(n+1)} F'^2 + \frac{2}{(n+1)} Q e^{-\beta_1 \eta} + \frac{2}{(n+1)} N_3 Gr \theta = 0 \tag{6}$$

$$\left[N_4 + \frac{4}{3} Rd \right] \theta'' + N_5 Pr \left[F \theta' + \frac{2}{(n+1)} \lambda \theta \right] + N_1 Pr Ec F'^2 = 0 \tag{7}$$

The wall and free stream boundary conditions reduce to:

$$\begin{aligned} F(\alpha_1) &= \alpha_1 \frac{1-n}{1+n}, \quad F'(\alpha_1) = 1, \quad \theta(\alpha_1) = 1, \\ F'(\alpha_1) &\rightarrow 0, \quad \theta(\alpha_1) \rightarrow 0 \end{aligned} \tag{8}$$

Here, the prime indicates the partial derivative with respect to η . $Q, \beta_1, Gr, Rd, Pr, \lambda, Ec$ and $\alpha_1 = A \sqrt{\frac{(n+1)U_0}{2} \frac{U_0}{\vartheta_f}}$, respectively, denote the modified Hartmann number, dimensionless Riga parameter associated with the magnetic and electrode width, thermal Grashof number, thermal radiation parameter, Prandtl number, heat source parameter, Eckert number and the wall thickness parameter in which n is velocity power index. The constant terms arising in Eqs. (7, 8) i. e. $N_1 \dots N_5$ are defined as:

$$N_1 = \frac{\mu_{hnf}}{\mu_f}, \quad N_2 = \frac{\rho_{hnf}}{\rho_f}, \quad N_3 = \frac{(\rho\beta)_{hnf}}{(\rho\beta)_f}, \quad N_4 = \frac{k_{hnf}}{k_f}, \quad N_5 = \frac{(\rho c_p)_{hnf}}{(\rho c_p)_f} \tag{9}$$

To further simplify the problem, we define the following stream and temperature functions:

$$F(\eta) = F(\eta - \alpha_1) = f(\xi) \text{ and } \theta(\eta) = \theta(\eta - \alpha_1) = \theta(\xi) \quad (10)$$

Now substituting the above functions in Eqs. (6)–(8), the boundary layer equations are transformed to:

$$\frac{N_1}{N_2} f''' + ff'' - \frac{2}{(n+1)} f'^2 + \frac{2}{(n+1)} Qe^{-\beta_1(\xi+\alpha_1)} + \frac{2}{(n+1)} N_3 Gr \theta = 0 \quad (11)$$

$$\left[N_4 + \frac{4}{3} Rd \right] \theta'' + N_5 Pr \left[f\theta' + \frac{2}{(n+1)} \lambda \theta \right] + N_1 Pr Ec f'^2 = 0 \quad (12)$$

The dimensionless boundary conditions (8) emerge as:

$$\begin{aligned} f(0) &= \alpha_1 \frac{1-n}{1+n}, F'(0) = 1, \theta(0) = 1, \\ F'(\infty) &\rightarrow 0, \theta(\infty) \rightarrow 0 \end{aligned} \quad (13)$$

Important Riga sensor wall characteristics are the skin friction factor and heat transfer rate. Using the transformations defined earlier, the appropriate expressions for dimensionless skin-friction coefficient and local Nusselt number are given by Farooq et al. [8], Hayat et al. [20]:

$$Re_x^{\frac{1}{2}} C_{fx} = N_1 \sqrt{\frac{(n+1)}{2}} f''(0), \quad (14)$$

$$Re_x^{-\frac{1}{2}} Nu_x = -N_4 \sqrt{\frac{(n+1)}{2}} \left(1 + \frac{4}{3} Rd \right) \theta'(0), \quad (15)$$

where

$$Re_x = \frac{U_0(x+b)}{\nu_f} \text{ is the local Reynolds number.}$$

3 Numerical Solution

The non-dimensional boundary layer flow Eqs. (11)–(12) describing the hybrid nanofluid flow along the Riga plate are highly nonlinear and coupled. Hence, it is exceedingly difficult if not impossible to obtain exact solutions. A computational approach is, therefore, adopted. The efficient fourth-order Runge–Kutta method available in the `bvp4c` built-in function of MATLAB is deployed. The procedure is summarized in Fig. 2. Further details are given in Bég [43] and Keskin [44]:

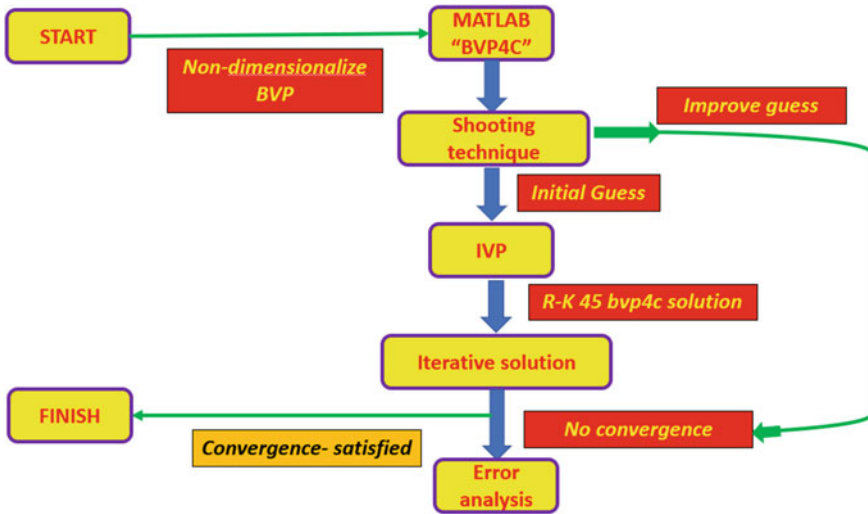


Fig. 2 MATLAB bvp4c methodology

The physical non-dimensional parametric values are chosen as: $Q = 0.2$, $\beta = 0.3$, $\alpha_1 = 1.4$, $Gr = 0.5$, $Rd = 1.2$, $Pr = 2.2$, $Ec = 0.1$, $n = 1.2$, $\lambda = 0.2$, $\phi_1 = 0.02$ and $\phi_2 = 0.03$ for the numerical calculations of the results throughout the study. This data is extracted from multiple sources to be physically representative of actual Riga sensor systems [15, 20, 36, 42]. To assess the accuracy of the bvp4c numerical method for the obtained results, a comparison of the rate of heat transfer $-\theta'(0)$ for distinct values of Prandtl number Pr with the published literature works of Mabood et al. [45], Wang. [46], Salahuddin et al. [47] and Hayat et al. [48] as displayed in Table 4. It is observed that very close agreement is achieved confirming the accuracy of the present MATLAB bvp4c numerical solutions.

Table 4 Numerical comparison of dimensionless rate of heat transfer $-\theta'(0)$ when $n = 1$, $Rd = \lambda = Ec = Q = 0$

Pr	Mabood et al. [45]	Wang [46]	Salahuddin et al. [47]	Hayat et al. [48]	Present MATLAB results
0.70	0.453964	0.453968	0.453965	0.453964	0.4539645
2.0	0.911487	0.911484	0.911487	0.911485	0.9114871
3.0	1.243656	1.243659	1.243657	1.243654	1.2436568
7.0	1.895439	1.895438	1.895436	1.895437	1.8954390

4 Numerical Results and Discussion

The influence of key thermophysical and magnetic parameters on the hybrid nanofluid velocity and heat transport characteristics have been computed and are visualized in Figs. 3, 4, 5, 6, 7, 8, 9, 10, 11, 12, 13, 14, 15 and 16 and Tables 5 and 6.

It is noteworthy that in all the plots asymptotically smooth distributions are computed in the free stream (at the maximum value of ξ) confirming that an adequately large infinity boundary condition has been prescribed in the MATLAB bvp4c solver.

Figures 3 and 4 illustrate the evolution in velocity $f'(\eta)$ and temperature field $\theta(\eta)$ for distinct values of Q . $Q = \frac{\pi j_0 M_0}{8 \rho_f U_0^2}$ and is directly proportional to the magnetic field strength (M_0). With an increment in Q values, there is a strong accentuation in velocity profiles (Fig. 2), which exhibit a monotonic decay from the wall (sensor surface). Peak velocity is always computed at the Riga plate surface (where $\xi = 0$) and the velocity decays into the free stream (edge of the boundary layer). Flow acceleration is, therefore, generated since the modified magnetic body force, $+\frac{2}{(n+1)} Q e^{-\beta_1(\xi+\alpha_1)}$, in the momentum Eqn. is assistive, not inhibitive, since it aligned with the sensor (plate surface) and is not transverse to it, as in Lorentzian forces encountered in conventional magnetohydrodynamics [49]. Momentum (hydrodynamic) boundary layer thickness is, therefore, reduced with greater values of magnetization parameter, Q , since the flow is accelerated Temperature as observed in Fig. 4, is conversely suppressed with increasing values of Q . Since the aligned magnetic body force assists momentum development, the nanofluid does not expend extra work as it does not have to drag

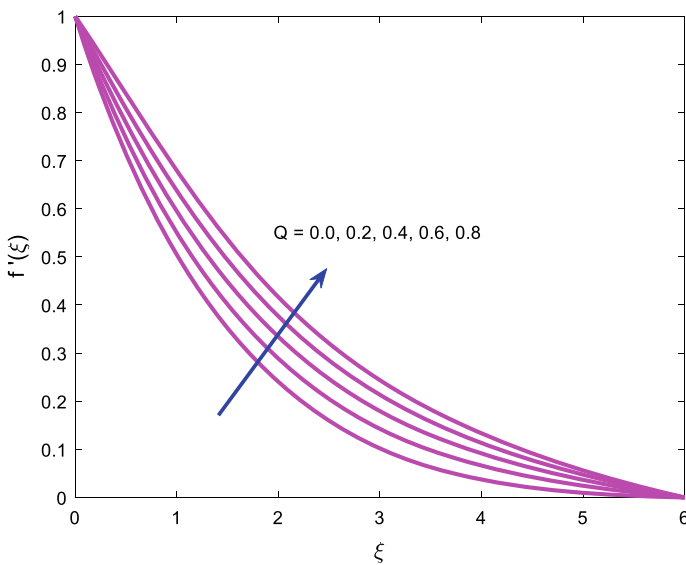


Fig. 3 Velocity function $f'(\xi)$ versus Q

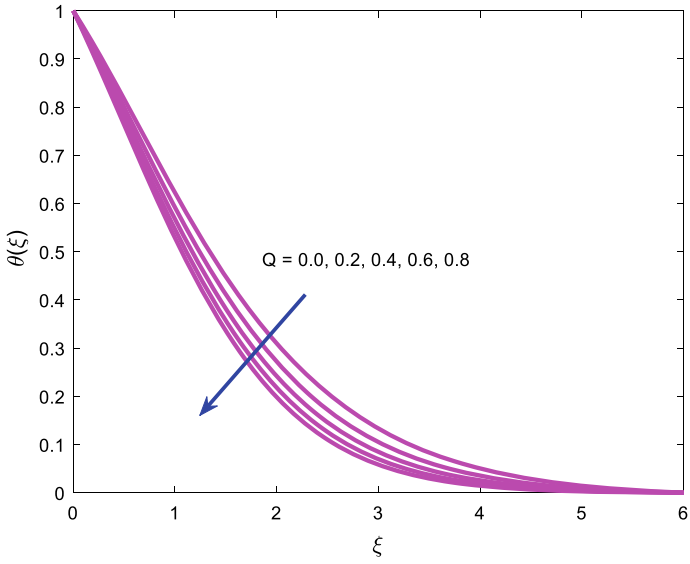


Fig. 4 Temperature function $\theta(\xi)$ versus Q

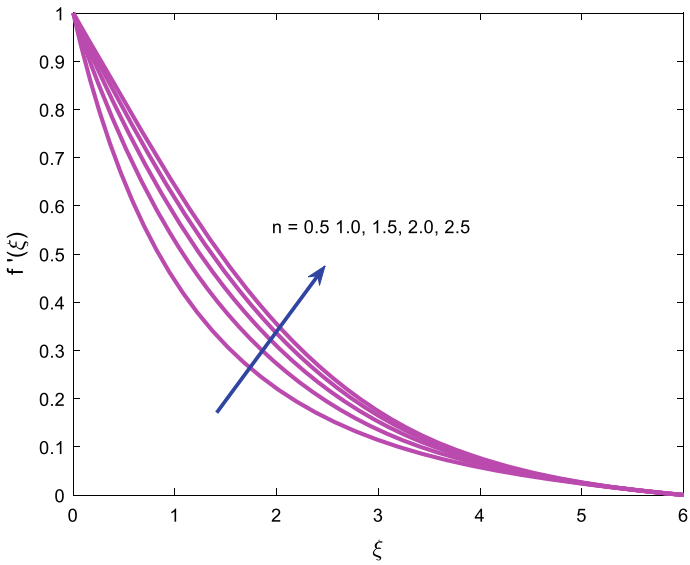


Fig. 5 Velocity function $f'(\xi)$ versus n

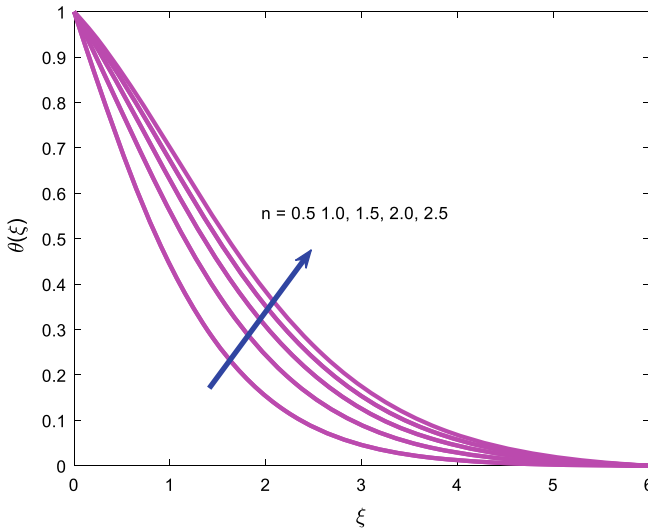


Fig. 6 Temperature function $\theta(\xi)$ versus n

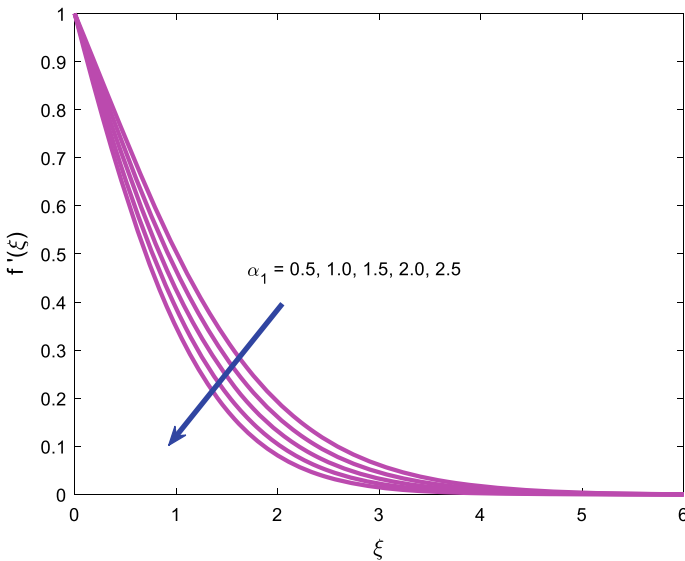


Fig. 7 Velocity function $f'(\xi)$ versus α_1

against the magnetic field. This induces a cooling effect in the regime and decreases thermal boundary layer thickness. The behaviour is, therefore, the opposite of that encountered in classical MHD boundary layer flow [49] where temperatures under a *transverse* magnetic field are always elevated.

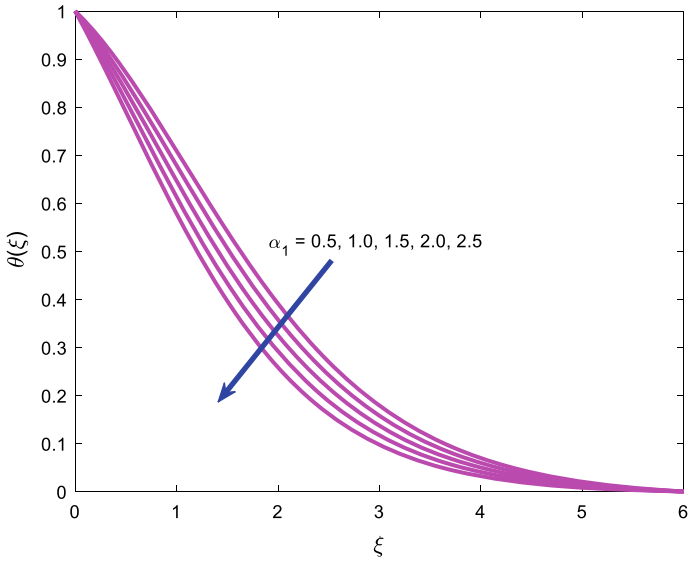


Fig. 8 Temperature function $\theta(\xi)$ versus α_1

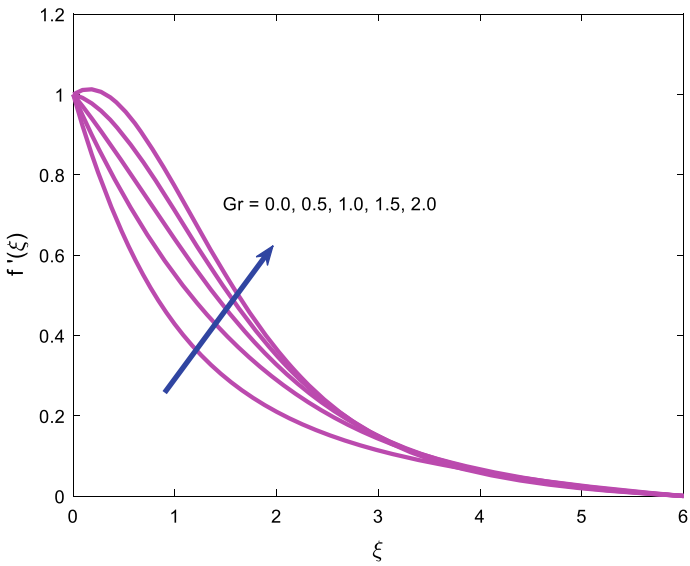


Fig. 9 Velocity function $f'(\xi)$ versus Gr

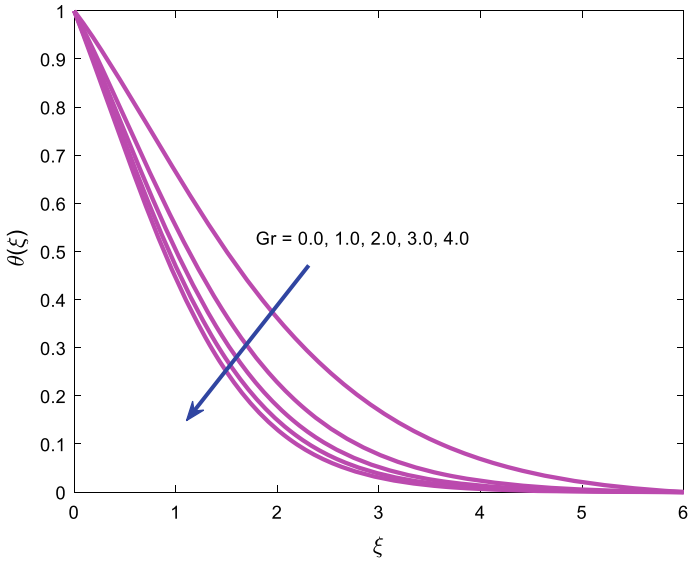


Fig. 10 Temperature function $\theta(\xi)$ versus Gr

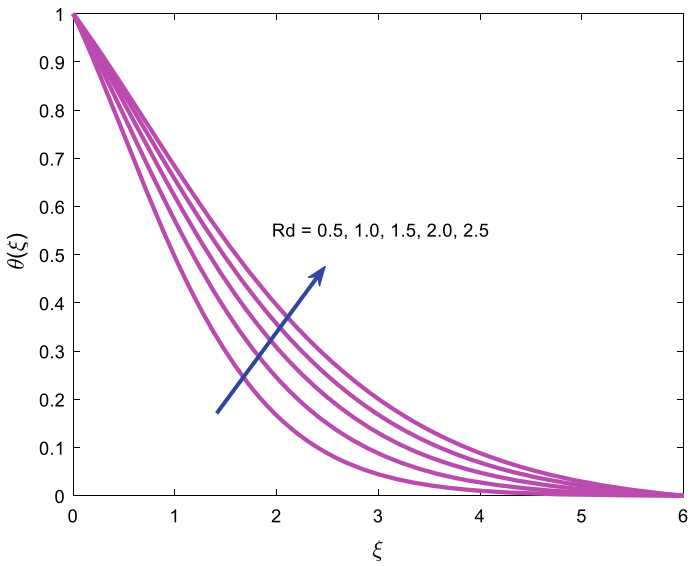


Fig. 11 Temperature function $\theta(\xi)$ versus Rd

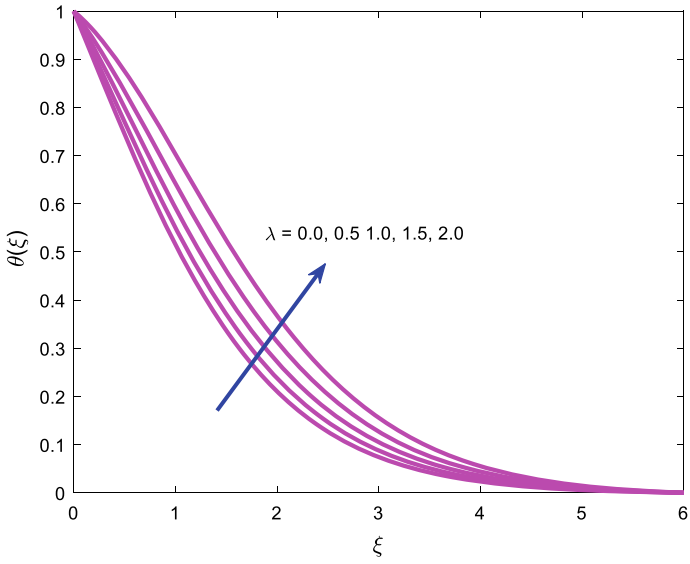


Fig. 12 Temperature function $\theta(\xi)$ versus λ

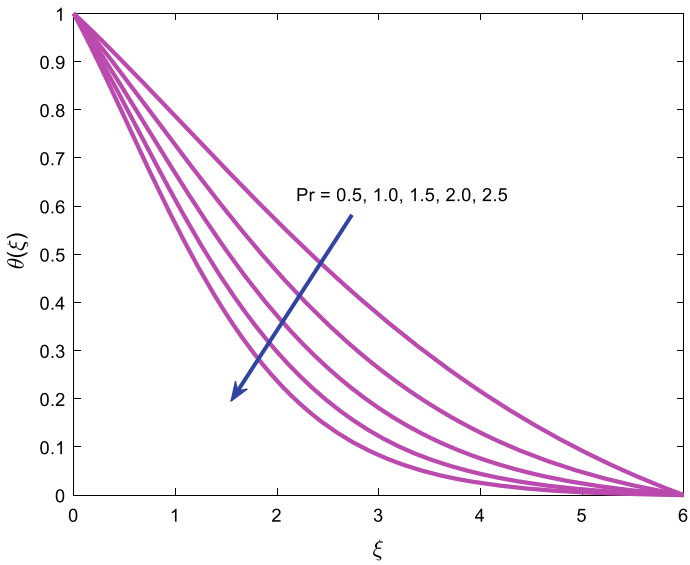


Fig. 13 Temperature function $\theta(\xi)$ versus Pr

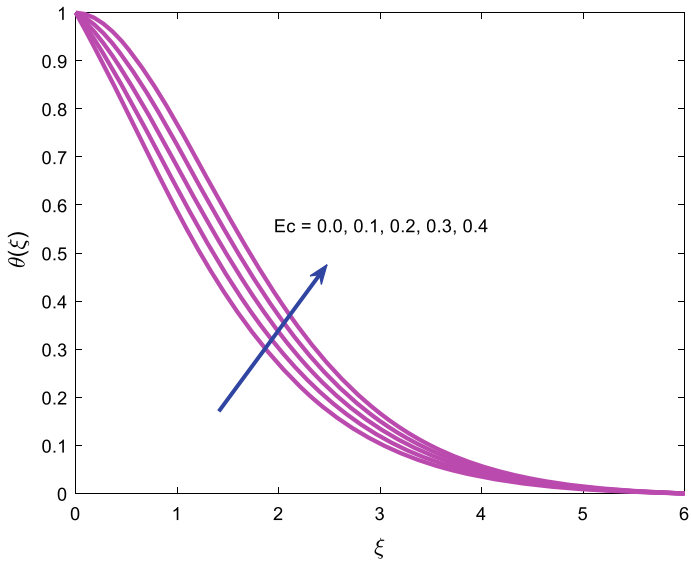


Fig. 14 Temperature function $\theta(\xi)$ versus Ec

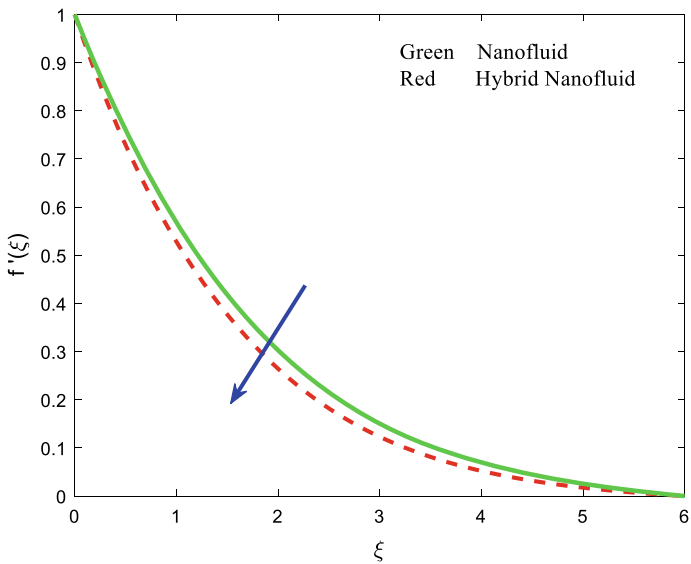


Fig. 15 Comparison of mono nanofluid and hybrid nanofluid for $f'(\xi)$

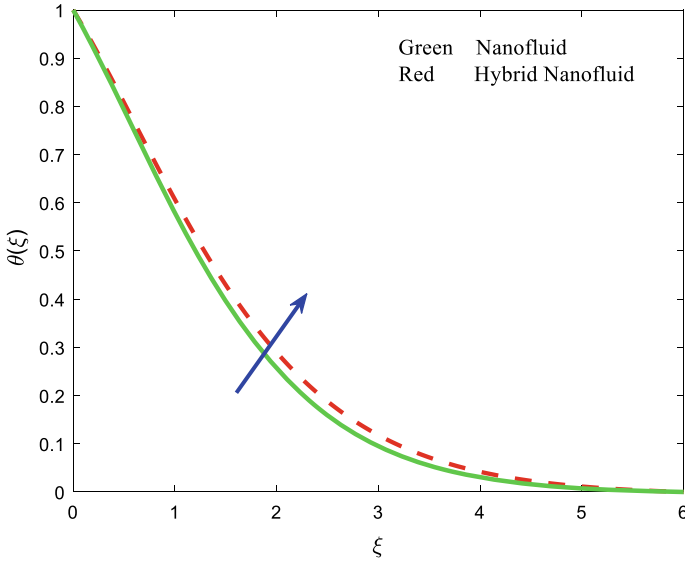


Fig. 16 Comparison of mono nanofluid and hybrid nanofluid for $\theta(\xi)$

Table 5 Numerical computations of the dimensionless skin friction factor C_{fx} for two distinct nanofluids

Q	β	Gr	α	n	C_{fx}	
					Mono nanofluid	Hybrid nanofluid
0.2	0.3	0.5	1.4	1.2	0.566209	0.714170
0.6					0.397092	0.489221
1.0					0.232727	0.270669
1.4					0.072766	0.058121
	0.6				0.607590	0.768090
	1.0				0.632059	0.800771
	1.5				0.644266	0.817414
		1			0.728781	0.931455
		2			0.618861	0.784391
		3			0.514778	0.645667
			0.5		0.575687	0.728122
			2		0.556342	0.700271
			3		0.535639	0.671753
				0.5	0.715440	0.934000
				1.5	0.596200	0.758391
				2.0	0.493334	0.605439

Table 6 Numerical computations of the dimensionless rate of heat transfer Nu_x for two distinct nanofluids

Rd	Pr	λ	Ec	Gr	Nu_x	
					Mono nanofluid	Hybrid nanofluid
1.2	2.2	0.2	0.1	0.5	0.566209	0.714170
2					1.222707	1.419665
3					1.438991	1.686848
4					1.652563	1.947586
	0.71				0.609273	0.706267
	1.5				0.843072	0.967541
	2.4				1.088999	1.247000
		0.3			0.802766	0.901473
		0.4			1.478200	0.567169
		0.5			0.206406	0.167373
			0.2		1.014023	1.153928
			0.3		0.990835	1.120152
			0.4		0.967770	1.086590
				1	1.157652	1.346831
				2	1.316094	1.549327
				3	1.423612	1.682047

Figures 5 and 6 illustrate the behaviour of velocity power index parameter n on the hybrid nanofluid velocity and temperature. The impact of n on both flow distributions is similar. It is observed that both velocity and temperature are accentuated with greater n . Larger values of the velocity power index indicate more intensive wall motion on the Riga surface. This boosts momentum and accelerates the flow producing a thinner hydrodynamic boundary layer. Similarly, thermal diffusion is also intensified, and thermal boundary layer thickness is elevated.

Figures 7 and 8 display the profiles for hybrid nanofluid velocity and temperature with a variation in wall thickness parameter, α_1 . It is found that with an increment in thickness parameter α_1 , the hybrid nanofluid velocity and temperature are both considerably decreased. Momentum boundary layer thickness is, therefore, elevated due to the reduction in shearing action at the Riga plate surface; whereas thermal boundary layer thickness is suppressed. The wall thickness effect is only associated with the wall stream function boundary condition, $f(0) = \alpha_1 \frac{1-n}{1+n}$ in Eq. (11) and $\alpha_1 = A \sqrt{\frac{(n+1)}{2} \frac{U_0}{\vartheta_f}}$ indicating that the primary effect is on the momentum diffusion. However, due to the strong coupling of the momentum and energy Eqs. (9) and (10), the temperature field is also influenced. The thickness of the Riga sensor surface, therefore, exerts a non-trivial influence on the boundary layer dynamics. Larger α_1 indicates a thicker wall, which produces flow deceleration and cooling. The results computed concur with other studies including Salahuddin et al. [47].

Figures 8 and 9 display the impact of thermal Grashof number Gr on the velocity $f'(\eta)$ and temperature function $\theta(\eta)$. The hybrid nanofluid fluid velocity is strongly enhanced with a boost in values of Gr both in close proximity and further from the Riga plate surface. The thermal buoyancy force in Eq. (9), i.e. $+\frac{2}{(n+1)}N_3Gr\theta$, clearly assists momentum development in the boundary layer. Stronger thermal buoyancy, therefore, reduces the hydrodynamic boundary layer thickness. For the case of $Gr = 0$, forced convection is present indicating an absence of natural convection currents and velocity is minimized (momentum boundary layer thickness is maximum for this scenario). For $Gr = 2$, i.e. thermal buoyancy force being greater than viscous hydrodynamic force, an overshoot is computed in the velocity near the wall. This is absent for all other values of Gr . Figure 10 shows that conversely there is a reduction in the hybrid nanofluid temperature with a greater thermal Grashof number. The intensification in natural convection currents acts to accelerate the flow but suppresses thermal diffusion in the boundary layer, leading to a strong cooling effect. Thermal boundary layer thickness is, therefore, also decreased with greater values of Gr .

Figure 11 portrays the influence of thermal radiation Rd on temperature field $\theta(\eta)$. An augmentation of temperature is clearly generated with larger values of Rd . The thermal conduction term $[N_4 + \frac{4}{3}Rd]\theta''$ in the energy Eq. (9) is modified by the presence of thermal radiation. When radiation is absent, $Rd = 0$. This energizes the boundary layer and encourages thermal diffusion. Temperatures are, therefore, elevated as is thermal boundary layer thickness. Similar observations have been reported by Bhatti et al. [22], Kayikci et al. [34] and Shamshuddin et al. [35]. The Rosseland diffusion model while limited to optically thick nanofluids does provide a good approximation for boundary layer flows and correctly predicts an elevation in temperature.

Figure 12 illustrates the effect of heat source parameter, λ on temperature evolution through the boundary layer, i.e. with ξ coordinate. Physically the presence of a heat source ($\lambda > 0$) may be associated with a hot spot on the Riga source or a volumetric heat generation mechanism. This adds thermal energy to the boundary layer via the convective nonlinear term, $+N_5Pr\left[\frac{2}{(n+1)}\lambda\theta\right]$ featuring in the energy Eq. (9). This enhances thermal boundary layer thickness. The converse case of a heat sink ($\lambda < 0$) is not considered. Evidently in the absence of a heat source or sink ($\lambda = 0$) temperature is minimized in the regime.

Figure 13 depicts the impact of the Prandtl number Pr on the dimensionless temperature function. A strong reduction in the hybrid nanofluid temperature is induced with elevation in Pr . There is an inverse proportionality of the Prandtl number to thermal conductivity. Higher Pr , therefore, corresponds to lower thermal conductivities. This suppresses temperatures in the boundary layer and reduces thermal boundary layer thickness.

Figure 14 reflects the influence of Eckert number Ec on the temperature field. It is apparent that temperature is enhanced significantly with increasing values of Eckert number. This parameter arises in the term, $+N_1PrEc f''^2$, in Eq. (9). It represents the kinetic energy dissipated due to internal friction in the nanofluid. As a result, heat is generated which elevates temperatures and increases thermal boundary layer

thickness. Clearly, the neglect of viscous heating ($Ec = 0$) in mathematical models leads to an under-prediction in temperatures.

Figures 15 and 16 visualize the relative performance of unitary (mono) nanofluid and hybrid nanofluid for velocity $f'(\eta)$ and temperature $\theta(\eta)$. From Fig. 15, it is evident that velocity is lower for hybrid nanofluid and higher for mono nanofluid. In other words, the presence of a single nanoparticle is beneficial for flow acceleration whereas multiple nanoparticles induce flow deceleration. Conversely, temperatures as observed in Fig. 16 are greater for hybrid nanofluid compared with unitary nanofluid. The presence of more nanoparticles clearly increases ballistic collisions in the base fluid which produces heat. Thermal conductivity is, therefore, higher for hybrid nanofluids testifying to their advantage in heat transfer performance relative to unitary nanofluids.

Dimensionless friction factor C_{fx} and heat transfer rate, i. e. local Nusselt number, Nu_x values computed for a range of selected control parameters for two distinct nanofluids i.e., unitary nanofluid and hybrid nanofluid are displayed in Tables 5 and 6. It is observed from Table 5 that the friction factor declines for an upsurge in values of modified Hartmann magnetic number, Q , Grashof number, Gr and velocity power-law index parameter, n whereas the non-dimensional friction factor enhances with increasing value of Riga plate electrode parameter, β and wall thickness parameter, α_1 . Considerably higher magnitudes of skin-friction coefficient are computed for the hybrid nanofluid compared with the mono nanofluid. Table 6 shows that the Nusselt number, Nu_x is improved with increment in Grashof number, Gr , radiative parameter, Rd , Prandtl number, Pr and heat source parameter, λ whereas it is clearly depleted with increasing Eckert number, Ec . Furthermore, lower magnitudes of local Nusselt number are produced for mono nanofluid compared with the hybrid nanofluid.

5 Conclusions

Motivated by examining near-wall electromagnetic sensor transport phenomena, a theoretical study of two-dimensional (2D) steady ternary hybrid nanofluid convective hydromagnetic flow from a Riga vertical plate has been presented. $Ti_6Al_4V-AA7075-H_2O$ hybrid nanofluid is considered. Variable plate thickness, thermal radiation, thermal buoyancy, heat source and viscous dissipation effects have been incorporated in the model. Rosseland's diffusion flux model has been deployed for radiative heat transfer. The dimensionless ordinary differential boundary value problem has been solved with the `bvp4c` function in MATLAB. Validation of the numerical solutions with earlier special cases from the literature has also been conducted. The main findings of the present study may be summarized as follows:

- Hybrid nanofluid velocity $f'(\eta)$ is elevated strongly with a greater modified Hartmann magnetic number, Q .

- Both velocity and temperature are enhanced with larger values of the velocity power-law index, n .
- Hybrid nanofluid temperature is decreased with stronger thermal buoyancy forces, i.e. higher thermal Grashof number, Gr .
- Temperature and thermal boundary layer thickness are both increased with radiation parameter, Rd .
- Temperature is elevated with greater heat source parameter λ and Eckert number, Ec .
- Skin friction factor C_{fx} declines with an increase in modified Hartmann number Q , Grashof number, Gr and power-law index n , whereas it is strongly boosted with increasing value of Riga plate electrode parameter, β and wall thickness parameter, α_1 .
- Wall heat transfer rate, i.e. local Nusselt number, Nu_x of the mono-nanofluid is lower than that of hybrid nanofluid since much greater temperatures are achieved in the latter confirming the heat transfer enhancement benefits of deploying multiple nanoparticles simultaneously.

The present work has identified some interesting characteristics of hybrid nanofluids in electromagnetic sensor boundary layer flows. However, attention has been restricted to Newtonian nanofluids and steady-state transport. Future work may address *rheological behaviour and unsteady effects* and will be communicated imminently.

References

1. Daniel YS, Aziz ZA, Ismail Z, Salah F (2018) Impact of thermal radiation on electrical MHD flow of nanofluid over nonlinear stretching sheet with variable thickness. *Alex Eng J* 57:2187–2197
2. Wakif A, Chamkha A, Animasaun IL et al (2020) Novel physical insights into the thermodynamic irreversibilities within dissipative EMHD fluid flows past over a moving horizontal Riga plate in the coexistence of wall suction and joule heating effects: a comprehensive numerical investigation. *Arab J Sci Eng* 45:9423–9438
3. Gailitis A (1961) On the possibility to reduce the hydrodynamic drag of a plate in an electrolyte. *Appl Magnohydrodyn Rep Inst Phys Riga* 13:143–146
4. Avilov VV (1998) Electric and magnetic fields for the Riga plate. Technical report, FRZ, Rossendorf
5. Pantokratoras A, Magyari E (2009) EMHD free-convection boundary-layer flow from a Riga-plate. *J Eng Math* 64(3):303–315
6. Magyari E, Pantokratoras A (2011) Aiding and opposing mixed convection flows over the Riga plate. *Comm Nonlinear Sci Numer Sim* 16:3158–3167
7. Pantokratoras A (2011) The Blasius and Sakiadis flow along a Riga-plate. *Prog Comput Fluid Dyn* 11(5):329–333
8. Farooq M, Anjum A, Hayat T et al (2016) Melting heat transfer in the flow over a variable thickness Riga plate with homogeneous-heterogeneous reactions. *J Mol Liq* 224:1341–1347
9. Shafiq A, Hammouch Z, Turab A (2018) Impact of radiation in a stagnation point flow of Walters' B fluid towards a Riga plate. *Therm Sci Eng Prog* 6:27–33

10. Anjum A, Farooq M, Javed M, Ahmad S, Malik MY, Alshomrani AS (2018) Physical aspects of heat generation/absorption in the second-grade fluid flow due to Riga plate: application of Cattaneo–Christov approach. *Results Phys* 9:955–960
11. Nasir NAAM, Ishak A, Pop I (2019) Stagnation point flow and heat transfer past a permeable stretching/shrinking Riga plate with velocity slip and radiation effects. *J Zhejiang Univ Sci A* 20:290–299
12. Shamshuddin MD, Satya Narayana PV (2020) Combined effect of viscous dissipation and Joule heating on MHD flow past a Riga plate with Cattaneo–Christov heat flux. *Indian J Phys* 94:1385–1394
13. Mishra SR, Shamshuddin MD, Bég OA, Kadir A (2019) Viscous dissipation and Joule heating effects in non-fourier MHD squeezing flow, heat and mass transfer between Riga plates with thermal radiation: variational parameter method solutions. *Arab J Sci Eng* 44:8053–8066
14. Shamshuddin MD, Mabood F, Rajput GR, Bég OA, Barduudin IA (2022) Thermo-solutal dual stratified convective magnetized fluid flow from an exponentially stretching Riga plate sensor surface with thermophoresis. *Int Comm Heat Mass Transfer* 134:105997 (10 pages). <https://doi.org/10.1016/j.icheatmasstransfer.2022.105997>
15. Francis LA, Poletkin K (eds) (2022) *Magnetic sensors and devices-technologies and applications*. CRC Press, Florida
16. Choi SUS (1995) Enhancing thermal conductivity of fluids with nanoparticle. *Proc ASME Int Mech Eng Congr Expo* 66:99–105
17. Eastman JA, Choi SUS, Li S, Thompson LJ, Lee S (1996) Enhanced thermal conductivity through the development of nanofluids. *MRS Online Proc Libr Arch* 457
18. Buongiorno J (2006) Convective transport in nanofluids. *ASME J Heat Transf* 128:240–250
19. Ahmad A, Asghar S, Afzal S (2016) Flow of nanofluid past a Riga plate. *J Magn Magn Mater* 402:44–48
20. Hayat T, Abbas T, Ayub M, Farooq M, Alsaedi A (2016) Flow of nanofluid due to convectively heated Riga plate with variable thickness. *J Mol Liq* 222:854–862
21. Abbas T, Ayub M, Bhatti M, Rashidi M, Ali M (2016) Entropy generation on nanofluid flow through a horizontal Riga plate. *Entropy* 18(6):223
22. Bhatti MM, Abbas T, Rashidi MM (2016) Effects of thermal radiation and electromagnetohydrodynamics on viscous nanofluid through a Riga plate. *Multidiscip Model Mater Struct* 12(4):605–618
23. Ayub M, Abbas T, Bhatti MM (2016) Inspiration of slip effects on Electromagnetohydrodynamics (EMHD) nanofluid flow through a horizontal Riga plate. *Eur Phys J Plus* 131:193
24. Ahmad R, Mustafa M, Turkyilmazoglu M (2017) Buoyancy effects on nanofluid flow past a convectively heated vertical Riga-plate: a numerical study. *Int J Heat Mass Trans* 111:827–835
25. Iqbal Z, Mehmood Z, Azhar E et al (2017) Numerical investigation of nanofluidic transport of gyrotactic microorganisms submerged in water towards Riga plate. *J Mol Liq* 234:296–308
26. Ramzan M, Bilal M, Chung JD (2017) Radiative Williamson nanofluid flow over a convectively heated Riga plate with chemical reaction—a numerical approach. *Chin J Phys* 55(4):1663–1673
27. Rasool G, Zhang T (2019) Characteristics of chemical reaction and convective boundary conditions in Powell-Eyring nanofluid flow along a radiative Riga plate. *Heliyon* 5:e01479
28. Rasool G, Zhang T, Shafiq A (2019) Second grade nanofluidic flow past a convectively heated vertical Riga plate. *Phys Scr* 94(12):125212
29. Abbas T, Hayat T, Ayub M et al (2019) Electromagnetohydrodynamic nanofluid flow past a porous Riga plate containing gyrotactic microorganism. *Neural Comput Appl* 31:1905–1913
30. Rooman M, Jan MA, Shah Z et al (2021) Entropy optimization and heat transfer analysis in MHD Williamson nanofluid flow over a vertical Riga plate with nonlinear thermal radiation. *Sci Rep* 11:18386
31. Rasool G, Wakif A (2021) Numerical spectral examination of EMHD mixed convective flow of second grade nanofluid towards a vertical Riga plate using an advanced version of the revised Buongiorno’s nanofluid model. *J Therm Anal Calorim* 143:2379–2393

32. Shafiq A, Mebarek-Oudina F, Sindhu TN et al (2021) A study of dual stratification on stagnation point Walters' B nanofluid flow via radiative Riga plate: a statistical approach. *Eur Phys J Plus* 136:407
33. Bhatti MM, Michaelides EE (2021) Study of Arrhenius activation energy on the thermo-bioconvection nanofluid flow over a Riga plate. *J Therm Anal Calorim* 143:2029–2038
34. Kayikci S, Eswaramoorthi S, Postalcioglu S et al (2023) Thermal analysis of radiative water-and glycerin-based carbon nanotubes past a Riga plate with stratification and non-Fourier heat flux theory. *J Therm Anal Calorim* 148:533–549
35. Shamsuddin M, Shahzad F, Jamshed W, Bég OA, Eid MR, Bég TA (2023) Thermo-solutal stratification and chemical reaction effects on radiative magnetized nanofluid flow from an exponentially stretching sensor plate: computational analysis. *J Magn Magn Mater* 565:170286 (11 pages). <https://doi.org/10.1016/j.jmmm.2022.170286>
36. Sarkar J, Ghosh P, Adil A (2015) A review on hybrid nanofluids: recent research, development and applications. *Renew Sustain Energy Rev* 43:164–177
37. Zaib A, Haq RU, Chamkha AJ, Rashidi MM (2018) Impact of partial slip on mixed convective flow towards a Riga plate comprising micropolar TiO₂-kerosene/water nanoparticles. *Int J Numer Methods Heat Fluid Flow* 29:1647–1662
38. Abbas N, Nadeem S, Malik MY (2020) Theoretical study of micropolar hybrid nanofluid over Riga channel with slip conditions. *Phys A Stat Mech Appl* 551:124083
39. Khashi'ie NS, Md Arifin N, Pop I (2020) Mixed convective stagnation point flow towards a vertical Riga plate in hybrid Cu-Al₂O₃/water nanofluid. *Mathematics* 8(6):912
40. Nadeem S, Ahmad S, Khan MN (2021) Mixed convection flow of hybrid nanoparticle along a Riga surface with Thomson and Troian slip condition. *J Therm Anal Calorim* 143:2099–2109
41. Asogwa KK, Mebarek-Oudina F, Animasaun IL (2022) Comparative investigation of water-based Al₂O₃ nanoparticles through water-based CuO nanoparticles over an exponentially accelerated radiative Riga plate surface via heat transport. *Arab J Sci Eng* 47:8721–8738
42. Wilson J (2008) *Sensor technology handbook*, 1st edn. Elsevier USA
43. Bég OA (2012) Numerical methods for multi-physical magnetohydrodynamics. In: Ibragimov MJ, Anisimov MA (eds) *New developments in hydrodynamics research*, chapter 1, pp 1–112. Nova Science, New York
44. Keskin AÜ (2019) *Boundary value problems for engineers: with MATLAB solutions*. Springer, USA
45. Mabood F, Khan WA, Ismail AIM (2015) MHD boundary layer flow and heat transfer of nanofluids over a nonlinear stretching sheet: a numerical study. *J Magn Magn Mater* 374:569–576
46. Wang CY (1989) Free convection on a vertical stretching surface. *Z Angew Math Mech* 69:418–420
47. Salahuddin T, Malik MY, Hussain A, Bilal S, Awais M (2016) MHD flow of Cattaneo–Christov heat flux model for Williamson fluid over a stretching sheet with variable thickness: using numerical approach. *J Magn Magn Mater* 401:991–997
48. Hayat T, Tehseen A, Ayub M, Farooq M, Alsaedi A (2016) Flow of nanofluid due to convectively heated Riga plate with variable thickness. *J Mol Liq* 222:854–862
49. Hughes WF, Young FJ (1966) *The Electro-magneto-dynamics of fluids*. Wiley, New York

Chapter 13

Heat Transfer in EMHD Hyperbolic Tangent Ternary Hybrid Nanofluid Flow Over a Darcy-Forchheimer Porous Wedge Surface: A Numerical Simulation



V. Bharathi, J. Prakash, Dharmendra Tripathi, O. Anwar Bég, Ashish Sharma, and Ravi Kr. Sharma

Abstract Engineers are finding more and more uses for sophisticated electrostatic nano-coatings. This new information prompted us to look into the theoretical and computational aspects of an unsteady EMHD incompressible two-dimensional heat-transfer tangent hyperbolic ternary hybrid nanofluid boundary layer coating flow outside of a two-dimensional porous wedge surface with the implication of Forchheimer-Darcy medium. The effects of electrical and magnetic fields, as well as the effects of surface/injection, suction, and zeta potential, are taken into account. The boundary conditions for convective heat transfer are analyzed. The watery base fluid (H_2O) is combined with three metallic nanoparticles (Fe, Cu and Ag) to form the ternary compound nanofluid. Using suitable similarity variables, the controlling conservation partial differential equations for continuity and momentum and

V. Bharathi

Department of Mathematics, Rajalakshmi Engineering College (Autonomous), Chennai 602105, Tamil Nadu, India

e-mail: bharathiv42@gmail.com

J. Prakash

Department of Mathematics, Avvaiyar Government College for Women, Karaikal, U.T of Puducherry 609602, India

e-mail: prakashjayavel@yahoo.co.in

D. Tripathi (✉)

Department of Mathematics, National Institute of Technology, Srinagar, Uttarakhand 246174, India

e-mail: dtripathi@nituk.ac.in

O. A. Bég

Multi-Physical Engineering Sciences Group, Department of Mechanical and Aeronautical Engineering, Salford University, Manchester M54WT, UK

e-mail: O.A.Beg@salford.ac.uk

A. Sharma · R. Kr. Sharma

Department of Mechanical Engineering, Manipal University, Jaipur, India

© The Author(s), under exclusive license to Springer Nature Singapore Pte Ltd. 2023

D. Tripathi et al. (eds.), *Nanomaterials and Nanoliquids: Applications in Energy and Environment*, Advances in Sustainability Science and Technology,

https://doi.org/10.1007/978-981-99-6924-1_13

their related boundary conditions at the wedge surface and unconstrained stream are changed. MATLAB is used to computationally answer the arising ordinary differential nonlinear boundary value problem. Previous research is used to verify the results. With the aid of visual aids, the effects of the controlling factors on fluid movement and heat transmission properties are explored and debated. Both the positive and negative values of the electric field are considered in the discussion of the findings. For high values of the rheological parameter and Forchheimer number in both positive and negative electric fields, the velocity dispersion drops. The skin friction coefficient was enhanced for the increasing values of the zeta potential parameter and suction/injection parameter. The temperature distribution increases for the large value of the heat source/sink parameter and Brinkman number in both the positive and negative values of the electric field. The Nusselt number decays due to an increment in the permeability parameter.

Keywords Wedge flow · Heat transfer · Magnetic field · Electroosmotic flow · Forchheimer-Darcy medium · Ternary hybrid nanofluids

1 Introduction

Fluid movement is a key concept in many areas of science and engineering, such as aerodynamics, hydrodynamics, chemical engineering, and biological engineering, but not limited to these. Predicting and manipulating the behavior of fluids in different contexts requires an appreciation for the mathematics of fluid movement. Fluid flow analysis depends on wedge geometry, which is when two surfaces meet at an angle to make a sharp edge. Aircraft wing and turbine blade design are just a few examples of where knowledge of the shape of fluid movement around a wedge has been put to use [1–4]. Non-Newtonian fluids have attracted a lot of interest because of their unusual characteristics and wide range of possible uses in sectors as diverse as the health, military, and energy industries. Optimizing the use of such fluids requires a thorough comprehension of their movement behavior. The flow behavior of non-Newtonian fluids has been studied using a variety of shapes, including wedge geometry. In 1940, Rosenhead [5] came up with a mathematical solution for the radial flow of a viscous fluid in two dimensions inside a convergent or divergent wedge that was based on an elliptic function. When a non-Newtonian fluid with no elasticity was put inside a cylinder, the perceived viscosity was linked to the third rate of invariant deformation [6]. At the same time, Tadmor [7] used the power law model to find a mathematical solution for the velocity distribution inside a cylinder's annulus at different Reynolds numbers. Moffatt et al. [8] used a mathematical method to determine that, for unmixed fluid flow between convergent barriers of varying viscosity in two dimensions, the velocity gap quickly grew with a rise in the Reynolds number. Converging incompressible, slow viscous fluid flow through cones and wedges has also been studied by Hull and Pearson [1], Durban [9], Brewster et al. [10], and Bird et al. [11], who all used mathematical techniques to derive approximative answers.

Falkner and Skan got the flow over a moving wedge in [12], which is where the Falkner-Skan equation comes from. This is the point at which the equation began to take shape. Studies on the Falkner-Skan flow have been generated by a multitude of researchers over the course of a significant number of years as a direct consequence of the influence of a number of different thermophysical variables [13]. Later, Watanabe [14] investigated the flow behavior of fluids as they passed over a wedge while being subjected to injection and pressure. Ishak et al. [15] conducted an investigation into the MHD flow that occurred before the wedge began to move. Ali et al. [16] found an analytical solution to the Falkner-Skan problem by using a computational technique called the finite element method. Research works on tangent hyperbolic fluid under wedge geometry have been studied in [17–20].

Electromagneto hydrodynamics (EMHD) is a branch of physics that combines the ideas of electromagnetism, fluid mechanics, and plasma physics to explain what happens to fluids that are electrically sensitive when they are near electromagnetic fields. In EMHD, researchers examine both the effects of electromagnetic forces on the fluid and the effects of the fluid on the electromagnetic field. This area of research has many real-world applications, such as fusion energy, aeronautical engineering, environmental science, and biological engineering. Electroosmosis, magnetohydrodynamic (MHD) waves, MHD turbulence, and oscillations are some of the processes found in EMHD. MHD power generators, plasma rockets, and magnetic confinement fusion devices are just a few examples of the many devices and systems that require knowledge of these processes for their construction and improvement [21–24]. Tso and Sundaravadivelu [25] investigate the effect of electromagnetic fields on the surface pressure between parallel plate microchannels. Chakraborty and Paul [26] investigate the effect of EMHD power on a liquid flow in a microchannel with parallel plates. The influence of a second-law study of flow in a cylindrical conduit considering the impacts of a magnetic field was addressed by Nagaraju et al. [27]. Bhatti et al. [28] investigated EMHD flow with heat transfer in third-grade fluid involving minute particulates as part of their research. They found that increasing the number of electric components resulted in a greater increase in the fluid's movement. The boundary-layer EMHD flow of an electrically conducting tangent hyperbolic nanofluid past a Riga surface of varying thickness was studied by Mahdy and Hoshoudy [29]. The velocity field and the skin friction coefficient were found to be maximized at the Hartmann number. Asogwa et al. [18] investigated the Dufour effect and activation energy of a nanofluid with a hyperbolic tangent across a radiative Riga stretching surface. Prakash et al. [30] address a theoretical investigation into the incompressible bioconvection flow of a non-Newtonian nanofluid from a bi-directional extending surface subjected to magnetic and electrical fields that are mutually orthogonal to one another. The following research articles [31–35] describe some fascinating findings.

The temperature characteristics of nanofluids, which are liquid concentrations of nanoparticles in a base fluid, are improved in comparison to those of the base fluid itself. By combining three different kinds of nanoparticles, we get a ternary composite nanofluid with enhanced efficiency. *Ternary hybrid nanofluids (TNF)* have lately garnered a lot of interest in the scientific community because of their improved temperature characteristics and the wide range of engineering disciplines in which they could be used. The influence of the magnetic field on the movement of THNF in the vicinity of a stretching sheet was investigated by Manjunatha et al. [36]. The temperature characteristics of $\text{Al}_2\text{O}_3\text{-SiO}_2\text{-TiO}_2$ modified NF transportation were studied by Dadheech et al. [37]. The laminar flow of THNF was established by Sundar et al. [38]. The mixed convection radiation stream of THNF was given a partial slide thanks to the work of Cao et al. [39]. Animasaun et al. [40] investigated the effects that magnetic flux intensity had on the dynamical behavior of THNF. Sahu et al. [41] utilized a number of different water-based trihybrid nanofluids ($\text{Al}_2\text{O}_3 + \text{Cu} + \text{CNT}/\text{water}$) in their investigation of the impermanent and constant characteristics of the natural circulation loop. Utilizing trihybrid nanoparticles results in increased productivity while simultaneously reducing the rate of entropy generation.

The researchers were encouraged to develop the existing nanofluid concept in order to enhance the heat transfer capability as a result of the high demand for a cooling agent with improved heat transfer capability in the industries. As a direct consequence of this, the hybrid nanofluid was found, and it was found to have improved heat transmission characteristics. As a result of this impetus, additional experimental research into tri-hybrid nanofluids is currently being carried out in the hope of achieving a higher rate of heat transmission. Nanoparticles of three distinct classes are suspended in a tri-hybrid nanofluid. These nanoparticles have distinct chemical and physical interactions. The aforementioned body of literature served as the impetus for the current research, which investigates the patterns of an EMHD hyperbolic tangent ternary nanofluid as it travels across a wedge flow porous surface using the Forchheimer-Darcy medium, suction or injection, and zeta-potential. Nano-molecules of Fe, Cu, and Ag, combined with nano-molecules of basic H_2O , constitute the ternary hybrid nanofluids that are the subject of this research. The purpose of this study is to investigate the application of ternary hybrid nanofluids as a mechanism for the enhancement of heat transmission in wedge flow permeable surfaces. First, a significant amount of quantitative transformation is performed, and then calculations are carried out using the bvp4c technique in MATLAB. Graphical representations and discussions of the significance of developed variables in terms of velocity, surface friction coefficient, heat transmission, and the Nusselt number are presented. The discoveries could have implications for low-density heat exchangers and other systems that transmit temperatures.

2 Mathematical Formulation

2.1 Definition of the Problem

A tangent hyperbolic ternary hybrid nanofluid embedded in a Darcy-Forchheimer porous medium moves through the surface of a permeable wedge in a two-dimensional laminar flow. As can be seen in Fig. 1, a cartesian coordinate system (\bar{x}, \bar{y}) is chosen with the center set at the wedge's tip, the \bar{x} -axis directed along the wedge's surface, and the \bar{y} -axis perpendicular to the wedge's surface. This is done so that a triangle with the base at the tip can be used to symbolize the wedge.

The present study notes that the flow is induced by the elongation of the wedge at a wall velocity denoted as $U_w = \frac{b\bar{x}^m}{1-c\bar{t}}$, and the external flow of the fluid at a stream velocity denoted as $U_e = \frac{a\bar{x}^m}{1-c\bar{t}}$. These velocities are influenced by a magnetic field $B = (0, B_0)$ that acts perpendicularly to the surface of the wedge. The variable denoted by \bar{t} is representative of time, while the parameters $a, b, m,$ and c are constant. It should be noted that $b > 0$ and $b < 0$, respectively, indicate the rate of expansion and contraction of the wedge. The Falkner-Skan power-law (FSP) constraint (m) mandates that the wedge angle aligns with a specific parameter. This constraint necessitates the utilization of an arbitrary fixed number, denoted as m , and the gradient of the Hartree pressure factor is represented $\beta = \frac{2m}{1+m}$. This value corresponds to $\beta = \frac{\Omega}{\pi}$ for the entirety of the wedge angle. Assume the temperature surface T_w of the wedge vary in power law forms as $T_w = T_\infty + \frac{T_0 U_w \bar{x}}{v_f(1-c\bar{t})}$ in which T_∞ is the ambient constant value of temperature.

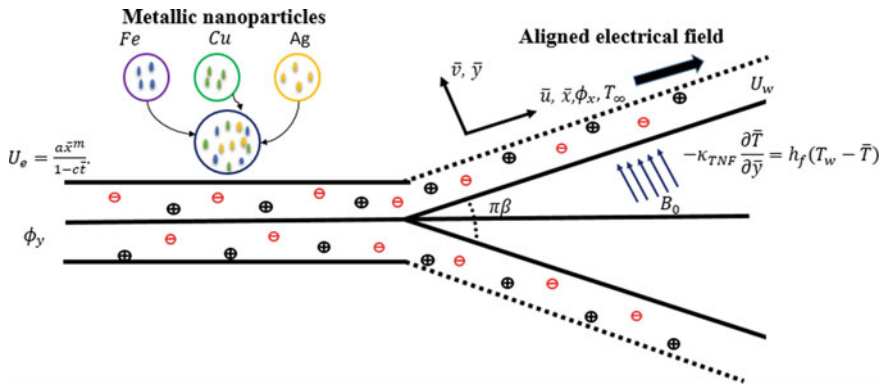


Fig. 1 Geometry of the problem

2.2 Governing Equations of the Problem

The governing equations for an incompressible, hyperbolic tangent nanofluid under the effect of electric and magnetic fields are given by

$$\frac{\partial \bar{u}}{\partial \bar{x}} + \frac{\partial \bar{v}}{\partial \bar{y}} = 0, \tag{1}$$

$$\begin{aligned} \frac{\partial \bar{u}}{\partial \bar{t}} + \bar{u} \frac{\partial \bar{u}}{\partial \bar{x}} + \bar{v} \frac{\partial \bar{u}}{\partial \bar{y}} = & -\frac{1}{\rho_{TNF}} \frac{\partial \bar{P}}{\partial \bar{x}} + v_{TNF} \left[(1-n) + \sqrt{2}n\Gamma \frac{\partial \bar{u}}{\partial \bar{y}} \right] \frac{\partial^2 \bar{u}}{\partial \bar{y}^2} \\ & - \left(\frac{\sigma B_0^2}{\rho_{TNF}} + \frac{v_{TNF}}{K} \right) \bar{u} - F \bar{u}^2 + \frac{\rho_e \phi_x}{\rho_{TNF}} \end{aligned} \tag{2}$$

$$\begin{aligned} \frac{\partial \bar{T}}{\partial \bar{t}} + \bar{u} \frac{\partial \bar{T}}{\partial \bar{x}} + \bar{v} \frac{\partial \bar{T}}{\partial \bar{y}} = & \alpha_{TNF} \frac{\partial^2 \bar{T}}{\partial \bar{y}^2} + \frac{v_{TNF}}{c_{pTNF}} \left[(1-n) \left(\frac{\partial \bar{u}}{\partial \bar{y}} \right)^2 + \frac{n\Gamma}{\sqrt{2}} \left(\frac{\partial \bar{u}}{\partial \bar{y}} \right)^3 \right] \\ & + \frac{\sigma B_0^2}{(\rho c_p)_{THF}} (u - U_e)^2 + \frac{F(\bar{u} - U_e)^3}{c_{pTNF}} + \frac{Q_0(\bar{T} - T_\infty)}{(\rho c_p)_{THF}}. \end{aligned} \tag{3}$$

in which \bar{u}, \bar{v} are velocity components, $\bar{P}, v_{TNF}, \rho_{TNF}, \mu_{TNF}, \Gamma, n, \sigma, \phi_x,$ and ρ_e are the pressure, TNF (ternary hybrid nanofluid) of kinematic viscosity, TNF density, coefficient of TNF viscosity, constant time, power law index, electric conductivity, applied electric field strength, and electrical net charge thickness of TNF. F is the nonuniform inertia coefficient (Forchheier resistance factor), which is fixed as $F = \frac{C_b}{\sqrt{K}}$, in which K and C_b are the permeability of the medium and drag force, Temperature $\bar{T}, \alpha_{TNF} = \frac{\kappa_{TNF}}{(\rho c_p)_{TNF}}$ is the TNF of thermal diffusivity in which κ_{TNF} is the thermal conductivity of TNF, $(\rho c_p)_{THNF}$ is the specific heat capacity of TNF, Q_0 acted as the heat absorption ($Q_0 < 0$) and heat generation ($Q_0 > 0$). Pressure can be calculated from the inviscid flow outside the boundary layer because it is independent in the direction perpendicular to the boundary layer.

The velocity of fluid $U_e(x, t) = \frac{ax^m}{1-cl}$ at the wedge farther along in space the boundary layer which is assumed in Eq. (2). When $\bar{u} = U_e, \bar{v} = 0,$ and $\phi_x = \phi_y$ are taken into account outside of the boundary layer, the x -momentum equation may be written as

$$-\frac{1}{\rho_{TNF}} \frac{\partial \bar{P}}{\partial \bar{x}} = \frac{\partial U_e}{\partial \bar{t}} + U_e \frac{\partial U_e}{\partial \bar{x}} + \left(\frac{\sigma B_0^2}{\rho_{TNF}} + \frac{v_{TNF}}{K} \right) U_e + F U_e^2 - \frac{\rho_e \phi_y}{\rho_{TNF}}. \tag{4}$$

Flip Eq. (4) in Eq. (2) can be rewritten the governing equations for an incompressible, hyperbolic tangent nanofluid is

$$\frac{\partial \bar{u}}{\partial \bar{t}} + \bar{u} \frac{\partial \bar{u}}{\partial \bar{x}} + \bar{v} \frac{\partial \bar{u}}{\partial \bar{y}} = \frac{\partial U_e}{\partial \bar{t}} + U_e \frac{\partial U_e}{\partial \bar{x}} + \nu_{TNF} \left[(1 - n) + \sqrt{2}n\Gamma \frac{\partial \bar{u}}{\partial \bar{y}} \right] \frac{\partial^2 \bar{u}}{\partial \bar{y}^2} - \left(\frac{\sigma B_0^2}{\rho_{TNF}} + \frac{\nu_{TNF}}{K} \right) (\bar{u} - U_e) - F(\bar{u}^2 - U_e^2) + \frac{\rho_e(\phi_x - \phi_y)}{\rho_{TNF}} \tag{5}$$

The metallic nanoparticles characteristic of ρ_1, ρ_2, ρ_3 are the densities, ϕ_1, ϕ_2, ϕ_3 are the volume fractions, the thermal conductivity of $\kappa_{nf,1}, \kappa_{nf,2}, \kappa_{nf,3}$ are defined as Fe nanoparticle, Cu nanoparticle, Ag nanoparticle respectively, ρ_f is the density of the base fluid (Table 1). The dynamic viscosity of the base fluid is μ_f and B, C are viscosity enhancement coefficients. The base fluid of specific heat denoted as κ_f and i th type of shape nanoparticles is defined as \bar{m}_i . These notation included in Tables 2 and 3 pertains to the thermophysical constants of the nanoparticles as well as the base fluid, respectively.

Table 1 Thermophysical characteristics of metallic nanoparticles [42–45]

Thermophysical properties	Ternary hybrid nanofluid (TNF)
Density	$\rho_{TNF} = \phi_1\rho_1 + \phi_2\rho_2 + \phi_3\rho_3 + (1 - \phi_1 - \phi_2 - \phi_3)\rho_f$
Dynamic viscosity	$\mu_{TNF} = \mu_f(\phi_1(1 + B_1\phi + C_1\phi^2) + \phi_2(1 + B_2\phi + C_2\phi^2) + \phi_3(1 + B_3\phi + C_3\phi^2))$
Specific heat capacity	$(\rho c_p)_{TNF} = \rho_1c_{p,1}\phi_1 + \rho_2c_{p,2}\phi_2 + \rho_3c_{p,3}\phi_3 + (1 - \phi_1 - \phi_2 - \phi_3)(\rho c_p)_f$
Thermal conductivity	$\kappa_{TNF} = (\kappa_{nf,1}\phi_1 + \kappa_{nf,2}\phi_2 + \kappa_{nf,3}\phi_3)/\phi,$ $\frac{\kappa_{nf,i}}{\kappa_f} = \frac{\kappa_{p,i} + (\bar{m}_i - 1)\kappa_f + (\bar{m}_i - 1)\phi(\kappa_{p,i} - \kappa_f)}{\kappa_{p,i} + (\bar{m}_i - 1)\kappa_f - \phi(\kappa_{p,i} - \kappa_f)}$

Table 2 Parameters for defining the shape and properties of nanoparticles

Shape of nanoparticles	\bar{m}	B	C
Platelets	5.7	37.1	612.6
Cylindrical	4.9	13.5	704.4
Spherical	3	2.5	6.2

Table 3 Thermophysical properties of metallic nanoparticles [42–45]

Oxides	H ₂ O	Fe	Cu	Ag
Density (Kg m ⁻³)	997.1	7900	8960	10,500
Specific heat (J/Kg K)	4182	447	386	400
Thermal conductivity (W/mK)	0.602	80.4	400	429

2.3 Electrical Potential

Modeling of electrical potential transmission in the electrical double layer is done using the Boltzmann-Poisson equation (EDL).

$$\operatorname{div} \mathbf{D} = \rho_e. \quad (6)$$

Here, $\mathbf{D}(= \epsilon_{ef} \overline{\Phi})$, The rate of volumetric change, denoted by $\overline{\rho}_e$ and ϵ_{ef} is the permittivity of the dielectric. Then:

$$\operatorname{div}(-\epsilon_{ef} \operatorname{grad} \overline{\Phi}) = \rho_e. \quad (7)$$

At every point on the permeable wedge surface, the permittivity is the same everywhere.

$$\nabla^2 \overline{\Phi} = -\frac{\rho_e}{\epsilon_{ef}}, \quad (8)$$

and

$$\rho_e = \overline{z}_1 (n^+ - n^-), \quad (9)$$

in which the numbers n^+ and n^- represent the anticipated cation and anion densities at a concentration of n_0 , respectively.

Assuming no EDL overlap, the Boltzmann distribution may be written as:

$$n^\pm = n_0 \exp\left(\pm \frac{\overline{z}_1 \overline{\Phi}}{K_B T_w}\right). \quad (10)$$

Here the charge of electronic and charge balance are represented by \overline{z}_1 and \overline{z}_1 , Boltzmann constant denoted by K_B and T_w is the average electrolytic solution temperature.

To apply Eq. (10), just replace the values of the ion counts in Eq. (9).

$$\rho_e = -2\overline{z}_1 \overline{z}_1 n_0 \sinh\left(\frac{\overline{z}_1 \overline{\Phi}}{K_B T_w}\right) \quad (11)$$

The Boltzmann-Poisson equation (Eq. 8) is modified by inserting the second-order differential equation for charge density (Eq. 11) to get the electrical potential distribution.

$$\frac{\partial^2 \overline{\Phi}}{\partial x^2} + \frac{\partial^2 \overline{\Phi}}{\partial y^2} = -2\overline{z}_1 \overline{z}_1 n_0 \sinh\left(\frac{\overline{z}_1 \overline{\Phi}}{K_B T_w}\right). \quad (12)$$

2.4 Dimensional Boundary Conditions

The relevant boundary conditions are defined as follows:

$$\bar{u} = U_w(\bar{x}) = -\gamma U_e(\bar{x}), \bar{v} = V_w, -\kappa_{TNF} \frac{\partial \bar{T}}{\partial \bar{y}} = h_f(T_w - \bar{T}), \bar{\phi} = \bar{\xi} \quad \text{at } \bar{y} = 0, \quad (13)$$

$$\bar{u} = U_e(\bar{x}), \bar{T} \rightarrow T_\infty, \bar{\phi} \rightarrow 0 \quad \text{as } \bar{y} \rightarrow \infty. \quad (14)$$

Here $\gamma = -(\frac{b}{a})$ is referred as a moving constant parameter, $\gamma > 0$ denoted as contracting wedge and $\gamma < 0$ indicates that stretching wedge and if $\gamma = 0$ denoted as situated wedge, κ_f and h_f are the thermal conductivity and heat convective coefficient of nanofluid.

2.5 Scaling Analysis

Taking into consideration the stream function $\psi(x, y)$ in such a way that $\bar{u} = \frac{\partial \psi}{\partial \bar{y}}$; $\bar{v} = -\frac{\partial \psi}{\partial \bar{x}}$ and then using the similarity transformation in the manner shown below:

$$U_e = \frac{a\bar{x}^m}{1 - c\bar{t}}, U_w = \frac{b\bar{x}^m}{1 - c\bar{t}}, V_w = \frac{v_0}{\sqrt{1 - c\bar{t}}}, \psi = \frac{\sqrt{2v_f\bar{x}U_e}}{\sqrt{1 + m}} f, \quad (15)$$

$$\eta = y \frac{\sqrt{(1 + m)U_e}}{\sqrt{2v_f\bar{x}}}, \theta = \frac{\bar{T} - T_\infty}{T_w - T_\infty}, \phi = \frac{\bar{z}_1 \bar{e} \bar{\Phi}}{K_B T_w}$$

By substituting the aforementioned transformations, Eqs. (1, 3, and 5) is made to be fulfilled in the same manner, and Eqs. (12, 13, and 14) are transformed to

$$\begin{aligned} & \left(\frac{\mu_{TNF}}{\mu_f} \right) f''' \left((1 + n) + nWe\sqrt{1 + m} f'' \right) + \frac{A}{1 + m} (2 - f''\eta - 2f') \\ & + \beta(1 - f'^2) + ff'' - \frac{(M^2 + \left(\frac{\mu_{TNF}}{\mu_f} \right) Da) (f' - 1)}{\left(\frac{\rho_{TNF}}{\rho_f} \right) (1 + m)} + \frac{Fr}{1 + m} (f'^2 - 1) \quad (16) \\ & + \frac{U_E}{\left(\frac{\rho_{TNF}}{\rho_f} \right)} \phi'' = 0. \end{aligned}$$

$$\begin{aligned}
 & \left(\frac{\kappa_{TNF}}{\kappa_f} \right) \theta'' - \left(\frac{(\rho c_p)_{TNF}}{(\rho c_p)_f} \right) \frac{APr}{(1+m)} (4\theta + \eta\theta') - 2 \left(\frac{(\rho c_p)_{TNF}}{(\rho c_p)_f} \right) Pr\theta f' \\
 & + Pr \left(\frac{(\rho c_p)_{TNF}}{(\rho c_p)_f} \right) \theta' f + \left(\frac{\rho_{TNF}}{\rho_f} \right) \frac{Fr\delta Br}{2(1+m)} (f' - 1)^3 \\
 & + \frac{Q\theta Pr}{(1+m)} + \frac{M^2\delta Br}{(1+m)} (f' - 1)^2 \\
 & + \left(\frac{\mu_{TNF}}{\mu_f} \right) \frac{(1+m)Br}{2} \delta f''^2 \left((1-n) + \frac{n}{2} f'' \sqrt{1+m} We \right) = 0.
 \end{aligned} \tag{17}$$

$$(1+m)\phi'' = \kappa^2 \sinh(\phi). \tag{18}$$

with respective boundary condition as

$$f' = -\gamma, f = \frac{S}{\sqrt{1+m}}, \left(\frac{\kappa_{TNF}}{\kappa_f} \right) \theta' = \frac{Bi(\theta - 1)}{\sqrt{1+m}}, \phi = \xi \quad \text{at } \eta = 0, \tag{19}$$

$$f' = 1, \theta \rightarrow 0, \phi \rightarrow 0 \quad \text{as } \eta \rightarrow \infty, \tag{20}$$

where $M^2 = \frac{2\sigma B_0^2 \bar{x}}{U_e \rho_f}$, $A = \frac{c}{a\bar{x}^{m-1}}$, $Da = \frac{2\bar{x}v_f}{KU_e}$, $Fr = 2\bar{x}F$, $We = \frac{\Gamma U_e^{\frac{3}{2}}}{\sqrt{\nu_f \bar{x}}}$, $Pr = \frac{\nu_f}{\alpha_f}$, $Ec = \frac{U_e^2}{(c_p)_f T_0}$, $Br = EcPr$, $Q = \frac{2\bar{x}Q_0}{(\rho c_p)_f U_w}$, $Bi = \frac{h_f}{\kappa_f} \sqrt{\frac{2\nu_f \bar{x}}{U_e}}$, $S = -\frac{v_0 \sqrt{2\bar{x}}}{\sqrt{\nu_f u_e (1-c\bar{t})}}$, $\xi = \frac{\tilde{z}e\tilde{\xi}}{K_B T_v}$ and $\delta = \frac{2v_f(1-c\bar{t})}{U_w \bar{x}}$ are the magnetic parameter, unsteadiness parameter, permeability (porous) parameter, Forchheimer number, Weissenberg number, Prandtl number, Eckert number, Brinkman number, heat source/sink parameter (generation and absorption parameter) Biot number, parameter of suction ($S < 0$) and injection ($S > 0$), potential of zeta parameter and dimensionless constant. Also, $U_E = \frac{U_{HS}}{U_e}$ is the electric field parameter in which $U_{HS} = -\frac{K_B T_v \epsilon_{ef} (\phi_x - \phi_y)}{\mu_f \tilde{z} e}$ is the Helmholtz-Smoluchowski velocity and $\kappa = \frac{m_1^2 v_f \bar{x}}{U_e}$ is electroosmosis parameter in which $m_1^2 = \frac{4\tilde{z}^2 e^2 n_0}{\epsilon_{ef} K_B T_v}$ is Debye-Hückel parameter.

3 Interested Physical Quantities

3.1 Skin Friction Coefficient

The skin friction coefficient (wall friction) is the physical magnitude of engineering importance in this study, and it is designated as the surface shear stress as

$$C_f = \frac{\tau_w}{\rho_f U_e^2}, \quad (21)$$

$$\text{where } \tau_w = \mu_{TNF} \left[(1-n) \frac{\partial u}{\partial y} + \frac{n\Gamma}{\sqrt{2}} \left(\frac{\partial u}{\partial y} \right)^2 \right]_{y=0}.$$

By substituting and using the similarity transformation, we obtain the following relations

$$\sqrt{Re} C_f = \left(\frac{\mu_{TNF}}{\mu_f} \right) \left[\sqrt{1+m}(1-n) + \frac{(1+m)}{2} n We f''(0) \right] f''(0), \quad (22)$$

where $Re = \frac{U_e x}{\nu_f}$ is a Reynolds number.

3.2 Nusselt Number (Rate of Heat Transfer Coefficient)

The local Nusselt number can be defined as

$$Nu = \frac{x q_w}{\kappa_f (T_w - T_\infty)}, \quad (23)$$

$$\text{where } q_w = - \left[\kappa_{TNF} \frac{\partial T}{\partial y} \right]_{y=0}.$$

By substitution and using the similarity transformation, we have

$$\frac{Nu}{\sqrt{Re}} = -\sqrt{1+m} \left(\frac{\kappa_{TNF}}{\kappa_f} \right) \theta'(0). \quad (24)$$

The utilized constants are defined as follows.

4 Numerical Approach

Because of their nonlinear nature, ODEs are notoriously difficult to categorize sensibly. For this, we use the `bvp4c` shooting method in MATLAB to build sets of ordinary differential Eqs. (16–18) with boundary constraints (19, 20). The `Bvp4c` formula is basically a Lobatto-IIIa collocation technique for numerical analysis, and it is used to execute a numerical analysis. When the proper variables are used, the higher-order differential method may be discretized into a first-order ODE like:

$$\begin{aligned} f &= y(1); f' = y(2); f'' = y(3); f''' = y'(3); \theta = y(4); \theta' = y(5); \\ \theta'' &= y'(5); \phi = y(6); \phi' = y(7); \phi'' = y'(7), \end{aligned} \quad (25)$$

where

$$\begin{aligned}
 y'(3) &= \frac{\left(-\frac{A}{1+m}(2 - y(3)\eta - 2y(2)) - \beta(1 - y(2)^2) - y(1)y(3) + \frac{(M^2 + A_s A_p D\alpha)(y(2)-1)}{A_p(1+m)} + \frac{Fr}{1+m}(y(2)^2 - 1) + \frac{U_E}{A_p}(1+m)y'(5)\right)}{A_s(1+n) + nWe\sqrt{1+m}y(3)}, \\
 y'(5) &= \left(\left(\frac{(\rho c_p)_{TNF}}{(\rho c_p)_f}\right) \frac{APr}{(1+m)}(4y(4) + \eta y(5)) + 2\left(\frac{(\rho c_p)_{TNF}}{(\rho c_p)_f}\right) Pr y(4)y(2)\right. \\
 &\quad - Pr\left(\frac{(\rho c_p)_{TNF}}{(\rho c_p)_f}\right) y(5)y(1) - \left(\frac{\rho_{TNF}}{\rho_f}\right) \frac{Fr\delta Br}{2(1+m)}(y(2) - 1)^3 \\
 &\quad - \frac{Qy(4)Pr}{(1+m)} - \frac{M\delta Br}{(1+m)}(y(2) - 1)^2 \\
 &\quad \left. - \left(\frac{\mu_{TNF}}{\mu_f}\right) \frac{(1+m)Br}{2} \delta y(3) \left((1-n) + \frac{n}{2}y(3)\sqrt{1+m}We\right)\right) \left(\frac{\kappa_{TNF}}{\kappa_f}\right), \\
 y'(7) &= \frac{\kappa^2 \sinh(y(6))}{(1+m)}
 \end{aligned}$$

with respective boundary condition as

$$y(2) = -\gamma, y(1) = \frac{S}{\sqrt{1+m}}, y(5) - \left(\frac{\kappa_f}{\kappa_{TNF}}\right) \frac{Bi(y(4) - 1)}{\sqrt{1+m}} = 0, y(6) = \xi \text{ at } \eta = 0, \tag{26}$$

$$y(2) = 1, y(4) \rightarrow 0, y(6) \rightarrow 0 \text{ as } \eta \rightarrow \infty. \tag{27}$$

The mesh selection and error function are revitalized by the presence of a continuous solution. The disparity stayed the same, with a magnitude of 10^{-9} . At the value of $\eta = 8$, all numerical solutions are almost asymptotically correct.

5 Discussion of Numerical Results

In order to understand the problem, the Eqs. (16–18) with respective boundary conditions (19, 20) and relevant parameters are used to calculate the velocity profile ($f'(\eta)$), the local skin friction coefficient $\sqrt{Re}C_f$, the heat transfer distribution ($\theta(\eta)$) and the rate of heat transfer $\sqrt{Re}Nu$ in Figs. 2, 3, 4 and 5. This makes it possible to conduct an analysis of the interaction that exists between the various multi-physical effects that take place in the non-Newtonian bio-nano electromagnetic functional covering boundary layer regime. Because the orientation of the electric field is one of the most significant factors in determining how the transport processes are controlled in the wedge flow charged metallic nanofluid covering, it is essential to remember that the graphs contain two different values for the electric field parameter U_E that were investigated. The direction of the longitudinal electric field shown in Fig. 1 is the same as an electric field with a negative U_E parameter value. On the other hand, an axial electric field pointing in the direction shown in Fig. 1 leads to a positive number for the U_E measure of the electric field. This analysis employs a ternary hybrid nanofluid of three types of metallic nanoparticles, such as Fe, Cu and Ag with base fluid H_2O . The standard fixed nanoparticle value of Fe

is $\phi_1 = 0.05$, Cu is $\phi_2 = 0.03$, Ag is $\phi_3 = 0.02$ and the rest of the values are clearly displayed in Tables 1, 2 and 3. The MATLAB BVP4c is used to provide graphical and numerical solutions. The MATLAB BVP4c is used to provide graphical and numerical solutions. Previous studies were compared to the current analytical method to ensure its validity. The current findings for the velocity, $f'(\eta)$, are shown in Table 4 and compared to the older calculations of White [46]. The current MATLAB bvp4c answers are proven to be accurate as evidenced by the excellent association obtained. It shows very good agreement, which confirms the validity of the flow model analysis and the accuracy of the numerical method used in the computation.

The impact of significant parameters like unsteadiness parameter (A), permeability parameter (Da), Forchheimer number (Fr), electroosmosis parameter (κ), wedge flow constant parameter (m), magnetic parameter (M), power law index parameter (n) and Weissenberg number (We) on velocity graphs (Fig. 2) are elucidated in the presence of $U_E = -2$ and $U_E = 2$. The effect of the unsteadiness parameter on the velocity across the wedge flow is depicted in Fig. 2a. The impact of the unsteadiness parameter on the velocity across the wedge flow depends on the value of the negative and non-negative values of the electric field parameter ($U_E = -2$ and $U_E = 2$). As the unsteadiness parameter is raised, the movement of mixed nanofluids exhibits a more pronounced velocity profile for the both cases of $U_E = -2$ and $U_E = 2$. Because the axial motion becomes much more rigid, the momentum border layer thickens.

The effect of the permeability parameter on the velocity profile $f'(\eta)$ for both $U_E > 0$ and $U_E < 0$ is demonstrated in Fig. 2b. In electrokinetics, fluid motion is induced by the motion of charged ions in an electric field. Both the electric parameter (a measure of the intensity of the electric field) and the porosity parameter (a measure of the permeability of the medium) can influence this movement. If the electric parameters are positive, then the fluid velocity across the wedge will increase as a consequence of an increase in the Darcy velocity caused by a rise in the porosity parameter. This is because an increase in permeability would enable a greater volume of fluid to pass through the medium, increasing the surface area exposed to the electric field. It is system dependent on how the permeability parameter influences the flow rate across the wedge for negative electric parameters. A reduced fluid velocity across the wedge may be the result of a lower Darcy velocity, which can be caused by a rise in permeability. This is because the electric field exerted on the fluid may be mitigated if there is more fluid movement around the charged particles, as might be the case with a greater permeability. On the other hand, there may be situations in which a greater hydraulic movement across the wedge is noted as permeability increases.

Figure 2c shows the impact of the Forchheimer number (Fr) on the hybrid nanofluid velocity, again for $U_E > 0$ and $U_E < 0$. In $Fr = 2\bar{x}F$ gives a definition for the term Fr . The Forchheimer number is a dimensionless measure that is used to describe the amount by which an inertial impact causes a fluid movement to deviate from Darcy's law. The Forchheimer number term in Eq. (16), i.e. $+Fr(f'^2 - 1)$ enables the primary momentum to be directly influenced by Darcy's law. The velocity across the wedge flow is sensitive to the Forchheimer number for

Fig. 2 Impact of **a** A , **b** Da , **c** Fr , **d** κ , **e** m , **f** M , **g** n , **h** We on $f'(\eta)$ in the presence of $\kappa = 1, m = 2, n = 0.2, We = 0.5, Fr = 0.5, M = 2, Da = 1, A = 1, \xi = 1, S = 0.5$ and $\gamma = 0.2$

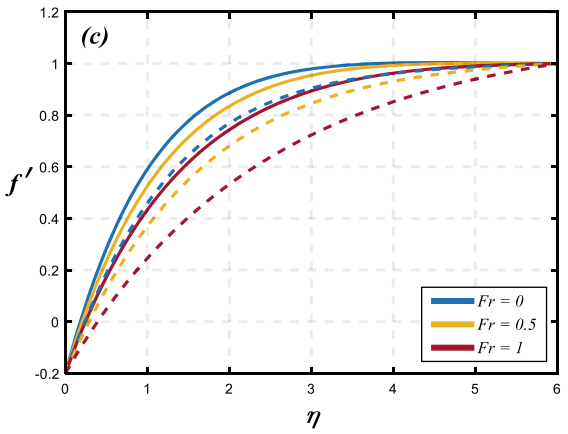
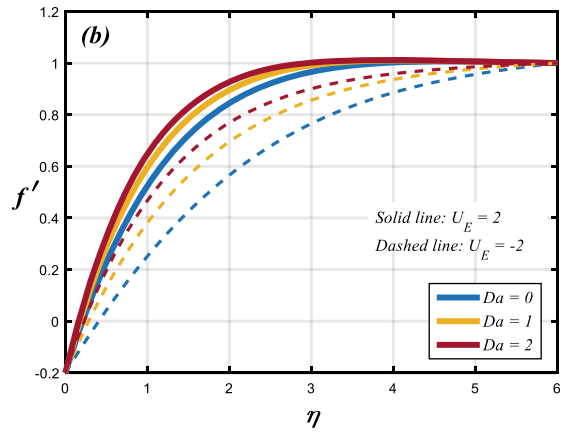
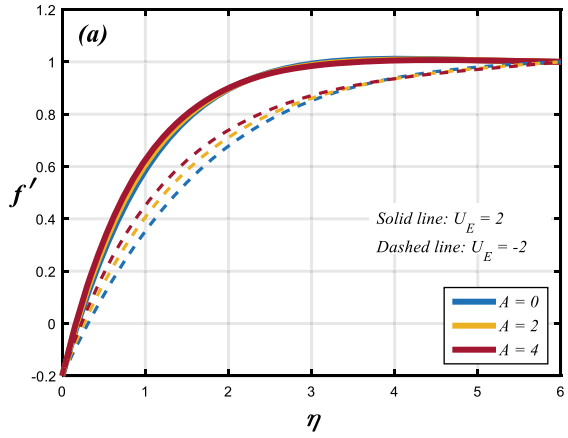


Fig. 2 (continued)

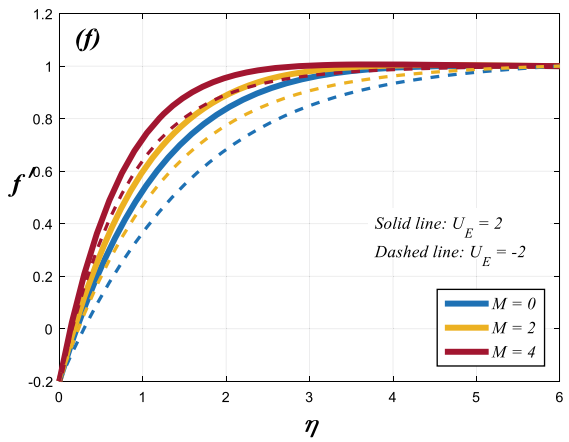
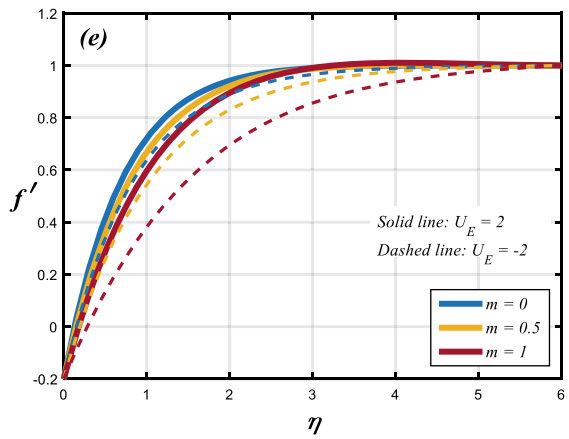
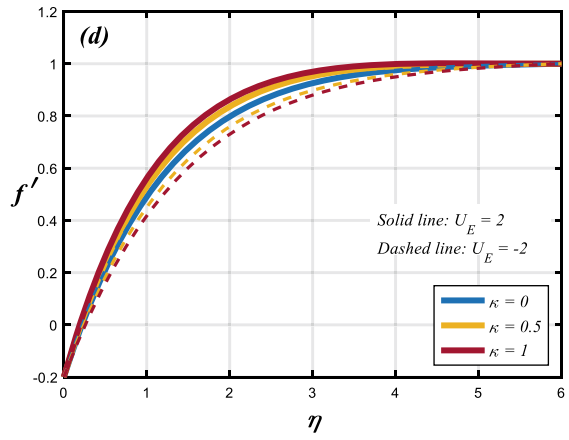
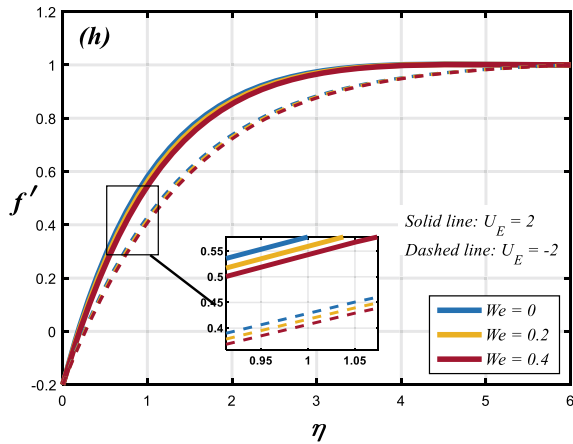
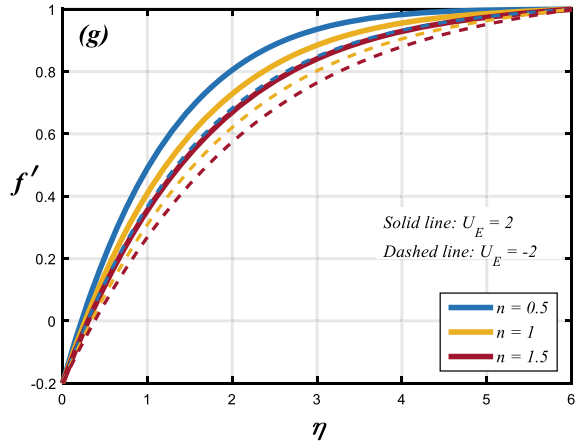


Fig. 2 (continued)



both positive and negative values of the electric parameter. Due to a greater pressure reduction across the wedge, fluid velocity drops with increasing Forchheimer numbers. Figure 2d illustrates the effect of the electroosmotic parameter (κ) on the motion of the composite nanofluid, once more for $U_E > 0$ and $U_E < 0$. When U_E is greater than zero, an increase in κ causes an increase in axial velocity; however, when U_E is less than zero, the opposite impact, a decrease in acceleration, is generated. This behavior is maintained throughout the entirety of the system, that is, at each and every number of η . Figure 2e shows the effect that the wedge flow constant parameter (m) has on the axial velocity curve for both positive and negative values of U_E . It is noticed that velocity decreases as the wedge flow constant parameter increases for both cases of $U_E > 0$ and $U_E < 0$. For both positive and negative values of U_E , Fig. 2f displays the impact of the magnetic parameter (M) on the velocity profile. The Fe, Cu and Ag nanoparticles have excellent electric and magnetic field transmission. The underlying scientific mechanism for this effect is that an increase

Fig. 3 Impact of **a** ξ , **b** We , **c** n , **d** m , **e** S , **f** γ , **g** Da on $\sqrt{Re}C_f$ versus M in the presence of $\kappa = 1, m = 2, n = 0.2, We = 0.5, Fr = 0.5, Da = 1, A = 1, \xi = 1, S = 0.5$ and $\gamma = 0.2$

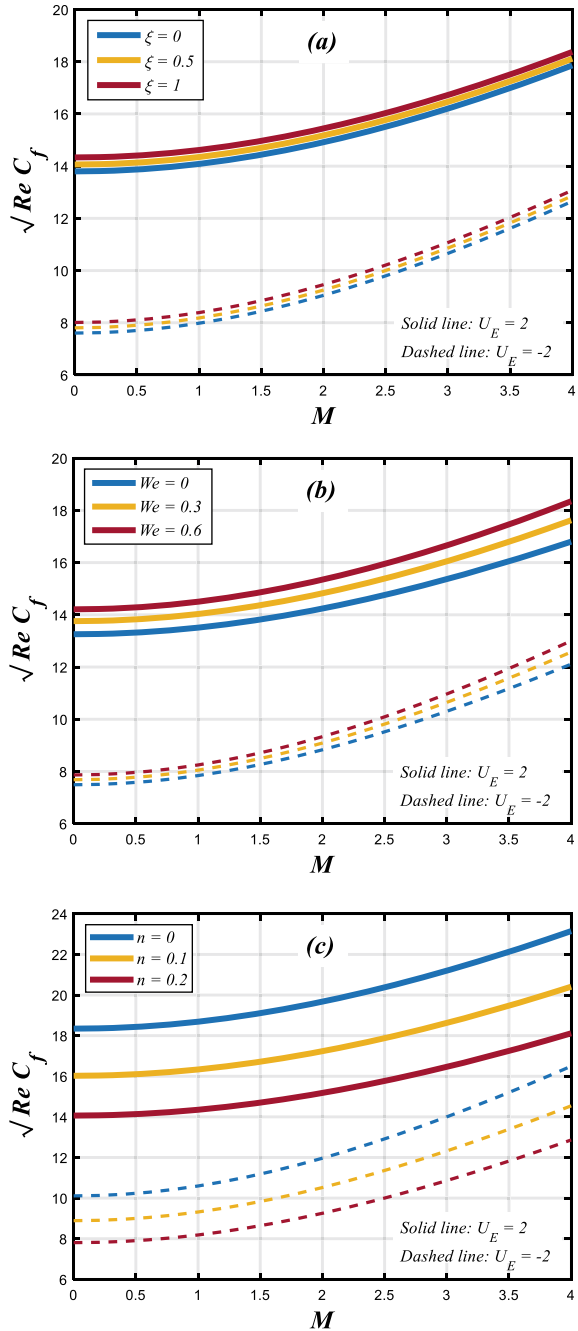


Fig. 3 (continued)

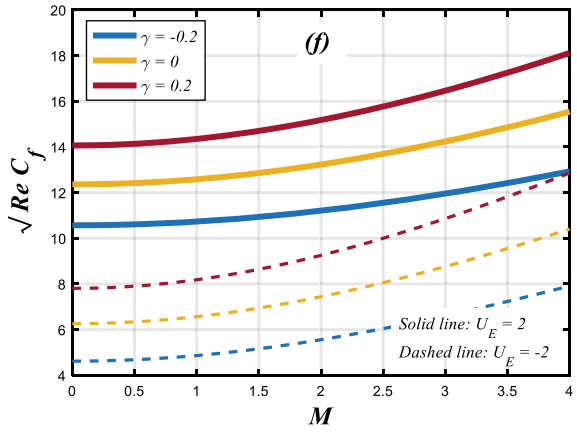
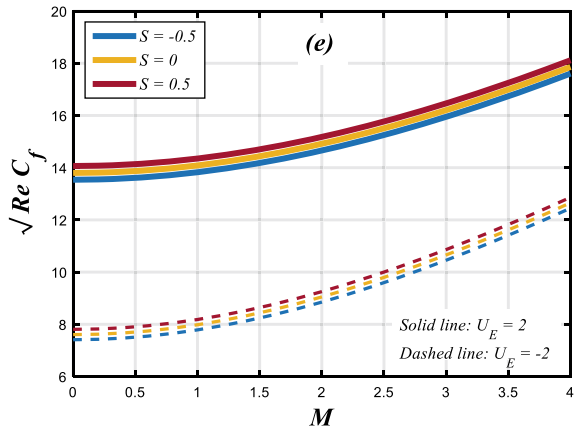
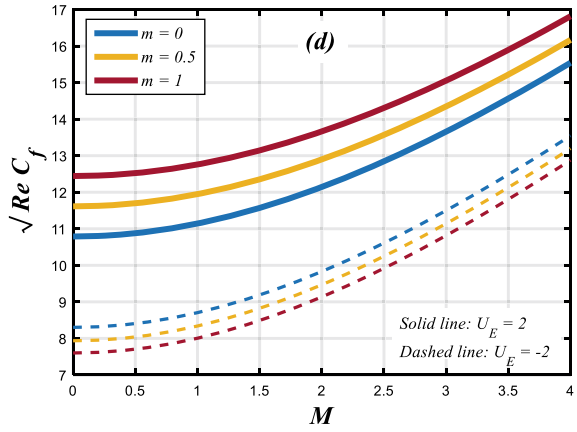
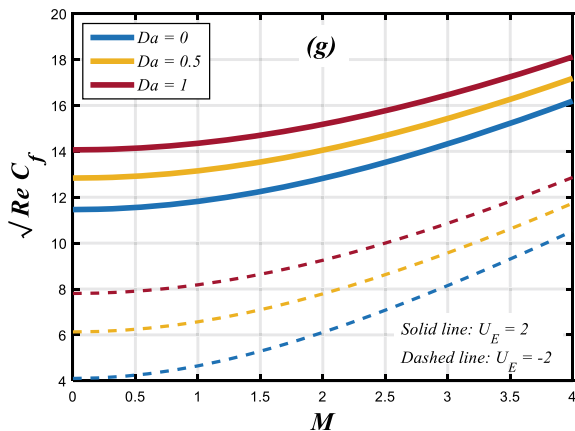


Fig. 3 (continued)



in the magnetic parameter strengthens the Lorentz force, which in turn aids fluid movement. The influences of power law index number (n) and Weissenberg number (We) on the dimensionless velocity profiles are presented in Fig. 2g, h, respectively, for the both cases of $U_E = -2$ and $U_E = 2$. According to the laws of physics, an increase in n corresponds to an increase in the viscosity, which in turn decreases the fluid velocity. These pictures make it abundantly clear that both n and We exhibit an identical pattern of quantitatively diminishing behavior on the velocity patterns. When the numbers of n and We are increased, it is seen in Fig. 2g, h that there is a corresponding decrease in the thickness of the boundary layer for both positive and negative values of U_E .

The impacts of various physical characteristics on the skin friction coefficient (wall friction) are shown in Fig. 3a–g for the two distinct instances of $U_E = -2$ and $U_E = 2$. The impacts of the zeta potential parameter on the wall friction $\sqrt{Re}C_f$ versus M for $U_E = -2$ and $U_E = 2$ are shown in Fig. 3a. The electrokinetic potential of the surface of a substance can be measured using a method called zeta potential. It is essential in determining how the substance and the elements around it interact, so pay close attention to it. The zeta potential has the ability to alter the characteristics of the boundary layer that is located close to the surface of a wedge flow, which in turn has an effect on the skin friction coefficient in the presence of $U_E = -2$ and $U_E = 2$. When the zeta potential is positive, the surface of the wedge will have a positive charge due to the presence of the zeta potential. Because of this, negatively charged ions from the fluid around it will be drawn to it, resulting in the formation of a dispersed double layer close to the surface. This layer will have a smaller potential difference and be thicker than the layer that develops when the zeta potential is equal to zero. It will also have a greater thickness. As a consequence of this, there will be a significant amount of opposition to the movement, and the coefficient of skin friction will be accentuated. For the two cases of $U_E = -2$ and $U_E = 2$, Fig. 3b, c shows the impacts of rheological factors (We and n) on the skin friction coefficient (wall friction). An increase in the Weissenberg number (We) typically results in an increase

Fig. 4 Impact of **a** Br , **b** Fr , **c** Q , **d** We , **e** ξ , **f** S , **g** Bi on $\theta(\eta)$ in the presence of $\kappa = 1, m = 2, n = 0.2, We = 0.5, Fr = 0.5, M = 2, Da = 1, A = 1, Pr = 1, \delta = 1, Br = 1, Q = 1, \xi = 1, S = 0.5$ and $\gamma = 0.2$

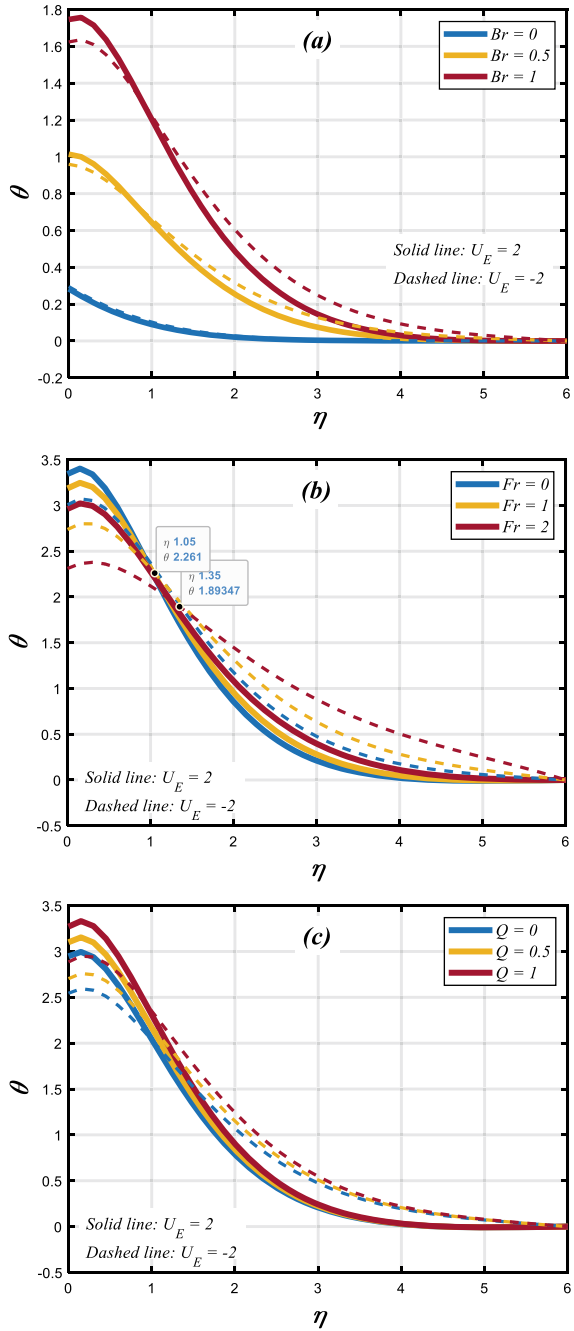


Fig. 4 (continued)

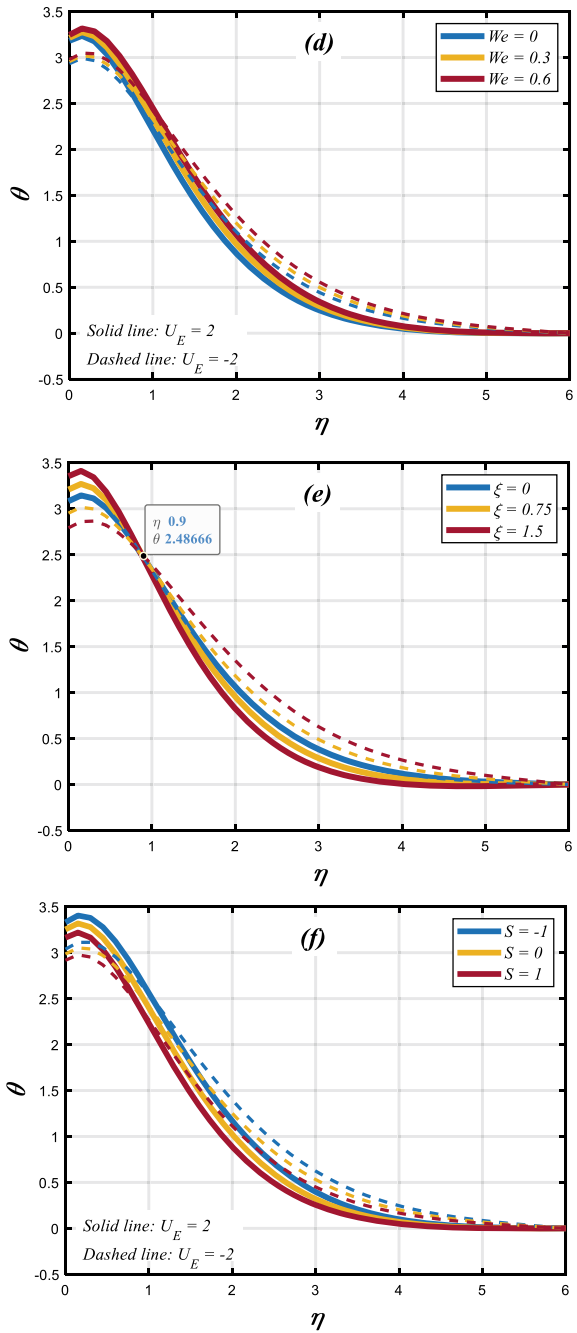
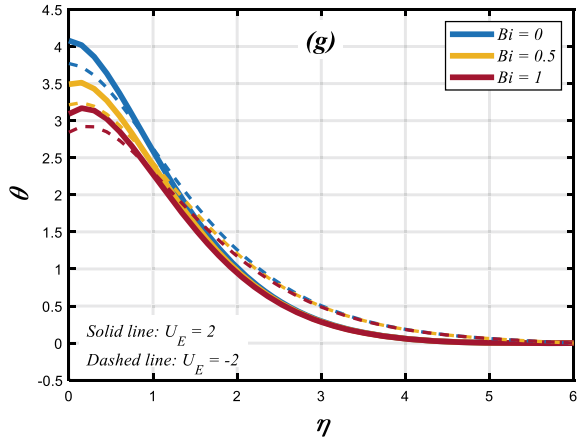


Fig. 4 (continued)



in the skin friction coefficient, and this effect can be seen for both positive and negative values of the electric parameter. This happens because the viscoelastic nature of the fluid makes it easier for vortices to form close to the surface of the wedge. This, in turn, leads to an increase in the shear stress and, consequently, the skin friction coefficient. The influence of the n on the skin friction coefficient $\sqrt{Re}C_f$ is less noticeable for both negative and positive values of the electric parameter in Fig. 3c. Furthermore, in some instances, the skin friction coefficient may diminish with an increase in the power law index number. Because of this, there is less resistance to flow at the surface of the wedge. This is due to the fact that a negative electric field has a tendency to diminish the non-Newtonian behavior of the TNF. For the two cases of $U_E = -2$ and $U_E = 2$, Fig. 3d shows the impacts of m (wedge flow constant parameter) on the $\sqrt{Re}C_f$. When $U_E (= 2)$ is positive, the electric field tends to retard the TNF motion near the wedge surface, resulting in an increase in the $\sqrt{Re}C_f$. As the m increases, leading to an increase in the $\sqrt{Re}C_f$ entire the wedge surface. This effect is more prominent for large values of m . The behavior of m reversed situation is observed in the negative value of $U_E (= -2)$. For the two cases of $U_E = -2$ and $U_E = 2$, Fig. 3e show the impacts of suction ($S < 0$)/injection ($S > 0$) parameter on the skin friction coefficient ($\sqrt{Re}C_f$). The suction and injection parameters are used to control the flow behavior in electrohydrodynamic (EHD) systems, where electric fields are used to influence the TNF flow. In a wedge flow, which is a common geometry used to study EHD flows, the skin friction coefficient is an important parameter that characterizes the amount of drag on the THF. For both cases of $U_E = -2$ and $U_E = 2$, increasing the suction parameter will lead to a decrease in the $\sqrt{Re}C_f$, while increasing the injection parameter will lead to an increase in the skin friction coefficient. This is because suction removes fluid from the surface, which reduces the shear stress, while injection adds fluid to the surface, which increases the shear stress. Figure 3f illustrates the impacts of constant moving wedge parameter (γ) characteristics on the skin friction coefficient (wall friction) for the two distinct instances of $U_E = -2$ and $U_E = 2$. It is essential to point out that

Fig. 5 Impact of **a** A , **b** Da , **c** κ , **d** m , **e** n , **f** Pr , **g** Q on $\sqrt{Re} Nu$ versus M in the presence of $\kappa = 1, m = 2, n = 0.2, We = 0.5, Fr = 0.5, Da = 1, A = 1, Pr = 1, \delta = 1, Br = 1, Q = 1, \xi = 1, S = 0.5$ and $\gamma = 0.2$

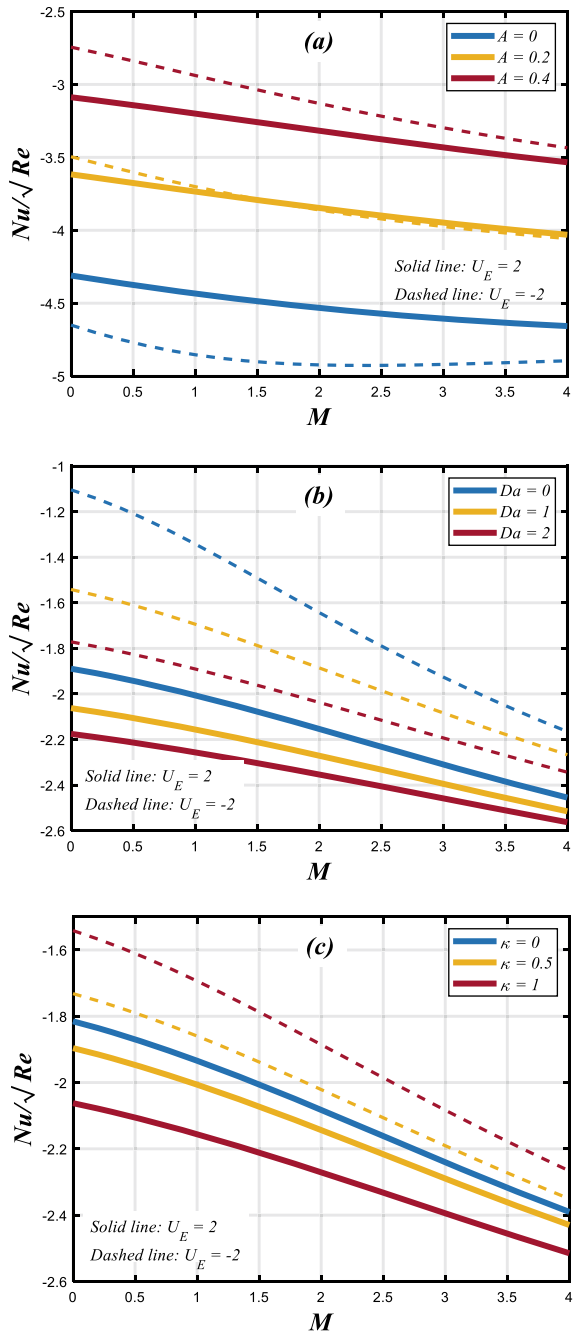


Fig. 5 (continued)

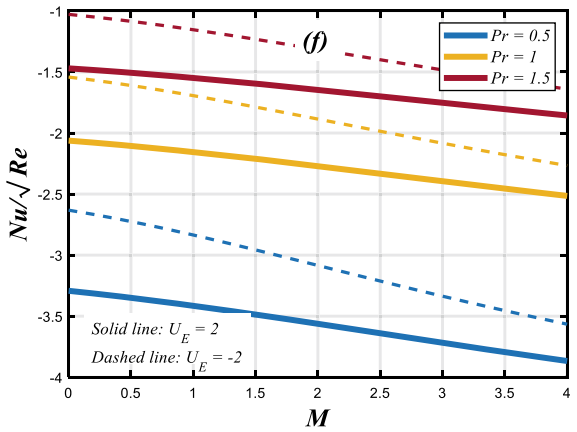
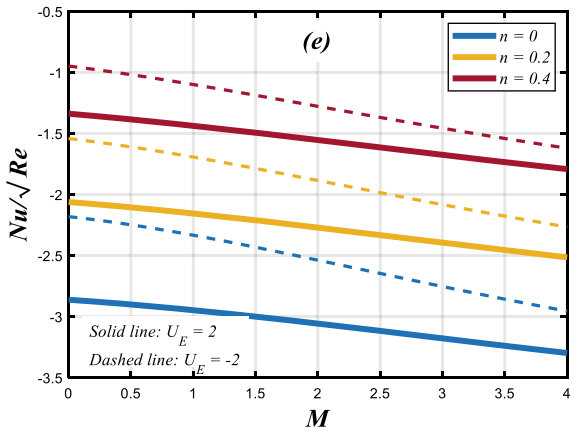
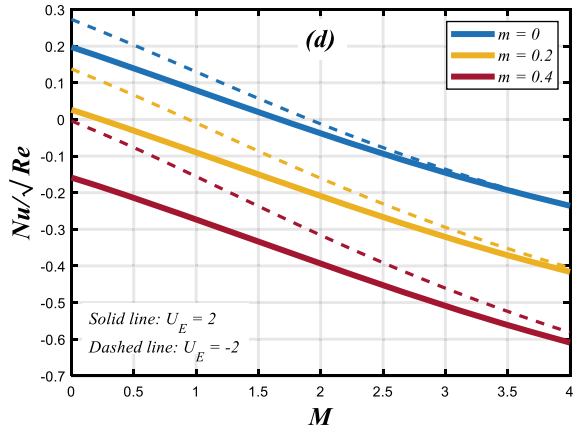


Fig. 5 (continued)

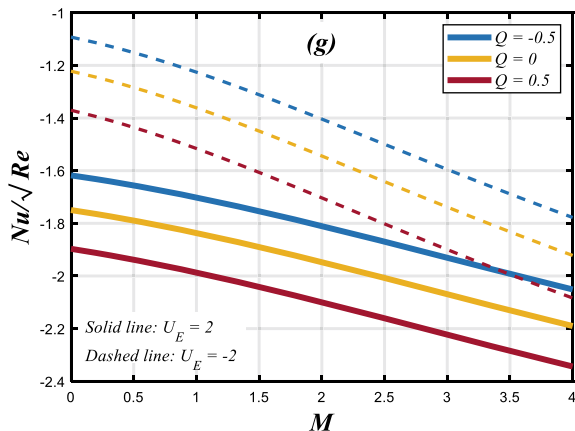


Table 4 Correlation of the current findings with earlier research for $f'(\eta)$

η	White [46]	Present solution
	$f'(\eta)$	$f'(\eta)$
0.0	0	0
0.5	0.23423	0.234276697704929
1.0	0.46063	0.4606277711046274
2.0	0.81669	0.816685225121935
3.0	0.96905	0.969049598861173
4.0	0.99777	0.997772151844778

γ is the constant moving wedge parameter (velocity ratio parameter). When $\gamma \geq 0$, it relates to a moving wedge that has the same direction as the free stream velocity, and when $\gamma \leq 0$, it relates to a moving wedge that has the opposite direction. It is clear that the $\sqrt{Re}C_f$ of the THF gets better as the γ goes up, both when the wedge is still and when it is moving, in both shear thickening and shear thinning fluids. This is the case for shear-thickened fluids as well as shear-thinned fluids. When compared to the situation of a motionless wedge, it is abundantly obvious that the $\sqrt{Re}C_f$ of the TNF is greater in the scenario involving a moving wedge for both cases of $U_E > 0$ and $U_E < 0$. Figure 3g shows how the permeability (porous) parameter affects skin friction coefficient (wall friction) for the two cases of $U_E = -2$ and $U_E = 2$. An increase in the porosity parameter results in an increase in the $\sqrt{Re}C_f$ for both $U_E = -2$ and $U_E = 2$. This is because the existence of the porous material causes an increase in the resistance to the passage of fluid, which causes the skin friction coefficient to increase.

Figure 4a–g has been drawn so that the effects of the different flow parameters on the temperature profiles when $U_E = -2$ and $U_E = 2$ are present and can be studied. Figure 4a is plotted to examine the influence of the Brinkman number on the temperature profile for both cases of $U_E = -2$ and $U_E = 2$. The amount

of influence that the Brinkman number has on the temperature distribution of a substance is considerable for both cases of $U_E = -2$ and $U_E = 2$. A large Brinkman number indicates that the viscous forces dominate over thermal diffusion, and the fluid functions like a solid, with heat being transmitted primarily by convection. This is because thermal diffusion is limited by viscous forces. On the other hand, a low Brinkman number indicates that thermal diffusion predominates over viscosity forces, and the fluid functions like a liquid, with heat being primarily transferred by convection. This is the case when the fluid has a high thermal conductivity. For both a positive and negative value of the electric parameter, the electric field helps to accelerate the flow, resulting in a more pronounced boundary layer near the wedge surface. In this case, increasing the Brinkman number leads to a thicker boundary layer and a more gradual temperature gradient near the wedge surface. The effect of the Fr on the temperature profile ($\theta(\eta)$) for both $U_E > 0$ and $U_E < 0$ is demonstrated in Fig. 4b. For both positive and negative electric parameters, the Forchheimer number has a profound effect on the temperature distribution across the wedge flow. The growth of the Forchheimer index, in the first phase ($0 \leq \eta \leq 1.35$), inhibits TNF movement due to a negative electric field, and in the first phase ($0 \leq \eta \leq 1.05$), inhibits TNF mobility due to a positive electric field. The early portion of the temperature curve tends to decrease when the F is raised. The temperature of the TNF drops as a result of the higher Darcy force caused by a rise in Fr . As a result, in the non-porous situation, where the momentum boundary layer width is minimal, the temperature profile is obviously maximum in the phase with $Fr = 0$. An explanation of the effect of the heat source/sink measure is provided in Fig. 4c. The electric characteristics of the temperature distribution across the wedge flow, both positive and negative, are significantly impacted. Increasing the heat source/sink parameter raises the temperature distribution across the wedge flow for both positive and negative electric parameters. As more heat is generated, the electrothermal effect becomes more dominant, driving the flow and temperature ranges. Wedge flows have a greater temperature difference when the hot surface is closer to the flow than the chilled surface. In Fig. 4d, the effect of the Weissenberg number on the temperature distribution all the way across the wedge flow is shown when the electric parameter is present as $U_E > 0$ and $U_E < 0$. Increasing We can have the effect of enhancing the flow instability and leading to more substantial temperature fluctuations. This effect can occur for both positive and negative values of the electric parameter. Figure 4e illustrates the impact of the zeta potential parameter, on the temperature distribution for both electric field parameter scenarios, i.e. $U_E > 0$ and $U_E < 0$. When an electric field is present, the temperature gradient across a wedge flow can be greatly affected by a quantity called the zeta potential, which describes the surface charge of a substance in touch with a TNF. Electrokinetic processes like electrophoresis and electroosmosis, induced by an applied electric field to a fluid, can alter the spatial distribution of temperatures in the TNF. If the electric measure zeta is negative, the zeta potential will have a negative effect on the temperature distribution across a wedge flow. (i.e. *the direction of the applied electric field*). If the electric parameter is positive (i.e. *the electric field is applied in the direction of movement*), then a positive zeta potential will tend to amplify the temperature

increase at the wall, while a negative zeta potential will tend to dampen it. The effect of the suction/injection parameter on the temperature distribution is shown for both the $U_E = -2$ and $U_E = 2$ instances in Fig. 4f. The suction/injection component, which measures the mass movement into or out of the flow, can influence the temperature distribution by modifying the convective heat transfer coefficient. Suction ($S < 0$) at the wedge's surface weakens the flow, reducing the convective heat transmission rate, and increasing the temperature spread. The opposite is true for injection ($S > 0$), which strengthens the flow and increases the convective heat transmission rate while decreasing the temperature distribution. The temperature distribution along the wedge flow is affected by the electric parameter ($U_E > 0$ and $U_E < 0$) and the Biot number in Fig. 4g. When the Biot number is small, the temperature across the wedge flow is almost always the same. This is because heat moves through the TNF faster than it moves at the contact. The temperature curve across the wedge flow shows a sharp gradient near the TNF interface when the Biot number is large because heat transfer within the TNF is sluggish compared to heat transfer at the interface. The electric field tends to inhibit the thermal boundary layer, the area of the fluid closest to the TNF surface where heat transmission is most concentrated, for both positive and negative electric factors ($U_E > 0$ and $U_E < 0$). Because of this, the electric field causes the temperature gradient across the wedge flow to be flattened than it would be without it. The electric field intensity and Biot number determine the extent of the flatness.

Figure 5a–g is the sketch of the local Nusselt number or rate of heat transfer coefficient (RHTC) $\sqrt{Re}Nu$ versus magnetic parameter M for various values of A , Da , κ , m , n , Pr and Q in the two different cases of electric field parameter scenarios, i.e. $U_E > 0$ and $U_E < 0$. It demonstrates that for larger A , the $\sqrt{Re}Nu$ improves for both cases of the electric parameter ($U_E > 0$ and $U_E < 0$) which is clearly portrayed in Fig. 5a. The Nusselt number for flow over a wedge is sensitive to both the permeable Darcy parameter and the electric parameter, which is presented in Fig. 5b. The electric component reflects the influence of an applied electric field on fluid dynamics and thermal exchange. The Nusselt number drops, suggesting less convective heat transmission, when the permeable Darcy parameter is raised. This is because a greater amount of hydraulic resistance is created when the Darcy constant is increased. The impacts of electroosmosis parameter on the wall friction $\sqrt{Re}C_f$ versus M for $U_E = -2$ and $U_E = 2$ are shown in Fig. 5c. When the electric parameter is positive, the convective transfer of heat coefficient, or Nusselt number, tends to rise with the increased value of the electroosmosis parameter. Since electrohydrodynamic (EHD) movement can be induced by an external electric field, improved fluid mingling and disturbance can result in greater convective heat transmission. However, the Nusselt number tends to decrease for negative values of the electric constant. This is because ion depletion layers can develop near the wedge's surface in a negative electric field, decreasing the effective thermal boundary layer and thus the convective heat transfer rate. For the two cases of $U_E = -2$ and $U_E = 2$, Fig. 5d shows the impacts of m on the $\sqrt{Re}Nu$. As the m increases, leading to a decrease in the $\sqrt{Re}Nu$ entire the wedge surface for both cases of positive and negative electric parameters ($U_E > 0$ and $U_E < 0$). Figure 5e shows that for both

positive and negative values of electric factors, the impact of the power law index number (n) on the Nusselt number $\sqrt{Re}Nu$ versus magnetic parameter M . This is due to the fact that greater values of the power law index indicate greater shear rates, which in turn boost convective heat transmission across the wedge flow. As can be seen in Fig. 5f, the Nusselt number $\sqrt{Re}Nu$ for the wedge flow depends on both the Prandtl number and the electric parameter ($U_E > 0$ and $U_E < 0$). A surface's ability to conduct heat is quantified by its Nusselt number. The diffuse heat transmission rate is the foundation for this. When the electric parameter is either positive or negative, the electric field speeds up the flow of fluid in the wedge in the direction of flow. As a consequence, the Nusselt number rises as the heat transmission rate rises. The effects of heat source/sink parameter (Q) on local Nusselt number $\sqrt{Re}Nu$ for both positive and negative electric factors ($U_E > 0$ and $U_E < 0$) are shown in Fig. 5g. When discussing wedge flow, the term "heat source/sink parameter" refers to a parameter that characterizes the rate at which heat is generated or consumed by the fluid as it flows over a surface that is curved like a wedge. When the electric parameter is either positive or negative, the electric field exerts a pulling force on the fluid that causes it to move closer to the surface of the wedge. Because of this, the rate of heat transmission via convection rises, and the Nusselt number also rises as a direct consequence. However, if you increase either the heat source or the heat sink parameter, you will also see an increase in the rate at which the fluid either generates heat or absorbs heat. This results in an even greater increase in the rate of heat transmission due to convection, and the Nusselt number goes up by an even greater amount. As a result, when the electric parameter is either negative or positive, an increase in the heat source/sink parameter results in an even further increase in the Nusselt number.

6 Conclusions

The boundary layer flow and EMHD heat transfer of a tangential hyperbolic ternary hybrid nanofluid caused by a porous wedge surface in the presence of zeta potential and a heat source/sink have been analyzed numerically. The Biot number and the Forchheimer resilience component are considered. Graphs and tables have been used for the physical study. Here is a summary of the most important results, which set the stage for future gadgets made by lab researchers:

- (1) The importance of the current study of unstable mixed convection flow is shown by the fact that the electric field component has a strong effect on things like velocity, heat transfer, wall friction, and heat transfer coefficients.
- (2) For both positive and negative electric factors ($U_E > 0$ and $U_E < 0$), increasing the values of the Weissenberg number, the power law index parameter, and the Forchheimer number resulted in a decrease in velocity, while the reverse was true for the unsteadiness parameter and the porous parameter.

- (3) The rise in the Weissenberg number and the porous parameter both contributed to an increase in the wall friction for both cases of ($U_E > 0$ and $U_E < 0$).
- (4) In the presence of a negative and positive electric field, the heat transfer increases due to growth in the Weissenberg number, heat source/sink parameter, Brinkman number, and the reverse nature of the Biot number.
- (5) The local rate of heat transfer coefficient is a decreasing function of the porous parameter, wedge flow constant and heat source/sink parameter for both case of ($U_E > 0$ and $U_E < 0$).

References

1. Hull AM, Pearson JRA (1984) On the converging flow of viscoelastic fluids through cones and wedges. *J Nonnewton Fluid Mech* 14:219–247
2. Prakash JR, Rao KK (1991) Steady compressible flow of cohesionless granular materials through a wedge-shaped bunker. *J Fluid Mech* 225:21–80
3. Jyotsna R, Rao KK (1997) A frictional kinetic model for the flow of granular materials through a wedge shaped hopper. *J Fluid Mech* 346:239–270
4. Tolboom RAI, Dam NJ, Meulen JJT (2005) Quantitative planer Raman imaging through a spectrograph: visualisation of a supersonic wedge flow. *Exp Fluids* 38:720–730
5. Rosenhead L (1940) The steady two-dimensional radial flow of viscous fluid between two inclined plane walls. *Proc R Soc Lond A* 175:436–467
6. Tanner RI (1966) Non-Newtonian fluid parameter estimation using conical flows. *Ind Eng Chem Fundam* 5:55–59
7. Tadmor Z (1966) Non-Newtonian tangential flow in cylindrical annuli IV. *Polym Eng Sci* 6:203–212
8. Moffatt HK, Hooper A, Duffy BR (1982) Flow of non-uniform viscosity in converging and diverging channels. *J Fluid Mech* 117:283–304
9. Durban D (1986) On generalized radial flow patterns of viscoplastic solids with some applications. *Int J Mech Sci* 28:97–110
10. Brewster ME, Chapman SJ, Fitt AD, Please CP (1995) Asymptotics of slow flow of very small exponent power-law shear-thinning fluids in a wedge. *Eur J Appl Math* 6:559–571
11. Bird C, Breward CJW, Dellar P, Edwards CM, Kaouri K, Richardson G, Wilson SK (2002) Mathematical modeling of pipe-flow and extrusion of composite materials. European Study Group with Industry, Unilever Research, Lancaster, UK, pp G1–G16
12. Falkneb V, Skan SW (1931) LXXXV. Solutions of the boundary-layer equations. *Lond Edinb Dublin Philos Mag J Sci* 12:865–896
13. Ali B, Hussain S, Nie Y, Rehman AU, Khalid M (2020) Buoyancy effects on Falkner Skan flow of a maxwell nanofluid fluid with activation energy past a wedge: finite element approach. *Chin J Phys* 68:368–380
14. Watanabe T (1990) Thermal boundary layers over a wedge with uniform suction or injection in forced flow. *Acta Mech* 83:119–126
15. Ishak A, Nazar R, Pop I (2009) MHD boundary-layer flow past a moving wedge. *Magnetohydrodynamics* 45:103–110
16. Ali B, Hussain S, Nie Y, Khan SA, Naqvi SIR (2020) Finite element simulation of bioconvection Falkner-Skan flow of a Maxwell nanofluid fluid along with activation energy over a wedge. *Phys Scr* 95:095214
17. Ramesh Reddy P, Abdul Gaffar S, Hidayathulla Khan BMD, Venkatadri K, Beg OA (2021) Mixed convection flows of tangent hyperbolic fluid past an isothermal wedge with entropy: a mathematical study. *Heat Transf* 50(3):2895–2928

18. Asogwa KK, Goud BS, Shah NA et al (2022) Rheology of electromagnetohydrodynamic tangent hyperbolic nanofluid over a stretching riga surface featuring dufour effect and activation energy. *Sci Rep* 12:14602
19. Ali B, Naqvi RA, Mariam A, Ali L, Aldossary OM (2021) Finite element study for magneto-hydrodynamic (MHD) tangent hyperbolic nanofluid flow over a faster/slower stretching wedge with activation energy. *Mathematics* 9:25
20. Khan M, Rasheed A, Salahuddin T, Ali S (2021) Chemically reactive flow of hyperbolic tangent fluid flow having thermal radiation and double stratification embedded in porous medium. *Ain Shams Eng J* 12(3):3209–3216
21. Hickey OA et al (2011) Influence of charged polymer coatings on electro-osmotic flow: molecular dynamics simulations. *Macromolecules* 44(23):9455–9463
22. Melanson JE et al (2001) Dynamic capillary coatings for electroosmotic flow control in capillary electrophoresis. *TrAC Trends Anal Chem* 20:365–374
23. Burgreen D, Nakache FR (1964) Electrokinetic flow in ultrafine capillary slits. *J Phys Chem* 68:1084–1091
24. Qiao (2006) Control of electroosmotic flow by polymer coating: effects of the electrical double layer. *Langmuir* 22(16):7096–7100
25. Tso CP, Sundaravadivelu K (2001) Capillary flow between parallel plates in the presence of an electromagnetic field. *J Phys D Appl Phys* 34:3522
26. Chakraborty S, Paul D (2006) Microchannel flow control through a combine electromagneto-hydrodynamic transport. *J Phys D Appl Phys* 39:5364
27. Nagaraju G, Jangili S, Ramana Murthy JV et al (2019) Second law analysis of flow in a circular pipe with uniform suction and magnetic field effects. *J Heat Transf* 141:012004
28. Bhatti MM, Zeeshan A, Ellahi R (2017) Electromagnetohydrodynamic (EMHD) peristaltic flow of solid particles in a third grade fluid with heat transfer. *Mech Ind* 18:314
29. Mahdy A, Hoshoudy GA (2019) EMHD time dependent tangent hyperbolic nanofluid flow by a convective heated riga plate with chemical reaction. *Proc Inst Mech Eng Part E J Process Mech Eng* 233(4). <https://doi.org/10.1177/0954408918805>
30. Prakash J, Tripathi D, Akkurt N et al (2022) Tangent hyperbolic non-Newtonian radiative bioconvection nanofluid flow from a bi-directional stretching surface with electro-magneto-hydrodynamic, Joule heating and modified diffusion effects. *Eur Phys J Plus* 137:472. <https://doi.org/10.1140/epjp/s13360-022-02613-x>
31. Cho CC, Chen CL, Chen CK (2012) Electrokinetically-driven non-Newtonian fluid flow in rough microchannel with complex-wavy surface. *J Non-Newtonian Fluid Mech* 173–174:13–20
32. Rashid M, Nadeem S, Shahzadi I (2020) Permeability impact on electromagnetohydrodynamic flow through corrugated walls of microchannel with variable viscosity. *Adv Mech Eng* 12(7):1–11. <https://doi.org/10.1177/1687814020944336>
33. Prakash J, Tripathi D (2020) Study of EDL phenomenon in Peristaltic pumping of a Phan-Thien-Tanner fluid through asymmetric channel. *Korea-Aust Rheol J* 32:271–285. <https://doi.org/10.1007/s13367-020-0026-1>
34. Nazeer M, Ali N, Ahmad F et al (2020) Effects of radiative heat flux and Joule heating on electro-osmotically flow of non-Newtonian fluid: analytical approach. *Int Commun Heat Mass Transf* 117:104744
35. Prakash J, Tripathi D, Anwer Beg O, Tiwari AK, Kumar R (2022) Thermo-electrokinetic rotating non-Newtonian hybrid nanofluid flow from an accelerating vertical surface. *Heat Transf* 51(2):1746–1777
36. Manjunatha S, Puneeth V, Giresha BJ, Chamkha AJ (2022) Theoretical study of convective heat transfer in ternary nanofluid flowing past a stretching sheet. *J Appl Comput Mech* 8(4):1279–1286
37. Dadheech PK, Agrawal P, Sharma A, Nisar PK, Purohit SD (2021) Transportation of Al₂O₃-SiO₂-TiO₂ modified nanofluid over an exponentially stretching surface with inclined magnetohydrodynamic. *Therm Sci* 25(Spec. issue 2):279–285
38. Sundar LS, Chandra Mouli KVV, Said Z, Sousa ACM (2021) Heat transfer and second law analysis of ethylene glycol-based ternary hybrid nanofluid under laminar flow. *J Therm Sci Eng Appl* 13(5). <https://doi.org/10.1115/1.4050228>

39. Cao W, Animasaun IL, Yook S-J, Oladipupo VA, Ji X (2022) Simulation of the dynamics of colloidal mixture of water with various nanoparticles at different levels of partial slip: ternary-hybrid nanofluid. *Int Commun Heat Mass Transf* 135:106069. <https://doi.org/10.1016/j.icheatmasstransfer.2022.106069>
40. Animasaun IL, Yook S-J, Muhammad T, Mathew A (2022) Dynamics of ternary-hybrid nanofluid subject to magnetic flux density and heat source or sink on a convectively heated surface. *Surf Interface* 28:101654. <https://doi.org/10.1016/j.surfin.2021.101654>
41. Sahu M, Sarkar J, Chandra L (2021) Steady-state and transient hydrothermal analyses of single-phase natural circulation loop using water-based tri-hybrid nanofluids. *AIChE J* 67:17179. <https://doi.org/10.1002/aic.17179>
42. Zhu H, Lin Y, Yin Y (2004) A novel one-step chemical method for preparation of copper nanofluids. *J Colloid Interface Sci* 277:100–103
43. Masuda S, Nagao M, Takahaty K, Konoshi Y, Gallyas F, Tabira T, Sasaki R (1993) Functional erythropoietin receptor of the cells with neuronal characteristics. *J Biol Chem* 268:11208–11216
44. Lee S, Choi SUS, Li S, Eastman JA (1999) Measuring thermal conductivity of fluids containing oxide nanoparticles. *Trans ASME J Heat Transf* 121:280–289
45. Eastman JA, Choi SUS, Li S, Yu W, Thompson LJ (2001) Anomalously increased effective thermal conductivities of ethylene glycol-based nanofluids containing copper nanoparticles. *Appl Phys Lett* 78:718–720
46. White FM (2006) *Viscous fluid flows*, 3rd edn. McGraw-Hill, New York

Chapter 14

Sensitivity Analysis and Numerical Investigation of Hybrid Nanofluid in Contracting and Expanding Channel with MHD and Thermal Radiation Effects



Ahmad Zeeshan, M. Zeeshan Khan, Imran Khan, and Zeshan Pervaiz

Abstract In the current study, the author investigated the sensitivity of hybrid-nanofluid flow in expanding and contracting the channel with both MHD and thermal radiation effects. The mathematical model of the flow problem is developed. The lower plate is stationary and heated externally. The upper plate is porous which contracts/expands with respect to the time and allows a coolant fluid inside the channel. The governing momentum and temperature equations are transformed by the similarity transformation into the non-linear ordinary differential equations. The obtained ODEs are then solved analytically by the Homotopy Analysis Method (HAM) along with the defined boundary conditions. Copper and silver nanoparticles are mixed with the base fluid water. The numerical solution is obtained using the Mathematica package (BVPh 2.0). Then using Response Surface Methodology (RSM), the correlation between different parameters and the responses are shown through tables and graphs.

Keywords Hybrid Nanofluids · Magneto-hydrodynamics · Sensitivity analysis · Thermal radiation · RSM

Nomenclature

b	Distance between the upper and lower plates
$b(t)$	Expand or contract function
b_0	Initial channel height
$A_i, i = 1, 2, 3, 4, 5$	Constant parameters in hybrid nanofluids

A. Zeeshan (✉) · M. Z. Khan · I. Khan · Z. Pervaiz
Department of Maths and Stats, International Islamic University, Islamabad, Pakistan
e-mail: ahmad.zeeshan@iiu.edu

© The Author(s), under exclusive license to Springer Nature Singapore Pte Ltd. 2023
D. Tripathi et al. (eds.), *Nanomaterials and Nanoliquids: Applications in Energy and Environment*, Advances in Sustainability Science and Technology,
https://doi.org/10.1007/978-981-99-6924-1_14

α	Expansion ratio
$f(\eta), g(\eta)$	Composition form of temperature
k^*_{mf}	Mean absorption co-efficient of hybrid nanofluid
M	Magnetic parameter
N	Radiation parameter
σ^*	Stefan-Boltzmann constant
Λ	Wall permeability
Pr	Prandtl number
P^-	Dimensional pressure
P	Non-dimensional pressure
Re	Reynold number
Br	Brinkman number
Ec	Eckert number
t	Time
T	Temperature
T_1	Temperature at the lower plate
T_2	Temperature at the upper plate
u^-	Dimensional velocity in the x direction
u	Non-dimensional velocity in the x direction
\bar{v}	Dimensional velocity in the y direction
V	Non-dimensional velocity in the y direction
F	Stream function variable
θ	Temperature
A	Temperature difference
ϕ_1, ϕ_2	Nanoparticles volume fractions

Subscripts

F	Host fluid
hnf	Hybrid nanofluid
P	Particle

1 Introduction

In all industrial sectors, including manufacturing, transportation, power generation, and highly sophisticated electronic equipment, cooling and heating are crucial. For cooling equipment that undertakes energy conveyance, cooling solutions are extremely necessary. Ethylene glycol, engine oil, and water are the most commonly used fluids in energy transportation because of their fluidity. Such fluids have limited heat transfer capabilities. So they alone are not able to provide the thermal efficiency

that the advanced technological equipment desires. On the other hand, metallic materials dissipate more heat through conduction than conventional liquids. So, the desire was to make a substance by combining the properties of both substances to produce a heat transport medium that behaves like a liquid and conducts heat like metals. The efficiency of a thermal system depends on the material used for heat transport. According to the first law of thermodynamics, the total energy of the universe remains the same, but it may be converted from one form to another. So, dissolving nano-sized metallic particles in a base fluid, like oils or water, would perhaps take out all the thermal transport issues. Rashidi et al. [1] study several aspects in relation to the significance of entropy generation and second law analysis for heat exchangers in order to acquire deep insight into the flaws of the system and opportunities for performance improvement.

Compared to regular fluids, nanofluids have a higher thermal conductivity. This is due to the base fluid's ability to properly suspend metallic nanoscale particles. These fluids were first prepared by Choi and Eastman in 1995 [2]. It was one of the most obvious aspects of improving the thermal conductivity of fluids. Later, several mathematical models, such as the continuum model for the nanofluid flow [3], suspension or dispersion phase model [4], and the reputed model that is commonly used, known as the Buongiorno's model [5], were established in a brainstorming way. Recently, many researchers have been investigating nanofluids. Sheikholeslami [6] investigated analytically the MHD nanofluid flow. Their results show that the maximum average Nusselt number is obtained at an optimum angle of turn. This angle has a great impact on streamlines. The momentum and heat transfer of nanofluids through channels and via various geometries were topics of discussion for many researchers. Zeeshan and Bhatti [7] studied the impacts of heat-mass transfer on nanofluid flow along with the slip effect due to the peristaltic motion. The results obtained show that the fluid velocity increases near the wall because of the slip effect but decreases due to the nanoparticle volume fraction. Lee investigated the stability of Al_2O_3 -Cu (Alumina-Copper) nanofluid flow using the base fluid ethylene glycol [8]. Majeed et al. [9] investigated the effects of heat transport phenomena and magnetized Casson nanofluid flow on boundary layer flow over a nonlinear stretching surface.

Later, researchers began to lean towards a nanosuspension known as a hybrid nanofluid [10]. These fluids allow two different kinds of metallic particles to disperse into the host fluid. Thus, if we select the appropriate metallic nanoparticles, it might improve the heat transmission properties. The current work investigates a major improvement in hybrid nanofluid's thermal transport properties. Zeeshan et al. [11] studied the hybrid nanofluid containing $Cu-Al_2O_3$ in the base ethylene glycol in the presence of MHD. Maskeen et al. [12] examined the flow characteristics and the performance of heat transport of alumina-copper/water hybrid nanofluid flowing past a stretching cylinder with regard to Lorentz magnetic forces and the thermal radiation effect. Acharya et al. [13] examined the Hall effect on $Cu-TiO_2$ (copper plus titanium dioxide) hybrid nanofluids flowing past a rotating disc. Saqib et al. [14] developed the exact analytical solution for temperature and velocity profiles of alumina-copper hybrid nanosuspension by employing the Laplace transformation technique and Caputo Fabrizio fractional derivative. Waini et al. [15] investigated

the steady fluid flow and heat transfer of copper-alumina/water hybrid nanofluid flow over a surface with nonlinear stretching/shrinking effects. Hassan et al. [16] looked at the characteristics of the Cu-Ag/water hybrid nanofluid flow and the effectiveness of convective heat transfer.

To study the heat transfer properties of specific physical instances, researchers have been running experiments with adjoining nanoparticles and a base fluid [17]. Besides that, the applied magnetic field to the flow plays an important role in controlling heat transfer and momentum of boundary-layer flows in many industrial operations, such as magneto-hydrodynamic power generation systems [18]. Ellahi investigated the MHD flow of a non-Newtonian nanofluid through a pipe [19]. He manifested that the fluid motion decreases with increasing magnetic parameters. So, the velocity distribution becomes larger than the temperature distribution. Hayat [20] studied the effects of thermophoresis and Brownian motion on MHD hybrid nanofluid flow. Hamad and El-Gaied [21] described the two-dimensional magneto-hydrodynamic steady boundary layer $Al_2O_3-H_2O$ nanofluid flow with applied convective surface boundary conditions over a moving permeable plate. Numerical approaches are presented to illustrate the effects of the wall velocity parameter, suction parameter, convective heat transfer, power law exponent, and nanoparticle concentration on temperature, velocity, Nusselt number, and skin friction coefficient. The three-dimensional MHD rotating nanofluid flow across a permeable stretched surface was taken into consideration by Majeed and Zeeshan [22]. The impacts of nonlinear inertial forces with MHD effects are examined. Alsaedi [23] quantitatively examined the MHD hybrid nanofluid flow incorporating graphene plus copper nanoparticles in the host fluid, kerosene oil. Pattnaik et al. [24] investigated the flow of an electrically conducting micropolar nanofluid from a vertically extending surface near a porous medium in the presence of the MHD effect. They found that the skin friction and coupling stress coefficients decreased with a higher Lorentzian drag effect (M). In the industrial state, radiative heat transfer is particularly important for the design of gas turbines, nuclear power plants, dependable machinery, and other propulsion appliances like missiles, satellites, aircraft, and spacecraft. Radiative heat transport effects on magnetohydrodynamic nanofluid flow between two horizontally placed rotating plates were investigated by Sheikholeslami and DD Ganji [25]. They looked at how mass and heat characteristics were affected by the Reynolds number, rotation parameter, radiation parameter, magnetic parameter, and Brownian parameter. The investigation of the entropy generation of a non-Newtonian Carreau nanofluid flow over a contracting sheet was taken into account by Abbas and Bhatti [26]. They also discussed the effects of magneto-hydrodynamic (MHD) on the flow. Shahid et al. [27] used the Cattaneo-Christov heat flux model to study the Maxwell viscoelastic MHD flow via a porous stretched sheet. In their models, the impacts of thermal radiation and chemical reactions are also taken into account. Sensitivity analysis is used in the field of engineering to determine how entirely different variable values affect the expected output or responses. In many scientific and industrial domains, experimental design is very important. An experimenter may plan and design experiments for this purpose, and then assess the findings to arrive at a conclusion. One of the most commonly used experimental designs for optimization is the response surface

methodology (RSM). It is a widely used mathematical and statistical method for assessing a mechanism, where several variables influence the response of interest. To create a correlation between input parameters and output variables, the Response Surface Methodology (RSM) is used. Chan et al. [28] used the thermal characteristics of an H_2O -bionanofluids flow across a wedge to do parameter sensitivity analysis on industrially significant variables such as wall heat flux, skin friction, and mass flux on the wall. Dilawar et al. [29] talked about the sensitivity of the relevant parameter for a Newtonian fluid flow in a two-dimensional convective wedge across a semipermeable wedge surface. Abdelmalek et al. [30] carried out a sensitivity analysis to analyze the impact of the magnetic parameter, Stefan blowing parameter, and shrinking/stretching parameter upon reduced Sherwood and Nusselt numbers. Rashidi et al. [31, 32] applied response surface methodology (RSM) to create the parameter sensitivity for semipermeable thermal exchangers. In a recent work, Mackolil and Mahanthesh [33] explored the sensitivity of the rate of heat transfer in Marangoni 's convection flow. They used RSM to determine the sensitivity of important factors like the Nusselt number, utilizing a variety of relevant input parameters.

This study aims to investigate the sensitivity of a hybrid nanofluid flow in an asymmetric porous channel with an applied MHD field force and radiative heat impact. The channel consists of two parallel plates. The upper plate is contracting/expanding and is cooled down by injecting coolant fluid with a uniform velocity v_w and the lower plate is fixed and heated externally. Graphical observations of the effects of different parameters on the flow problem have been made.

2 Mathematical Formulation

An unsteady, two-dimensional, radiative flow of an incompressible fluid between two parallel and squeezing flat plates is considered, as shown in Fig. 1. A uniform and transverse magnetic field is applied to the flow. The lower wall of the channel, which is kept motionless and heated externally, is represented by the x-axis. To cool down the upper wall, a coolant fluid is injected through the upper wall having a uniform velocity v_w , which contracts and expands with respect to the time function $b(t)$.

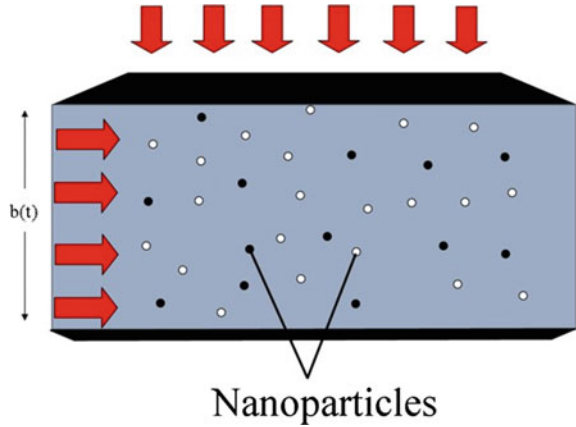
The nanoparticles and fluid phase are both assumed to be in a thermally stable state having no slip velocity along the wall. Considering the above-stated assumptions, the governing continuity, momentum and temperature equation of the flow are as follows [34].

$$\bar{v}_{\bar{y}} + \bar{u}_{\bar{x}} = 0. \quad (2.1)$$

$$\rho_{hnf}(\bar{u}_t + \bar{u}\bar{u}_{\bar{x}} + \bar{v}\bar{u}_{\bar{y}}) = -P_{\bar{x}} + \mu_{hnf}(\bar{u}_{\bar{x}\bar{x}} + \bar{u}_{\bar{y}\bar{y}}) - \sigma B_0 \bar{u}. \quad (2.2)$$

$$\rho_{hnf}(\bar{v}_t + \bar{u}\bar{v}_{\bar{x}} + \bar{v}\bar{v}_{\bar{y}}) = -P_{\bar{y}} + \mu_{hnf}(\bar{v}_{\bar{x}\bar{x}} + \bar{v}_{\bar{y}\bar{y}}) - \sigma B_0 \bar{v}. \quad (2.3)$$

Fig. 1 Flow geometry of the problem



$$\begin{aligned}
 (\rho C_p)_{hnf} (T_t + \bar{u}T_{\bar{x}} + \bar{v}T_{\bar{y}}) &= k_{hnf} (T_{\bar{x}\bar{x}} + T_{\bar{y}\bar{y}}) + \sigma B_0 \bar{u}^2 \\
 &+ \mu_{hnf} (2(\bar{u}_{\bar{x}})^2 + 2(\bar{v}_{\bar{y}})^2 + (\bar{u}_{\bar{y}} + \bar{v}_{\bar{x}})) - q_{rd\bar{y}} \quad . \quad (2.4)
 \end{aligned}$$

Along with boundary conditions, [35]

$$\bar{u} = 0, \bar{v} = -v_w = \Lambda \dot{b}, T(\bar{x}, \bar{y}) = T_2 at \bar{y} = b(t),$$

$$\bar{u} = 0, \bar{v} = 0, T(\bar{x}, \bar{y}) = T_1 at \bar{y} = 0. \quad (2.5)$$

\bar{u} and \bar{v} are the dimensional velocity components in the x and y directions, respectively. σ_{hnf} denotes the hybrid nanofluid’s electrical conductivity, ρ_{hnf} is its density, μ_{hnf} denotes dynamic viscosity, $(\rho C_p)_{hnf}$ its heat capacitance k_{hnf} represents effective thermal conductivity and $\Lambda = \frac{\bar{v}_w}{b}$ depicts the wall permeability. For radiation, using the Rosseland approximation, we have

$$q_{rd} = \frac{\sigma^*}{3k_{hnf}^*} \frac{\partial T^4}{\partial y}.$$

Here, k_{hnf}^* represents the average absorption coefficient of a hybrid nanofluid and σ^* is a well-known Stefan-Boltzmann constant. Expanding T^4 up to T_∞ in the Taylor series and neglecting the higher terms.

$$T^4 = 4T_\infty^3 T - 3T_\infty^4.$$

Introducing the stream function

$$\bar{\psi} = \frac{v\bar{x}}{b}\bar{F}(\eta, t), \bar{u} = \frac{v\bar{x}}{b^2}\bar{F}_\eta \text{ and } \bar{v} = -\frac{v}{b}\bar{F}, \tag{2.6}$$

where $\eta = \frac{y}{b}$.

Now, replacing \bar{u} and \bar{v} from Eq. (2.6) in Eq. (2.3) and Eq. (2.2), and eliminating the pressure term, the result is as follows.

$$\bar{F}_{\eta\eta\eta\eta} + \frac{A_1}{A_2}((\alpha\eta + \bar{F})\bar{F}_{\eta\eta\eta} + (3\alpha - \bar{F}_\eta)\bar{F}_{\eta\eta}) - \frac{A_1}{A_2}b^2v_f^{-1}\bar{F}_{\eta\eta t} - \frac{A_5}{A_2}M^2\bar{F}_{\eta\eta} = 0. \tag{2.7}$$

Along with boundary conditions

$$\bar{F}(0) = \bar{F}_\eta(0) = 0, \bar{F}_\eta(1) = 0 \text{ and } \bar{F}(1) = \frac{A_1}{A_2}Re \tag{2.8}$$

Here, A_1, A_2 and A_3 are fixed ratios that are defined as

$$A_1 = \frac{\rho_{hnf}}{\rho_f}, A_2 = \frac{\mu_{hnf}}{\mu_f}, A_5 = \frac{\sigma_{hnf}}{\sigma_f} \tag{2.9}$$

Reynold's number is given as $= \frac{bv_w}{\nu}$. A similar solution can be established with respect to both time and space by the transformation defined by Majdalani et al. [36]. This can be achieved by choosing α as static and $F = F(\eta)$, which leads to $F_{\eta\eta t} = 0$. The expansion ratio must be provided by its initial value to understand this condition.

$$\alpha = \frac{b\dot{b}}{\nu_f} = \frac{b_0\dot{b}_0}{\nu_f}, \tag{2.10}$$

where b_0 and \dot{b}_0 denote the initial channel height and the channel's growth ratio, respectively. Now by integrating Eq. (2.10) w.r.t time, we get

$$\frac{b}{b_0} = \sqrt{1 + 2\nu_f\alpha t b_0^{-2}}, \tag{2.11}$$

$v_w = \Lambda\dot{b}$ by supplying Λ as a constant injection coefficient for the physical circumstance identifies the injection velocity variation. From Eq. (2.10) and Eq. (2.11), it is clear that (Tables 1, 2).

$$\frac{b}{b_0} = \frac{v_w(t)}{v(t)} = \sqrt{1 + 2\nu_f\alpha t b_0^{-2}}. \tag{2.12}$$

Table 1 Thermophysical properties of the base fluid and nanomaterials

	Water (H_2O)	Copper (Cu)	Silver (Ag)	Alumina
ρ/kgm^{-3}	997.1	8933	10,500	3970
$C_p/Jkg^{-1} K^{-1}$	4179	386	235	765
$k/Wm^{-1} K^{-1}$	0.613	401	429	40
$\sigma/\omega m^{-1}$	$0.0510^{-10} 6.3 * 10^7 10^{-12}$			

Table 2 Mathematical representation of the physical quantities of hybrid nanofluids

Viscosity	$\mu_{hnf} = \mu_f / (1 - \phi_1 - \phi_2)^{2.5}$
Heat capacitance	$(\rho C_p)_{hnf} = (1 - \phi_1 - \phi_2)(\rho C_p)_f + \phi_1(\rho C_p)_1 + \phi_2(\rho C_p)_2$
Density	$\rho_{hnf} = (1 - \phi_1 - \phi_2)\rho_f + \phi_1\rho_1 + \phi_2\rho_2$
Heat conductivity	$\frac{k_{hnf}}{k_f} = \begin{cases} \frac{k_1\phi_1 + k_2\phi_2}{(\phi_1 + \phi_2)} + 2k_f + 2(k_1\phi_1 + k_2\phi_2) - 2(\phi_1 + \phi_2)k_f \} \\ \frac{k_1\phi_1 + k_2\phi_2}{(\phi_1 + \phi_2)} + 2k_f - 2(k_1\phi_1 + k_2\phi_2) - 2(\phi_1 + \phi_2)k_f \} \end{cases}$

According to the said assumptions, Eq. (2.7) becomes

$$\bar{F}_{\eta\eta\eta\eta} + \frac{A_1}{A_2}((\alpha\eta + \bar{F})\bar{F}_{\eta\eta\eta} + (3\alpha - \bar{F}_\eta)\bar{F}_{\eta\eta}) - \frac{A_5}{A_2}M^2\bar{F}_{\eta\eta} = 0. \tag{2.13}$$

Along with BCs

$$\bar{F}(0) = 0, \bar{F}(1) = 1, \bar{F}_\eta(0) = 0 \text{ and } \bar{F}_\eta(1) = 0 \tag{2.14}$$

The fluid’s temperature can be stated as [37]

$$T(\bar{x}, \eta) = T_1 + \frac{\mu_f v_w}{\rho b C_p} \left[f(\eta) + \frac{\bar{x}^2}{b^2} g(\eta) \right]. \tag{2.15}$$

The temperature in non-dimensional form using Eq. (2.15) can be obtained as [38]

$$\theta = \frac{T - T_1}{T_2 - T_1} = Ec(f + x^2g), \tag{2.16}$$

where Ec denotes the Eckert number and is given as $= \frac{\mu_f v_w}{(\rho b C_p)(T_2 - T_1)}$.

Now, introducing the normalized parameters [38]

$$\begin{aligned} \bar{\psi} &= \psi b v_w, \bar{u} = u v_w, \bar{v} = v v_w, \bar{x} = x b(t) \\ \bar{y} &= y b(t), \bar{F} = F Re, \bar{p} = p \rho v_w^2. \end{aligned} \tag{2.17}$$

From Eq. (2.13), we achieved

$$F_{\eta\eta\eta\eta} + \frac{A_1}{A_2}((\alpha\eta + ReF)F_{\eta\eta\eta} + (3\alpha - ReF_{\eta})F_{\eta\eta}) - \frac{A_5}{A_2}M^2F_{\eta\eta} = 0, \quad (2.18)$$

and the boundary conditions from Eq. (2.14) becomes

$$F(0) = 0, F_{\eta}(0) = 0, F_{\eta}(1) = 0 \text{ and } F(1) = 1. \quad (2.19)$$

Using Eqs. (2.16) and (2.17) in Eq. (2.4), we have

$$A_4Ec(f_{\eta\eta} + x^2g_{\eta\eta}) + A_3Br(\alpha\eta + ReF)(f_{\eta} + x^2g_{\eta}) + A_5BrM^2ReF_{\eta}^2x^2 + A_2BrRe(4F_{\eta}^2 + x^2F_{\eta\eta}^2) + \frac{4}{3}N(f_{\eta\eta} + x^2g_{\eta\eta}), \quad (2.20)$$

where $N = \frac{4\sigma^*T_{\infty}^3}{k_{hnf}^*k_f}$ is the radiation parameter. By comparing the coefficients of terms containing x^2 and without x^2 of Eq. (2.20),

$$A_4Ecf_{\eta\eta} + A_3Br(\alpha\eta + ReF)f_{\eta} + 4A_2BrReF_{\eta}^2 + \frac{4}{3}Nf_{\eta\eta} = 0, \quad (2.21)$$

$$A_4Ecg_{\eta\eta} + A_3Br(\alpha\eta + ReF)g_{\eta} + A_5BrM^2ReF_{\eta}^2 + A_2BrReF_{\eta\eta}^2 + \frac{4}{3}Ng_{\eta\eta} = 0, \quad (2.22)$$

where $M^2 = \frac{\sigma_f B_0^2 \alpha^2}{\mu_f}$, $Pr = \frac{v_f(\rho C_p)}{k_f}$ represents the magnetic parameter and Prandtl Number, respectively. Also,

$Br = Ec.Pr$, while A_3 and A_4 are the fixed ratios such that $A_3 = \frac{(\rho C_p)_{hnf}}{\rho_f}$ and $A_4 = \frac{k_{hnf}}{k_f}$.

In terms of f and g , the boundary conditions from Eq. (2.5) become

$$\left. \begin{aligned} at\eta = 0, f = g = 0 \\ at\eta = 1, f = \frac{1}{Ec}, g = 0 \end{aligned} \right\} \quad (2.23)$$

The dimensionless Nusselt number(Nu) in this situation is given as

$$Nu = -\frac{k_{hnf}}{k_f} \frac{\partial T}{\partial \eta} \frac{1}{(T_2 - T_1)} = -A_4\theta'(0). \quad (2.24)$$

3 Solution of the Problem

Here, the mathematical Eqs. (2.21), (2.22) and (2.18) along with boundary conditions (2.19) and (2.23) are solved with the help of the Homotopy Analysis Method (HAM) [39, 40] by choosing suitable initial guess that satisfy the boundary conditions. The auxiliary linear operators are

$$L_1(F) = F'''' , \tag{3.1}$$

$$L_2(F) = \theta'' . \tag{3.2}$$

The above auxiliary linear operators satisfy the conditions

$$L_1(X_1\eta^3 + X_2\eta^2 + X_3\eta + X_4) = 0, \tag{3.3}$$

$$L_2(X_5\eta + X_6) = 0, \tag{3.4}$$

where $X_i (i = 1, 2, 3, \dots, 6)$ are all constants.

The zeroth order deformation is given as

$$(1 - r)L_1(F(\eta, r) - F_0(r)) = rh_1N_1F(\eta, r), \tag{3.5}$$

$$F(0, r) = 0, F'(0, r) = 0, F(1, r) = 1, F'(1, r) = 0. \tag{3.6}$$

$$(1 - r)L_2(\theta(\eta, r) - \theta_0(r)) = rh_2N_2(F(\eta, r), \theta(\eta, r)), \tag{3.7}$$

$$\theta(0, r) = 0, \theta(1, r) = 1. \tag{3.8}$$

The kth-order deformation is

$$L_1(F_k - x_k F_{k-1}) = h_1 N_1^k, \tag{3.9}$$

$$F_k(0) = 0, \quad F'_k(0) = 0, \quad F'_k(1) = 0, \quad F_k(1) = 1. \tag{3.10}$$

$$L_2(\theta_k - x_k \theta_{k-1}) = h_2 N_2^k, \tag{3.11}$$

$$\theta_k(0) = 0, \theta_k(1) = 1. \tag{3.12}$$

Here,

$$\begin{aligned}
 N_1^k(\eta) = & \frac{\partial F_{k-1}}{\partial \eta^4} + \alpha \left(\eta \frac{\partial^3 F_{k-1}}{\partial \eta^3} + 3 \frac{\partial^2 F_{k-1}}{\partial \eta^2} \right) \\
 & + Re \sum_{m=0}^{k-1} F_{k-m-1} \frac{\partial^3 F_m}{\partial \eta^3} - Re \sum_{m=0}^{k-1} \frac{\partial F_{k-m-1}}{\partial \eta} \frac{\partial^2 F_m}{\partial \eta^2}, \tag{3.13}
 \end{aligned}$$

$$\begin{aligned}
 N_2^k(\eta) = & \left(A_4 + \frac{4}{3Ec} N \right) \frac{\partial^2 \theta_{k-1}}{\partial \eta^2} + A_3 \alpha Pr \eta \frac{\partial \theta_{k-1}}{\partial \eta} \\
 & + A_3 Pr Re. \sum_{m=0}^{k-1} \frac{\partial \theta_{k-m-1}}{\partial \eta} F_m + A_2 Br Re \sum_{m=0}^{k-1} \left(4 \frac{\partial F_{k-m-1}}{\partial \eta} \frac{\partial F_m}{\partial \eta} + x^2 \frac{\partial^2 F_{k-m-1}}{\partial \eta^2} \frac{\partial^2 F_m}{\partial \eta^2} \right) \\
 & + A_5 Br Re Mx^2 \left(\frac{\partial F_{k-m-1}}{\partial \eta} \frac{\partial F_m}{\partial \eta} \right) \tag{3.14}
 \end{aligned}$$

The general solutions to the problem are

$$F_k(\eta) = F_\eta^*(\eta) + X_1 + X_2\eta + X_3\eta^2 + X_4\eta^3 \dots, \tag{3.15}$$

$$\theta_k(\eta) = \theta_\eta^*(\eta) + X_5 + X_6\eta \dots, \tag{3.16}$$

For the above two series, the convergence is highly dependent on h1 and h2. By choosing suitable h_1 and h_2 , Eqs. (3.5) and (3.7) are convergent.

So, the solution becomes

$$F = F_0(\eta) + \sum_{m=1}^k F_m(\eta). \tag{3.17}$$

$$\theta = \theta_0(\eta) + \sum_{m=1}^k \theta_m(\eta). \tag{3.18}$$

The differential equations are solved using Mathematica. The first-order solutions of velocity and temperature are given as

$$\begin{aligned}
 F_{\eta}(\eta) = & \frac{1}{A_2} \eta^2 (-2A_2 \\
 & + h_1(A_5 M^2(0.2 - 0.5\eta + 0.3\eta^2) \\
 & + A_1(Re(0.385714 - 0.9\eta^2 + 0.8\eta^3 - 0.285714\eta^4) + (-0.3 + 1.5\eta - 1.2\eta^2)\alpha)) \\
 & + \frac{1}{A_2} 2\eta(A_2(3 - 2\eta) \\
 & + h_1(A_5 M^2(-0.05 + 0.2\eta - 0.25\eta^2 + 0.1\eta^3) \\
 & + A_1(Re(-0.228571 + 0.385714\eta - 0.3\eta^3 + 0.2\eta^4 - 0.0571429\eta^5) \\
 & + (-0.05 - 0.3\eta + 0.76\eta^2 - 0.4\eta^3)\alpha)). \}
 \end{aligned}
 \tag{3.19}$$

$$\begin{aligned}
 \theta(\eta) = & \eta(2 - 0.15A_3h_2Re - 1\eta + 0.25A_3h_2Re\eta^3 - 0.1A_3h_2Re\eta^4 \\
 & + A_2h_2Re(-2.4 + 12\eta^3 - 14.4\eta^4 + 4.8\eta^5) \\
 & - 0.16666666666666666A_3h_2\alpha + 0.16666666666666666A_3h_2\alpha\eta^2 \\
 & + h_3(1.3333333333333333 + 0.01666666666666666A_3Re - 0.6A_5MRe \\
 & + A_4(1 - \eta) - 1.333333333333333\eta + 0.25A_3Re\eta^3 + 3A_5MRe\eta^3 \\
 & - 0.4A_3Re\eta^4 - 3.6A_5MRe\eta^4 + 0.1333333333333333A_3Re\eta^5 \\
 & + 1.2A_5MRe\eta^5 \\
 & + A_2Re(-6 + 18\eta - 24\eta^2 + 12\eta^3 + 0.16666666666666666A_3M\eta^2\alpha \\
 & - 0.16666666666666666A_3\eta^3\alpha)) + 0.14444444444444444A_3Reh_2\alpha \\
 & + 0.13333333333333333A_3h_2\eta^2\alpha - 0.15555555555555555A_3h_2\alpha \\
 & + 0.16666666666666666A_3h_2Re\eta^3 \\
 & + A_1h_2Re(-03.4\eta + 14\eta^3 - 12.455\eta^4 + 4.99\eta^5) \\
 & - (2 - 0.1111A_3h_2Re - 1\eta + 0.7777A_3Re\eta^3 - 0.13333A_3\eta^4 \\
 & + (A_4(1 - \eta) - 1.444444\eta^2 + 0.21111A_3Re\eta^3 + 3A_5MRe\eta^3 \\
 & - (1.5555555555555555A_1\eta^2\alpha - 0.17777777777777777A_3\eta^3\alpha) + 1.6666A_5M\eta^5 \\
 & + A_2Re(11\eta - 21\eta^2 + 13\eta^3) + 0.188888).
 \end{aligned}
 \tag{3.20}$$

4 Response Surface Methodology

In many experimental and computational efforts, statistical-mathematical experimental design is an important component. The RSM approach associates one or more input variables with the response variables. Additionally, it is employed for optimization. RSM examines the impacts of different variables on the responses.

Table 3 Design input factors and their levels

		Levels		
Input parameters	Symbol	-1	0	1
M	A	0	3	6
N	B	0	0.5	1
A	C	0	0.45	0.9
Ec	D	0	0.5	1

Response surface methodology (RSM) heavily depends on the capacity to create an accurate approximation for the output function. In this communication, M , N , α and Ec are the input parameters, that are symbolically denoted by A, B, C and D, respectively, and the Nusselt number is the response variable. Defining a correlation between the independent (coded) variables (A, B, C, D) and the target response(Nu) is based on the general second-order equation, that is given as

$$Nu = \lambda_0 + \lambda_1 A + \lambda_2 B + \lambda_3 C + \lambda_4 D + \lambda_{11} A^2 + \lambda_{22} B^2 + \lambda_{33} C^2 + \lambda_{44} D^2 + \lambda_{12} AB + \lambda_{13} AC + \lambda_{14} AD + \lambda_{23} BC + \lambda_{24} BD + \lambda_{34} CD \tag{4.1}$$

Here, λ_i and λ_{ij} are the unknown constant coefficients, which can be found through RSM. A central composite design(CCD) technique introduced by Box and Wilson [42] was utilized to carry out computational or numerical experiment. The Nusselt number is based on four independent input variables that are denoted by the letters A, B, C and D. 31 runs along with 30 degrees of freedom(DOF) are optimal for choosing three stages of variables, i.e. low, medium and high (-1, 0, 1). Table 3 contains the independent input variables with their respective mathematical symbols(A, B,C, D) and the three levels(1, 0, 1). The experimental design and the output response(Nu) for both lower and upper plates are tabulated in Tables 4 and 5, respectively.

5 Parametric Analysis

In this section, the behaviour of the temperature profile and Nusselt number of hybrid nanoliquid flow through two parallel and squeezing plates are discussed through the Homotopy analysis method (HAM). The MHD and thermal radiation impacts on the flow are presented graphically.

From Fig. 2, it is noticed that when the magnetic parameter is maximum it produces more Lorentz force, which causes the resistance in ow. As a result, the temperature distribution becomes high. The temperature distribution becomes high. The temperature profile is a decreasing function of the radiation parameter, as indicated in Fig. 3. The results are compared with the works done by Dogonchi et al. [41]. Figures 4 and 5 show the impacts of the magnetic parameter and radiation parameter on the Nusselt number with respect to Reynold number respectively. Figure 4 indicates that

Table 4 Experimental design and response results for Nu_x at lower plate

Runs	Coded values				Real values				Responses
	A	B	C	D	M	N	α	Ec	
1	-1	-1	-1	-1	0	0	0	0	-1.40725
2	1	-1	-1	-1	6	0	0	0	-1.40764
3	-1	0	-1	-1	0	1	0	0	-1.3924
4	1	1	-1	-1	6	1	0	0	-1.39262
5	-1	-1	1	-1	0	0	0.9	0	-1.6902
6	1	-1	1	-1	6	0	0.9	0	-1.69031
7	-1	1	1	-1	0	1	0.9	0	-1.52597
8	1	1	1	-1	6	1	0.9	0	-1.52591
9	-1	-1	-1	1	0	0	0	1	-2.33573
10	1	-1	-1	1	6	0	0	1	-2.77069
11	-1	1	-1	1	0	1	0	1	-1.77957
12	1	1	-1	1	6	1	0	1	-2.06666
13	-1	-1	1	1	0	0	0.9	1	-2.53049
14	1	-1	1	1	6	0	0.9	1	-2.91774
15	-1	1	1	1	0	1	0.9	1	-1.88585
16	1	1	1	1	6	1	0.9	1	-2.11705
17	-1	0	0	0	0	0.5	0.45	0.5	-1.95374
18	1	0	0	0	6	0.5	0.45	0.5	-2.16189
19	0	-1	0	0	3	0	0.45	0.5	-2.53181
20	0	1	0	0	3	1	0.45	0.5	-1.83116
21	0	0	-1	0	3	0.5	0	0.5	-1.97166
22	0	0	1	0	3	0.5	0.9	0.5	-2.13281
23	0	0	0	-1	3	0.5	0.45	0	-1.49709
24	0	0	0	1	3	0.5	0.45	1	-2.21914
25	0	0	0	0	3	0.5	0.45	0.5	-2.05142
26	0	0	0	0	3	0.5	0.45	0.5	-2.05142
27	0	0	0	0	3	0.5	0.45	0.5	-2.05142
28	0	0	0	0	3	0.5	0.45	0.5	-2.05142
29	0	0	0	0	3	0.5	0.45	0.5	-2.05142
30	0	0	0	0	3	0.5	0.45	0.5	-2.05142
31	0	0	0	0	3	0.5	0.45	0.5	-2.05142

Table 5 Experimental design and response results for Nu_x at upper plate

Runs	Coded values				Real values				Responses
	A	B	C	D	M	N	α	Ec	
1	-1	-1	-1	-1	0	0	0	0	-1.31407
2	1	-1	-1	-1	6	0	0	0	-1.31453
3	-1	0	-1	-1	0	1	0	0	-1.34849
4	1	1	-1	-1	6	1	0	0	-1.34878
5	-1	-1	1	-1	0	0	0.9	0	-0.789908
6	1	-1	1	-1	6	0	0.9	0	-0.790672
7	-1	1	1	-1	0	1	0.9	0	-1.1039
8	1	1	1	-1	6	1	0.9	0	-1.10449
9	-1	-1	-1	1	0	0	0	1	-0.42691
10	1	-1	-1	1	6	0	0	1	0.0111688
11	-1	1	-1	1	0	1	0	1	-0.982244
12	1	1	-1	1	6	1	0	1	-0.686116
13	-1	-1	1	1	0	0	0.9	1	-0.315362
14	1	-1	1	1	6	0	0.9	1	0.107263
15	-1	1	1	1	0	1	0.9	1	-0.931901
16	1	1	1	1	6	1	0.9	1	-0.609333
17	-1	0	0	0	0	0.5	0.45	0.5	-0.788056
18	1	0	0	0	6	0.5	0.45	0.5	-0.570774
19	0	-1	0	0	3	0	0.45	0.5	-0.225666
20	0	1	0	0	3	1	0.45	0.5	-0.910278
21	0	0	-1	0	3	0.5	0	0.5	-0.781081
22	0	0	1	0	3	0.5	0.9	0.5	-0.613298
23	0	0	0	-1	3	0.5	0.45	0	-1.147
24	0	0	0	1	3	0.5	0.45	1	-0.558112
25	0	0	0	0	3	0.5	0.45	0.5	-0.693817
26	0	0	0	0	3	0.5	0.45	0.5	-0.693817
27	0	0	0	0	3	0.5	0.45	0.5	-0.693817
28	0	0	0	0	3	0.5	0.45	0.5	-0.693817
29	0	0	0	0	3	0.5	0.45	0.5	-0.693817
30	0	0	0	0	3	0.5	0.45	0.5	-0.693817
31	0	0	0	0	3	0.5	0.45	0.5	-0.693817

Fig. 2 Impact of M on temperature distribution (θ) when $Re = \alpha = Ec = 1$, and $Br = 0.1$

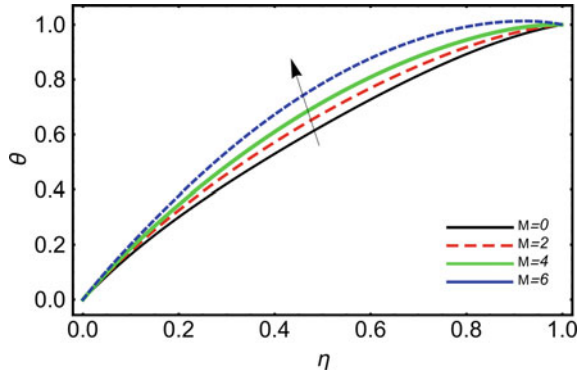
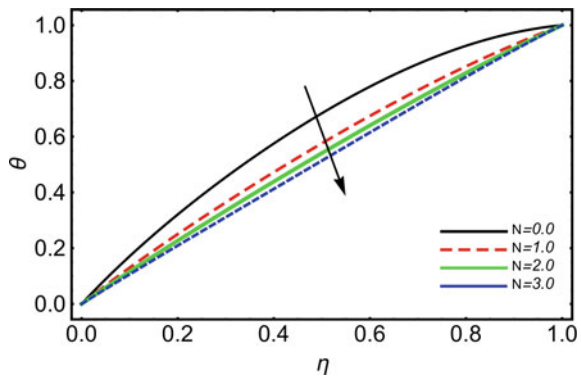


Fig. 3 Impact of radiation parameter (N) on θ when $Re = \alpha = Ec = 1$ and $Br = 0.1$



the Nusselt number rises at the upper wall and falls at the lower wall. It is because, at the lower wall, the velocity of the fluid layer relative to the solid surface is zero. In this case, the heat transfer rate by convection is dominated by conduction. Figure 5 shows that at the lower wall, the Nusselt number becomes high by increasing the radiation parameter. But at the upper wall, the increasing radiation parameter has an opposite effect on the Nusselt number.

6 Analysis of Variance (ANOVA)

Analysis of variance (ANOVA) is the set of statistical models and the associated estimating techniques that are used to study how different means differ from each other. It is a method of statistical analysis in which the significance of data collection is assessed through comparison and measurement. ANOVA indicates which equation components in correlations should be retained. In order to access the regression model's fit, we used statistical software (MINITAB-19) and the sequential f-test

Fig. 4 Effect of M on Nusselt number (Nu): upper plate “a” and lower plate “b” when $\alpha = 1, Br = 1, Ec = 0.1$ and $\phi_1 = \phi_2 = 0.04$

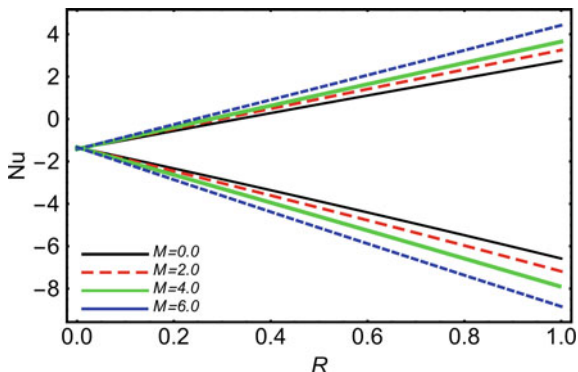
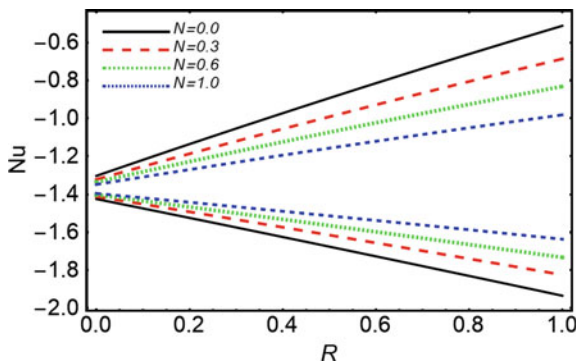


Fig. 5 Impact of N on Nusselt number (Nu): upper plate “a” and lower plate “b” when $\alpha = 0.5, Br/A = 0.1, Ec = 0.01$ and $\phi_1 = \phi_2 = 0.04$



with 31 runs. The results are shown in Tables 6 and 7 for both lower and upper plates, respectively.

An individual F-value and P-value are assigned to each term in the Eq. (4.1). The accuracy of the model can be measured through the P value, while the F-value measures the range of values around the average value. For higher F-values, the outcome is labelled as more significant, and for lower P-values (≤ 0.05), the result’s significance is more stable. When the F-value is close to one, it means that there is little to no variation in the data, indicating that the variation between groups is not statistically significant. The goodness-of-fit of the RSM model is thoroughly explained by the values of R-squared and adjusted R-squared. The values of R-squared(R^2) and adjusted R-squared ($Adj-R^2$) for the response variable, Nusselt number, at both lower and upper plates are presented in Tables 8 and 9, respectively. Tables 8 and 9 make it evident that R^2 and $Adj-R^2$ have high values ($R^2 = 98.75\%$, $Adj-R^2 = 97.66\%$ for the lower plate, and $R^2 = 98.49\%$, $Adj-R^2 = 97.16\%$ for upper plate), predicting the perfect correlation between the independent input variables (A, B, C, and D) and the output response(Nu_x).

Table 6 ANOVA analysis for Nusselt number at lower plate

Source <i>Nu_x</i>	DOF	Adj SS	Adj MS	F-Value	P-Value	Significance
Model	14	3.83691	0.27406	74.38	0.000	Significant
Linear	4	3.17929	0.79482	215.70	0.000	Significant
A	1	0.13335	0.13335	36.87	0.000	Significant
B	1	0.78737	0.78737	217.68	0.000	Significant
C	1	0.12369	0.12369	34.20	0.000	Significant
D	1	2.79545	2.79545	772.83	0.000	Significant
Square	4	0.17781	0.04445	12.06	0.000	Significant
<i>A</i> ²	1	0.00098	0.00098	0.27	0.610	Insignificant
<i>B</i> ²	1	0.02820	0.02820	7.80	0.013	Significant
<i>C</i> ²	1	0.00162	0.00162	0.45	0.512	Insignificant
<i>D</i> ²	1	0.12462	0.12462	34.45	0.000	Significant
Interaction	6	0.47981	0.07997	21.70	0.000	Significant
AB	1	0.00579	0.00579	1.60	0.224	Insignificant
AC	1	0.00068	0.00068	0.19	0.671	Insignificant
AD	1	0.11220	0.11220	31.02	0.000	Significant
BC	1	0.01463	0.01463	4.05	0.061	Insignificant
BD	1	0.34428	0.34428	95.18	0.000	Significant
CD	1	0.00697	0.00697	1.93	0.184	Insignificant
Error	16	0.05896	0.00368	–	–	–
Lack of Fit	10	0.05896	0.00590	–	–	–
Pure Error	6	0.00000	0.00000	–	–	–
Total	30	3.89587	–	–	–	–

7 Sensitivity Analysis

Sensitivity analysis is a technique for forecasting how a decision will turn out if the situation differs from the main hypotheses. The degree of change brought about by the parameters is measured by the sensitivity of a response variable. It aids in determining the degree to which an output depends on a specific input value. When the sensitivity is positive or negative, the parameters and the response variables are said to be positively or negatively correlated, respectively. The Nusselt number stated in Eq. 4.1 in terms of the coded variables for both lower and upper plates is then reduced to

$$\begin{aligned}
 Nu_x = & -2.0633 - 0.0861A + 0.2091B - 0.0829C - 0.3941D - 0.1042B^2 \\
 & + 0.2191D^2 - 0.0837AD + 0.1467BD
 \end{aligned}
 \tag{7.1}$$

Table 7 ANOVA analysis for Nusselt number at upper plate

Source Nu_x	DOF	Adj SS	Adj MS	F-Value	P-Value	Significance
Model	14	4.58508	0.32751	90.54	0.000	Significant
Linear	4	3.83987	0.95997	265.39	0.000	Significant
A	1	0.15953	0.15953	43.29	0.000	Significant
B	1	0.87421	0.87421	237.24	0.000	Significant
C	1	0.23108	0.23108	62.71	0.000	Significant
D	1	1.91446	1.91446	519.55	0.000	Significant
Square	4	0.26066	0.06516	18.02	0.000	Significant
A^2	1	0.00035	0.00035	0.09	0.763	Insignificant
B^2	1	0.02589	0.02589	7.03	0.017	Significant
C^2	1	0.00223	0.00223	0.61	0.448	Insignificant
D^2	1	0.08853	0.08853	24.02	0.000	Significant
Interaction	6	0.48455	0.08076	22.33	0.000	Significant
AB	1	0.00365	0.00365	0.99	0.334	Insignificant
AC	1	0.00001	0.00001	0.00	0.966	Insignificant
AD	1	0.13718	0.13718	37.23	0.000	Significant
BC	1	0.02557	0.02557	6.94	0.018	Significant
BD	1	0.22308	0.22308	60.54	0.000	Significant
CD	1	0.09032	0.09032	24.51	0.000	Significant
Error	16	0.05787	0.00362	–	–	–
Lack of Fit	10	0.05787	0.00579	–	–	–
Pure Error	6	0.00000	0.00000	–	–	–
Total	30	4.64296	–	–	–	–

$$Nu_x = -0.6818 + 0.0941A - 0.2204B + 0.1133C + 0.3261D + 0.0999B^2 - 0.1847D^2 + 0.0926AD - 0.04BC - 0.1181BD - 0.0751CD. \quad (7.2)$$

The sensitivity functions of Nusselt number to the independent input variables (A, B, C and D) for both lower and upper plates are can be obtained from the Eqs. 7.1 and 7.2, which are given by the equations from Eqs. 7.3 to 7.10. For lower plate

$$\frac{\partial Nu}{\partial A} = -0.0861 - 0.0837D. \quad (7.3)$$

$$\frac{\partial Nu}{\partial B} = 0.2091 - 0.2084B + 0.1467D. \quad (7.4)$$

$$\frac{\partial Nu}{\partial C} = -0.0829. \quad (7.5)$$

Table 8 Estimated Regression co-efficient for Nu_x at lower plate

Term	Co-efficient	P-value	Significance
Constant	-2.0633	0.000	Significant
A	-0.0861	0.000	Significant
B	0.2091	0.000	Significant
C	-0.0829	0.000	Significant
D	-0.3941	0.000	Significant
A^2	0.0194	0.610	Insignificant
B^2	-0.1042	0.013	Significant
C^2	0.0250	0.512	Insignificant
D^2	0.2191	0.000	Significant
AB	0.01901	0.224	Insignificant
AC	0.0065	0.671	Insignificant
AD	-0.0837	0.000	Significant
BC	0.0302	0.061	Insignificant
BD	0.1467	0.000	Significant
CD	0.0209	0.184	Insignificant
	$R^2 = 98.75\%$	$Adj R^2 = 97.66\%$	

Table 9 Estimated Regression co-efficient for Nu_x at the upper plate

Term	Co-efficient	P-value	Significance
Constant	-0.6818	0	Significant
A	0.0941	0	Significant
B	-0.2204	0	Significant
C	0.1133	0	Significant
D	0.3261	0	Significant
A^2	-0.0116	0.763	Insignificant
B^2	0.0999	0.017	Significant
C^2	-0.0293	0.448	Insignificant
D^2	-0.1847	0	Significant
AB	-0.0151	0.334	Insignificant
AC	0.0006	0.966	Insignificant
AD	0.0926	0	Significant
BC	-0.04	0.018	Significant
BD	-0.1181	0	Significant
CD	-0.0751	0	Significant
	$R^2 = 98.49\%$	$Adj R^2 = 97.16\%$	

$$\frac{\partial Nu}{\partial D} = -0.3941 - 0.0837A + 0.1467B + 0.4382D. \tag{7.6}$$

For upper plate.

$$\frac{\partial Nu}{\partial A} = 0.0941 + 0.0926D. \tag{7.7}$$

$$\frac{\partial Nu}{\partial B} = -0.2204 + 0.1998B - 0.04C - 0.1181D. \tag{7.8}$$

$$\frac{\partial Nu}{\partial C} = 0.1133 - 0.04B - 0.0751C. \tag{7.9}$$

$$\frac{\partial Nu}{\partial D} = 0.3261 + 0.0926A - 0.1181B - 0.0751C - 0.3694D. \tag{7.10}$$

The regression coefficients for the Nusselt number at both the lower and upper plates are presented in Tables 10 and 11, respectively. The higher value is statistically insignificant. The greater p-value is statistically in significant, so the change in the input will have no impact on the output. So, the terms having a greater p-value (> 0.05) are removed from the model. From Table 8, the terms A, B, C, D, B², D², AD and BD are the significant terms for the Nusselt number at the lower plate. The significant terms for the Nusselt number at the upper plate are A, B, C, D, B², D², AD, BC, BD and CD, which are presented in Table 9. The heat transfer sensitivity toward the different parameters at low levels of C and medium levels of D is tabulated in Tables 10 and 11 for both the lower and upper plates, respectively. From Table 10, it can be seen that the sensitivity towards A and C is constant for all the levels of A and B. The sensitivity towards B decreases, whereas the sensitivity towards D increases as B is incremented from a low level to a high level.

Table 10 Sensitivity analysis of *Nux* at the lower plate when C = -1 and D = 0

A	B	$\frac{\partial Nu_x}{\partial A}$	$\frac{\partial Nu_x}{\partial B}$	$\frac{\partial Nu_x}{\partial C}$	$\frac{\partial Nu_x}{\partial D}$
	-1	-0.12795	0.3558	-0.0829	-0.17500
-1	0	-0.12795	0.2516	-0.0829	-0.10165
	1	-0.12795	0.1474	-0.0829	-0.02830
	-1	-0.12795	0.2516	-0.0829	-0.42610
0	0	-0.12795	0.2516	-0.0829	-0.35275
	1	-0.12795	0.1474	-0.0829	-0.27940
	-1	-0.12795	0.3558	-0.0829	-0.67720
1	0	-0.12795	0.2516	-0.0829	-0.60385
	1	-0.12795	0.1474	-0.0829	-0.53050

Table 11 Sensitivity analysis of Nux at the upper plate when $C = -1$ and $D = 0$

A	B	$\frac{\partial Nux}{\partial A}$	$\frac{\partial Nux}{\partial B}$	$\frac{\partial Nux}{\partial C}$	$\frac{\partial Nux}{\partial D}$
	-1	0.1404	-0.27945	0.07575	0.1414
-1	0	0.1404	-0.17955	0.05575	0.08235
	1	0.1404	-0.07965	0.03575	0.0233
	-1	0.1404	-0.27945	0.07575	0.4192
0	0	0.1404	-0.17955	0.05575	0.36015
	1	0.1404	-0.07965	0.03575	0.3011
	-1	0.1404	-0.27945	0.07575	0.6970
1	0	0.1404	-0.17955	0.05575	0.0.63795
	1	0.1404	-0.07965	0.03575	0.57890

The sensitivity at the upper plate is discussed in Table 11. It is observed that the sensitivity towards A is constant. Columns 4 and 5 of Table 11, respectively, show that as the level of B increases, the sensitivity towards B is increasing while decreasing towards C, but there is no change with respect to A. The sensitivity towards D is an increasing function of the parameter A but decreases with respect to B (Figs. 10, 11).

The residuals and lack-of-fit must be taken into account when talking about sensitivity. The distinction between any data point and the regression line is referred to as a residual, or residual error. Error in this instance simply refers to an unexplained discrepancy; it does not imply that the analysis is flawed. When the model is unable to accurately depict the connectedness between the input parameters and the output response, there is a lack of fit. The residual plots shown in Figs. 6 and 7 indicate that the histograms are less skewed and more similar to a symmetrical distribution. The observed and fitted values exhibit a significant correlation when the residual diagrams are contrasted with the fitted values. For the Nusselt number at the lower plate, it has been found from Fig. 6 that the largest residuals of all the outputs lie in the region between -0.03 and + 0.06. On the upper plate, the largest residuals are found in the region between -1.35 and + 0.2. Figures 6b and 7b make it evident that the probability plots are in good agreement because, as the observation order is incremented, the residuals of the Nusselt number for both plates diminish. Moreover, it exhibits the best connection between observed values and fitted values.

Positive sensitivity values imply that increasing independent input variables results in an increased output response. While the negative sensitivity means that increasing independent input variables results in a decreased output response. The sensitivity plots for Nusselt number at both lower and upper plates are presented in Figs. 8a and 9a to c respectively.

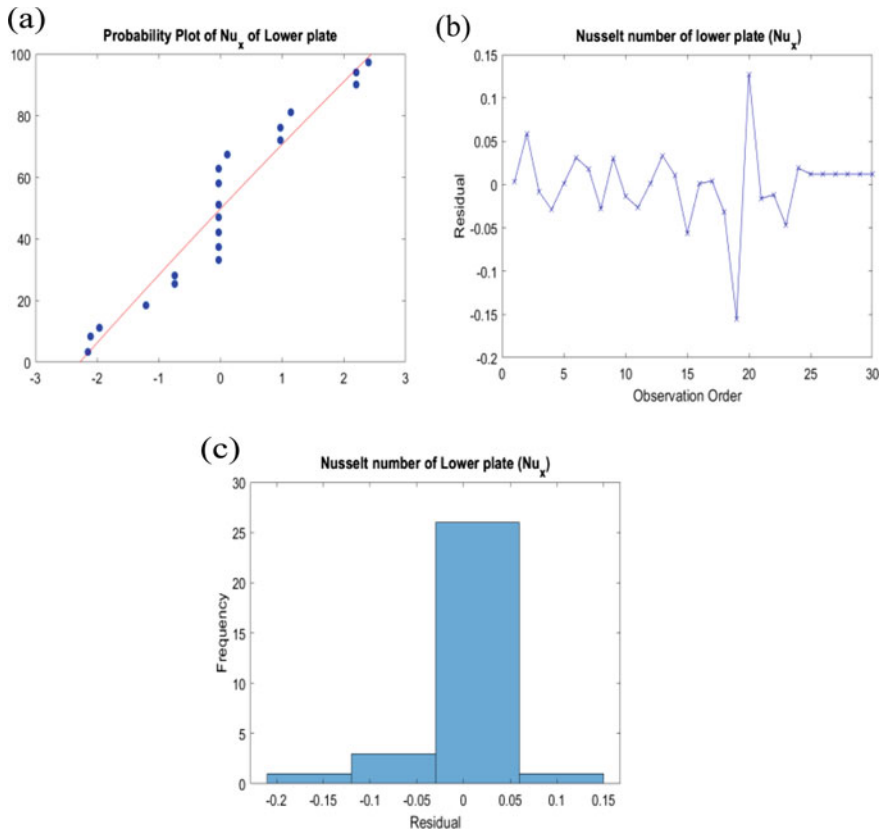


Fig. 6 Residual plots for Nusselt at the lower plate

8 Concluding Remarks

In this chapter, radiative heat transport and hybrid-nanofluid flow between two parallel plates (the lower plate is stationary while the upper plate contracts or expands at the rate $b(t)$ in the presence of MHD) are discussed. The given partial differential equations that govern the flow problem are transformed by the similarity transformation into ODEs. The transformed ODEs are solved analytically through HAM. The numerical solution is then obtained by using the Mathematica package (BVPh 2.0). After that, a sensitivity analysis is performed on the findings to check out how the output responses are dependent on various controlling variables. The following results were obtained:

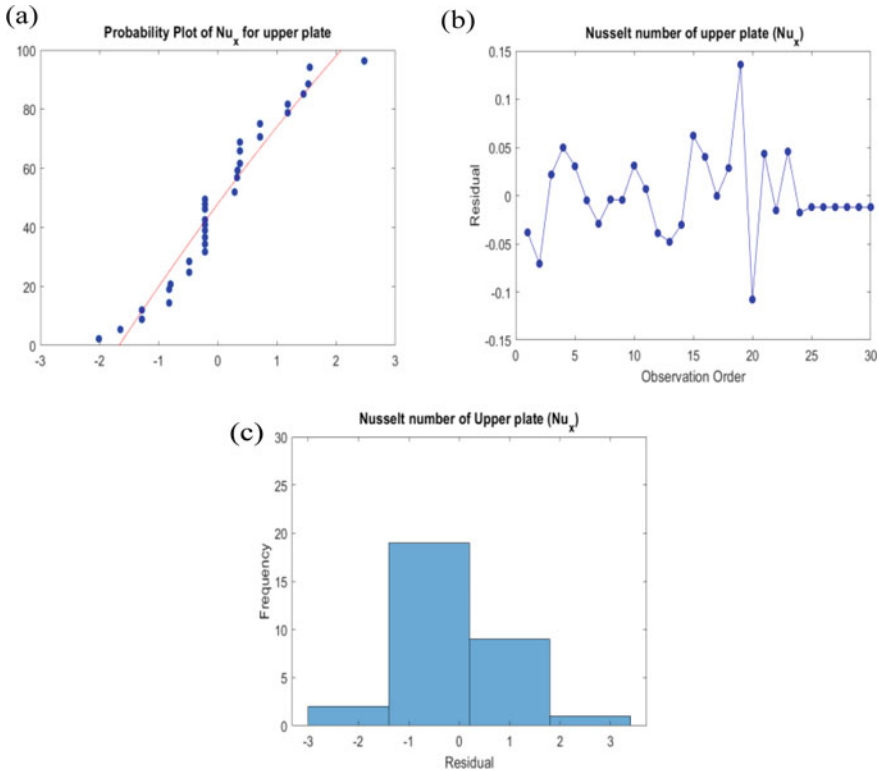


Fig. 7 Residual plots for Nusselt at the upper plate

- The large values of R^2 and $Adj-R^2$ show that the input independent variables have a perfect correlation with the output responses.
- For the Nusselt number at the lower plate, it has been found from Figure A that the largest residuals of all the outputs lie in the region between
- -0.03 and $+0.06$. While the largest residuals for the upper plate are found in the range of -1.35 to $+0.2$.
- The negative sensitivity of the Nusselt number towards the magnetic parameter and expansion ratio is constant for all the values of the magnetic and radiation parameters at the heated plate.
- Increasing the radiation parameter results in a decreasing sensitivity of the Nusselt number towards the radiation parameter at the lower plate, and vice versa for the upper plate.

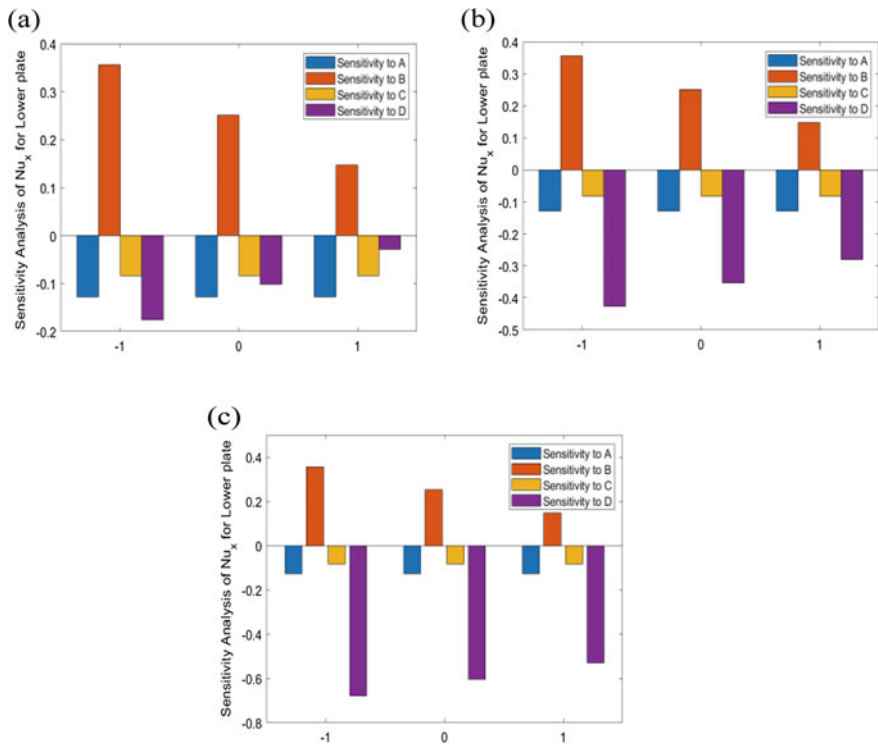


Fig. 8 Sensitivity plots for Nusselt number at lower plate when **a** $A = B = 0$, **b** $A = C = 0$, **c** $A = D = 0$

- The sensitivity of Nu_x to the radiation parameter is constant with respect to the magnetic field strength, while the sensitivity to the radiation parameter is decreasing in the case of the lower plate. The opposite trends are observed for the upper plate.
- With an increase in the magnetic field strength, Nu_x at the upper plate becomes more sensitive but less sensitive to the radiation parameter when the radiation parameter is incremented.

First of all, we discuss the sensitivity of the Nusselt number on the lower plate that is heated externally. The general trend observed from Fig. 8a to c shows that the negative sensitivity of the Nusselt number towards the magnetic parameter and

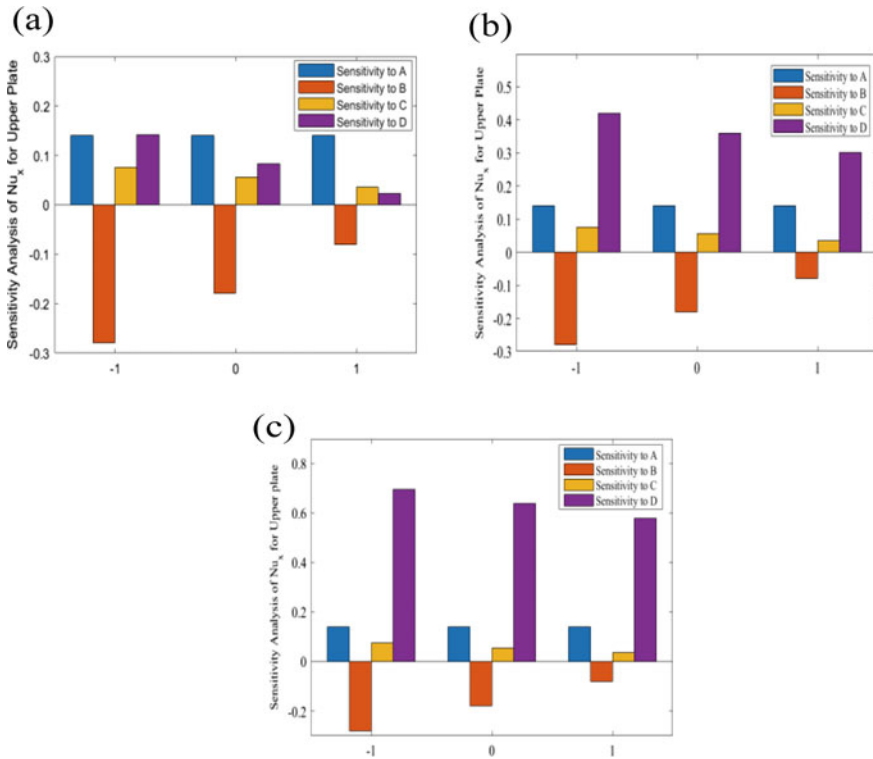


Fig. 9 Sensitivity plots for Nusselt number at the upper plate when **a** $A = B = 0$, **b** $A = C = 0$, **c** $A = D = 0$

expansion ratio is constant for all the values of the magnetic and radiation parameters, while the sensitivity towards the radiation parameter is positive and the sensitivity towards the Eckert number is negative. From Fig. 8a, it can be seen that the sensitivity of the Nusselt number towards the magnetic parameter is constant, but it decreases when the radiation parameter is increased. Figure 8b indicates that the negative sensitivity of the Nusselt number towards the Eckert number increases when the radiation parameter is increased from a low to a high level. Similar trends are observed in Fig. 8c.

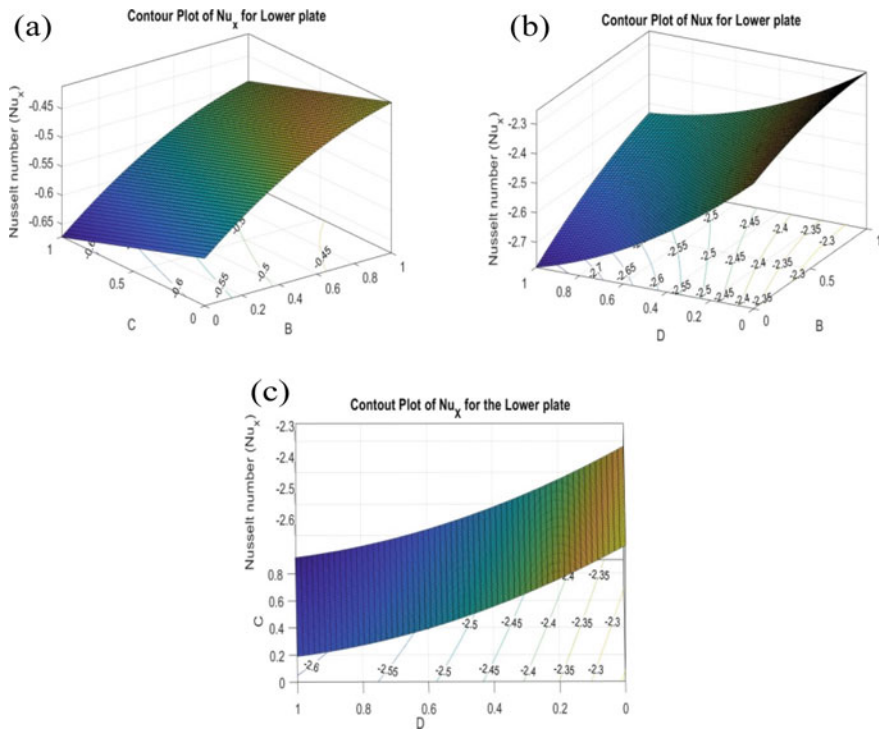


Fig. 10 Contour and 3D surface plots for Nusselt at the lower plate

Now, we will discuss the sensitivity of the Nusselt number on the upper plate. The general trend observed from Fig. 9a to c shows that there is no change in the positive sensitivity of the Nusselt number towards the magnetic parameter at any level of the magnetic and radiation parameters. Figure 9a indicates that the sensitivity towards the radiation parameter is negative and increases with increasing the level of the radiation parameter but is constant with respect to the magnetic parameter. The positive of Nu_x sensitivity towards the Eckert number decreases with increasing radiation parameters but increases with increasing magnetic parameters. Similar patterns may be seen in Fig. 9c.

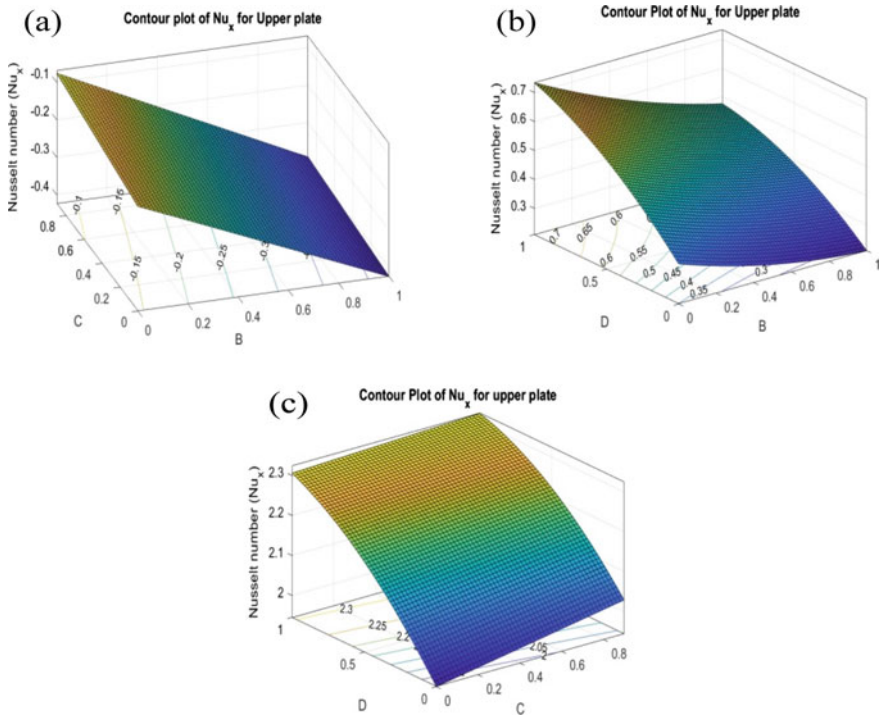


Fig. 11 Contour and 3D surface plots for Nusselt at upper plate

References

1. Rashidi MM, Mahariq I, Nazari MA, Accouche O, Bhatti MM (2022) Comprehensive review on exergy analysis of shell and tube heat exchangers. *J Therm Anal Calorim* 147:12301–12311
2. Choi SU, Eastman JA (1995) Enhancing thermal conductivity of fluids with nanoparticles. Lemont: Argonne National Lab
3. Hamilton RL, Crosser OK (1962) Thermal conductivity of heterogeneous two-components system. *Ind Eng Chem Fundam* 1(3):187–191
4. Xuan Y, Roetzel W (2000) Conceptions for heat transfer correlation of nanofluid. *Int J Heat Mass Transf* 43(19):3701–3707
5. Boungiorno J (2006) Convective transport in nanofluids. *J Heat Mass Transf* 128(3):240–250
6. Sheikholeslami M, Ganji DD, Gorji-Bandpay M (2012) Natural convection heat transfer in a nanofluid filled semi-annulus enclosure. *Int Commun Heat Mass Transf* 39:565–574
7. Bhatti MM, Zeeshan A (2017) Heat and Mass transfer analysis on peristaltic flow of particle-fluid suspension with the slip effects. *J Mech Med Bio.* 17(02):1750028
8. Eastman JA, Choi SUS, Li S, Yu W, Thompson LJ (2001) Anomalous increased effective thermal conductivities of ethylene glycol based nanofluids containing copper nanoparticles. *Appl Phys Lett* 78(6):718–720
9. Majeed A, Rifaqat S, Zeeshan A, Alhodaly MS, Noori FM (2022) Impact of velocity slip and radiative magnetized Casson nanofluid with chemical reaction towards a nonlinear stretching sheet: Three-stage Lobatto collocation scheme. *Int J Moder Phys B.* 5:2350088
10. Sarkar J, Ghosh P, Adil A (2015) A review on hybrid nanofluids: recent research, development and applications. *Renew Sustain Energy Rev* 43:164–177

11. Zeeshan A, Khan I, Weera W, Mohamed A (2022) Heat transfer analysis of Cu and Al₂O₃ dispersed in ethylene glycol as a base fluid over a stretchable permeable sheet of MHD thin-film flow. *Scient Reports*. 12(1):1–4
12. Maskeen MM, Zeeshan A, Mehmood OU, Hassan M (2019) Heat transfer enhancement in hydromagnetic aluminumcopper/water hybrid nanofluid flow over a stretching cylinder. *J Therm Anal Calorim* 138:1127–1136
13. Acharya N, Beg R, Kundo PK (2019) Influence of Hall current on radiative nanofluid flow over a spinning disk: a hybrid approach. *Phys E Low Dimens Syst Nano-struct*. 111:103–112
14. Saqib M, Khan I, Shafie S (2019) Application of fractional differential equations to heat transfer in hybrid nanofluid: modeling and solution via integral transforms. *Adv Differ Equ* 52:1–18
15. Waini I, Ishak A, Pop I (2019) Hybrid nanofluid flow and heat transfer over a non-linear permeable stretching/shrinking surface. *Int J Numer Meth Heat Fluid Flow*. 29(9):3110–3127
16. Hassan M, Marin M, Ellahi R, Alamri SZ Exploration of convective heat transfer and flow characteristics synthesis by CuAg/water hybrid-nanofluids
17. Kakac S, Pramuanjaroenkij A (2009) Review of convective heat transfer enhancement with nanofluids. *Int J Heat Mass Transf* 52:3187–3196
18. Davidson PA (2001) *An Introduction to magneto hydrodynamics*. Cambridge University Press
19. Ellahi R (2013) The effects and temperature dependent viscosity on the flow of non-Newtonian nanofluid in a pipe: Analytical solutions. *Applied Mathematical Model* 37:1451–1467
20. Hayat T, Tasser M, Alsaedi A, Alhuthali MS (2015) Magnetohydrodynamics three-dimensional flow of viscoelastic nanofluid in the presence of nonlinear thermal radiation. *J Magn Magn Mater* 385:222–229
21. El-Gaied A, Hamad MAA (2013) MHD forced convection laminar boundary layer flow of alumina-water nanofluid over a moving permeable flat plate with convective surface boundary condition. *J Appl Math*. 403210.
22. Majeed A, Zeeshan A, Alam T (2022) Mathematical analysis of MHD CNTs of rotating Nanofluid flow over a permeable stretching surface. *Arabian J Sci Eng*. 12:1–11
23. Alsaedi A, Muhammad K, Hayat T (2022) Numerical study of MHD hybrid nanofluid flow between two coaxial cylinders. *Alexandria Eng J*. 61(11):8355–8362
24. Pattnaik PK, Bhatti MM, Mishra SR, Abbas MA, Beg OA (2022) Mixed Convective- Radiative dissipative magnetized micropolar nanofluid flow over a stretching surface in porous media with double stratification and chemical reaction effects: ADM-Pade Computation. *J of Mathematics*, Article ID 9888379.
25. Sheikholeslami M, Ganji DD, Younus M, Ellahi R (2015) Effect of thermal radiation on magneto-hydrodynamics nanofluid flow and heat transfer by means of two phase model. *J Magn Magn Matr*. 373:36–43
26. Bhatti MM, Abbas T, Rashidi MM, El-Sayed M (2016) Numerical simulation of entropy generation with thermal radiation on MHD carreau nanofluid towards a shrinking sheet. *Entropy* 18:200
27. Shahid A, Bhatti MM, Beg OA, Kadir A (2018) Numerical study of radiative Maxwell viscoelastic magnetized flow from a stretching permeable sheet with the Cattaneo-Christov heat flux model. *Neural Comput Appl* 30:3467–3478
28. Chan SQ, Aman F, Mansur S. (2018) Sensitivity analysis on thermal conductivity characteristics of a water-based bionanofluid flow past a wedge surface. *Math Probl Eng*. Article ID 9410167
29. Hussain D, Asghar Z, Zeeshan A, Alsulami H. Analysis of sensitivity of thermal conductivity and variable viscosity on wall heat flux in flow of viscous fluid over a porous wedge. *Int Comm in Heat and Mass Transf*. doi.org/<https://doi.org/10.1016/j.icheatmasstransfer.2022.106104>
30. Abdelmalek Z, Mahanthesh B, Basir MF, Imtiaz M, Mackolil J, Khan NS, Nabwey HA, Tlili I (2020) Mixed radiated magneto Casson fluid flow with Arrhenius activation energy and Newtonian heating effects: Flow and sensitivity analysis. *Alexandria Eng J* 59(5):3991–4011
31. Rashidi S, Bovand M, Esfahani JA (2015) Heat transfer enhancement and pressure drop penalty in porous solar heat exchangers: A sensitivity analysis. *Energy Convers Manage* 103:726–738
32. Rashidi S, Bovand M, Esfahani JA (2015) Structural optimization of nanofluid flow around an equilateral triangular obstacle. *Energy* 88:385–398

33. Mackolil J, Mahanthesh B (2021) Optimization of heat transfer in the thermal Marangoni convective flow of a hybrid nanomaterial with sensitivity analysis. *Appl Math Mech* 42(11):1663–1674
34. Hatami M, Sheikholeslami M, Ganji DD (2014) Nanofluid flow and heat transfer in an asymmetric porous channel with expanding or contracting wall. *J Mol Liq* 195:230–239
35. Marin M, Nicaise S (2016) Existence and stability results for thermoelastic dipolar bodies with double porosity. *Contin Mech Therm* 28(6):1645–1657
36. Majdalani J, Zhou C (2003) Moderate to large injection and suction driven channel flows with expanding or contracting walls. *J Appl Math Mech Z Angew Math Mech*. 83(3):181–196
37. Sriniv S, Subramanyam A, Ramamohan TR (2012) A study on thermal-diffusion and diffusion-thermo effects in a two-dimensional viscous flow between slowly expanding or contracting walls with weak permeability. *Int J Heat Mass Transf* 55:3008–3020
38. Majdalani J, Zhou C, Dawson CA (2002) Two-dimensional viscous flow between slowly expanding or contracting walls with weak permeability. *J Biomech* 35(10):1399–1403
39. Mabood F, Khan WA, Ismail AI (2014) Optimal homotopy asymptotic method for heat transfer in hollow sphere with robin boundary conditions. *Heat Tran Asian Res*. 43(2):124–133
40. Khan LA, Raza M, Mir NA, Ellahi R (2020) Effects of different shapes of nanoparticles on peristaltic flow of MHD nanofluids filled in an asymmetric channel. *J Therm Anal Calorim* 140(3):879–890
41. Dogonchi AS, Alizadeh M, Ganji DD (2017) Investigation of MHD Go-water nanofluid flow and heat transfer in a porous channel in the presence of thermal radiation effect. *Advanced powder Tech* 28:1815–1825
42. Ghorbanian A, Tahari M, Hatami M (2017) Physical optimization of a wavy porous cavity filled by nanofluids in the of solar radiations using the box-Bahnken design (BBD). *Eur Physi J*. 132(6):1–19
43. Opanuga AA, Gbadeyan JA, Iyase SA, Okagbue HI (2016) Effect of thermal radiation on the entropy generation of hydromagnetic flow through porous channel. 17(2):59–68